Geostatistical methods for improved quantification of ice mass bed topography

Submitted by Oliver Thomas Bartlett to the University of Exeter

as a thesis for the degree of

Doctor of Philosophy in Physical Geography

In March 2020

I certify that all material in this thesis which is not my own work has been identified and that no material has previously been submitted and approved for the award of a degree by this or any other University.

Signature:

For Cynthia and George,

For always believing in the dream no matter what it was at the time.

Thank you.

Abstract

Contribution to global mean sea level rise by ice sheets, ice caps and glaciers is accelerating. The total volume of water stored globally in terrestrial ice is estimated by a multitude of methods but principally by the interpolation of ice-thickness data. For the ice sheets and large Arctic ice caps, ice thickness is predominantly measured by airborne radio-echo sounding surveys which use radio waves to detect the bed of the surveyed ice mass. While such surveys are now extensive, large portions of ice masses are generally unsurveyed due to their size. In order to quantify ice thickness and subsequently ice volume over the entirety of an ice mass, interpolation of the input measurements is used. Throughout this whole process, uncertainties arise. Initially, from the radio-echo sounding (RES) survey and subsequently, in the interpolation. Compounding this is the absence of ground-truthing for measurements and interpolations due to the inaccessibility of ice mass beds. Hence, there is a requirement to find alternative means of quantifying uncertainty in ice thickness measurements and subsequently derived bed topography, and analyses made from these data to reduce the uncertainty in sea level change projections.

This thesis develops and applies methods which aim to reduce uncertainty in ice thickness and bed topography datasets. Using high-resolution elevation data, this study exploits the likely similarity between currently ice-covered topography and formerly glaciated topography in the Arctic to generate datasets which provide alternative validation for ice mass bed topography. For the first time topographic error in RES surveying is quantified and corrections are formulated for treating future and historic ice thickness and bed topography data. Additionally, the propagation of these uncertainties through interpolations of bed topography is quantified and reduced, focussing on the Greenland Ice Sheet. Finally, the full suite of methods is applied to ice caps in the Canadian Arctic to generate, for the first time, ice cap wide topography for ice caps in the region that hold approximately a third of the freshwater outside of the continental ice sheets. By quantifying and reducing uncertainty in datasets of bed topography and ice thickness this thesis assesses the perceived stability of the continental ice sheets and large ice Arctic ice caps. From this, the implications of this for near and far term global mean sea-level rise are investigated.

Acknowledgements

I would like to acknowledge the National Environmental Research Council Great Western Four Plus Doctoral Training Partnership for funding this research.

To Steve Palmer, thank you for your support from day one of me starting this PhD. Not just in your dedicated and enthusiastic supervision of my project but also as a mentor and a friend. Thank you for the opportunities to travel to incredible cold places. You will forever have my gratitude for the support in Nepal and making that trip something we can laugh about. Finally, thank you to both you and Katharine for putting me up at the beginning when my poor planning skills meant I was otherwise living in a hostel/the library.

To Tim Barrows, thank you for not only providing supervision to my PhD but also for being a friend and a fountain of wisdom for undertaking a doctoral degree. I will forever be grateful to you for the support in Nepal and making it a trip to remember for the right reasons. Apart from Paradise Lodge which can never be remembered for a right reason.

To Ali Graham, Anne Le Brocq and Damien Mansell thank you for the additional academic support and extra-curricular discussions along the way which have shaped both this project and my development as an academic. Here's to hopefully working with you all again.

Thank you to Dustin Schroeder for extending an invitation for me to work with his Radio Glaciology group at Stanford and helping guide the development of parts of this PhD. The opportunity to visit Stanford and collaborate with you and your group has been invaluable.

Thank you to Mickey MacKie, Stephen Cornford, Matthew Palmer, and Mathieu Morlighem for insightful comments and discussions which have helped focus parts of this research.

Thank you to Helen, Paddy, Rory and Lottie Plewman for hosting me on my visits to the states, a huge chunk of this research wouldn't have happened without you

My heartfelt thanks go out to Su and Brad Bartlett for the everlasting support that you have provided throughout my life leading up to this, for always supporting my decisions (even if they meant not going on to build aeroplanes) and picking me up whenever I needed that extra faith in myself. Without your dedication to, well…

me, I wouldn't be where I am today. The following words and pretty maps are for you.

To Laura and Paddy Bartlett thank you for all the love and support over the how ever many years old you are now. Other than the childhood years when you royally got on my nerves.

Tom Murrant, Jodie Gough, Nikos Sfoungaros, and Joe Booth you were truly exceptional housemates. Thank you for keeping me relatively sane over the past 3.5 years. The banter had in the Saxon Road kitchen will live long in the memory.

Frank Burton-Choonara, Joe Plenty, Matt Fletcher, Alex Bell and Dan Askew, the home boys, as always your love and support have kept me going. Without the annual Cobra meeting at Maharajah (or whatever it's called these days to get around hygiene standards) I quite simply would've given up.

Thank you, Sam Dawkins. Thank you for the away days. Thank you for the sessions. Thank you for the support from the day we first took a cheeky rendezvous on mentoring duty.

To Ryan Moss, thanks man without you I wouldn't have even got here to do this, you are nothing short of an absolute hero.

To Tom Roland, cheers mate. From one Bristol boy to another thank you for being my chief source of footie chat in Exeter, it genuinely made all the difference. Also thank you for giving me the opportunity to develop a new skill to shoe-horn into this thesis. I look forward to working with you in the future.

Thank you to the Parkers Road and Watson Road mandem, and whatever the name of our WhatsApp group is at the time of submission. Your support throughout undergrad is one of the main reasons I managed to complete education lads. Next time we're in the Steel City the Balti King is on me lads.

To Lottie Pearson, Daneen Cowling, and Vicky Naylor, thanks for letting me vent to you in the office about pretty much everything and for making said office a much less blue place.

I would also like to thank Nina Leonard.

Table of Contents

List of figures and tables

Figures

Tables

Definitions

Outlined below are abbreviations used throughout this thesis.

CAA	Canadian Arctic Archipelago
DEM	Digital elevation model
DME	Difference from Mean Elevation
EGA	East Greenland Analogue
GrIS	Greenland Ice Sheet
MO	Margin orthogonal
MP	Margin parallel
OIB	Operation IceBridge
POW	Prince of Wales ice cap
QEI	Queen Elizabeth Islands
RES	Radio-echo sounding
RMSD	Root-mean-square deviation
RMSE	Root-mean-square error

Chapter 1: Introduction

1.1 Rationale

Global mean sea-level (GMSL) rise is one of a suite of consequences of climate change that pose socioeconomic and ecological hazards to humanity (Clark et al., 2016). Increasingly, mass loss from ice sheets, ice caps and glaciers is outpacing the contribution of thermal expansion to sea-level rise (IPCC, 2019). Quantification of the total volume of freshwater held by terrestrial ice-masses is fundamental for assessing the cryosphere's sea-level budget and for projecting its potential contribution to sea-level rise in the future (WCRP, 2018). Additionally, the rate at which the cryosphere will contribute is required for assessing the possible near and far-term impacts of GMSL rise (Golledge et al., 2019). The Greenland and Antarctic Ice Sheets are the largest potential contributors to future sea-level rise and are currently contributing six times as much as they were during the 1990s (Shepherd et al., 2018; Shepherd et al., 2019). Consequently, an estimated 17.8 mm has been added to GMSL from the continental ice sheets since 1992. However, the rate at which they will continue to contribute remains highly uncertain (Shepherd and Nowicki, 2017). This largely arises from the complexity involved in modelling rapid responses of the ice dynamic component of mass loss from the ice sheets to climatic forcing (Ritz et al., 2015; Pattyn et al., 2018). A fundamental control on this is the bed topography beneath the ice sheets as it determines the broad direction of ice flow and the amount of friction at the bed which either enables or precludes fast flow regimes (Bamber et al., 2013; Favier et al., 2014). Crucially, this is also highly uncertain in places and further research is required to refine it (Shepherd and Nowicki, 2017). Hence, this thesis will aim to reduce the uncertainty in ice mass bed topography and consequently, reduce uncertainties in ice dynamic mass loss and the future contribution of ice masses to sea-level rise.

Current sea-level projections, made by the Coupled Model Intercomparison Project Phase 6 (CMIP6, Eyring et al., 2016), will use dynamic ice sheet models as part of the ensemble for the first time (Ice Sheet Model Intercomparison Project Phase 6 [ISMIP 6], Nowicki et al., 2016, Barthel et al., 2020). Accordingly, the accuracy of projections from these is reliant on the accuracy of ice sheet models, which in turn are reliant on the accuracy of the input data. Two of the fundamental boundary conditions for these models are ice thickness and ice sheet bed

elevation datasets (Larour et al., 2012; Cornford et al., 2013). These are widely derived from the interpolation of ice thickness measurements made by airborne radio-echo sounding (RES) surveys (Bamber et al., 2013). While uncertainty in the airborne RES surveys that comprise most ice thickness measurements are parameterised (Paden et al., 2010; Blankenship et al., 2012), they are often generalised (Lapazaran et al., 2016). Surveys which cross-profile the major outlets of the Greenland and Antarctic Ice Sheets provide a base input for quantifying ice discharge to the oceans (Rignot and Kanagaratnam, 2006; Shepherd et al., 2012). Whereas, outlet centreline flights are important to numerical modelling as bed topography in this direction is a fundamental control on both ice velocity and ice mass stability (Oerlemans, 1997; Gladstone et al., 2012). To refine RES inputs to ice sheet models and estimates of mass loss from ice discharge, this thesis will endeavour to quantify uncertainty in RES measurements in more detail than previously achieved.

Extensive volumes of data exist for ice thickness and bed topography (Gärtner-Roer et al., 2014). From such data, ice volume estimates for the continental ice sheets correspond to a potential contribution to GMSL rise of 64.6 m (Fretwell et al., 2013; Morlighem et al., 2017). Additionally, for ice caps and glaciers, the potential contribution is estimated to be 0.4 m (Huss and Farinotti, 2012). Currently, uncertainties in ice thickness and bed topography data are generally approximated from 10 – 70 m to account for the various errors which arise in the methods used for measurement (Rignot et al., 2019; Enderlin et al., 2014; King et al., 2018). Furthermore, these uncertainties are propagated and exacerbated through to analytical outputs made from ice thickness data. Initially, through ice mass wide datasets of subglacial topography (Morlighem et al., 2017; Morlighem et al., 2020). Subsequently, uncertainties that are carried through and augmented by the generation of subglacial topography then impact estimates of the dynamic component of ice mass loss (Shepherd et al., 2019), and projections of its potential sea-level contribution (van de Wal et al., 2019). However, these uncertainties are not necessarily well constrained due to the logistical challenge of validating ice thickness measurements. This thesis investigates how to quantify and reduce the impact of such uncertainties in the absence of independently validated measurements of ice thickness.

1.2 Background

1.2.1 Terrestrial ice mass balance and sea-level

Ice sheets, ice caps and glaciers globally are losing mass in response to rising mean Earth surface temperature (Church et al., 2013). Terrestrial ice mass loss leads to glacioeustatic sea-level rise, the rate of which is increasing (WCRP, 2018). Currently, 1.38 ± 0.35 mm yr^{-1} of GMSL rise is being added to the oceans from the cryosphere (WCRP, 2018). Forecasting how this rate will change in the future is complex and highly uncertain (van de Wal et al., 2019).

Glacioeustatic sea-level rise is a consequence of net negative mass balance across terrestrial ice masses. Generally, alpine and land-terminating ice cap and ice sheet margins have negative mass balance when surface ablation outweighs accumulation from snowfall. For marine-terminating glaciers, overall negative mass balance occurs where solid ice discharge across the grounding line, the dynamic mass balance, outweighs the positive component of surface mass balance. Overall negative mass balance is therefore exacerbated for marine-terminating glaciers where the surface mass balance component is also negative. Consequently, freshwater is added to the oceans more than it is sequestered in snowfall over terrestrial ice (Bamber et al., 2018a). However, it is important to note that ice grounded below sea-level and below the buoyancy height does not increase sea-level as the mass is lost from the ice sheet (Sutterly et al., 2014). Furthermore, where meltwater is utilised as a resource or drains into endoheric basins from ice caps and glaciers it does not raise sea-level (Brun et al., 2017).

Global terrestrial ice mass balance rate has most recently been estimated at -665 ± 48 Gt yr^{-1} for 2012 – 2016 (1.85 ± 0.13 mm yr^{-1} sea-level equivalent, Bamber et al., 2018b). Importantly, high interannual variability exists in the mass balance signal over the observation period (Bamber et al., 2018b). Interannual variability is largest for surface mass balance processes where it ranges from $\pm 100 - \pm 250$ Gt yr^{-1} for the ice sheets (Rignot et al., 2019; McMillan et al., 2016), and $\pm \sim 40$ Gt yr^{-1} over glaciers and ice caps (Marzeion et al., 2017). This makes extrapolating the mass balance rates into the future problematic (Wouters et al., 2013). Furthermore, although variability in dynamic mass balance is typically lower (~ 20 Gt yr^{-1}, Mouginot et al., 2019), it comprises complex processes which are inherently difficult to model into the future (Stearns and van der Veen, 2018;

Catania et al., 2020). Hence, measuring mass balance accurately and widely as possible aids any attempt to predict changes to terrestrial ice mass balance rates into the future (Bamber et al., 2018b). Additionally, research into the processes that influence the various components of mass balance may better inform future predictions.

Multiple methods are used to monitor mass balance. Namely, satellite altimetry (Wingham et al., 2006), gravimetry (Velicogna and Wahr, 2006), and the mass budget method (Rignot et al., 2008). However, only the mass budget method can partition the surface and dynamic processes contributing to the overall mass balance of an ice mass using an input/output approach (van den Broeke et al., 2009). Understanding mass balance processes so that they can be well constrained in numerical models is essential for robust projections of GMSL contribution from ice sheets, ice caps and glaciers (Goelzer et al., 2018; Seroussi et al., 2019). This is of particular importance for the dynamic component of mass balance, as it is hypothesised that GMSL rise exceeding 1 m by the end of the century requires significant dynamic mass loss from the continental ice sheets (Church et al., 2013; DeConto and Pollard, 2016).

Dynamic mass balance is determined from solid ice discharge across an outlet glacier grounding line (Howat et al., 2007). To estimate this quantity, measurements of ice thickness or bed topography and velocity are required. Velocity is typically well sampled as it is derived from regularly acquired satellite imagery with nearly global coverage (Joughin et al., 2010; Fahnestock et al., 2015). However, measurements of ice thickness and bed topography are far more difficult to acquire at scale. Hence, these inputs are either derived from sparsely acquired geophysical measurements (Rodriguez-Morales et al., 2014; Pritchard, 2014), or from unsampled areas where these measurements have been interpolated (Bamber et al., 2013). Consequently, thickness and bed topography errors contribute an order of magnitude more uncertainty (10 - 100 m) than velocity measurements (1 - 10 m yr^{-1}) to dynamic mass balance calculation (van Wychen et al., 2016; Mankoff et al., 2019). While there are ongoing efforts to refine these uncertainties (Morlighem et al., 2020), much they are still largely unconstrained (Lapazaran et al., 2016).

Although terrestrial ice volume in the Arctic is an order of magnitude less than in the Antarctic (Vaughan et al., 2013) since the early 1990s ice loss in the region

has contributed to approximately 30% of eustatic sea-level rise and has been the largest regional source of terrestrial ice loss (Box et al., 2018). Into the future, the relative contribution of northern hemisphere ice loss is dependent on whether dynamic instabilities transpire across the West Antarctic Ice Sheet (DeConto and Pollard, 2016). However, these processes are highly uncertain (Pattyn et al., 2018). Consequently, ice mass loss in the northern hemisphere is a pressing concern for coastal communities planning for current century sea-level rise (Calov et al., 2018; Golledge et al., 2019). Current projections emphasise the increasing rate and predominance of Arctic ice mass loss contribution to rising sea levels (Golledge et al., 2019; Hanna et al., 2020). Additionally, the rising regional mean temperature is expected to enhance the contribution of ice dynamics from the Greenland Ice Sheet, particularly across outlets where solid ice discharge is currently minimal (Mouginot et al., 2019; Mankoff et al., 2019). Increased dynamic mass loss from Greenland is, therefore, a crucial component of future GMSL rise. As the dynamic component of mass loss can only be derived from the mass budget method, any uncertainties in the inputs to this method limit the predictive capabilities of ice sheet models aiming to predict the ice dynamic component of GMSL contribution (Barthel et al., 2020). One of these fundamental inputs is terrestrial ice mass bed topography. As such efforts are continually made to improve quantification of this crucial condition, which is correspondingly the overarching aim of this thesis.

Discussed in the following sections are the ice masses investigated in detail by this thesis and their contribution to GMSL. These ice masses are the Greenland Ice Sheet (GrIS, section 1.2.1.1) and ice caps and glaciers in the Canadian Arctic Archipelago (CAA, section 1.2.1.2).

1.2.1.1 Greenland Ice Sheet

The GrIS has a potential GMSL rise contribution of approximately 7.42 ± 0.05 m (Figure 1.1; Morlighem et al, 2017). Furthermore, it is now estimated to be the single largest contributor to the current rate of sea-level rise at ~1 mm yr^{-1} (Box and Sharp, 2017, WCRP, 2018). Mass is predominantly lost from the ice sheet due to surface runoff, -139 ± 38 GT yr^{-1}, as opposed to dynamically, -105 ± 47 GT yr^{-1} (Shepherd et al., 2019). Although historically, the dynamic output from the GrIS has dominated its contribution to GMSL rise, with $66 \pm 8\%$ of mass loss since 1972 having occurred dynamically (Mouginot et al., 2019). Moreover, ~12%

of this discharge occurred through less than 1% of the GrIS's outlet glaciers (MacMillan et al., 2016). This is important as significant potential exists for the remaining outlets to contribute considerably more with increased warming over the northernmost portions of the ice sheet (Tedesco et al., 2016; Moughnot et al., 2019). Nevertheless, multiple positive feedbacks are suggested for the GrIS that predict increasingly negative surface mass balance will be the dominant mechanism for mass loss into the future (Edwards et al., 2014; Calov et al., 2018). However, greater uncertainty exists for the dynamic component which currently makes up for approximately 49% of GrIS mass loss (Van den Broeke et al., 2016; Shepherd et al., 2019).
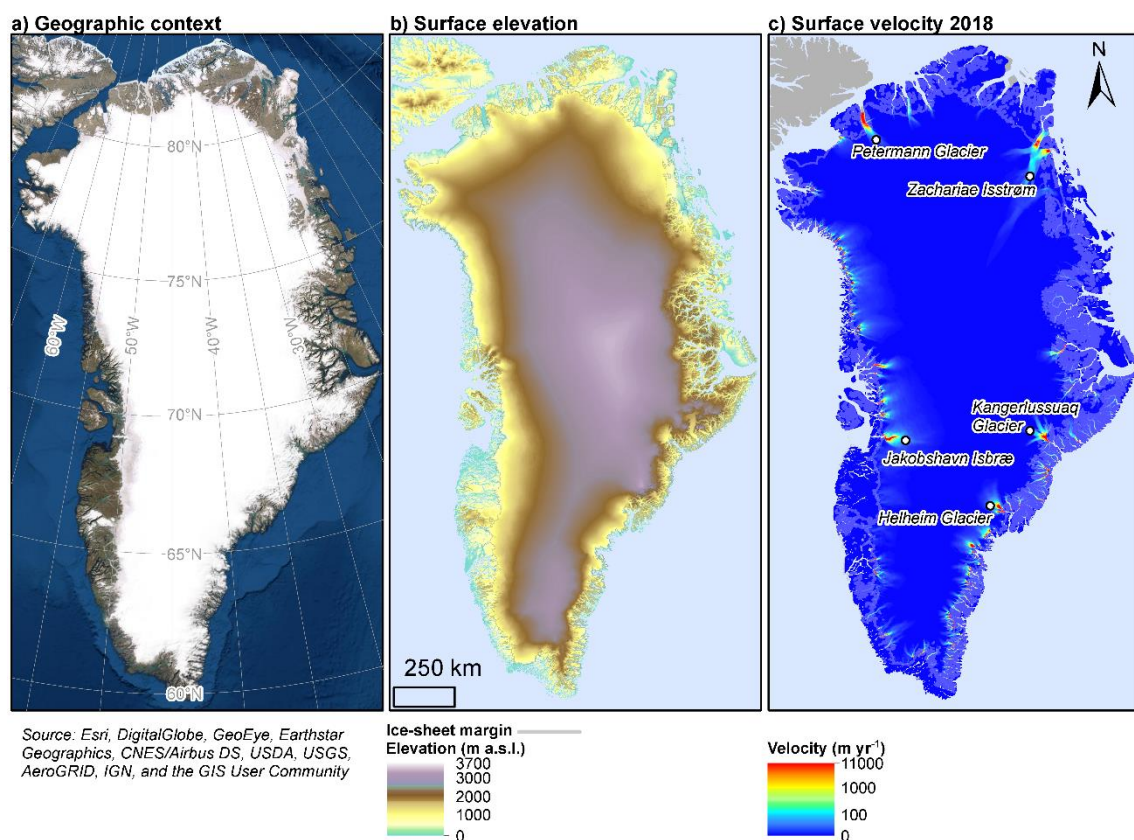
Figure 1.1 GrIS in context. a) Geographic context of the GrIS. b) Surface elevation of the GrIS and surrounding ice-free topography from the ArcticDEM (Porter et al., 2018). c) 2018 surface velocity composite of the GrIS from the MEaSUREs Greenland Ice Mapping Project (Joughin et al., 2018).

Mass loss from the GrIS has been highly variable for the observational period (Shepherd et al., 2012; Shepherd et al., 2019). Interannual variability in surface mass balance, 28%, is much greater than that of dynamic mass balance, 5% (MacMillan et al., 2016; Hanna et al., 2020). This is important as atmospheric

warming is deemed to be the dominant control on mass loss from the GrIS (Trusel et al., 2018). However, ice sheet albedo and melt events are intrinsically linked with complex atmospheric conditions that are notoriously difficult to model (Hanna et al., 2016). Additionally, biological albedo from ice sheet surface algal blooms is found to be increasingly important for GrIS surface melting and quantification of this influence is novel and ongoing (Stibal et al., 2017). All the above is compounded for marine-terminating outlet glaciers where oceanic changes also control mass loss (Schaffer et al., 2020). Simulations project current century mass loss from the GrIS to increase GMSL by 70 to 300 mm, dependent on model choice and climate scenario (Calov et al., 2018; Goezler et al., 2018). Similarly, variability in the modelled contribution from outlet glaciers is large, ranging from 8 to 45% of mass loss due in part to uncertainty in modelling dynamics (Aschwanden et al., 2019).

While dynamic mass balance is less variable, future trends are difficult to predict as currently only a handful of Greenland's ~300 outlet glaciers are dominating solid ice discharge from the ice sheet (Rignot and Mouginot, 2012; Mankoff et al., 2019). With atmospheric and oceanic warming, solid ice discharge will increasingly source from additional outlet glaciers particularly across the northern coastline (Mouginot et al., 2019; Hanna et al., 2020). It has been recently found that increased summer air temperatures correspond with mass loss acceleration around southeast and northeast GrIS outlet glaciers (Bevis et al., 2019). As the ice sheet is topographically sensitive to warming, there is potential for future melting to alter surface gradients and gravitational driving stresses, leading to increased acceleration and solid ice discharge (Bevis et al., 2019). Furthermore, floating ice tongues that occur across major outlets in the north of Greenland are likely to be removed by increased atmospheric warming (Mouginot et al., 2019), removing the buttressing effect they impose on the outlet glaciers upstream (Dupont and Alley, 2005). The associated speed up after removal of these ice tongues will significantly increase the discharge from the Northern and Northeast regions which contain ~ 3 m of potential GMSL rise (Mouginot et al., 2019). Undoubtedly, dynamic mass balance will remain a significant component of GrIS mass loss over the next century as it has over the observational period (Calov et al., 2018; Aschwanden et al., 2019; Mouginot et al., 2019). As such quantification

of ice discharge must be as accurate as possible, and the controlling processes well understood.

Measurement of GrIS bed topography has been conducted ever since seismic surveys undertaken in 1926 (Sorge, 1933). Now, nearly 600,000 kilometres of RES data exist which measure the ice sheet bed along survey flight-lines (Rodriguez-Morales et al., 2014). Furthermore, all of this has been interpolated to generate spatial complete 3D bed topography for the entire ice sheet. From these data, solid ice discharge has been measured and dynamic mass balance estimated (Enderlin et al., 2014; King et al., 2018; Shepherd et al., 2019). From these studies, the foundations for predicting how the GrIS will evolve with climate change exist (Nowicki et al., 2016; Aschwanden et al., 2019; Barthel et al., 2020). However, any uncertainty in the inputs, whether measured or interpolated will propagate through these analyses and future projections. Crucially for marginal areas, which are the most important in terms of discharge (Morlighem et al., 2014), RES surveys perform poorly (Gogineni et al., 2001; Farinotti et al., 2013; Gogineni et al., 2014), and uncertainties propagated through interpolation are greatest (Millan et al., 2018).

While high uncertainty exists concerning the rate of contribution from the Antarctic Ice Sheets (Golledge et al., 2019), it is widely expected that mass loss from the GrIS will accelerate and remain the largest single cryospheric source of GMSL over the next century (Figure 1.2; Golledge et al., 2019). Therefore, having well-constrained estimates of the factors which influence mass loss from the GrIS is essential for predicting the rate at which the ice sheet will add to GMSL. One of these factors being the bed topography of the ice sheet which strongly influences its dynamic mass loss (Morlighem et al., 2017; King et al., 2018). Hence, this thesis will comprehensively investigate the uncertainty in GrIS bed topography data and aim to quantify and reduce it where possible.
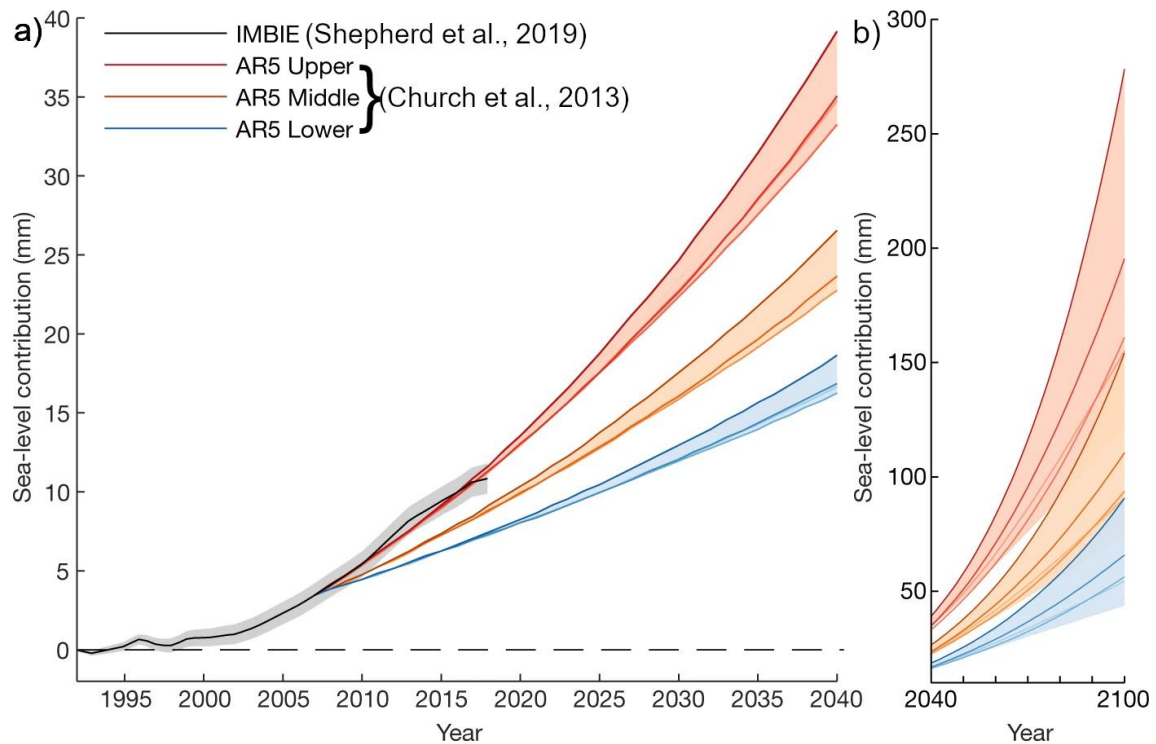
Figure 1.2 Estimated contribution to GMSL from the GrIS. a) Estimated sea-level contribution of the GrIS from 1990 to 2019 (black line with grey uncertainty bounds) compared with projected contribution from 2007 to 2040 from the 2013 IPCC report dependent on emissions scenarios (blue, RCP 2.6; orange, RCP 4.5; red, RCP 8.5; Church et al., 2013). b) IPCC projections from 2040 to 2100 for the three emissions scenarios. Adapted from Shepherd et al., 2019.

1.2.1.2 Canadian Arctic Archipelago ice caps and glaciers

Outside of the GrIS, glaciers and ice caps in the CAA (Figure 1.3) have the next largest total potential GMSL contribution of the Arctic ice masses (Huss and Farinotti, 2012; Farinotti et al., 2019). Importantly, glaciers and ice caps have until recently been the dominant source of GMSL rise (Hock et al., 2019; Zemp et al., 2019). Over the past 50 years, glaciers and ice caps have added ~3 cm to GMSL and at an accelerated rate over the past decade (Zemp et al., 2019). For 2006 to 2016, GSML rise contribution was observed at a rate of 0.92 ± 0.39 mm yr^{-1}, almost double the average rate for the observational period (0.5 ± 0.4 mm yr^{-1}, Zemp et al., 2019). This is exacerbated in the Arctic, where the regional mean temperature is rising at twice the rate of the global mean due to the Arctic amplification effect (Overland et al., 2016). Generally, this is expected to lead to increased melting of CAA ice caps which will have a compounding effect on current century sea-level rise (Hock et al., 2019). As it is expected that glaciers

in the CAA will be large contributors to current century sea-level rise they must be comprehensively researched (Zemp et al., 2019).

a) Geographic context

Source: Esri, Maxar, GeoEye, Earthstar Geographics, CNES/Airbus DS, USDA, USGS, AeroGRID, IGN, and the GIS User Community

b) Surface elevation

Elevation (m a.s.l.)
2700
2000
1000
0

c) Surface velocity

Velocity (m yr⁻¹)
500
300
150
0
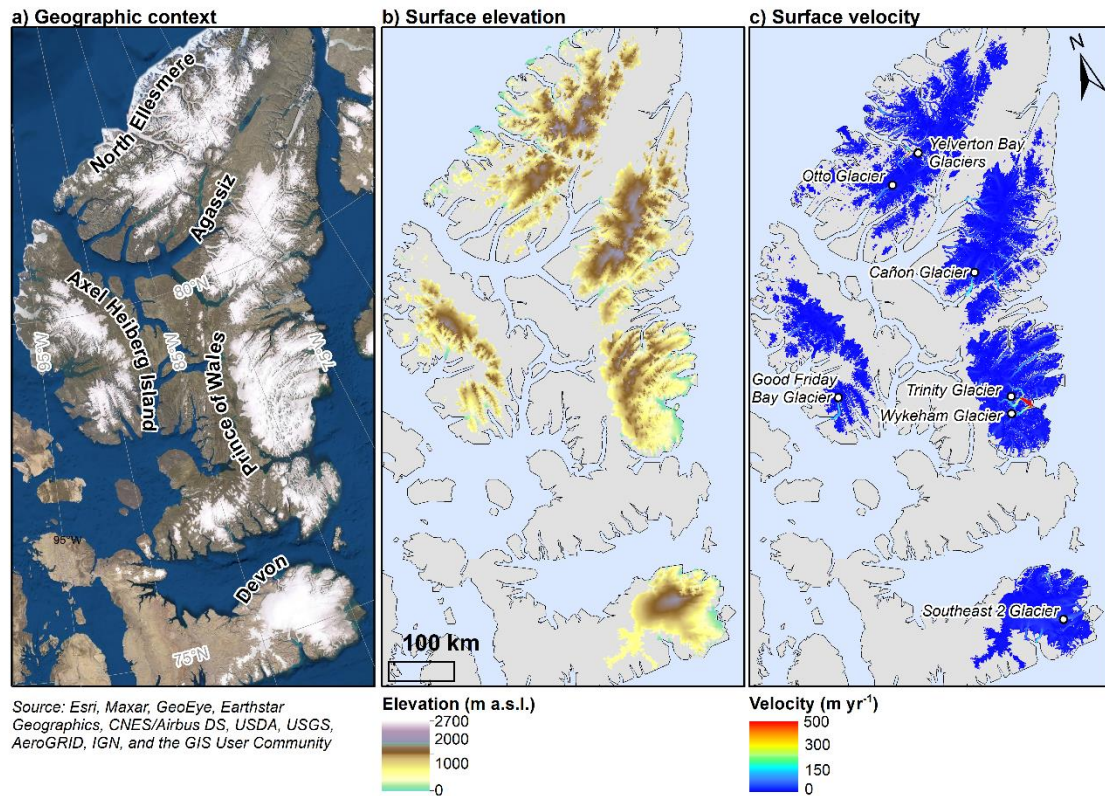
Figure 1.3 CAA ice caps in context. a) Geographic context of the CAA ice caps investigated in this thesis. b) Surface elevation from the ArcticDEM (Porter et al., 2018) for the CAA ice caps. c) 2018 surface velocity composite of the CAA ice caps from ITS_LIVE (Gardner et al., 2019).

Approximately one-third of terrestrial ice outside of the continental ice sheets is contained in glaciers and ice caps on the Queen Elizabeth Islands (QEI), in the Canadian Arctic Archipelago (Radic and Hock, 2010). The total sea level equivalent of ice in the northern CAA is estimated at 64.8 ± 16.8 mm w. e. (Farinotti et al., 2019). Over the past decade (2006 – 2016), mass loss from the region has added 0.5 ± 0.8 mm yr⁻¹ to GMSL (Zemp et al., 2019). This constitutes a fivefold acceleration when compared to the mean rate over the period 2003 – 2009 (0.09 mm yr⁻¹, Gardner et al., 2013). At least 14.7 ± 8.0 mm of GMSL rise equivalent is predicted to be lost from the entire CAA under the RCP 2.6 emissions scenario, with ~70% occurring from the QEI ice caps (Hock et al., 2019). For the RCP 8.5 emissions scenario, it is estimated as much as 33 mm of GMSL could be added from the entire CAA (Figure 1.4; Radic et al., 2014; Huss and Hock, 2015).
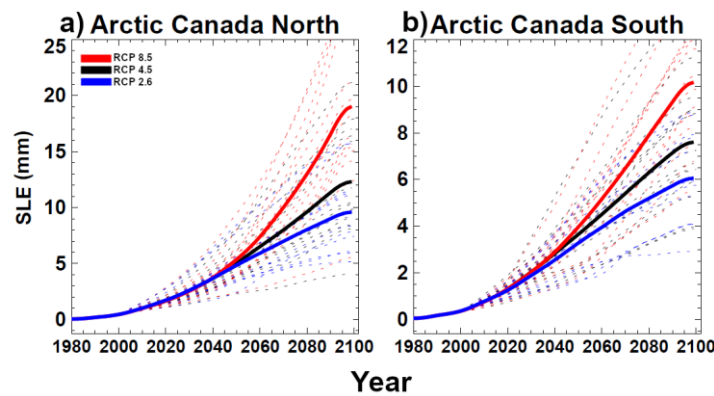
Figure 1.4 Estimated contribution to GMSL from the CAA. a) Estimated sea-level contribution of CAA ice caps in the Randolph Glacier Inventory region "Arctic Canada North" from 1980 to 2100 following the three highlighted RCP emissions scenarios from the 2013 IPCC report (WGMS, 2017; Church et al., 2013). b) Estimated sea-level contribution of CAA ice caps in the Randolph Glacier Inventory region "Arctic Canada South" from 1980 to 2100 following the three highlighted RCP emissions scenarios from the 2013 IPCC report. Adapted from Huss and Hock, 2015.

Mass balance in the region is typically dominated by surface processes as models suggest ablation occurs over the full extent of the ice caps in the Arctic summer (Colgan et al., 2015). However, complex dynamic variability is observed across the region's outlet glaciers (Van Wychen et al., 2016). Hence, dynamic mass loss in the region is complex and as yet not entirely well constrained. While mass balance observations across the region are limited (Millan et al., 2017), modelling studies have aimed to estimate it yet require higher resolution surface elevation data to adequately predict the surface mass balance component. Additionally, measurements of bed topography are numerous yet full 3D bed topography has only been quantified for one ice cap (Dowdeswell et al., 2004). Consequently, estimates and projections of dynamic mass balance are limited in scope.

CAA ice caps have been surveyed by airborne RES since the first successful tests over the North Ellesmere and Axel Heiberg Island ice caps in 1964 (Evans and Robin, 1966). With initial surveys of every ice cap having been achieved since 1977 (Koerner, 1977). From these measurements, multiple assessments of the dynamic contribution of CAA ice caps to GMSL have been conducted (Shepherd et al., 2007; Van Wychen et al., 2014; Millan et al., 2017). Current

estimates find dynamic discharge from the QEI ice caps to total 2.21 ± 0.68 Gt yr^{-1}. Interannual variability (~0.8 Gt yr^{-1}, 36% variability) complicates the discharge signal from the region. Most glaciers have decelerated, and discharge decreased yet two glaciers which contribute to ~60% of regional discharge have accelerated (van Wychen et al., 2014; Van Wychen et al., 2016). Additionally, very few flow orthogonal surveys have been flown, so many discharge estimates are calculated from interpolated ice thicknesses which introduces further uncertainties (Van Wychen et al., 2014).

Full 3D bed topography does not currently exist for all CAA ice caps except from the Devon Island ice cap (Dowdeswell et al., 2004). A requirement, therefore, exists to develop bed topography datasets for ice caps in the CAA (Moon et al., 2018). Furthermore, due to the absence of RES flux gate bed profiles (Van Wychen et al., 2016), uncertainty in the 3D bed topography must be fully quantified for robust determination of ice discharge in the region. To address these challenges, this thesis will look to develop bed topography data across CAA ice caps as well as quantify and reduce the uncertainty in such datasets.

1.2.2 Bed topography

As mentioned previously, subglacial topography plays a significant role in the evolution of the overlying ice mass. Fundamentally, bed topography is a first-order control on ice velocity (Schoof, 2002). Therefore, it is a principal control on the dynamic component of mass loss from an ice sheet, ice cap or glacier. Its influence occurs over increasing spatial scales, from metres to hundreds of kilometres (Layberry and Bamber, 2001). At the meter scale, bed topography influences important basal friction conditions which modulate the potential for enhanced flow (Paterson, 1994). Bedrock perturbations from tens of metres to kilometres alter local longitudinal stress gradients which modify regional flow (Layberry and Bamber, 2001). Finally, from tens of kilometres upwards, bed topography directs the large scale spatial direction of ice flow (Bentley, 1987; Bamber et al., 2000). Furthermore, ancillary influence on ice velocity arises from the control of meltwater availability to the bed to reduce basal friction (Chu, 2013), which is in part influenced by bed topography (Sergienko, 2013; Palmer et al., 2015).

Figure 1.5 Illustrates the latest bed topography datasets for the continental ice sheets (Morlighem et al., 2017; Morlighem et al., 2020). Mountain ranges interspersed by troughs and plains are exhibited across both ice sheets, all of which exert some control over the rate of ice motion above (e.g. Figure 1.5 labelled features; Layberry and Bamber, 2001; Bamber et al., 2000). Furthermore, enormous sub-sea level basins hydrologically connected to the ocean can be seen. These regions of bed topography have vast potential to influence the future of both ice sheets due to potential inherent dynamic instabilities (Schoof, 2007; DeConto and Pollard, 2016). The following section discusses the importance of bed topography on dynamic mass loss from ice masses and the requirement for accurate knowledge of the bed for predicting the rate of contribution to GMSL in the future.
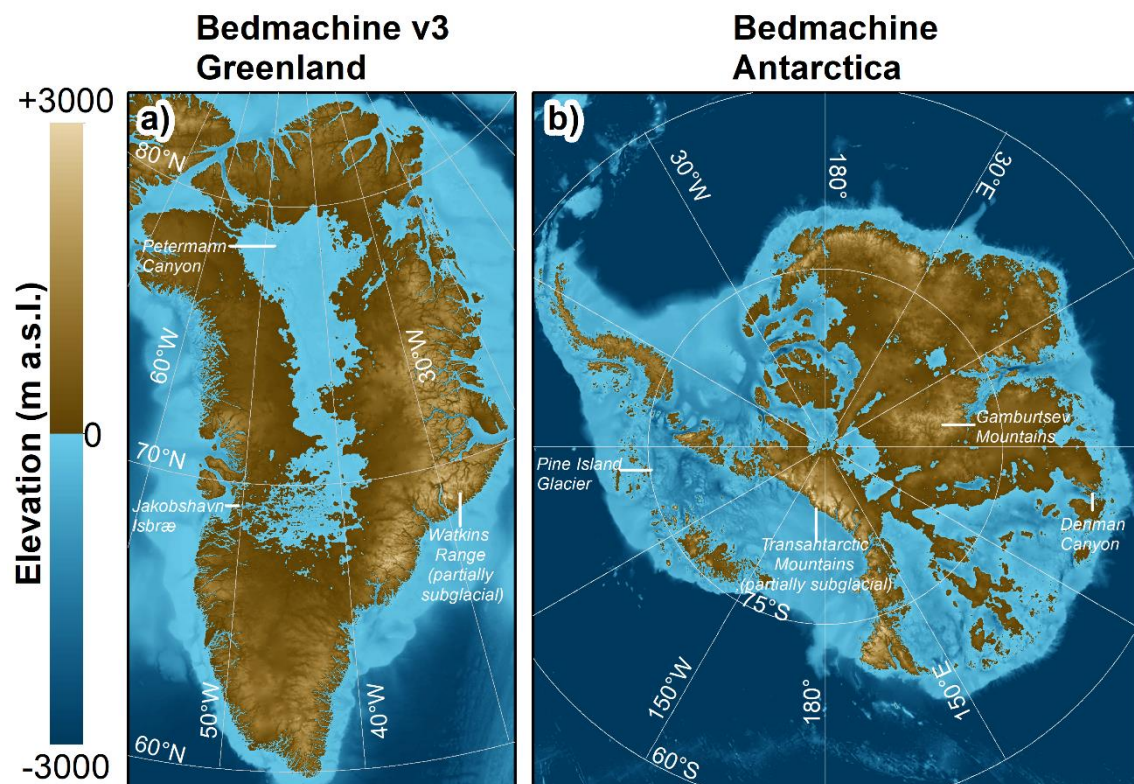
Figure 1.5 Latest bed topography datasets for the continental ice sheets. a) Bedmachine Greenland v3 (Morlighem et al., 2017). b) Bedmachine Antarctica (Morlighem et al., 2020). Examples of subglacial fjords and mountains are highlighted.

Marine terminating outlets of ice masses are susceptible to enhanced dynamics and consequently retreat due to processes controlled primarily by their bed topography. Outlet glaciers across the GrIS and CAA occupy deep, narrow fjords

(Catania et al., 2020; Van Wychen et al., 2014). Such bed geometry combined with the gravitational driving stress from the ice surface slope imposes a force balance which effects how fast the ice can move (van der Veen and Whillans, 1989). Subaerial and subaqueous melting alter the geometry of the outlet glacier which adjusts the gravitational component of flow (Post et al., 2011). Fjord geometry can significantly influence the subaqueous melt component and consequently, outlet glacier dynamics (Brough et al., 2019; Shaffer et al., 2020). Finally, the height above buoyancy, a function of the depth of the bed and the ice thickness, determines the effective pressure at the bed and how quickly the outlet glacier can flow (van der Veen, 1996; Stearns and van der Veen, 2018). This is essential, as the faster the glacier the greater the discharge from the ice mass. For the continental ice sheets, the above may be particularly exacerbated with the potential presence of macro-scale dynamic instabilities which enable significantly enhanced ice loss (Mercer, 1978; Schoof, 2007).

Marine ice sheet instability (MISI) is a process by which enhanced retreat of a marine-based ice sheet is heavily controlled by its bed topography (Hughes, 1975; Joughin and Alley, 2011). Retrograde bed slopes beneath ice sheet outlets grounded below sea-level present as an area of weakness with the advection of deep, warm oceanic waters to the grounding line (Figure 1.6; Schoof, 2007; Joughin et al., 2010). However, it is a theoretical self-sustaining positive feedback for which the potential to lead to accelerated, expansive mass loss is yet to be observed (Vaughn, 2008; Joughin et al., 2014; Edwards et al., 2019). Such bed slopes are common across West Antarctic Ice Sheet glacier beds (Ross et al., 2012). Additionally, they are observed beneath most of Greenlands largest outlets in terms of solid ice discharge (Morlighem et al., 2017; Mankoff et al., 2019). Furthermore, outlet glaciers from CAA ice caps exhibit reverse-sloping beds (Van Wychen et al., 2016; Harcourt et al., 2020). Consequently, the aforementioned regions are all susceptible to enhanced grounding line retreat and subsequently, enhanced dynamic mass loss (Schoof, 2007; Favier et al., 2014). Conversely, if and where the bed topography returns to a prograde slope it can then act to stabilise the outlet glacier after a period of enhanced retreat (Catania et al., 2018; Schoof et al., 2017).

Marine ice-cliff instability (MICI) is postulated to occur where ice thicknesses at marine-termini exceed 800 m so that unstable ice cliffs form that exceed 90 m in

height (Figure 1.6; Pollard et al., 2015; DeConto and Pollard, 2016; Bassis et al., 2012). The concept has been used to explain rapid and large increases in sea-level in the geologic past (DeConto and Pollard, 2016). Bed topography controls the possibility for MICI as its overall depth below sea-level dictates the thickness of overlying ice and how much is below sea-level and above floatation (DeConto and Pollard, 2016). Crucially, MICI can exacerbate MISI or cause enhanced mass alone where MISI cannot occur. Across the GrIS, ice cliffs at outlet glacier termini more than 100 m high are observed at Jakobshavn Isbræ and Helheim glacier (Nick et al., 2013; James et al., 2014). MICI has also been posed as a mechanism for the enhanced retreat of the Petermann glacier (Jakobsson et al., 2018). Importantly, the potential for the effect exists across much of the ice sheet interior as ice is sufficiently thick and connected to the ocean (Morlighem et al., 2017). However, large mass losses observed in the palaeo record do not require MICI to occur (Edwards et al., 2019). Hence, while it has the potential to lead to accelerated rates of mass loss, these may occur without MICI being the explanative factor. This highlights the complexity and uncertainty involved in predicting dynamic mass losses from ice masses into the future.
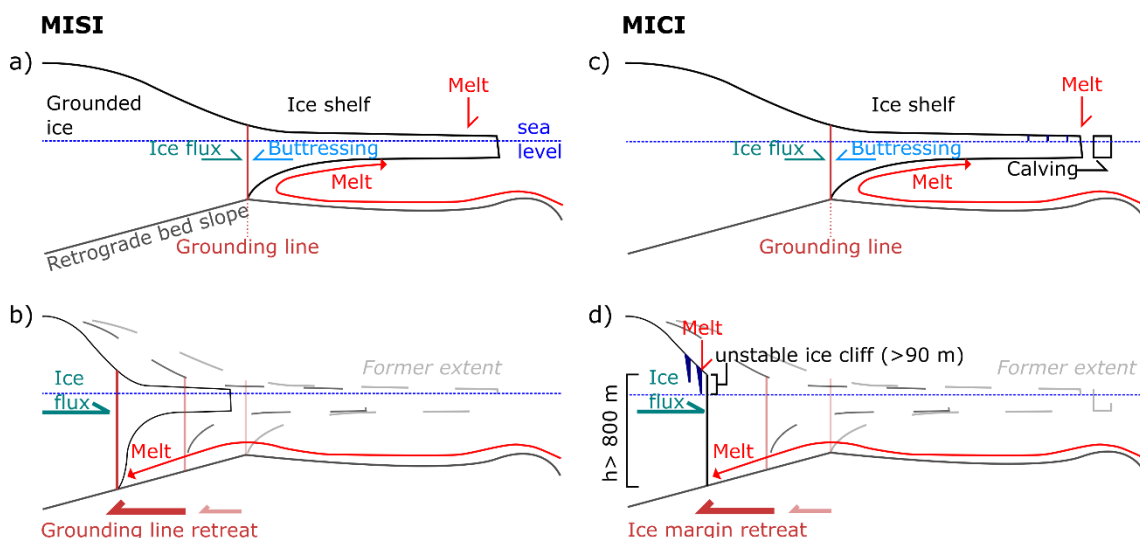
Figure 1.6 Schematic representation of MISI (a,b) and MICI (c,d). a) An ice sheet grounded at a stable grounding line position with an extensive floating ice shelf. b) Enhanced subaqueous melting from incursion of warm, deep water forces grounding line retreat, as the bed slope is retrograde this water has unrestricted access to the grounding line which accelerates its recession and is unable to stabilise. c) A thick, marine-terminating ice sheet (>800 m) with a buttressing ice shelf. d) Subaerial and subaqueous melting removes the ice shelf and unstable

ice cliffs (>90 m high) develop at the margin which readily fracture, and ice margin retreat is enhanced. Adapted from DeConto and Pollard, 2016.

From the above, a requirement exists to resolve as accurately as possible reverse-sloping regions of marine-terminating ice mass bed topography grounded below sea-level (Durand et al., 2011). Crucially, improved knowledge will aid assessment of the susceptibility of ice sheets and ice caps to enhanced mass loss (Moon et al., 2018; Catania et al., 2020). This will enable better predictive capacity for projections of solid ice discharge and consequently, GMSL contribution (Barthel et al., 2020). It is also crucial to have improved knowledge of bed topography in terms of ice thickness, due to the influence of buoyancy on enhanced ice flow and the potential for MICI (Stearns and van der Veen, 2018; Pollard et al., 2015)

Due to the influence of sub-kilometre scale bed perturbations on ice dynamics, it is crucially important that bed topography datasets are as accurate as possible (Durand et al., 2011). Additionally, as bed topography is an important control on dynamic mass balance it is a requirement to have accurate measurements of it across outlet glaciers. Correct measurement of bed topography and thickness is essential for estimating the height above floatation of ice in important outlets, as this controls enhanced ice flow and consequently heightened discharge (Stearns and van der Veen, 2018). Furthermore, the full mapping of areas of susceptible to MISI and MICI is crucial for assessing the potential future vulnerability of the ice sheets (Edwards et al., 2019; Morlighem et al., 2020) Hence, it remains a priority to improve knowledge of subglacial topography, ice thickness and bed conditions to accurately model future ice mass response to climate change (Moon et al., 2018). This thesis develops means for improving knowledge of subglacial topography to address this challenge.

1.2.3 Measuring ice mass wide thickness and bed topography

To quantity and predict ice mass contribution to sea-level change, it is necessary to measure ice volume and subglacial topography. Ice mass, derived from ice volume, constitutes the total potential contribution to sea-level rise of an ice sheet, ice cap or glacier (Alley et al., 2005). Whereas subglacial topography is a first-order control on the rate at which ice is dynamically removed from an ice mass (Schoof, 2002). Due to the spatial scale of ice sheets, ice caps, and glaciers,

remote sensing methods are required to measure these two fundamental quantities. Even so, achieving complete coverage is logistically challenging. Hence, interpolation is used to estimate the volume and bed topography of entire ice masses (e.g. Lythe et al., 2001; Bamber et al., 2001). The following sections (1.2.3.1 & 1.2.3.2) outline the background of these methods and the uncertainties and limitations this thesis aims to address.

1.2.3.1 Airborne radio-echo sounding of ice masses

Aircraft mounted radar systems have been operated over the polar ice sheets and ice caps for over five decades (Evans and Robin, 1966; Turchetti et al., 2008; Schroeder et al., 2020; Popov, 2020). Primarily, the objective has been to detect the bed and derive ice thickness for glaciological analyses (Bailey et al., 1964, Bingham and Siegert, 2007). Before widespread RES surveys, these measurements were collected through logistically intensive and sparsely acquired active seismic measurements (Bingham and Siegert, 2007). As airborne RES provides a more accurate and cost-effective means of data acquisition than other geophysical methods, it has become the principal method of measuring ice thickness and bed topography across ice masses of all scales (Rodriguez-Morales et al., 2014; Gärtner-Roer et al., 2014). This section outlines the background of RES, the major research programs conducted, and finally, the limitations and uncertainties that this thesis will aim to contribute to reducing.

RES systems have varied in design and capability dependent on the glaciological objective they are used to achieve (Plewes and Hubbard, 2001; Rodriguez-Morales et al., 2014; Schroeder et al., 2020). Nonetheless, they all consist of the same primary components. A transmitter emits a pulse of electromagnetic waves and a receiver records their return from any reflectors (Bingham and Siegert, 2007). Reflections occur from areas where there is a transition in relative permittivity, commonly referred to as the dielectric constant (Jezek et al., 1978). Hence, differences in the dielectric constant of features of an ice mass are what make RES effective. Glacial ice has a dielectric constant of 3 – 4 whereas, air (1), snow (4 - 30), water (80), and the underlying bedrock (geology dependent, >4) all differ (Evans, 1965; Jezek et al., 1978). Hence, reflections at the boundaries of these features enable delineation of the surface, internal layers and basal interface of an ice mass (Figure 1.7; Robin, 1975). From detection of the bed reflector, both the bed elevation and ice thickness can be determined

(Evans and Robin, 1966), the latter requiring the surface reflector or other surface elevation information. Mounting antenna arrays on aircraft comprises the most efficient way of detecting the bed and measuring ice thickness over 100s of kilometres (Evans and Robin, 1966; Bingham and Siegert, 2007).
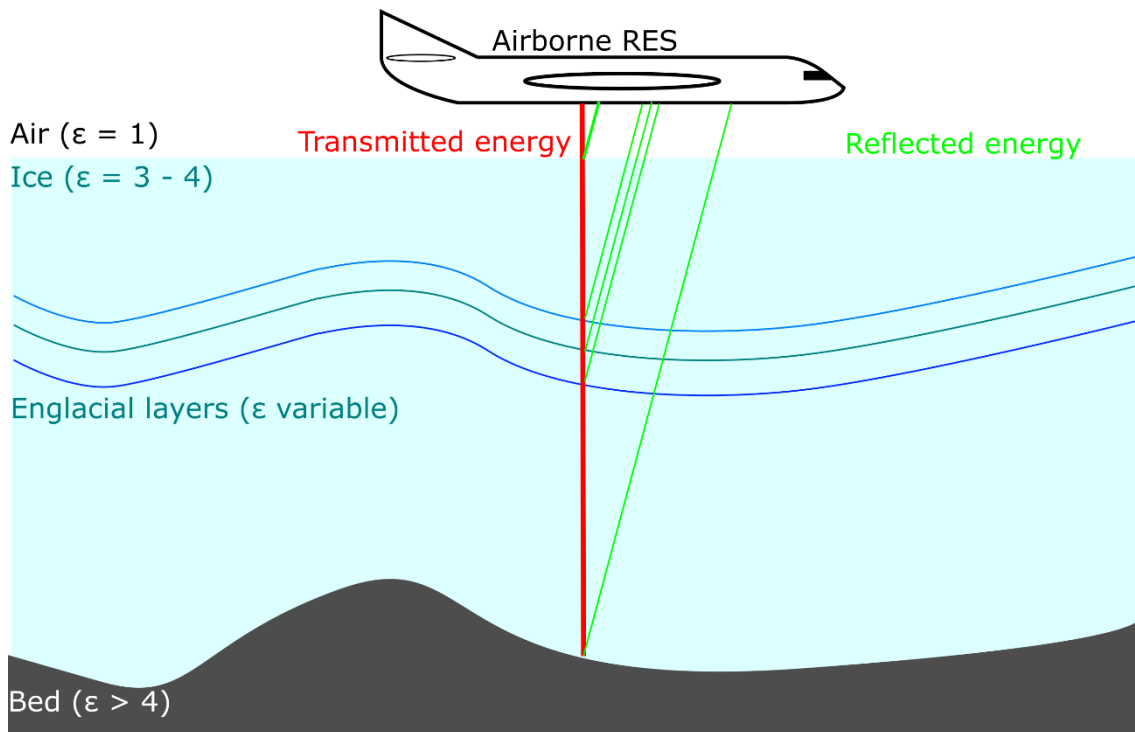
Figure 1.7 Schematic representation of airborne RES. A pulse (red) is transmitted from an aircraft-mounted transmitter through the air and ice and reflects off elements of the surveyed environment where the dielectric constant (ε) varies. The return is picked up by a receiver mounted on the aircraft and return strength and delay is recorded.

After RES of an ice mass, data processing is required to determine the elevation of the surface and bed reflectors. Figure 1.8 highlights a typical radargram from airborne RES of the GrIS. Returns from the surface are strong and appear distinctly on the radargram (Figure 1.8). However, the bed returns are weaker, hence, the bed elevation is more difficult to determine. To estimate the range from the surface to the bed (i.e. the ice thickness), the bed is "picked" (Gogineni et al., 2001). This is done either semi-automatically or manually using either the first or brightest bed reflector (Gogineni et al., 2001; Bamber et al., 2001; Fahnestock et al., 2001). For both methods, the radargram is visually enhanced to account for attenuation of the signal through thicker ice (Cooper, 1987; Fahnestock et al., 2001). Manual picking relies on analyst accuracy which is

estimated to be within 2 pixels. Consequently, the uncertainty from this method is double the radar system range resolution, which is the vertical distance recorded by one pixel (converted from two-way travel time, Gogineni et al., 2001). Semi-automatic picking implements an algorithm to pick reflectors based on either initial increases in return strength at depth (first return, e.g. Dowdeswell et al., 2002) or peaks of maximum return intensity (brightest echo, e.g. MacGregor et al., 2013). Subsequently, analyst input is required to quality control picks and determine the location in areas of ambiguous returns missed by the algorithm (Fahnestock et al., 2001; MacGregor et al., 2015). Both manual and semi-automatic methods add uncertainty to the ice thickness measurement, either through human error or analyst defined thresholds for bed picks.
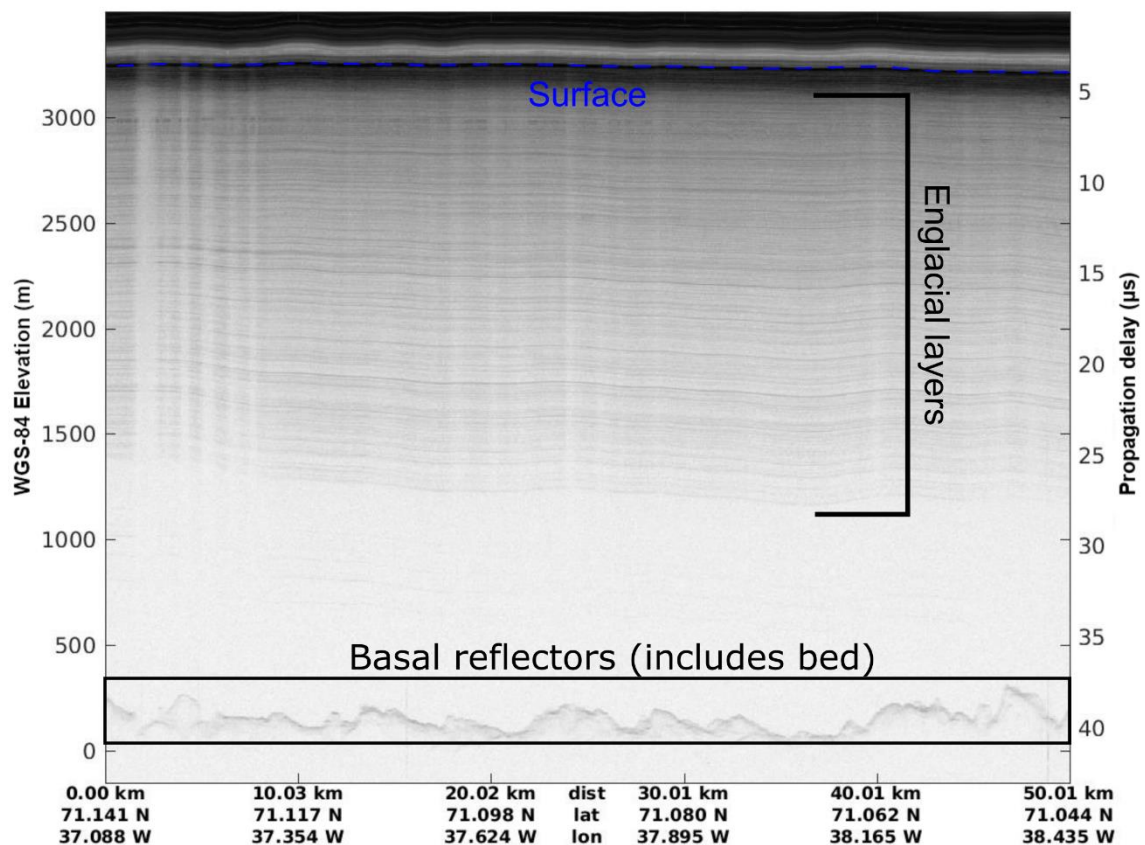
Figure 1.8 Annotated example of a radargram from a RES survey of the Greenland ice sheet. Stronger returns appear darker in the radargram. The bed is unpicked to illustrate the difficulty and uncertainty in determining an exact bed elevation from RES data (Dataset used: "East Central bed Gap IS-2" 201905512_01_061; CRESIS, 2020)

Airborne RES surveying of bed topography and ice thickness was first conducted over the GrIS in 1964 (Bailey et al., 1964; Turchetti et al., 2008), and is still widely in use today. Surveying campaigns have been flown over both Greenland and Antarctica since the 1970s, and currently available RES data constitutes a compilation of five decades of numerous regional scale flights conducted by a multitude of institutions (Popov, 2020; Shroeder et al., 2020). Most notably, NASA's Operation IceBridge (OIB) flew over 1000 missions, many of which undertook RES surveys, between 2009 and 2019. OIB was developed to bridge the ice sheet altimetry monitoring data gap between the culmination of the ICESat one mission and launch of ICESat-2 (Studinger et al., 2010). From the aforementioned campaigns, extensive surveying of both ice sheets has generated a vast amount of bed elevation and ice thickness data (Morlighem et al., 2017; Morlighem et al., 2020). Additionally, airborne and ground-based RES campaigns have been undertaken across glaciers and ice caps in both the Arctic and Antarctic. In the Arctic, RES surveys have been conducted over Canadian Arctic ice caps since the 1960s, with all ice caps having been surveyed since in the 1970s (Evans and Robin 1966; Koerner, 1977). Similarly, glaciers and ice caps in Svalbard and the Russian High Arctic have been extensively surveyed for over four decades (Drewry et al., 1980; Bogorodsky et al., 1985; Bassford et al., 2006a; Bassford et al., 2006b; Bassford et al., 2006c). In Antarctica, the South Shetland island ice caps have been surveyed since the 1990s (Macharet et al., 1997; Macharet et al., 2009). Consequently, ice thickness and bed topography are also extensively mapped for many polar ice masses outside of the continental ice sheets. Although uncertainties have been estimated and tested for the various RES instruments deployed on these surveys (Dowdeswell et al., 2002; Peters et al., 2005; Paden et al., 2010), it is difficult to validate them with certainty (Lapazaran et al., 2016). Therefore, large volumes of data and the latest continental bed topography datasets have broadly parameterised uncertainties that limit their quality.

While radar sounding of ice sheet bed topography is considered to be sufficiently accurate (Lapazaran et al., 2016), measurements are sparse and the nature of radar surveying exacerbates error in marginal sectors of ice sheets, areas which largely govern the rate of ice loss (Jezek et al., 2013; Morlighem et al., 2011; Pritchard et al., 2009). Rough bed topography, surface crevasses and subglacial

and englacial water content all contribute to enhanced scattering or attenuation of the radar signal, reducing the strength of the returns and thus limiting the accuracy of measurement (Gogineni et al., 2001; Jezek et al., 2013). Accuracy may also be limited by noise induced by offline reflections originating from features within the RES footprint but away from the intended survey line (Irvine-Fynn et al., 2006). Furthermore, where these conditions are excessively prevalent no bed return may be recorded (Gogineni et al., 2001). Quality of bed measurements is recorded in output RES data and uncertainty due to these errors is estimated to be to the order of tens of metres (Paden et al., 2010). Crossover analysis, where the difference between coincident RES measurements are quantified, is the most implemented estimate of uncertainty (Bamber et al., 2001; Ross et al., 2012; Young et al., 2017). Yet, it has been deemed to provide only an estimate of consistency in measurements, not a comprehensive error analysis (Lapazaran et al., 2016). Consequently, these uncertainties are themselves estimates, and the collection of a single bed elevation point from a wide footprint introduces a locational error that has yet to be quantified. Within a RES footprint, off-nadir returns act to obfuscate the nadir return thus reducing the accuracy of the measurement (Benham and Dowdeswell, 2003; Holt et al., 2006; Farinotti et al., 2013). Moreover, highly rough subglacial topography further increases these errors (Jordan et al., 2017). Additional uncertainty occurs for all RES measurements as all bed elevation and ice thickness measurements are treated as though they originate from directly beneath the aircraft. Furthermore, this error is an additional universal uncertainty that is not well quantified. Nevertheless, swath mapping, where elevation and thickness are measured over an entire footprint, is aiming to reduce this error for centreline flights but is a relatively new technique yet to be fully implemented (Holschuh et al., 2020; Schroeder et al., 2020).

Additional to the influence of the ice-sheet environment on RES uncertainty, errors in ice thickness, and subsequently derived bed topography, also arise from the radar system and data processing (Lapazaran et al., 2016). Radar wave velocity error results from the variable speed at which the sounding pulse travels through the different media which constitute the target ice mass. Ice thickness and density, the presence of snow, firn, and water, and varying temperature throughout the ice column all influence the speed at which the radar wave travels

through the ice mass. While this is accounted for using a constant transformation for two-way travel time throughout the ice column (Hempel et al., 2000), this leads to an overestimation of thickness in ablation zones and underestimation in accumulation zones, where firn is often abundant (Lapazaran et al., 2016). This is again accounted for with a constant transformation which is derived using *a priori* information (Dowdeswell and Evans, 2004). Timing error arises when picking the bed, which as mentioned previously is a function of the range resolution of the radar system and the parameters used for manual or semi-automatic picking (MacGregor et al., 2015). Up to 200 m of ice thickness timing error and radar wave velocity error combine to give a 2.5% uncertainty in ice thickness (Lapazaran et al., 2016). As radar wave velocity is dependent on ice thickness it increases linearly with thickness and approximately results in a 2% uncertainty. Timing error is dependent on system range resolution and analyst interpretation so its contribution to total ice thickness error diminishes with respect to radar wave velocity error with increased ice thickness.

Operation of moving RES equipment for surveys also contributes error to ice thickness as the system is being moved whilst sounding (airborne or ground-based, Lapazaran et al., 2016). Consequently, measurements are subject to positional uncertainty in the system GPS and the displacement of the return signal as it is received further along survey from where it was transmitted. The latter being dependent on the velocity of the operator or vehicle the system is mounted on as well as the timing error from the interpretation of the two-way travel time (table 1 in Lapazaran et al., 2016). To minimise these errors RES system trigger and refresh rates should be increased alongside the speed of the operator or vehicle carrying the system.

The errors highlighted above are often quantified and combined to give overall uncertainty for measurements taken by certain systems on given surveys. However, these are exclusive of the error arising from picking a point elevation from a wide footprint, which is investigated in this thesis.

Considering the above, it is therefore important to fully quantify, and where possible reduce, the uncertainty in RES as the measurements provide essential information on ice masses (Bingham and Siegert, 2007). An extensive back catalogue of ice thickness and bed elevation data exists which could be improved with better quantification of uncertainty. Additionally, planning of future missions

and interpretation of future acquisitions may be optimised with a greater understanding of airborne RES uncertainty. Finally, RES measurements must be accurate as possible before they are interpolated over large areas.

1.2.3.2 Interpolation of ice thickness and bed topography

Various interpolation methods have been employed to generate ice mass wide thickness and bed topography datasets. Most interpolators are definable as either deterministic or geostatistical (Herzfeld et al., 1996). Inverse distance weighting (IDW), spline-in-tension, and discretised thin-plate-spline (Topo to Raster, Hutchinson, 1988) are deterministic interpolators which have been used to interpolate bed topography (Figure 1.9, Dowdeswell et al., 2004; Le Brocq et al., 2010; Linsbauer et al., 2012). Whereas kriging, conditional simulation, and Bayesian inference are geostatistical interpolation methods which have been utilised (Figure 1.9, Bamber et al., 2013; Fretwell et al., 2013; Goff et al., 2014; Brinkerhoff et al., 2016; MacKie et al., 2020). For the ice sheets in Greenland and Antarctica, and indeed most ice masses, kriging has traditionally been the principal method to generate bed topography datasets spanning their entirety, due to its widespread availability and efficiency (Lythe et al., 2001; Bamber et al., 2001; Bamber et al., 2013; Fretwell et al., 2013). However, the most recent ice sheet wide datasets have looked to avoid the pitfalls of this interpolation and are modelled outputs based on the physical principle of conservation of mass (Morlighem et al., 2017; Morlighem et al., 2020).
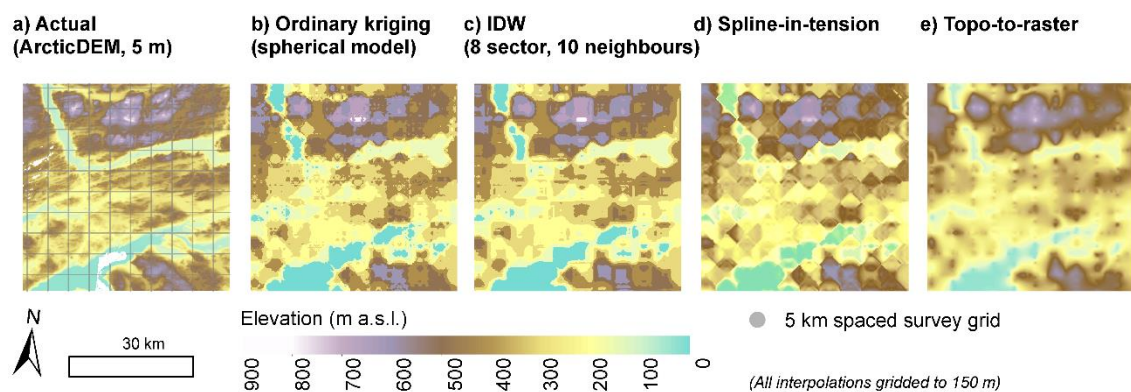
Figure 1.9 Examples of topographic grid results from commonly used geospatial interpolations where input measurements are collected along a 5 km spaced survey grid (b – e). a) measured topography according to the ArcticDEM (Porter et al., 2018), 5 km sampling grid is shown in grey. b) Ordinary kriging using a

spherical model, c) IDW interpolation using 10 neighbours within an 8 sector search window, d) Spline-in-tension, and e) Topo-to-raster (Hutchinson, 1988).

In 2001, after extensive airborne RES surveying of the continental ice sheets the first Antarctic and Greenland bed topography maps were produced (Lythe et al., 2001; Bamber et al., 2001). BEDMAP, the Antarctic dataset, was primarily derived using an inverse cubed, octagonal search IDW approach (Lythe et al., 2001). Whereas, ordinary kriging was used for the Greenland dataset (Deutsch and Journel, 1997; Bamber et al., 2001). Both datasets were gridded to 5 km resolution which is too coarse for numerical models to accurately reproduce ice dynamic behaviours which are influenced by topographic features that occur at shorter wavelengths than this resolution (Durand et al., 2011). Hence, after further extensive RES of the ice sheets, updated and improved bed topography datasets with one-kilometre spatial resolution were developed (Bamber et al., 2013; Fretwell et al., 2013). While this represented a fivefold improvement in quality, large scale ice dynamics can be influenced by bed perturbations less than a kilometre in size (Durand et al., 2011). As such, further refinement was required, and the latest datasets have moved away from geostatistical approaches to achieve this (Morlighem et al., 2011). By combining 400 m resolution surface velocity measurements and additional RES and bathymetry measurements (Morlighem et al., 2014; Williams et al., 2017), mass conservation approaches have developed the highest resolution ice sheet bed elevation datasets to date (150 m, figure 1.1, Morlighem et al., 2017; Morlighem et al. 2019). Nevertheless, similarly to kriging, this method is not without assumptions and uncertainties.

Kriging statistically predicts values over a spatial grid dependent on the distance between measured values and the weighted influence of neighbouring values (Deutsch and Journel, 1997). When applied to ice thickness a non-linear least squares variogram scheme is employed (Bamber et al., 2013). This method outputs ice thickness data to a spatial grid, the resolution of which is defined by the analyst dependent on the spatial density of input measurements (5 km, Bamber et al., 2001; 1 km or 2.5 km, Bamber et al., 2013). Increasingly so it is found that kriging produces ice thicknesses that cannot be accurately recreated in models of ice flow that are constrained by observations (Morlighem et al., 2011). This is a consequence of the inability of the method to adequately reproduce the anisotropy observed in glaciated landscapes (Seroussi et al.,

2011; Goff et al., 2014; Williams et al., 2017). Interpolation of a surface towards a regional mean results in a smoothing of the landscape which obfuscates bed features which exert a strong influence on ice dynamics (Sun et al., 2014). Hence, models using kriged bed topography as a boundary condition are less able to replicate observed dynamic behaviours. Furthermore, the interpolation generates "bullseye" style artefacts, where troughs are interspersed with unrealistic hill-like areas of increased elevation (Williams et al., 2017). These perturbations significantly hinder the modelling of ice dynamics. Due to the widespread use of kriging in previous datasets, its efficiency and the incorporation of previous datasets in model intercomparison projects (ISMIP6), there is a requirement to improve uncertainty in kriged bed topography datasets. This has been addressed for marginal areas using mass conservation methods (Morlighem et al., 2017; Morlighem et al., 2020), although these aren't without caveats. Additionally, in interior regions and where ice flows too slowly for mass conservation to be efficacious kriging is still used. Moreover, kriging uncertainty is largely approximated as an inverse distance relationship with respect to the input data and is not well validated. Consequently, in sparsely surveyed regions of ice masses, uncertainty is the highest and also least well constrained. Importantly, these areas contain large volumes of ice and as such the uncertainty in the overall volume of ice is increased. This thesis will aim to address this by developing methods which quantify and reduce uncertainty in these regions more robustly than previously. Hence, this thesis aims to improve the uncertainty of kriged bed topography to improve knowledge of subglacial topography at the scale of entire ice masses.

Instead of using a geostatistical approach for predicting the likely bed elevation between measurements, mass conservation calculates ice thickness through combining the measured thickness with ice velocity measurements to determine ice flux (Morlighem et al., 2011). This is conducted across a triangle mesh using a finite-element method from which the ice thickness, and subsequently bed elevation, at a point, can be derived by the amount of ice mass that is predicted to be moving through it (Morlighem et al., 2011). Furthermore, this method can be conducted at the resolution of ice velocity data (typically 400 m across Greenland (Joughin et al., 2010)) giving it increased accuracy over kriging (Figure 1.10; Morlighem et al., 2014). Optimal application of the method is achieved for

fast-flowing ice (>50 m yr^{-1}) where the flow field from the surface to the bed is less likely to diverge (Morlighem et al., 2011). However, uncertainty in slow-flowing regions may exceed 100 m, double the average error for the entire dataset, as the surface velocity is likely highly divergent from the velocity at the bed (Morlighem et al., 2013). Moreover, ice flow across Greenland, particularly at land-terminating margins where the ice moves slowly, has found to exhibit seasonal variability, in some cases exceeding 100% changes in velocity between summer and winter (Palmer et al., 2011; Sundal et al., 2011; Tedstone et al., 2015), further increasing the uncertainty that is currently estimated for these regions. Without consideration of this unquantified uncertainty, mass conservation performs well in areas of fast-flowing, thick ice, but even here there is variability (Morlighem et al., 2014; Joughin et al., 2010). Furthermore, like any derivation of bed topography, the output elevation is an estimate between areas of RES measurements. Hence, prediction accuracy can only be validated if a measurement is taken for the true bed topography (Morlighem et al., 2013), which is logistically challenging. Finally, regardless of the method used to estimate ice thickness and bed topography in regions without observations, any errors in the initial input measurements will be carried through into the final data product and likely exacerbated (Millan et al., 2018).
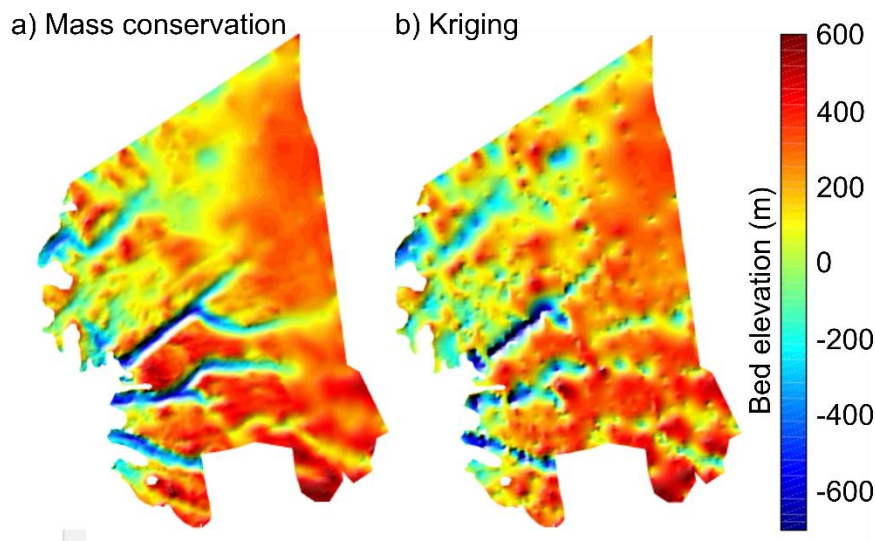
Figure 1.10 a) Mass conservation derived bed topography (Morlighem et al., 2017) compared with b) kriging derived topography (Bamber et al., 2013) for Upernavik, West Greenland. Adapted from Morlighem et al., 2020.

1.2.4 Summary

Accurate bed topography is essential for models aiming to predict ice sheet and ice cap response to climate change. Whilst, novel interpolations are improving estimates of the elevation of the subglacial landscape they are still challengeable in areas of slow and seasonably variable ice flow (Morlighem et al., 2013). Furthermore, many ice sheet models use interpolations derived from kriging methods despite widespread acknowledgement of its flaws (Nowicki et al., 2016). Increased input measurements can significantly improve these interpolations but it is also important they are in themselves as accurate as possible, which is determined by the nature of the airborne radar survey and its configuration (Gogineni et al., 2001). No significant quality assessment of radar survey design and interpolation accuracy exists (Lapazaran et al., 2016). It is therefore beneficial for ice-sheet models, flight survey designs and bed topography interpolations to conduct such quality control and develop a method for obtaining data in a way that is most beneficial to all of the above. Through quality assessment of bed topography interpolation methods and RES survey measurements, this thesis may contribute to the improvement of bed topography datasets, much needed for forecasting the response of polar ice masses to climate change (Moon et al., 2018).

1.3 Aim

As highlighted in the prior discussion, uncertainties in the measurement and interpolation of ice mass wide bed topography are widespread and rudimentary. This has a knock-on effect for the predictive capability of models aiming to project GMSL rise contribution from the cryosphere. As direct validation of bed topography measurements is logistically challenging, a pseudo-validation approach which accurately simulates bed elevation derivation is required. Hence, this thesis aims to:

Develop and apply geostatistical methods which simulate the acquisition and interpolation of bed elevation datasets to quantify and reduce the uncertainty in ice mass bed topography and subsequently derived analyses. From this, this thesis will contribute to improved quantification of uncertainty in the dynamic discharge component of ice sheet and ice cap mass balance. Subsequently, this

will contribute reduced uncertainty in the input conditions for models which aim to project ice mass contribution to sea-level rise.

1.4 Objectives

To achieve the aim of this work, this thesis has the following objectives:

- Develop a method to quantify the uncertainties in airborne radio-echo sounding measurements of ice thickness and bed topography and assess their impact on analyses conducted on such datasets (chapter three).

- Develop a method to quantify and reduce the uncertainties in three-dimensional, ice mass wide estimations of ice thickness and bed topography derived by kriging, and assess their impact on estimations of ice mass and perceived stability of ice masses (chapter four).

- Using the methods developed, derive a new dataset of ice thickness with accompanying uncertainty maps for selected Arctic ice caps and assess the potential implications for near term sea-level rise contribution (chapter five).

1.5 Summary

In this chapter, the rationale for this thesis and the context of where it will contribute to the existing literature has been outlined. Chapter two will outline the methods implemented and the concepts behind them. Chapters three through five are the results of this thesis and are written in the format of scientific journal articles. These chapters vary in length and structure dependent on the requirements of the journal they are submitted to. Publication status and authorship contributions are highlighted preceding the main text of the chapter. Chapter three describes the development and implementation of a synthetic RES survey dataset to investigate uncertainty in ice thickness measurements. Chapter four reports fully quantified uncertainty in ice sheet bed topography interpolation and includes the development of methods to better quantify and reduce this uncertainty. Chapter five combines and applies the full suite of methods developed in chapters three and four to RES survey data from the CAA, from which bed topography is derived for selected ice caps and the uncertainty in it fully quantified and minimised. Chapter six synthesises the work of the thesis, its

contribution to the field of glaciology, the limitations of the work done, and highlights potential future work that may arise from this thesis.

Chapter 2: Methodology

2.1 Introduction

This chapter introduces the data used throughout this thesis, provides the broad geographical context of the study and details the suite of methods employed.

Initially, the ArcticDEM dataset, which forms the primary input of this study, is introduced alongside the underpinning concept implemented throughout this study of using high-resolution elevation data from glaciated terrain as a pseudo-validation tool for subglacial elevation datasets. Subsequently, the four main study areas are highlighted, their selection explained including preliminary insights into where similar topography may be replicated in datasets of subglacial topography. From this, ice-covered regions where the results of this work are likely to be relevant, are highlighted.

Next, the novel synthetic RES method developed in this thesis is described along with how it will be used to quantify uncertainty in RES measurements. Additionally, the potential for developing corrections for RES measurements are explored. This method is discussed in the context of Operation IceBridge (OIB) flights conducted in Greenland, which is explored in detail in chapter three.

Following this, interpolation methods for deriving continuous of ice thickness and bed topography datasets from individual airborne RES observations is introduced. Background for the kriging interpolation method is provided in the context of this study. Subsequently, the application of kriging in this thesis is delineated. Methods to better quantify and reduce uncertainty in kriged bed topography datasets are proposed. In chapter four, these methods are applied and discussed in detail.

Finally, a compilation of the geospatial and geostatistical methods is delineated for application to ice thickness and bed topography datasets covering the Canadian Arctic Archipelago (CAA). This introduces methods explored further in chapter five, in which a full evaluation of the methods developed by this thesis is conducted by applying them to ice caps in the CAA.

2.2 ArcticDEM

2.2.1 Pan-Arctic high-resolution digital elevation

The ArcticDEM comprises a pan-Arctic, two-metre resolution digital surface model (Porter et al., 2018), which includes all land north of 60°. Automated stereo-photogrammetric processing of overlapping optical image pairs taken by the DigitalGlobe satellite constellation is used to generate high-resolution elevation models (e.g Figure 2.1; Noh and Howat, 2015). Moreover, as the generation of DEMs is automated and ongoing, the ArcticDEM captures elevation change across the Arctic over time (Porter et al., 2018; e.g. Harrison et al., 2019). Data are gridded to 2 m postings and available in strip or tile formats. Strips constitute temporal snapshots of surface elevation covering the dates of the stereographic image pairs used to derive the elevation. However, the spatial coverage of an individual strip is limited, so this thesis uses the tiled format. Tiles used by this thesis are outlined in the appendix (Table A2.1). ArcticDEM tiles comprise a best-quality mosaic of strip DEMS (Noh and Howat, 2018). Additionally, elevations are blended to remove edge error artefacts when overlapping strips are combined (Noh and Howat, 2018). Reduction of the dataset down to the best-quality elevation measurement at a given location limits the temporal resolution to the 8-year time domain of the dataset. However, as the work by this thesis requires accurate measurements of surface elevation over large regions, tiles were determined to be the most suitable input. Each DEM is vertically registered to IceSAT satellite altimetry data to give an absolute uncertainty of less than a metre (Noh and Howat, 2017). Within an individual DEM relative uncertainty between pixels is determined to be to the order of tens of centimetres (Porter et al., 2018).

Elevation gridded at 2 m is an order of magnitude more precise than typical RES along-track resolution, ~10 – 30 m (Paden et al., 2010; Peters et al., 2005; Jeofry et al., 2018), and at least two orders of magnitude more precise than the minimum cross-track resolution (323 m, Paden et al., 2010). Furthermore, the absolute uncertainty of ± 1 m is reduced in comparison to the vertical resolution, ~5 – 18 m (Paden et al., 2010; Peters et al., 2005). Therefore, it is well suited for assessing the accuracy of RES surveys through simulation. With such high precision, it is possible to fully quantify the maximum possible performance of RES instruments over various landscape configurations.
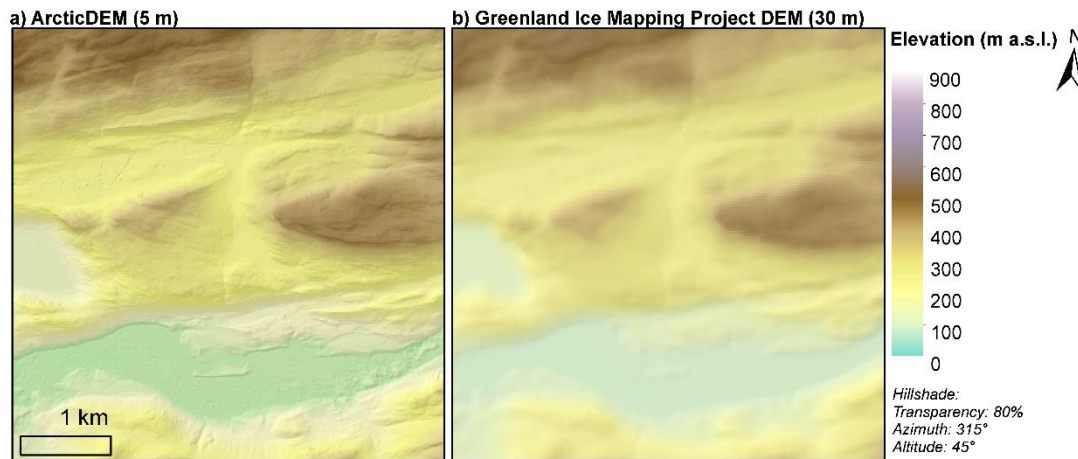
Figure 2.1 Comparison of a) ArcticDEM resolution (used in this thesis) with the next highest resolution data product available for Greenland (Greenland Ice Mapping Project (GIMP) DEM, Howat et al., 2014). a) ArcticDEM at 5 m resolution. b) GIMP DEM at 30 m resolution.

2.2.2 Linking glaciated topography with subglacial topography

A significant area of land in the Arctic was glaciated by northern hemisphere palaeo-ice sheets (~14 x 10^6 km^2 Figure 2.2a, Hughes et al., 1977; Clark et al., 2009; Hughes et al., 2016; Batchelor et al., 2019). Hence, glaciated topography is ubiquitous across the Arctic and has occurred across a significant portion of the ArcticDEM domain (Tile domain: ~23 x 10^6 million km^2, Porter et al., 2018), 61% of sub-tiles overlay maximum ice sheet extent. More specifically, the GrIS margin has been reconstructed to have extended beyond the current coastline as recently as 12 ka BP (Young and Briner, 2015). Recession of the margin has exposed previously subglacial topography proximal to the current land-terminating margins of the ice sheet. Terrain elevation for these expanses of ice-free topography is measured by the ArcticDEM (Porter et al., 2018), with a total coverage of 0.4 x 10^6 km^2 (Howat et al., 2014). Hence, high-resolution DEMs are available for all of the subaerial topography that was previously covered by the GrIS and can therefore be considered as analogues of the nearby, currently ice-covered topography. While the selected subaerial topography will have undergone modification by erosion and deposition since exposure, this thesis samples over 2 million point elevations and the surrounding relief of each, thereby capturing the influence of numerous topographic configurations on recorded elevation. Through this, enough areas with a similar variation in elevation at the

scale of a RES survey footprint will have been sampled to account for expected similar current subglacial topography. The idea that landscape characteristics extend beyond the ice margin in land-terminating areas is supported by results from RES surveys and bed topography datasets for the Kangerlussuaq (Lindbäck and Pettersson, 2015), Inglefield Land (west of Hiawatha impact crater, Kjær et al., 2018), and Peary Land (Solgaard et al., 2020) regions.

Assuming that subsets of the topography measured across the Arctic are comparable to subglacial landscapes, the acquisition of bed topography measurements can be simulated and the differences between the outputs and inputs fully quantified. This quantification then provides an assessment of the scale of uncertainties that can be expected in datasets which estimate the bed topography for geomorphologically similar landscapes.
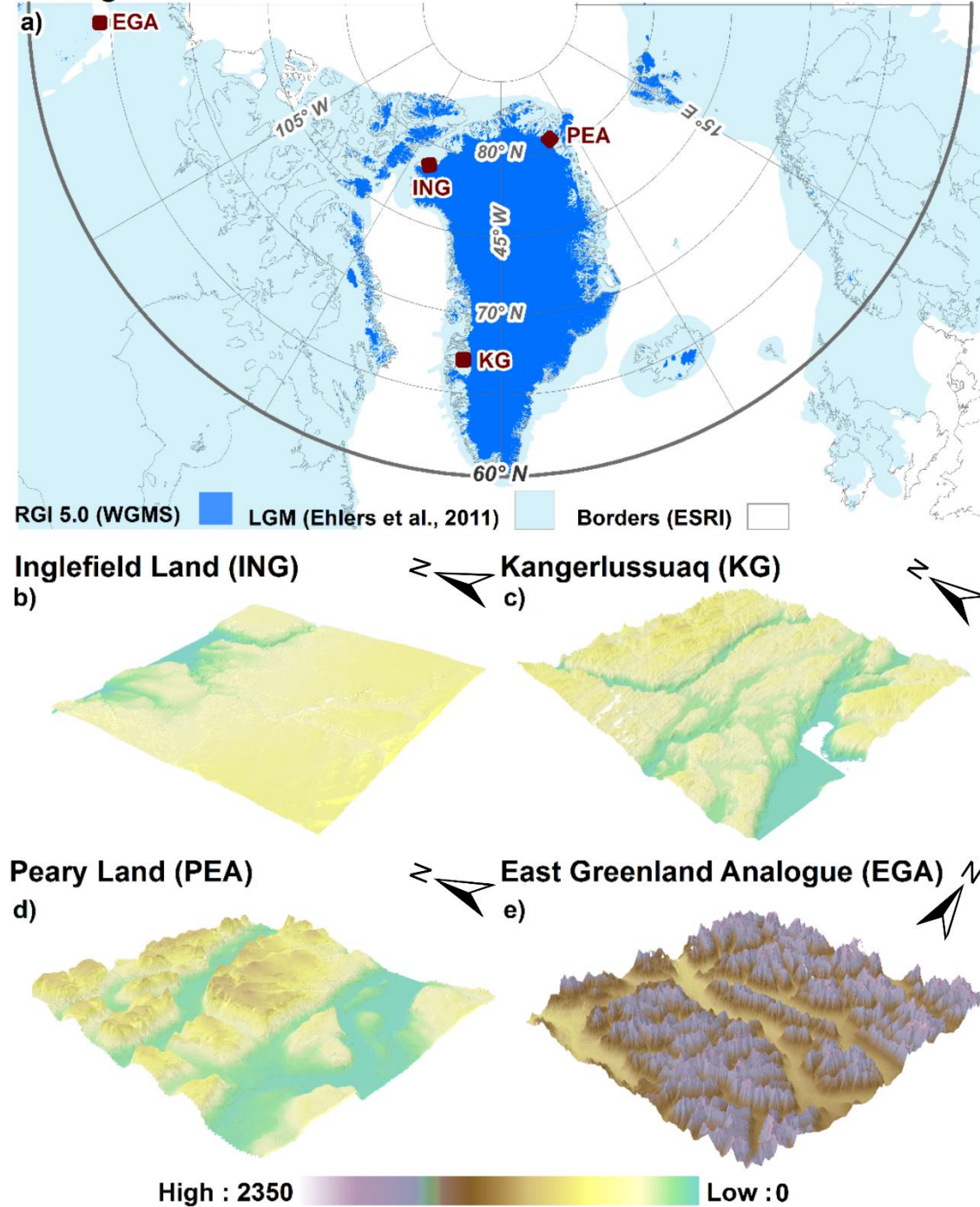
Figure 2.2 Study sites in context. a) The extent of Arctic and sub-Arctic glaciation is shown (current in dark blue, palaeo in light blue). ArcticDEM tiles are available for all land north of 60° N (double weighted grey graticule). A vertically exaggerated (5x) perspective for each site is shown, b) Inglefield Land, c) Kangerlussuaq, d) Peary Land, e) East Greenland Analogue (EGA, Mackenzie Mountains, Canada).

2.2.3 Geomorphological classes of glaciated landscapes

Glaciated landscape geomorphology is heavily influenced by the scale of the occupying ice mass, its long-term flow direction, and the temperature at the ice-bed interface (Sugden and John, 1976; Jamieson et al., 2014). Pioneering work by Sugden (1976, 1978) and Sugden and John (1976) established three broad, process-based, landscape classifications dependent on glacial erosion regime (Jamieson et al., 2014).

Firstly, "Alpine" landscapes occur where ice is topographically constrained, with a warm-based or polythermal basal temperature regime and further erodes previously eroded valleys "inherited" from the pre-glacial landscape (Sugden and John, 1976; Jamieson et al., 2014).

Secondly, landscapes of "Areal Scour" are formed by largely unconstrained, warm based ice, which typically occurs in central areas of the ice mass where ice is thick and warm based (Sugden and John, 1976; Jamieson et al., 2014). Additionally, these landscapes may occur at more localised scales under ice streams and where the bed is largely composed of sedimentary material (Sugden and John, 1976; Bingham and Siegert, 2009; Jamieson et al., 2014).

Thirdly, "Selective Linear Erosion" occurs via significant topographic steering of warm-based, thick ice which rapidly erodes large fjords or troughs into the landscape next to or in-between areas of minimal glacial modification beneath cold-based, thin ice (Sugden, 1974; Jamieson et al., 2014).

Finally, additional to the three classifications, the fourth type of landscape may occur in glacial environments whereby an ice mass preserves the original landscape as it is cold-based and too slow-flowing to cause significant erosion (Sugden, 1974). Landscapes fitting these four descriptions are prevalent across the Arctic and this thesis uses examples of each to investigate how well similar subglacial landscapes are measured by airborne RES surveys.

2.3 Study sites

Maps of the proglacial areas and how they are sampled are presented in detail in chapters three and four. Figure 2.2 outlines the proglacial areas in the context of previous glaciation and hence their suitability for use as regions of simulated ice sheet beds. Each site covered a 50 x 50 km area, except Inglefield land where

subaerial topography only extends 47 km from the ice sheet margin to the north coast of Greenland. Study area size was determined by computational capacity and DEM resolution was aggregated to 5 m to further decrease processing time. Figure 2.3 highlights regions across the Arctic and Antarctic which are estimated to be geomorphologically similar to the selected study sites (Sugden and John, 1976; Jamieson et al., 2014).
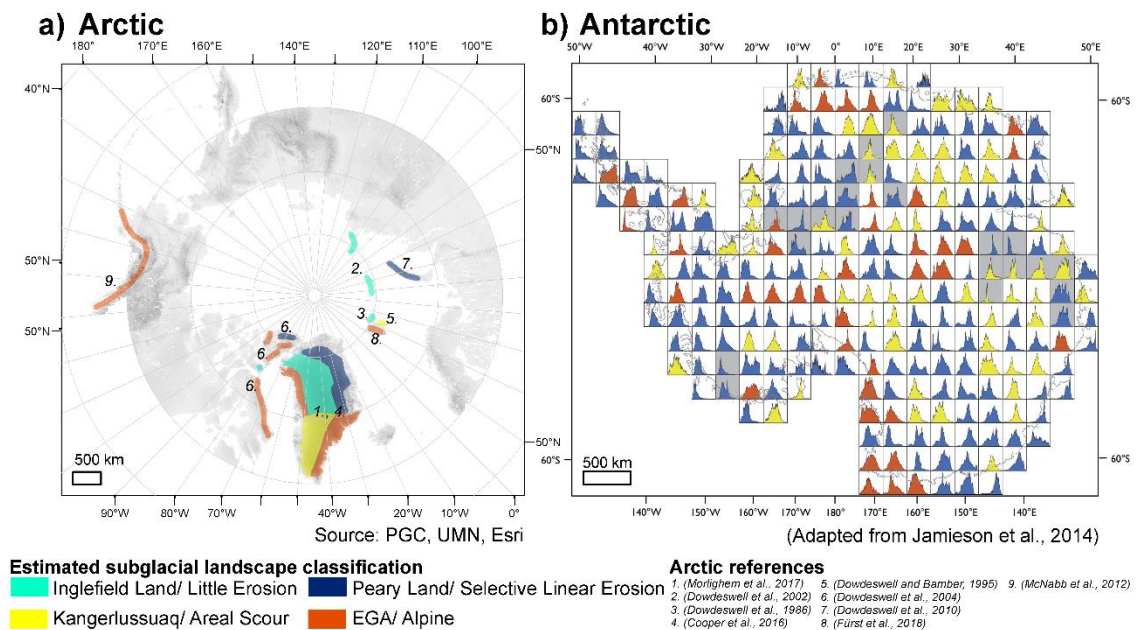
Figure 2.3 Broad approximation of areas of subglacial topography geomorphologically similar to study sites. a) the Arctic, b) Antarctica (adapted from Figure 7 of Jamieson et al., 2014). Colour highlighting represents the study site the region is most likely to represent (cyan, ING subdued areal scour; yellow, KG, areal scouring; blue, PEA, ice sheet selective linear erosion; orange, EGA, mountain valley glacier/ alpine style erosion).

2.3.1 Inglefield Land, North Greenland

Characterised by a large flat plateau with incised fluvial valleys, Inglefield Land has the lowest relief of the study sites (~600 m, figure 2.2 b)). Little evidence is found of ice sheet erosion (Sugden, 1974). Hence, the landscape was likely preserved under cold-based ice during times when the GrIS was more expansive. Such topography likely exists beneath the proximal region of the Greenland Ice Sheet and the deep interior (Bamber et al., 2013; Morlighem et al., 2017). Similar low, flat topography is found elsewhere in the Polar Regions e.g. under the Russian High Arctic ice caps on Severnaya Zemlya and Franz Josef Land

(Dowdeswell et al., 2002). Additionally, the Nordaustlandet ice caps in Svalbard (Dowdeswell et al., 1986) and the South Shetland Islands ice caps exhibit similarly low relief subglacial topography (Blindow et al., 2010). In regions where ice flow is largely topographically unconstrained and the bed topography is largely smooth, the results for Inglefield Land will be applicable (regions highlighted in cyan in figure 2.3).

2.3.2 Kangerlussuaq, Southwest Greenland

Rolling hills with intermittent overdeepened basins are prevalent across the region surrounding Kangerlussuaq in southwest Greenland. Widespread areal scouring from previous glaciation has shaped the landscape, with bedforms aligned along structural weaknesses in the regional geology (Sugden, 1974; Carrivick et al, 2016, figure 2.2c). Similar topography is ubiquitous in regions glaciated by palaeo-ice-sheets (e.g. Scotland, Clark et al., 2004). Consequently, large expanses are expected beneath both continental ice sheets (Jamieson et al., 2014; Cooper et al., 2016). The formation of this landscape requires thawed-bed conditions and predominantly topographically unconstrained ice flow (Sugden, 1978; Patton et al., 2016), which only occurs for sufficiently large ice masses. Outside of the ice sheets, land-terminating margins of southern CAA ice caps display similar topography to the Kangerlussuaq area. Additionally, Edgeøya and Barentsøya ice caps in Svalbard terminate on knock and lochan style terrain (Sugden and John, 1976; Dowdeswell and Bamber, 1995). Areas highlighted in yellow in figure 2.3 are estimated to have 'areal scour' bed topography, as found in the Kangerlussuaq region (Sugden 1978; Sugden and John 1976).

2.3.3 Peary Land, Northeast Greenland

Peary Land's landscape is dominated by flat-topped, unmodified plateaus 500 - 1500 m high, incised by multiple kilometre wide fjords (Larsen et al., 2016), largely a result of ice sheet, selective linear erosion (Sugden, 1974). Similar topography is found across the Arctic. Much of the northern and eastern coast of Greenland is comparable, as are glaciated areas of Ellesmere Island in Arctic Canada (Sugden, 1974; Dowdeswell et al., 2004). Novaya Zemlya exhibits similar wide fjords with regular flat-topped plateaus (Dowdeswell et al., 2010). In Antarctica, a significant proportion the ice sheet bed is estimated to be moulded

by selective linear erosion (Jamieson et al., 2014). Hence, much of the bed is expected to be topographically similar to Peary Land. Therefore, results concerning Peary Land style subglacial topography will apply to regions of selective linear erosion highlighted in blue in figure 2.3.

2.3.4 Mackenzie Mountains, Northwest Canada

As much of the southeast and northwest margins of the GrIS are marine-terminating, there is a paucity of high-resolution elevation data for proximal areas. These areas of Greenland are characterised by mountain valley glacier style erosion. Multiple tributary glaciers separated by mountain peaks converge into a main trunk which flows through an elongate trough (Sugden, 1974). To replicate such topography for this study's purposes, an analogous site was selected from the ArcticDEM which is referred to herein as the East Greenland Analogue (EGA) (Figure 2.4). The Mackenzie Mountains form a high relief landscape with oversteepened and overdeepened valleys separated by peaked mountains (Margold et al., 2013). Moreover, the topography is comparable in geometry to outlet glacier containing fjords on the north-western and south-eastern coasts of Greenland. Additionally, this region was formerly glaciated by the Cordilleran Ice Sheet and so was formerly subglacial topography (Eyles et al., 2018 and references therein). Similar topography is found throughout glaciated regions globally. In the Arctic, glaciers in Svalbard (Fürst et al., 2018), the Alaskan and Canadian Pacific icefields (McNabb et al., 2012), and outlets of ice caps in the Canadian Arctic Archipelago have analogous topography (Dowdeswell et al., 2004). In the Antarctic, similar topography is observed across the Antarctic Peninsula, many margin proximal mountain ranges, and up-glacier regions of large ice shelves (Sugden and John, 1978; Jamieson et al., 2014). As such, results for the EGA will have implications for subglacial topography in regions where alpine-style glaciation is most prevalent, highlighted in orange in figure 2.3.
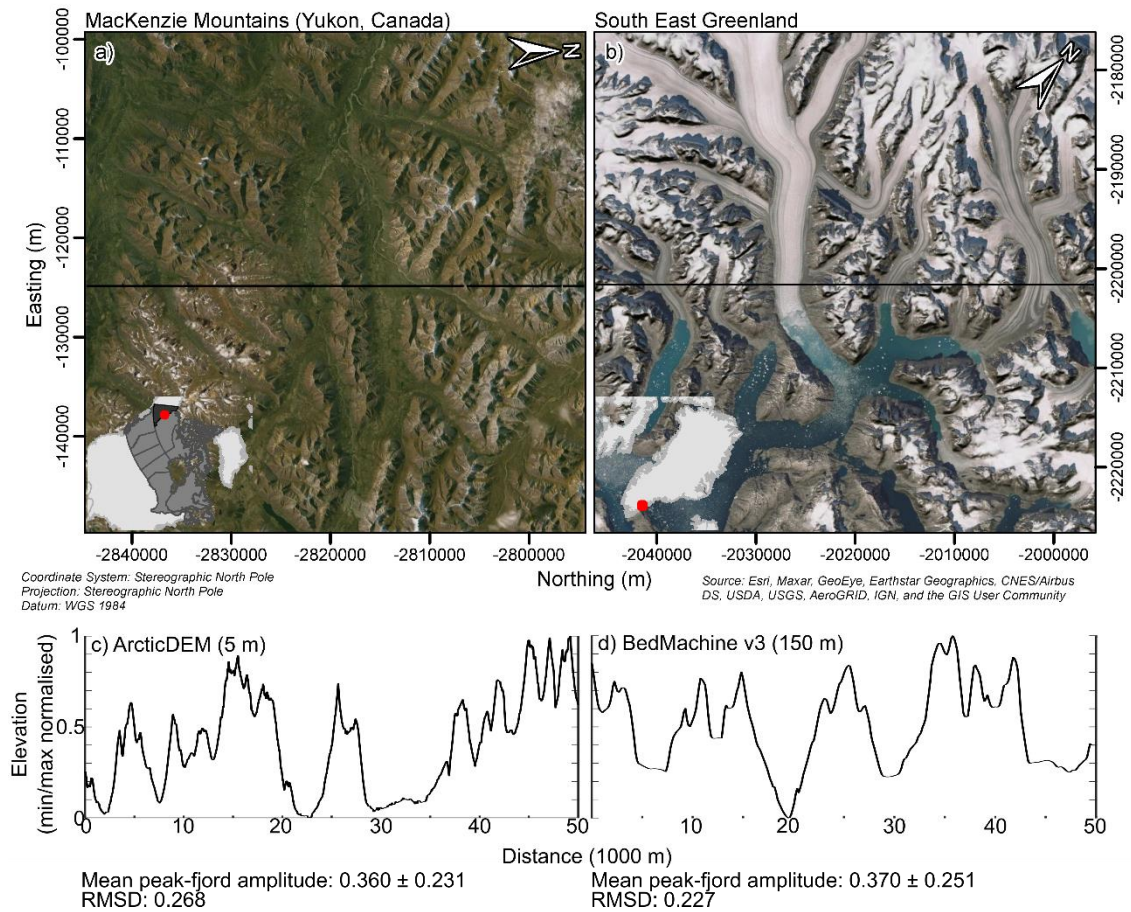
Figure 2.4 EGA geographic and topographic context. a) Region of the MacKenzie Mountains in Yukon Territory, Canada, black transect shows the location of the topographic profile in panel c). b) Helheim glacier and the surrounding area of South-East Greenland the EGA is chosen to replicate, black transect shows the location of topographic profile in panel d). c) Normalised elevation profile for comparison of peak-fjord amplitude and roughness (RMSD) with subglacial topography in South-East Greenland, elevation is derived from the ArcticDEM (Porter et al., 2018). d) Normalised elevation profile of estimated subglacial topography derived from BedMachine v3 (Morlighem et al., 2017).

2.3.5 Summary

These selected sites represent the wide continuum of terrain expected beneath ice masses. Each will be measured with varying accuracy by RES surveys. Roughness within the footprint of the survey will influence the strength of the nadir return compared to returns from the surrounding topography (Benham and Dowdeswell, 2003). It is hypothesised that Inglefield Land will be the most accurately measured of the sites due to its low relief and low range in roughness (Figure 2.5). While Peary Land exhibits the highest mean roughness (Figure 2.5)

the roughness range is also the largest due to the widespread occurrence of largely flat plateaus and fjord floors. Consequently, it is expected EGA topography will be subject to greater uncertainty as the majority of the topography is rougher than for Peary Land (Figure 2.5). Therefore, RES measurement error is expected to increase through the order the sites are presented in.

The magnitude of measurement error for the different landscapes has variable implications for analytical datasets derived from RES measurements. Primarily, in areas akin to Peary Land and the EGA which dominate the dynamic mass balance of ice masses (Rignot et al., 2018; Mankoff et al., 2019). Fjords and troughs with widely variable orientation and intermittent peaks and plateaus present as regions of high relief within a footprint and so the influence of off-nadir echoes is likely increased (Holt et al., 2006; Gogineni et al., 2014). This compounds the physical errors which typically arise from the sounding of marginal ice (Paden et al., 2010).
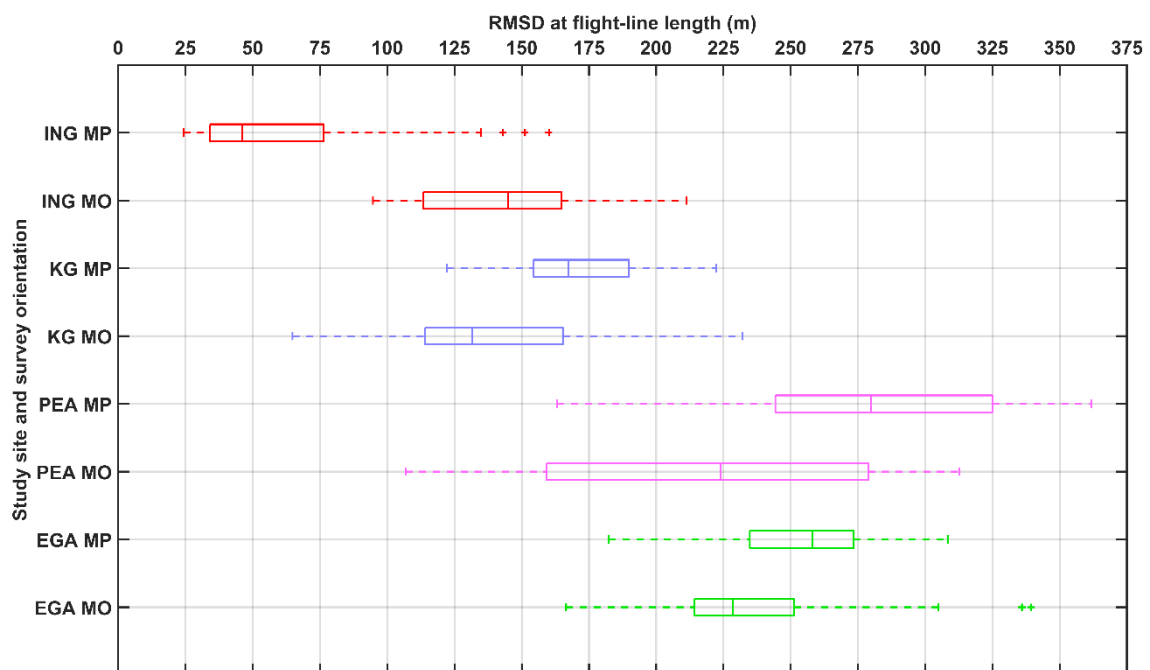
Figure 2.5 Study site roughness (RMSD) at the flight-line scale for typical RES survey geometries which constitute margin parallel (MP) and margin orthogonal flight-lines (described in 2.4.1). Box plots are coloured to represent the study sites matching figure 2.2.

From simulating RES surveys over these landscapes, this thesis will quantify the uncertainty in RES surveying of ice masses which overlie similar topography.

2.4 Geostatistical simulation of ice thickness measurement and interpolation

2.4.1 Geospatial simulation of airborne RES surveys

To emulate the derivation of subglacial topography from acquisition to output, synthetic RES surveys were conducted over the study site DEMs. As outlined in the introduction, airborne RES surveys are the principal method for obtaining measurements of ice thickness (Rodriguez-Morales et al., 2014; Pritchard et al., 2014). Hence, simulating the process to quantify the error will provide essential information for interpreting ice thickness data from previous and future surveys. Correspondingly, the simulation method developed by this work is based on OIB as the missions conducted constitute the most comprehensive acquisition of airborne ice thickness data to date (Studinger et al., 2010; Rodriguez-Morales et al., 2014; Pritchard et al., 2014; Morlighem et al., 2017). Additionally, as this thesis primarily focuses on the GrIS, the RES simulation is based on the Multichannel Coherent Radar Depth Sounder (MCoRDS, CReSIS, 2018), which was the instrument used for OIB missions in Greenland (Gogineni et al., 2001; Bamber et al., 2013; CReSIS, 2018).

To summarise, for a given RES sensor Cartesian location and the 3D geometry of the underlying surveyed DEM, the location of what would appear in a radargram as the brightest reflector is predicted (Figure 2.6). This approach was taken because the brightest reflector in a radargram is the most commonly used determinant of the bed elevation (MacGregor et al., 2013). Importantly, whichever reflector (first or brightest) is used for picking the bed, it is treated as the nadir elevation. However, it is important to highlight that strong return can come from anywhere within a RES footprint (Figure 2.6). Furthermore, as the footprint width is a function of the flying height of the aircraft and the distance to the bed, the area over which a return may come from is increased with ice thickness. OIB flights over the GrIS have a maximum estimated footprint width of 651 m (Paden et al., 2010). Along-track footprint length is much less extensive due to focussing of echoes to the zero-doppler bin (25 m for OIB over GrIS, Paden et al., 2010; Schroeder et al., 2016). Overall, it is not a certainty that the brightest reflector originates directly beneath the aircraft, which creates the potential for uncertainty in measured bed elevation that is not adequately quantified (Lapazaran et al., 2016). Hence, in this thesis, a method is developed to predict the location of the

brightest reflector and quantify the difference between the elevation at this location and that of the nadir position. Figure 2.6 illustrates the concept behind the RES simulation and why it is necessary to quantify the scale and probability of off-nadir elevation differences.
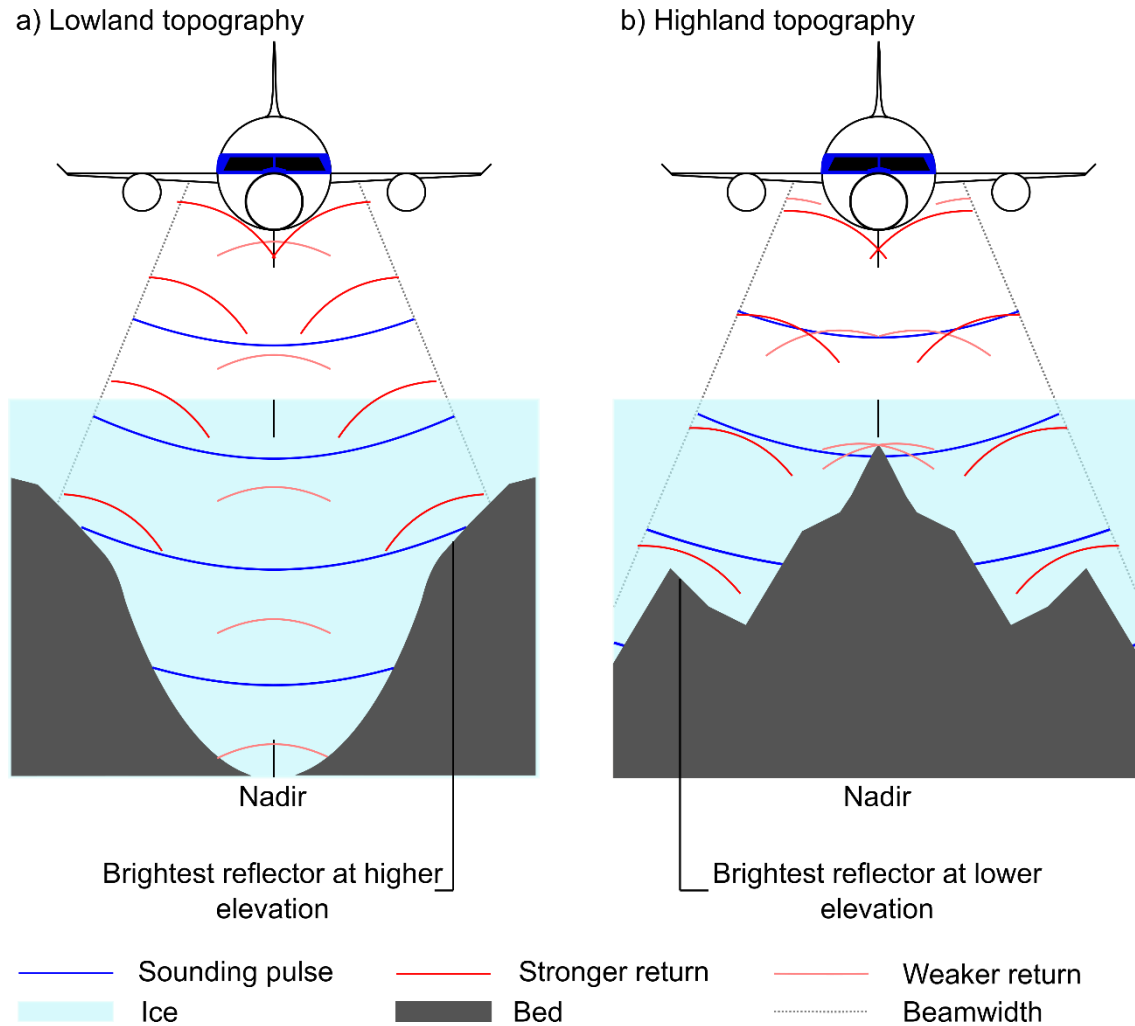
Figure 2.6 Schematic representation of the interaction of a radar pulse with underlying topography. a) For lowland topography, e.g. outlet glacier beds. b) For highland topography, e.g. areas adjoining fjords and troughs.

Following the estimated influence of off-nadir reflections highlighted in figure 2.6, figure 2.7 illustrates the concept in terms of the results of this thesis. The measured bed elevation (red) is shown to underestimate highland elevation and overestimate lowland elevation (Figure 2.7). Additionally, the terms used throughout this thesis regarding landscape features, ice thickness and the mismeasurement of the geometry of both are included (Figure 2.7).
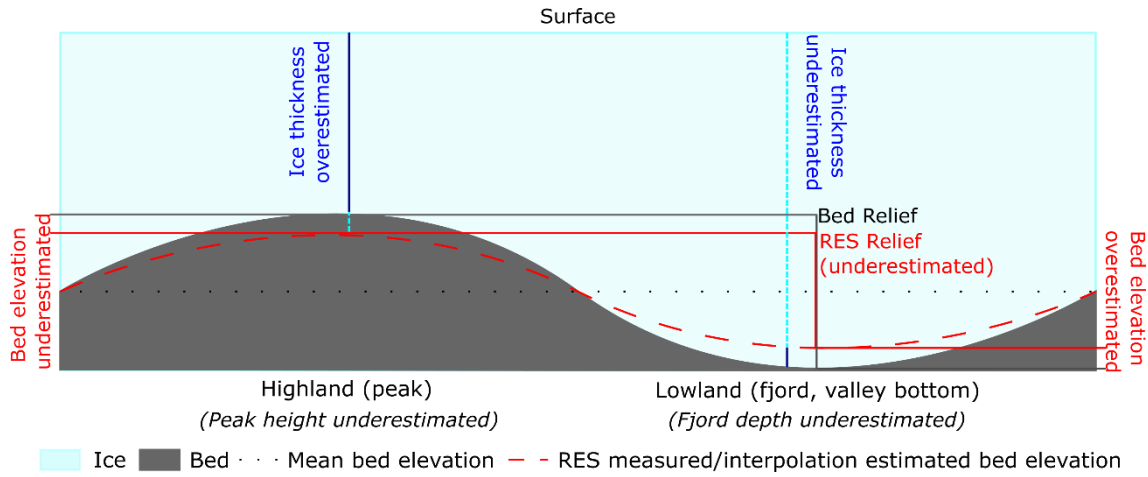
Figure 2.7 Schematic representation of landscape mismeasurement and associated terminology used in this thesis.

Firstly, synthetic survey grids are plotted at 1 km spacing over the study site DEMs. OIB flight-line survey grids are typically composed of margin parallel (MP) and margin orthogonal (MO) flight-lines (Studinger et al., 2010). MP lines are used to quantify ice flux through a surveyed region (Khan et al., 2015). Hence, any uncertainties quantified for flight-lines of this orientation will have direct implications for estimates of solid ice discharge from ice masses. On the other hand, MO flight-lines typically follow the centrelines of outlet glaciers. Along these flight-lines, the gradient and direction of the bed slope can be measured which are important characteristics for determining the stability of an outlet glacier (Schoof, 2007). Therefore, uncertainty quantified for these flight-lines will lead to improved modelling of outlet glaciers and assessment of their stability.

Surveys were simulated for two ice thickness setups. An "interior" setup, where the mean thickness of the simulated ice sheet was set at 2000 m. Also, a "marginal" setup, where mean ice thickness changed over a gradient up to a maximum of 1500 m at the furthest up-glacier location. Varied ice thickness was implemented to assess the impact of the distance of the sensor from the bed.

Once the initial setup was complete the footprint of the RES pulse at each survey posting was calculated (CReSIS, 2018). Survey postings were taken every 14 m emulating a typical Greenland OIB flight. Along-track footprint resolution was set at 25 m. Cross-track width of the footprint was determined from the maximum resolution that could be made according to the CReSIS radar depth sounder report (2018). Error in the cross-track direction is greatest (and resolution,

therefore, coarsest) where the subglacial topography is roughest. For rough surfaces, the cross-track resolution is determined by the antenna beamwidth-limited resolution, $\sigma_{y,beamwidth\text{-}limited}$. The cross-track resolution was derived through equation 2.1, where Za is the height of the aircraft above the ice sheet surface, h, is the ice thickness, β_y, is the beamwidth in radians, and k_y is the cross-track windowing factor:

$$\sigma_{y,beamwidth-limited} = 2(\frac{Za + h}{\sqrt{3.15}}) \tan (\frac{\beta_y k_y}{2}) \tag{2.1}$$

Flight altitude for OIB Greenland missions was typically 500 m. Thickness was determined locally within the maximum possible footprint size for the study area. MCoRDS beamwidth and windowing factors were 0.3 radians and 1.3 respectively.

Within each footprint, individual elevations from DEM pixels ($Pixel_z$) and distances from nadir for the pixels in the footprint were converted into delays following equation 2.2:

$$Delay_{Pixel} = \frac{\sqrt{(Pixel_z + h + Za)^2 + (\Delta Nadir_{x,y}, Pixel_{x,y})^2}}{3 \times 10^8} \tag{2.2}$$

Subsequently, the angle to the sensor for each elevation pixel in a local footprint was calculated trigonometrically. Zonal statistics were then computed for the angles to the sensor within the local footprint to determine the root mean square (RMS) of the slope of the bed topography with respect to the sensor position. Subsequently, this RMS slope value is used as an estimate of the scattering function width of the bed in each location, which was approximated as Gaussian following Schroeder et al., (2016). At each pixel, the angle of the surface with respect to the sensor was combined with the estimated scattering function width to weight the return from each pixel. Cells with angles exceeding the RMS slope value were lower weighted as these would be interpreted as less favourably angled to the sensor. At these locations, high levels of scattering away from the sensor are more likely compared to pixel locations which are oriented more towards the sensor position. Pixel weightings were determined from pixel angles to the sensor ($\angle_{Pixel}$) and the RMS slope ($\angle_{RMS}$) by the following function (equation 2.3):

$$Weighted\ Delay_{Pixel} = \frac{1}{\sqrt{2\pi}} e^{-(0.5\frac{\angle Pixel}{\angle RMS})^2} \qquad (2.3)$$

From this, the mean weighted delay for the entire footprint was calculated accordingly. Mean weighted delay was then differenced from all the delays within a footprint. The pixel with the minimum difference was identified as the location and elevation of the strongest echo.

As mentioned previously all bed elevation measurements picked from radargrams are treated as the nadir elevation. However, as it was expected that the elevation at the likeliest location of the strongest return was different to the nadir elevation it was termed the "simulated nadir elevation". Simulated nadir elevations were extracted and differenced from the DEM value at nadir. This difference is referred to from herein as the "off-nadir elevation difference".

The simulated nadir measurement and ArcticDEM elevation at nadir for each point are subject to uncertainty in the ArcticDEM. As mentioned in section 2.2.1, the absolute vertically uncertainty is currently estimated at $< \pm 1$ m and relative uncertainty within the DEMs is 0.1 m (Porter and others, 2018). Finally, this simulation does not include or parametrise the uncertainty in the synthetic bed measurement that would arise from the physical interaction of the radar beam with the ice sheet environment. The dielectric error was not parameterised but has been approximated at ± 10 m (Fujita et al., 2000). Scattering and attenuation errors arising from the presence of water within the ice sheet system and heavily crevassed ice are also not parameterised (Gogineni et al., 2001). However, this method aims to fully quantify the topographic uncertainty in RES measurements which has not previously been achieved. In chapter six the scope for expanding this simulation to include physical radar errors is evaluated.

2.4.2 RES survey measurement error assessment

Quantification and statistical assessment of synthetic RES survey uncertainty for each study site are fully described in the results of chapter three (section 3.4) and summarised below.

Error in RES surveying can be quantified from the differences between the simulated nadir bed elevation measurements and the input DEM values at nadir. In this thesis, the magnitude and probability of these off-nadir elevation differences are fully quantified. Firstly, descriptive statistics are calculated to

determine the typical characteristics of the error and identify any systematic biases (section 3.4.1.1). Secondly, probability density functions (PDFs) of the error are derived to establish the likelihood of the error occurring at various magnitudes (section 3.4.3, figure 3.5). Thirdly, off-nadir elevation differences are mapped to quantify the influence of subglacial landscape geometry on the scale of errors (figure 3.6). Finally, the errors are quantified in line with how RES measurements are used in the analysis of ice mass dynamic discharge (section 3.4.4, figure 3.7).

All results from this analysis and the following methods described in this chapter are reported with uncertainty bounds of ± 1σ.

2.4.3 Airborne RES measurement corrections

Full quantification of the scale and frequency of RES survey errors resulting from off-nadir elevation differences presents the possibility for deriving corrections. Three potential RES measurement corrections are established by this thesis in chapter three (section 3.5.2). Broadly, these corrections can be applied initially, to adjust all survey points according to the typical difference in the RES measured elevation and the DEM elevation (ordinary-least-squares regression, section 3.5.3). Secondly, these corrections can be applied probabilistically to quantify the uncertainty in a RES measurement based on the elevation it occurs at, with accompanying confidence intervals (section 3.5.4). Finally, corrections can be applied to a flux-gate profile of a surveyed outlet glacier to adjust estimates of ice discharge dependent on how the accumulation of errors alters the measured geometry of these features (section 3.5.5).

In chapters four and five these corrections are applied and tested to validate their efficacy.

2.4.4 Geostatistical interpolation of RES data

2.4.4.1 Kriging background

Kriging is a geostatistical interpolation method employed widely throughout geosciences (Haylock et al., 2008). It is predominantly used to predict a spatial quantity between sparse inputs (Matheron, 1963). Development of the method dates back to the 1930s (Kolmogorov, 1941), with considerable development as a geospatial technique undertaken in the 1960s and 1970s (Matheron, 1963,

Journel and Huijbregts, 1978). During this time the method was coined Kriging based on the earlier work of Krige (1951) who first investigated the application of statistics for geophysical investigations of gold mine valuation. For glaciology, it was first used to interpolate ice sheet bed topography between sparsely collected RES measurements by Herzfeld and Holmund in 1988 for Dronning Maud Land, Antarctica. From these early investigations it has been extensively used for mapping ice thickness and bed topography (e.g. Bamber et al., 2013; Fretwell et al., 2013), as well ice surface altimetry (e.g. Herzfeld et al., 1990; Bamber et al., 2013).

Kriging first showed promised for generating 3D bed topography maps at the scale of a continental ice sheet in the initial BEDMAP for Antarctica generated by Lythe and others, (2001). Soon after, it was implemented by Bamber and others, (2001), to derive the full bed topography of the GrIS at 5 km resolution. Since then it has been used, in combination with deterministic interpolators, to refine these initial bed datasets with the addition of further RES and other geophysical measurements (Le Brocq et al., 2010; Bamber et al., 2013; Fretwell et al., 2013). However, these datasets have since been superseded. Kriging fails to accurately reproduce sinuous channel morphology due to the constantly changing anisotropy over the scale of the interpolation (Williams et al., 2017). Consequently, areas crucial to the dynamics of ice sheets such as fjords and troughs are poorly replicated in kriged bed topography (Durand et al., 2011; Seroussi et al., 2011). Therefore, dynamic models of ice masses perform unrealistically where a kriged bed is used as an input (Morlighem et al., 2011).

To generate improved bed topography which overcomes the shortfalls of kriging, mass conservation approaches have been utilised (Morlighem et al., 2011). Mass conservation combines ice thickness measurements with surface velocity observations to infer ice sheet bed topography in regions of fast flow (>50 ma-1) (Morlighem et al., 2014). It is advantageous with regards to kriging, as the comparatively high resolution of surface velocity observations (400 m) allows for a seven-fold refinement of the overall dataset resolution (Morlighem et al., 2014). Consequently, however, the input velocity and derived bed topography are highly interdependent which introduces the potential for errors. Ice sheet velocity has been observed to be highly variable in marginal areas (Sundal et al., 2011). Additionally, although bed topography is a first-order control on ice velocity, other

seasonal factors, particularly the presence and abundance of meltwater may significantly augment ice flow (Palmer et al., 2011; Tedstone et al., 2015). Hence, input velocity may not be representative of a "steady-state flow", leading to bed topography which may be over or underestimated dependent on the relationship of the input flow speed in comparison to the long term dynamics of the ice sheet.

While mass conservation and streamline diffusion (finite-element modelling approach) has been applied in the latest bed topography datasets (Morlighem et al., 2017; Morlighem et al., 2020; Fürst et al., 2019), and alternative geostatistical and deterministic methods have been suggested and investigated (Dowdeswell et al., 2004; Le Brocq et al., 2010; Goff et al., 2014; Brinkerhoff et al., 2016) many ice sheet models and subsequent sea-level rise projections still depend on kriged datasets as inputs (Nowicki et al., 2016). Additionally, the majority of the Bedmachine Greenland v3 dataset is derived from kriging (~75% by area). Hence, this study focuses on developing methods for improving estimates of uncertainty in kriged datasets. The following section describes the method and section 2.4.2.3 outlines how it was applied throughout this thesis.

2.4.4.2 Kriging method

Geostatistical interpolation assumes spatial autocorrelation, whereby variables closer to each other are more similar than those further apart, to predict values in an unsampled location (Figure 2.8; McBratney and Webster, 1986). Kriging builds on this by assuming some of the spatial variation is attributable to natural randomness. Consequently, kriging can be used to make predictions accompanied by statistical uncertainty for that prediction (Figure 2.8; Oliver, 1990). Multiple methodological variations of kriging exist, but the most commonly used for the interpolation of ice mass bed topography is ordinary kriging (Jezek et al., 2013; Bamber et al., 2013). Ordinary kriging assumes a constant mean across the input data. This assumption is in part why the method fails to accurately reproduce channelised topography (Williams et al., 2017). However, across the typical distance between inputs across an ice sheet, it is deemed a reasonable assumption (Bamber et al., 2001). Furthermore, evidence from multiple studies suggests in the range of strong autocorrelation, method selection has very little influence on the output as variation in the topography is smooth in relation to the distance between observations (Herzfeld et al., 1990; Brinkerhoff et al., 2016). Regardless, the method has been employed extensively previously.

Hence, quantifying uncertainty in it is essential for improved interpretation of such bed datasets. In terms of ice thickness or subglacial topography interpolation, ordinary kriging is modelled as:

$$Z(s) = \mu + \epsilon(s)$$

(2.4)

where $Z(s)$ is the ice thickness or bed elevation, μ, is the input mean elevation, and $\epsilon(s)$ represents random autocorrelated errors in thickness or bed elevation.

Quantifying spatial autocorrelation for predicting unknown values based on their location is achieved through variography (Oliver, 1990; Herzfeld et al., 1993). This is usually quantified as semivariance, which equates to half of the squared difference between point observations. The semivariogram, semivariance with respect to the distance between points, was devised by Matheron (1963) as:

$$\gamma(h) = \frac{1}{2V} \iiint_V [f(M + h) - f(M)]^2 dV$$

(2.5)

where, in terms of ice thickness or bed elevation, M is a Cartesian location in the geometric domain of the ice sheet V. $f(M)$ is the ice thickness or bed elevation at that point and h the distance of separation between points. However, as the semivariogram is an unobservable theoretical function it requires estimating (Oliver, 1990). Consequently, geostatistical interpolation utilises the empirical semivariogram function. Lag distances are binned ($h \pm \delta$) so semivariance is instead determined for a range of distances opposed to every exact distance. This is defined as:

$$\hat{\gamma}(h \pm \delta) = \frac{1}{2|N(h \pm \delta)|} \sum_{(i,j) \in N(h \pm \delta)} |z_i - z_j|^2$$

(2.6)

where $N(h \pm \delta)$ is the number of point observations within a binned lag distance. Z replaces $f(M)$ as the ice thickness or bed elevation value. The squared difference of observed values is found for point pairs, i and j, summed, and subsequently normalised by the number of bins. Finally, the semivariogram is determined by halving the result.

As the empirical semivariogram cannot be computed at every lag step, various mathematical models are utilised for estimating the empirical semivariogram (Oliver, 1990). These models are fitted using an ordinary least squares approach. Previous mapping of bed topography has utilised both Gaussian and spherical models. However, the spherical model has been used for the majority of bed

topography mapping studies (Herzfeld et al., 2011; Bamber et al., 2013). The spherical model is defined by:

$$\gamma(h) = (s-n)\left(\left(\frac{3h}{2r} - \frac{h^3}{2r^3}\right)1_{(0,r)}(h) + 1_{(r,\infty)}(h)\right) + n1_{(r,\infty)}(h) \qquad (2.7)$$

where h is the lag distance, r the range and s the sill, n the nugget. Correspondingly, these three parameters are fundamental for describing semivariograms. The range is defined as the initial lag distance where the modelled semivariogram levels out (Matheron, 1963). Importantly, sample points separated by lag distances less than the range are spatially autocorrelated. The value of semivariance at the range lag distance and beyond is termed the sill (Matheron, 1963). Finally, the nugget is the intercept value of the model and accounts for measurement errors in the sampling method, random sources of spatial variation at distances smaller than the defined lag distance, or both (Matheron, 1963).
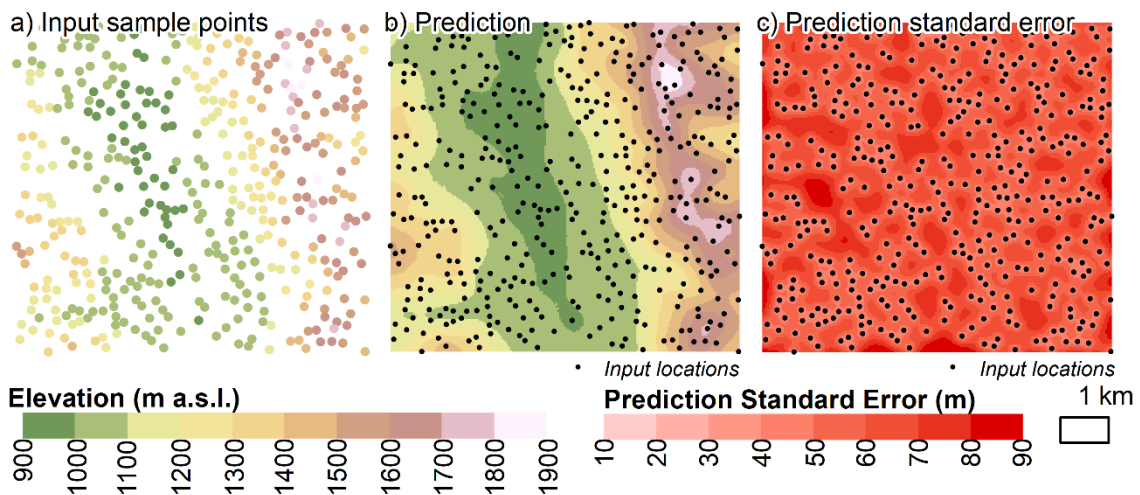
Figure 2.8 Illustration of interpolating a surface between sparsely collected input measurements using kriging. a) Input point elevation measurements. b) kriging prediction of elevations between the input measurements based on the semivariogram parameters. c) Estimated error in the prediction surface based on the semivariogram parameters, typically an inverse distance function where error increases logarithmically with distance from an input.

Figure 2.9 highlights an example of a spherical model fitted to input synthetic RES measurements and the cross-validation of the model fit. For consistency across this work and with previous work, spherical models were applied throughout all

kriging and optimised to minimise the RMSE of the cross-validation function (Figure 2.9).
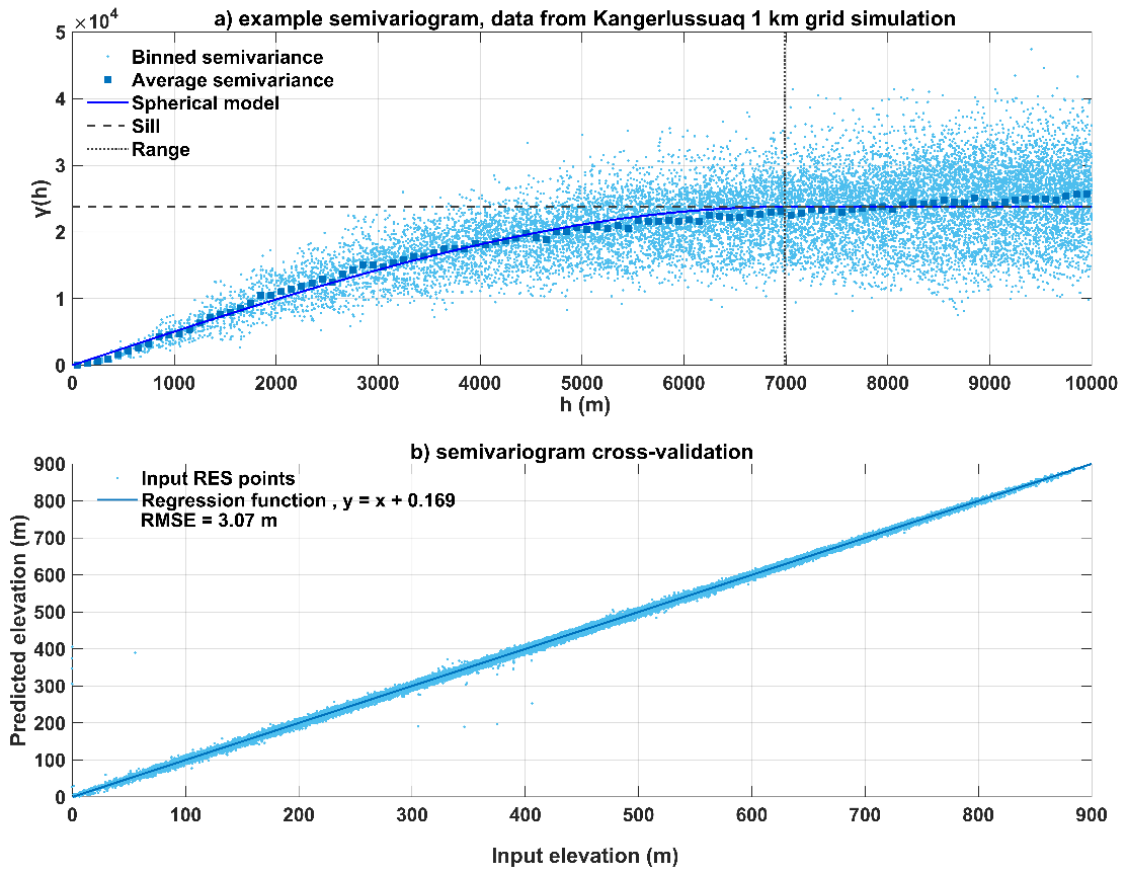
Figure 2.9 Example semivariogram used in this thesis. Data is from the Kangerlussuaq 1 km grid simulation. a) Empirical semivariogram for the synthetic RES measurements, a spherical model provided the best fit, γ(h) is the semivariance for the individual lag, and h is the lag distance. b) Cross-validation model for the semivariogram, the optimal model choice minimised the RMSE of the regression fit.

2.4.4.3 Interpolating ice thickness and bed topography

This thesis focuses on kriging as it has been the most widely used interpolator for generating subglacial topography. Kriging undertaken by this thesis for particular areas is described in the respective methods sections of chapters four and five (sections 4.3 and 5.3). The following summarises the overall approach to geostatistical interpolation by this work.

Synthetic RES survey point elevations are interpolated using an ordinary kriging model. Ordinary kriging using a spherical model was implemented following the method of Jezek and others, (2013). Similarly, five neighbouring points were selected, and 100 lags of 100 m were used, in line with previous studies (Jezek et al., 2013; Bamber et al., 2013). Finally, all kriging was optimised using the inbuilt iterative cross-validation in ArcMap 10.5.1. This procedure determines the sill and range parameters of the semivariogram which best fit the input data.

A nugget effect is usually implemented to account for error in ice thickness measurements, although alterations it makes to the output surface are minor (Herzfeld et al., 1993). As this study aimed to investigate these errors in isolation and how they migrate through acquisition to interpolation, no nugget was applied to the kriging of synthetic RES measurements. Furthermore, the synthetic RES simulation developed in this thesis does not account for errors arising from the physical properties of the radar signal and its interaction with the ice sheet environment, which is what the ~30 – 50 m errors parameterised by the nugget accounts for in previous work (Jezek et al., 2013; Bamber et al., 2013; Fretwell et al., 2013). Therefore, actual RES measurements in chapters four and five are interpolated with a 30 m nugget effect, replicating previous methodologies to keep uncertainty assessment concomitant.

High precision in the ArcticDEM (<1m absolute errors) allows for the incorporation of elevation data in the interpolation of bed topography, as any systematic measurement biases are smaller than those RES measurements of bed and surface elevation (Peters et al., 2005; Paden et al., 2010). Ice thickness is the measured and most often interpolated quantity with subglacial topography latter calculated by subtraction from a surface dataset (Dowdeswell et al., 2004). However, with high accuracy and high-density inputs, this thesis shows interpolating the ice bottom measurements in conjunction with ArcticDEM elevation measurements aides the generation of more accurate bed topography (Figure 2.10). By simulating the acquisition and interpolation of RES survey measurements for a synthetically generated small valley glacier, it was determined that the output bed surface more closely matched the ArcticDEM topography when elevation was the measurement interpolated opposed to ice thickness. RMSE for the elevation based interpolation was 65 m compared to 81 for ice thickness based interpolation (Figure 2.10). Application of this to a small

valley glacier, Sveigbreen in Svalbard (Navarro et al., 2015), it is found that the interpolation produces a deeper bed when elevation is used as the input (Figure 2.11). This is preferable because a well-established critique of kriging is that it often fails to adequately reproduce the full depth of valleys (Morlighem et al., 2014), particularly for glacial environments where the terrain is often overdeepened (Williams et al., 2017).
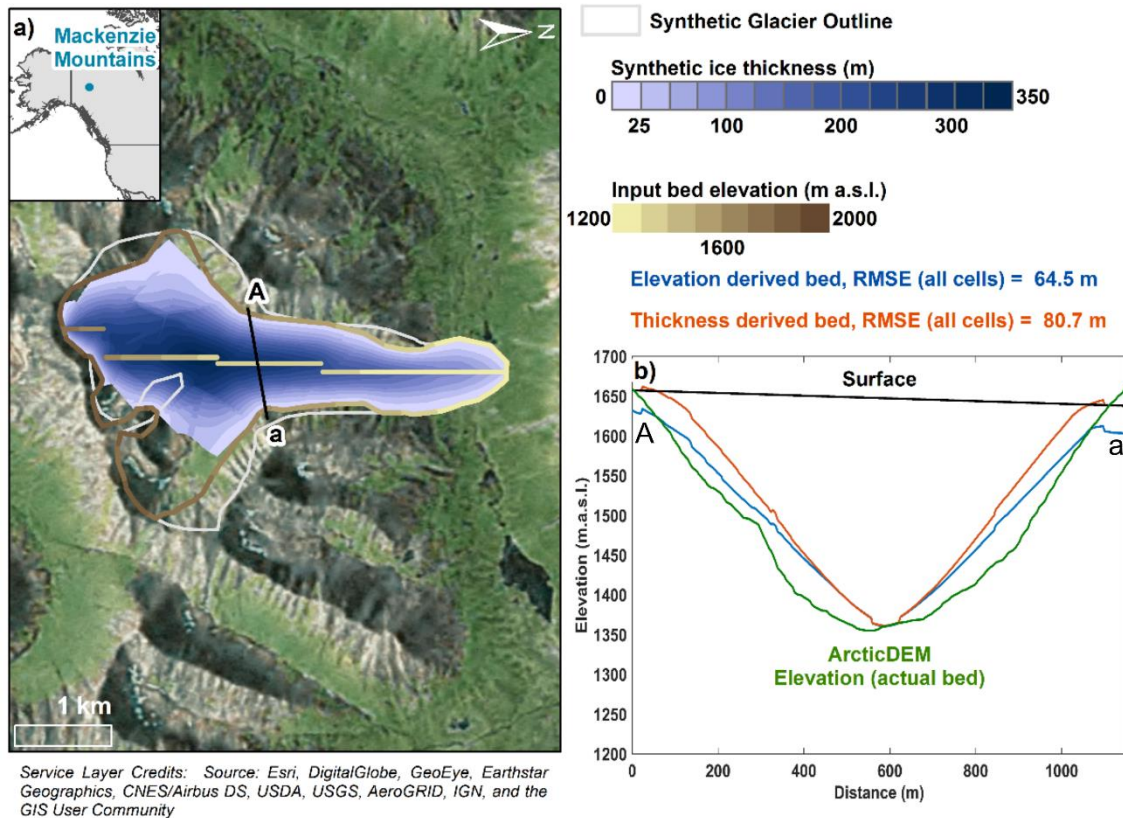
Figure 2.10. Interpolated ice thickness and bed topography for a synthetic glacier. The topography is from the EGA study site. a) Input measurements are coloured by elevation. Outline and survey point elevation is from the ArcticDEM. b) Profile A-a, the synthetic surface elevation is in black, orange shows bed topography from interpolating ice thickness, and bed topography from kriging elevation inputs is in blue.

70
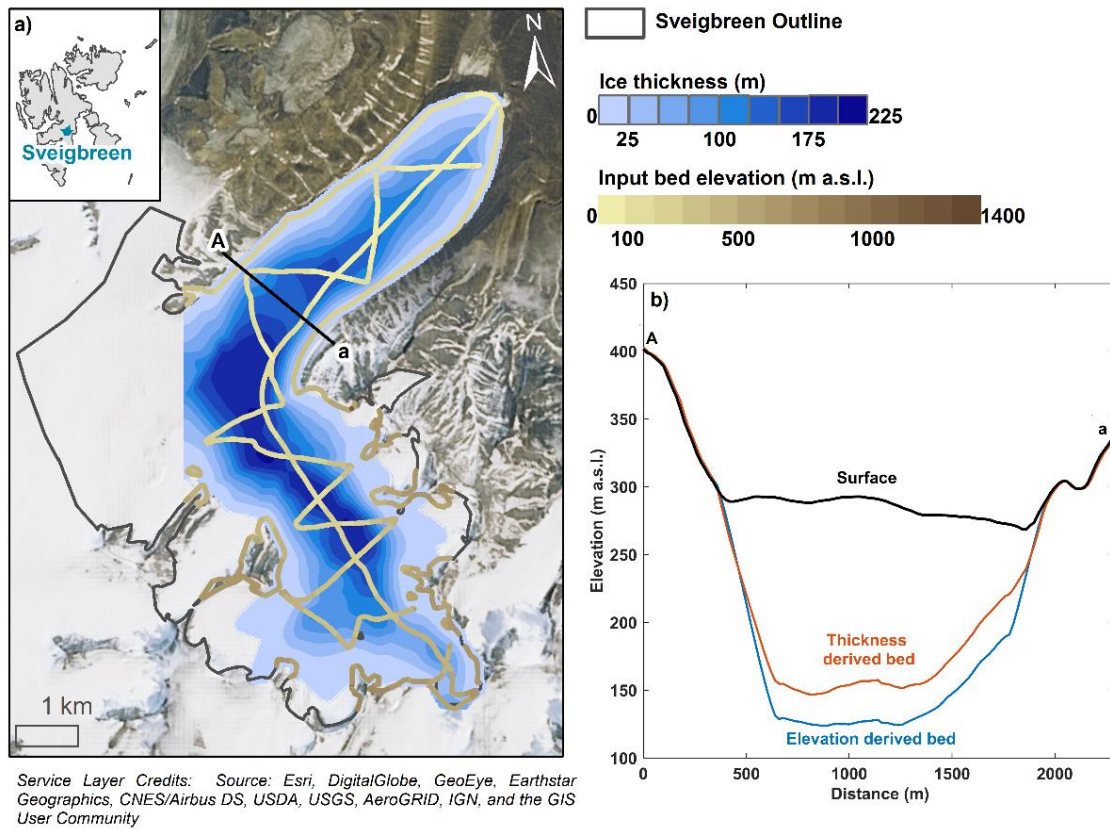
Figure 2.11. Interpolated ice thickness and bed topography for Sveigbreen, Svalbard. a) Input measurements are coloured by elevation. Outline point elevation is from the ArcticDEM, survey points (within glacier outline) are coloured by bed elevation (data from Navarro et al., 2015). b) Profile A-a, surface elevation in black, kriged bed topography from interpolating thickness is in orange, and kriged bed topography from interpolating elevation is shown in blue.

2.4.4.4 Interpolated surface error assessment

Described below is the development of functions used to quantify and reduce the error in kriged bed topography datasets. Quantification of the errors in the interpolated sectors of Bedmachine Greenland v3 is fully described in chapter four (sections 4.4.4). Furthermore, the implementation of the following error assessments is fully described in chapters four and five.

Various characteristics of the input data are expected to influence the quality of an interpolation output. Interpolation error is defined as the difference between the output surface from kriging and the input DEM elevation at a given location. Investigated here alongside interpolation error was the spatial density of the input data (section 4.4.2, figure 4.2), the distance of an interpolated point from the input data (sections 4.4.2, 4.4.3 figures 4.3, & 4.4), and the roughness of the input

71

terrain (RMSD) (section 4.4.2, figure 4.2). Furthermore, as kriging is known to tend towards the mean of the inputs (Goff et al., 2014; Williams et al., 2017), the error in the output surface was investigated relative to the difference of an interpolated point from the mean elevation. This difference is termed the difference from mean elevation (DME) throughout. Any relationship found between these factors and interpolation error was quantified using ordinary-least-squares regression and their viability as a correction or validation method assessed (section 4.4.4, figure 4.7). To quantify interpolation error, approximately 20,000 points were generated across each interpolated bed topography. In total, this resulted in 1.5 million sample points of interpolated elevation and DEM elevation. From this robust error, functions were derived.

Logarithmic distance error functions are standard outputs for geostatistical interpolations (Deutsch and Journel, 1997). These errors are widely reported as the uncertainty for ice-sheet bed topography datasets (Bamber et al., 2001; Bamber et al., 2013; Fretwell et al., 2013; Morlighem et al., 2017). However, they are rarely constrained by anything more complex than simple inverse distance weighted relationships. This thesis will quantify the actual difference of an interpolated elevation at a given location and derive an observation-based Euclidean distance error function. Figure 2.12 illustrates an example Euclidean distance error function compared with the estimated function for bed machine. The preliminary analysis highlights that this method has the potential for deriving reduced uncertainty.
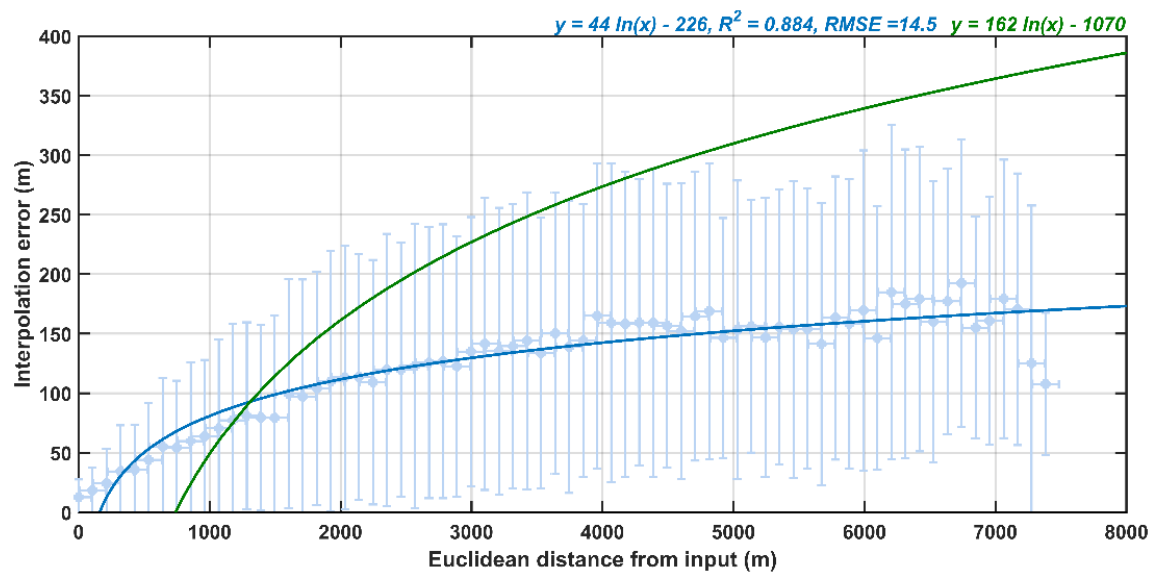
Figure 2.12. Euclidean distance error function for a sparsely sampled example site, Kangerlussuaq 15 km grid. An estimated distance error function for Bedmachine Greenland v3 is shown in green for comparison. Points are 100 m binned (x error bars) means of interpolation error, with accompanied standard deviation (y error bars).

The difference from mean elevation (DME) was calculated to quantify the relationship between the relative topographic positioning of a pixel and the interpolation error (preliminary e.g. Figure 2.13). This concept exploits the known tendency of kriging to smooth a landscape so that areas much higher than the mean are lowered and those below raised i.e. relief is underestimated. By calculating the DME of a pixel in an interpolated bed, the likelihood of the actual value being lower or higher than the interpolation may be derived. Ordinary least squares regressions were fitted to DME vs error. Initially, this was conducted for all the sample points across a proglacial area, to determine the raw relationship. Subsequently, running means of error for every 10 ms DME were fitted (Figure 2.13). While this method sacrifices 10 meters accuracy, this is lower than the ± 30 - 70 m widely reported for ice thickness in dynamic mass balance studies (Enderlin et al., 2014; Rignot et al., 2018; King et al., 2018; Mankoff et al., 2019), the benefit is a stronger relationship and therefore, a function that can be applied to kriged datasets. Even where this method doesn't reduce uncertainty it still improves it by determining a more likely error value based on the topography rather than the distance from inputs. Finally, the benefit of this method is it can predict real values of error, i.e. negative or positive, as opposed to the distance function which only determines absolute error, i.e. positive only (Figure 2.13). As the method works regionally and is developed on the 50 km x 50 km sample areas, it is employed throughout interpolation error assessment using a rectangular search neighbourhood of 50 km x 50 km.
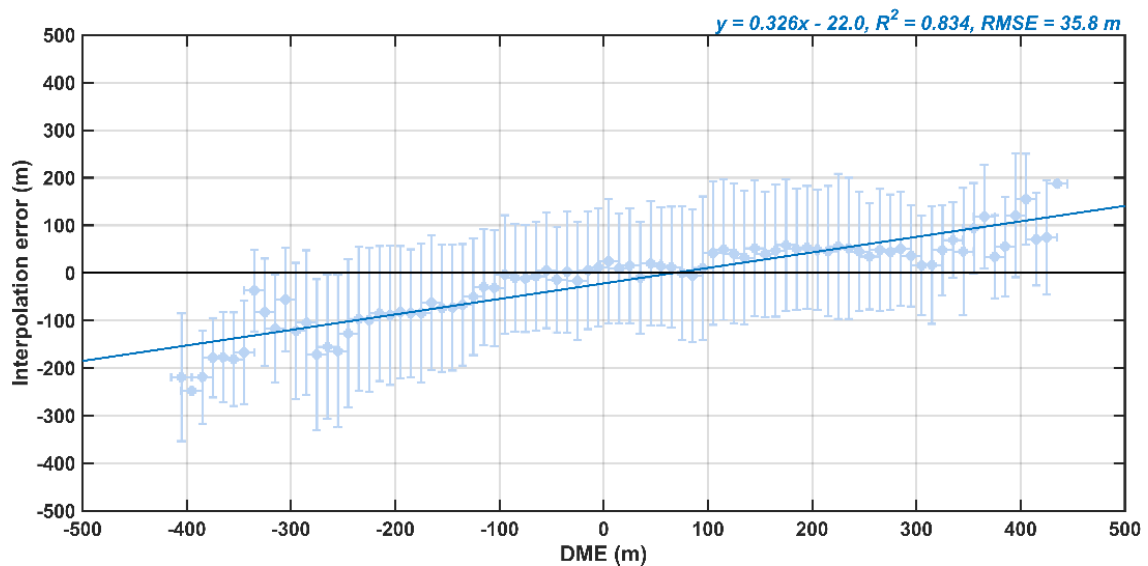
Figure 2.13. DME error function for a sparsely sampled example site, Kangerlussuaq 15 km grid. Points are 10 m binned (x error bars) means of interpolation error, with accompanied standard deviation (y error bars).0

2.5 Application of the full methodology

After full development of the individual methods in chapters three and four, they are combined and employed in chapter five for RES measurements of CAA ice caps in the QEI. Combination of the methods into a complete workflow is fully described in chapter five and summarised below.

2.5.1 Canadian Arctic Archipelago bed topography

Synthetic RES surveys are simulated over ArcticDEM tiles of proglacial areas proximal to ice caps in the CAA. Synthetic survey geometry is setup to mimic the density and configuration of airborne RES missions previously conducted over QEI ice caps (section 5.3, figure 5.1). Next, the synthetic measurements are interpolated, and the output surfaces are differenced from the input DEM to establish the Euclidean distance error function and DME error function for quantifying uncertainty in bed topography for the neighbouring ice caps (sections 5.3 & 5.4, figures 5.2 & 5.3). Following this, all available RES measurements taken over QEI ice caps are interpolated using ordinary kriging, to the same parameters as determined by the synthetic interpolation. Accordingly, bed topography is generated for the selected ice caps with accompanying quantification of uncertainty, representing the full application of the methods developed by this thesis.

2.5.2 Canadian Arctic Archipelago hypsometric analysis

Hypsometry is the frequency distribution of elevation across an ice mass. Supraglacial hypsometry affects how much ice is likely to be gained or lost from a shift in the equilibrium line altitude (ELA) (Jiskoot et al., 2009; MacGrath et al., 2017). A glacier with a greater frequency of high elevation will be more susceptible to rising ELA as a larger area of the glacier then begins to ablate. Conversely, glaciers with greater frequency of lower elevations will be less susceptible to rising ELAs as a significant area of the glacier already undergoes extensive ablation. Figure 2.14 highlights two glaciers in Svalbard with differing surface hypsometry to illustrate the concept. Subglacial hypsometry influences the potential for enhanced dynamics if an ice mass bed is contiguous with the ocean (Dowdeswell et al., 2004). An ice mass with a high frequency of low elevations, particularly sub-sea level elevations will be more exposed to subaqueous melting and marine-terminating margin retreat. However, if the bed topography is predominantly high elevation, and above sea-level, the influence of dynamic mass loss is significantly reduced and mass balance is predominantly influenced by surface mass balance (MacGrath et al., 2017; Dowdeswell et al., 2004).

Hypsometric indices are determined to assess the ratio of high elevation to low elevation across an ice mass surface or bed (Jiskoot et al., 2009; Dowdeswell et al., 2004). From these, ice masses may be classified depending on which threshold the hypsometric index meets and interpretations about their stability made (Table 2.1). These indices, *HI,* are determined by:

$$HI = \frac{(H_{max} - H_{med})}{(H_{med} - H_{min})} \qquad\qquad (2.8)$$

but if 0 < *HI* < 1, *HI = -1/HI*. $H_{max,}$ $H_{med,}$ and H_{min} are the ice mass maximum, median and minimum elevation respectively.

Table 2.1 Hypsometric indices following Jiskoot and others, 2009.

HI	Description	Supraglacial implications	Subglacial implications
HI <-1.5	Very top-heavy	Increased susceptibility to rising ELAs and negative surface mass balance.	Reduced influence of ice dynamics. High elevation grounded ice susceptible to rising ELA.
-1.5 < *HI* < -1.2	Top-heavy		
-1.2 < *HI* < 1.2	Equidimensional		
1.2 < HI < 1.5	Bottom-heavy	∧ ∨	∧ ∨
HI >1.5	Very bottom-heavy	Reduced susceptibility to rising ELA (however, increased susceptibility to elevation-albedo feedback)	Heightened influence of ice dynamics (If connected to the ocean higher susceptibility to enhanced dynamic mass loss)

Consequently, by conducting a full hypsometric analysis of supraglacial and subglacial topography across the CAA ice caps, inferences may be made about their susceptibility to changes in surface and dynamic mass balance. This will be novel for the bed elevation of the Agassiz, Axel Heiberg, North Ellesmere and Prince of Wales Ice Caps. Hence, for the first time, the stability of marine-terminating outlet glaciers across these ice caps will be inferred. Additionally, with the inclusion of surface hypsometry this thesis will ascertain the relative importance of dynamic stability of these ice caps with respect to surface mass balance which is currently the main driver of regional mass loss (Colgan et al., 2015).
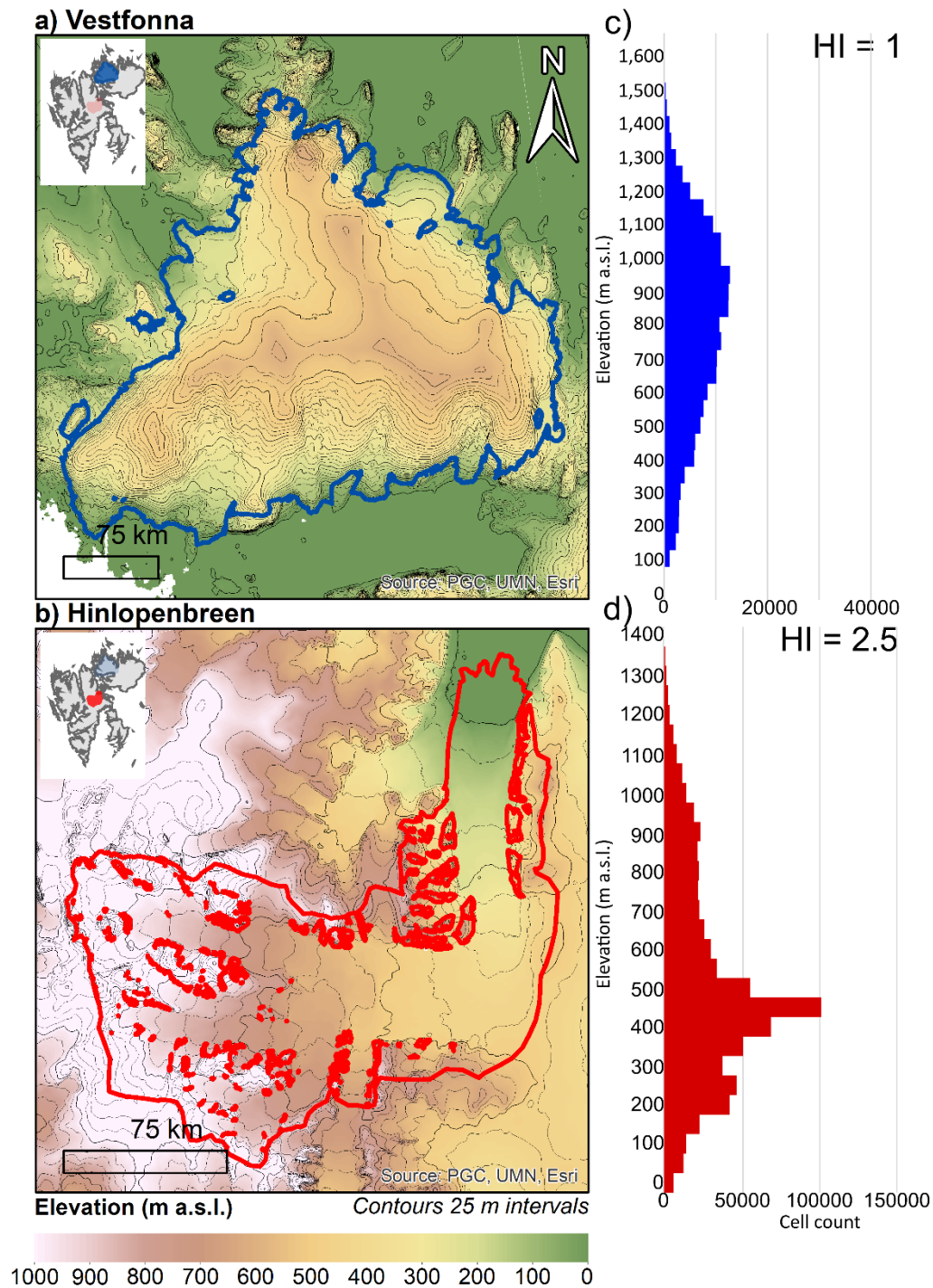
Figure 2.14 Supraglacial hypsometry of Vestfonna (a,c) and Hinlopenbreen (b,d), Svalbard. Low contour density highlights a greater frequency of similar elevations between contours. a) Vestfonna, a predominantly land-terminating ice cap with a HI of 1 is equidimensional. b) Hinlopenbreen a marine-terminating glacier is very bottom-heavy, *HI = 2.5*, illustrated by low contour density at low elevation.

2.6 Monte Carlo assessment of additional RES uncertainty on dynamic discharge

The error resulting from the topographic uncertainty defined and established in this thesis has implications for historic and future estimates of ice dynamic discharge derived from RES measurements and interpolations. To assess the impact of this uncertainty on dynamic discharge Monte Carlo simulations were undertaken. Results generated by this thesis will fit a probability density function. Here the Monte Carlo simulation will use the probability density of valley geometry mismeasurements to highlight how these propagate through to uncertainty in dynamic discharge estimates. Although computationally expensive Monte Carlo simulations are straight forward and can handle large datasets. Hence, this thesis will take previous estimates of dynamic discharge for the GrIS (Mankoff et al., 2019) and Antarctic Ice Sheets (Rignot et al., 2018) and simulate each dynamic discharge estimate 10,000 times with a random topographic uncertainty that falls within the probability density function of errors established by this work. The output will indicate how much additional uncertainty in dynamic discharge estimates could be expected that is not currently accounted for.

Equation 2.9 describes the Monte Carlo approach taken in this thesis:

$$Q_1 = Q_0 + (Q_0 X) \qquad\qquad (2.9)$$

Where Q_1 is the new dynamic discharge measurement when the propagation of a random uncertainty estimate X modifies the reported estimate Q_0. X is a randomly determined percentage uncertainty from a Pearson distribution defined by the mean, standard deviation, skewness and kurtosis of the probability density function of RES uncertainties.

Chapter 3: Geospatial simulations of airborne ice-penetrating radar surveying reveal elevation under-measurement bias for ice sheet bed topography

This chapter describes the development and application of synthetic radio-echo sounding for quantifying the error in ice thickness measurements caused by the geometry of the surveyed landscape. This chapter is in review for publication in Annals of Glaciology:

Bartlett, O.T., Palmer, S.J., Schroeder, D.M., MacKie, E.J., Barrows, T.T., Graham, A.G.C, 2020. Geospatial simulations of airborne ice-penetrating radar surveying reveal elevation under-measurement bias for ice sheet bed topography, Annals of Glaciology.

I developed and implemented the geospatial RES simulation, produced and analysed the results and wrote the manuscript. Palmer assisted with the analysis of the results, and the writing of the manuscript. Schroeder helped develop the geospatial RES simulation. Barrows, MacKie, and Graham reviewed and contributed comments to the manuscript.

3.1 Abstract

Airborne radio-echo sounding (RES) surveys are widely used to measure ice sheet bed topography. Bed topography influences overlying ice dynamics, which affects the quantity and rate at which ice is moved to the margin. Modelling ice dynamical response to climate change requires accurate and widespread measurement of bed topography. Measurement accuracy of RES surveys is influenced by both the geometry of bed topography and the survey design. Here we develop a novel approach for simulating RES surveys over glaciated terrain, to quantify the sensitivity of derived bed elevation to topographic geometry. Furthermore, we investigate how measurement errors influence quantification of glacial valley geometry. We find a negative bias across RES measurements, where off-nadir return measurement error is typically -1.8 ± 11.6 m. Topographic highlands are under-measured an order of magnitude more than lowlands. Consequently, valley depth and cross-sectional area is largely underestimated. While overall estimates of ice thickness are likely too high, we find large glacier valley cross-sectional area to be underestimated by -2.8 ± 18.1%. Therefore, estimates of ice flux through large outlet glaciers are likely too low when this effect is not taken into account. Additionally, bed mismeasurements potentially impact our appreciation of outlet glacier stability.

3.2 Introduction

Ice sheet thickness and bed elevation are fundamental boundary conditions for modelling ice sheet- climate interactions (Bamber and others, 2013). Measurement of these conditions over a continental scale requires remote sensing methods capable of penetrating ice. Successful detection of subglacial topography in Antarctica in the late 1950's (Turchetti et al., 2008), and of the Greenland Ice Sheet (GrIS) in the 1960s using radio-echo sounding (RES) paved the way for mounting such systems on aircraft to survey large areas (Dowdeswell & Evans, 2004; Evans & Robin, 1966). Hence, airborne RES surveys now comprise the principle method for measuring ice sheet bed topography. Various characteristics of ice sheets are known to affect RES survey accuracy, however highly rough topography (Jordan and others, 2017), subglacial and englacial water (Chu and others, 2016; Kendrick and others, 2018), and crevassed ice are sources of error for RES surveys as they scatter or attenuate the radar pulse (Gogineni et al 2001; Jezek and others, 2013). Moreover, measurement accuracy

is also influenced by the setup and movement of RES systems when surveying (Lapazaran and others, 2016). In addition to the inherent uncertainties of measuring bed topography with radar, the geometry of the data acquisition approach means that measurements are often collected along widely spaced flight-lines, with no data collected in-between (Studinger and others, 2010). Consequently, in order to derive regional or ice sheet-wide bed topography, interpolation between measurements is required. Various methods are employed to do this and the quality of the output is heavily reliant on the accuracy of the input data (Morlighem and others, 2014). While interpolations often incorporate uncertainty parameters to make up for the measurement error (Bamber and others, 2013; Morlighem and others, 2017), actual measurement error is rarely quantified as it requires physically accessing the ice sheet bed to independently validate a measurement of subglacial topography.

It is important to have an accurate estimate of bed topography, because it influences key components of the ice sheet system. Fundamentally, measured and interpolated bed topography gives an indirect measurement of total ice volume, from which an ice sheet's potential sea-level contribution is estimated (Bamber and others 2013). It is also crucial to understand the rates and character of ice loss from the ice sheet, because these are required to inform near-term policy relating to sea level rise (Church and others, 2013). Subglacial topography exerts a strong influence on ice flow, and so it is a significant factor in controlling ice discharge to the oceans (Durand and others, 2011), which accounts for roughly half of all mass loss in Greenland (Van den Broeke and others, 2016). Conditions at the ice-bed interface, such as the amount of free water and the magnitude of spatial roughness, largely dictate the maximum potential velocity of the overlying ice, by altering the basal traction at the ice-bed interface (Hoffman and others, 2016; Gudmundsson, 1997). Subsequently, this dictates the rate at which ice is moved to lower elevations where it melts or is removed in processes such as iceberg calving. Atmospheric warming is increasing the overall magnitude of meltwater delivered to the bed, and is increasing the spatial and temporal variability of this water input (Sundal and others, 2009), which in turn is likely to affect the dynamic response of portions of the ice sheet where bed hydrology is a factor (Sundal and others, 2011; van de Wal 2008). Additionally, highs and lows in bed topography influence the seasonal storage and distribution

of subglacial meltwater, further influencing basal friction regimes (Chu and others, 2016). Hence, having accurate estimates of bed topography and subglacial conditions is crucial to understanding which portions of an ice sheet are likely to respond to changes in meltwater supply.

This paper aims to quantify the topographic uncertainty in RES surveys and the influence of these measurement uncertainties on analysis conducted with RES data. By simulating RES surveys over formerly glaciated areas of precisely-known topography, we quantify the relationships between RES survey characteristics such as flight line orientation and spacing, and topographic characteristics such as relief, slope, and landscape feature orientation. Hence, we develop a synthetic RES data set for assessing bed measurement uncertainty in the absence of independent validation measurements in the ice-covered area of interest. Furthermore, we quantify the uncertainty in areas of key importance to ice flow, predominantly valleys where ice and meltwater are typically focussed by the underlying topography. From this, we establish how any mismeasurements of valley geometry may influence ice-sheet modelling and mass-conservation, which utilise relationships between ice dynamics and the geometry of such features. Using the knowledge elucidated in these investigations, we assess the potential for adjusting and re-interpreting previously acquired RES survey data and subsequent analyses, so that their accuracy may be increased.

3.3 Data and Methods

3.3.1 Study locations and datasets

The primary inputs to our synthetic surveys are digital elevation model (DEM) tiles from the ArcticDEM (Porter and others, 2018), aggregated to 5 m resolution for computational efficiency. In order to represent the variety of topographic landscapes beneath an ice sheet, we selected four regions of varying characteristics, representing the full range of topography we expect to lie beneath the GrIS. Three of these regions include proglacial areas (PGAs) proximal to the GrIS because these are likely to be representative of the adjacent subglacial topography (Lindbäck and others, 2014). As much of the proglacial topography in East Greenland is submerged by the Atlantic Ocean, DEMs are unavailable and bathymetric data are of insufficient spatial resolution for our purposes.

Region four, the McKenzie Mountains in Canada, was chosen as an analogue to the areas of eastern Greenland where the proglacial topography is largely characterised by wide, deep fjords with smaller tributary fjords. Additionally, this area was chosen because it was formerly glaciated by the Cordilleran Ice Sheet (Eyles and others, 2018 and references within). This fourth study site is referred to throughout the paper as the East Greenland Analogue (EGA). Figure 3.1 highlights our study sites and displays the orientation of the simulated flight surveys. Survey areas were designed to cover 50 x 50 km squares, except for Inglefield land where subaerial topography only extends 47 km from the ice sheet toward the sea.
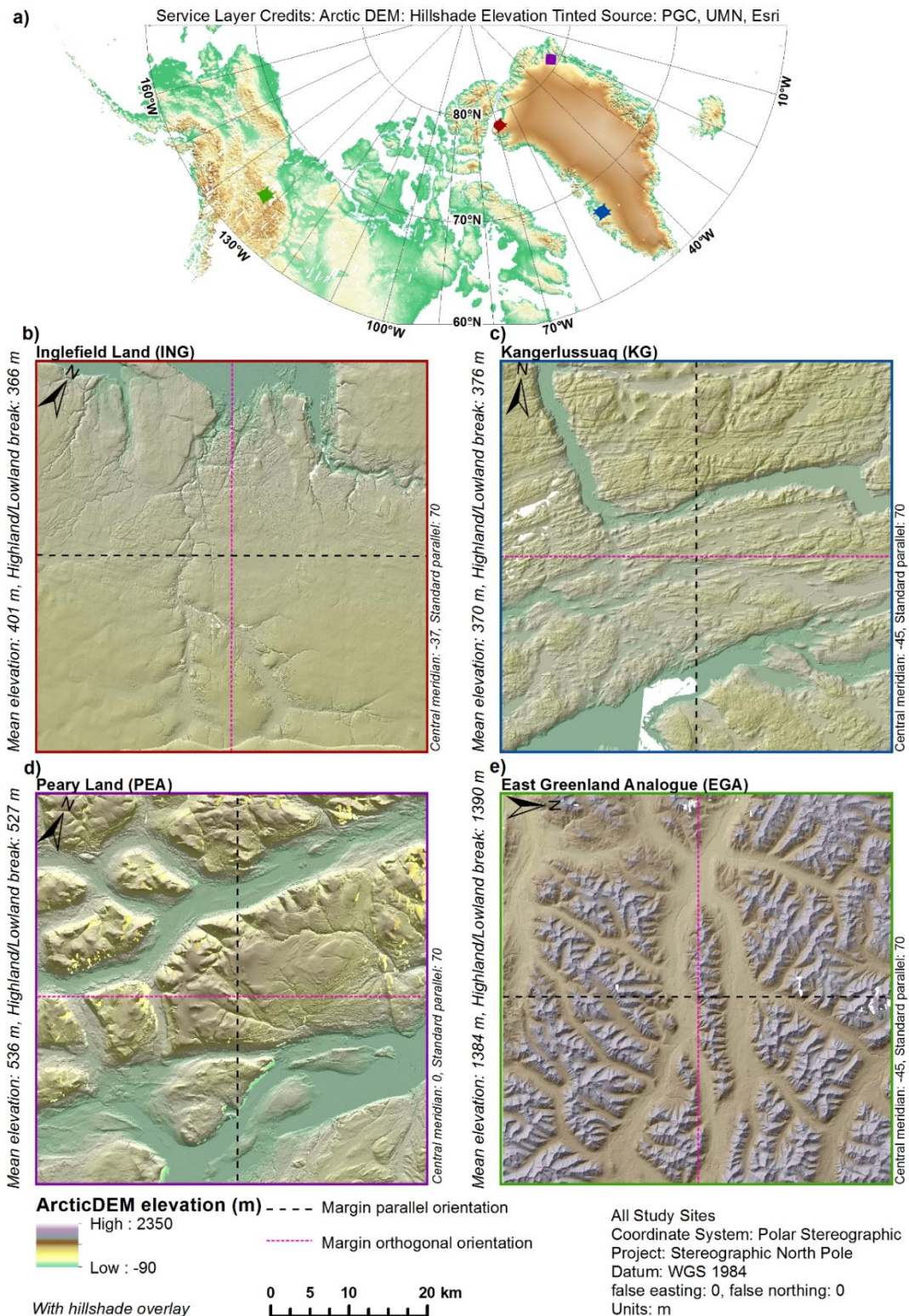
Figure 3.1 Study site locations, topography and survey geometries. a) Location of study sites. b) Inglefield land. c) Kangerlussuaq. d) Peary Land. e) East Greenland Analogue (EGA). Coloured site location boxes in a) correspond with subplot outlines b), c), d), and e). Hillshades have an aspect 315° of and an angle of 45°.

3.3.2 Geospatial RES survey simulation

RES surveys and bed elevation picking were simulated in ArcMap 10.5.1. Our simulation setup was based on NASA's Operation IceBridge flights using the MCoRDs system on a P-3 aircraft (CReSIS, 2018); because these comprise the majority of RES surveys conducted over the Greenland Ice Sheet (Studinger and others, 2010). The following model workflow is illustrated in figure 3.2.
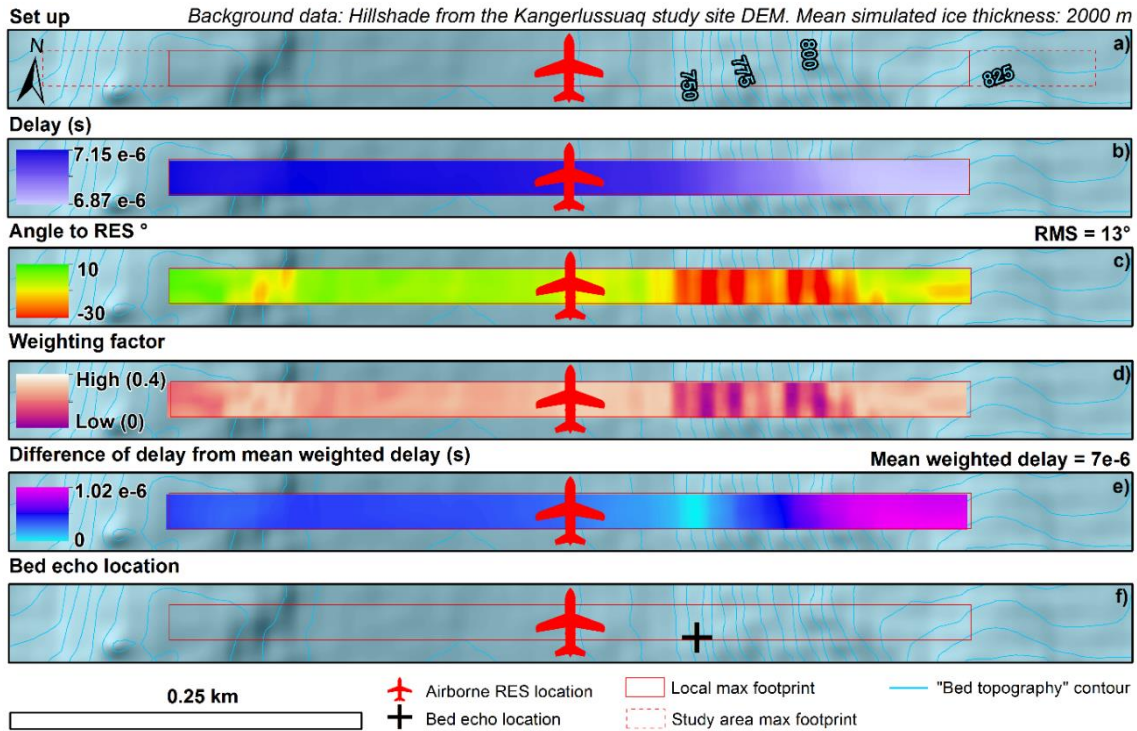
Figure 3.2. Geospatial RES Survey simulator workflow. a) Footprint calculation. b) Delays. c) Angle of surface to RES sensor. d) Return weighting factor. e) Difference of cell delay from the footprint mean weighted delay. f) Most likely location of the brightest reflector.

3.3.3 Simulation setup

Flight-lines were simulated across the study sites at one kilometre spacing in either margin parallel (MP) or margin orthogonal (MO) orientation. These orientations are adopted by IceBridge flights and occasionally combined to form grids (Studinger and others, 2010). Quality assessment along MP flight-lines was done in order to assess the measurement accuracy along profiles which are typically used as ice-flux gates for estimating discharge as part of the mass budget mass balance approach (Rignot and Kanagaratnam, 2006; Enderlin and

others, 2014; King and others, 2018). Moreover, these flight-lines comprise the principle inputs for mass conservation-based interpolations (Morlighem and others, 2017). MO flight-lines represent surveys along glacier centrelines which aim to capture the maximum depth of a glacier's constraining topography. Here, MO flight-lines were tested to the same extent as MP flight-lines so absolute uncertainties in any flight-line of such orientation could be assessed. Extensive assessment of errors in both orientations is essential for quantifying uncertainty along and across gridded surveys.

Along each flight-line, points were plotted every 14 m, resembling the sample postings of an IceBridge survey.

Raster layers were generated to simulate an ice sheet surface. For each study site, an ice sheet "interior" surface was generated which was equivalent to the mean study site elevation plus 2000 m, to simulate mean ice thickness of approximately 2000 m. To simulate a "marginal" situation, where the aircraft distance from the bed varies across the study site, a sloping ice sheet surface raster was generated which approximately replicated the surface slopes and surface elevations of the adjacent regions of the GrIS. For the EGA, approximate surface elevation data was taken from the eastern margin of the GrIS near Helheim Glacier.

3.3.4 Bed elevation measurement

From the spatial location of a survey point and the 3D geometry of the DEM beneath it, we simulated the location of what would appear in a radargram as the brightest reflector, measured the elevation of this location, and subsequently treated it as the "simulated nadir" elevation.

In the along-track direction, footprint size was set to 25 m which replicated the along-track resolution of the MCoRDS system. For each along-track position, we searched across track within the maximum footprint width to investigate from where the echo originated, rather than taking the common assumption that it came from directly below the aircraft.

For every point, the maximum footprint width was calculated to represent the coarsest resolution measurement that could be made at that point following the CReSIS Radar Depth Sounder report, 2018 (CReSIS, 2018). The maximum

resolution is related to the height of the aircraft above the ice sheet surface Za, the maximum ice thickness for the study site hmax, βγ is the beam width in radians (0.3) and κγ is the approximate cross-track windowing factor (CReSIS, 2018) (1.3), where:

$$MaxFP = 2\left(Za + \frac{h_{max}}{\sqrt{3.15}}\right)\tan(\frac{\beta_y k_t}{2}) \qquad \text{(Equation 3.1)}$$

Once the maximum footprint for each survey point was generated, a localised maximum footprint for each point was calculated using equation 1 substituting hmax with the maximum ice thickness within MaxFP at that point.

Within each local footprint, distances to and from the survey points were calculated trigonometrically and converted to delays by dividing by the speed of light (Figure 3.2b). As the simulation was designed to solely determine the influence of topographic and survey geometry on the most probable location of a return, adjustments relating to physical properties of the radar pulse through ice were not parameterised.

For each footprint, we determine the RMS slope of the surface in the across-track direction. Subsequently, this RMS slope value is used as an estimate of the scattering function width of the bed in each location, which we approximated as Gaussian (Schroeder et al., 2016). At each cell we use the angle of the surface with respect to the sensor and the estimated scattering function width to weight the return from each cell.

From the assigned cell weightings the mean weighted delay for the entire footprint was calculated accordingly (Figure 3.2d). Mean weighted delays for each footprint were compared with the delay values for the cells within them, with the likely location of the brightest reflector being determined as the elevation cell whose delay either equalled or most closely matched the mean weighted delay (Figure 3.2e, f).

For actual surveys, returns are treated as though they came from directly beneath the aircraft. To simulate this, the elevation at the location of the brightest echo was extracted to the nadir position (Figure 3.2f from the cross to the aircraft). Because the elevation at the likeliest location of the strongest return was expected to be different to the nadir elevation it was termed the "simulated nadir elevation". Once extracted, the simulated nadir elevation was differenced from

the nadir elevation. This difference is referred to from herein as the "off-nadir elevation difference".

3.3.5 Quantitative analysis of RES survey uncertainty

Descriptive statistics for the off-nadir elevation difference were calculated. Initially, this was done for each study site to investigate the magnitude of RES uncertainty across the different types of landscape. Subsequently, we calculated descriptive statistics for the off-nadir elevation difference across elevation provinces so that any difference in measurements within highlands and lowlands could be investigated with no a priori assumptions of landscape features. Highland and lowland provinces were determined by reclassifying the study site DEMs into two classes based upon the natural breaks inherent in the data, so that elevation values are grouped into classes that maximise the differences between the means of the two classes (boundaries stated in Figure 3.1).

For each MP flight-line, we measured valley cross-section, depth, width and area (referred to as CSA herein) from the DEM and the simulated elevation profiles. In order to semi-automate this process and keep the measurements consistent, we implemented the "findpeaks" function in MATLAB (2017a) (terminology outlined in figure 3.3). Prominence is equivalent to the depth of the valley cross-section, width at half-prominence as the valley cross-section width. CSA is used to quantify ice discharge so any measurement errors of CSA directly influence ice flux estimates and subsequent models and interpolations based on this quantity. CSA was calculated as the trapezoidal approximation of the bottom half of each valley cross-section, using the edge locations of the width at half-prominence as the integration limits. We implemented this integration as each profile is made up of points separated by the sampling distance of the RES survey and the trapezoid width simulates this, as opposed to interpolating a curve to represent the valley cross-section. A final manual check was made to remove valley measurements from either the DEM profile or simulated elevation profile which did not have a corresponding measurement on the alternate profile.
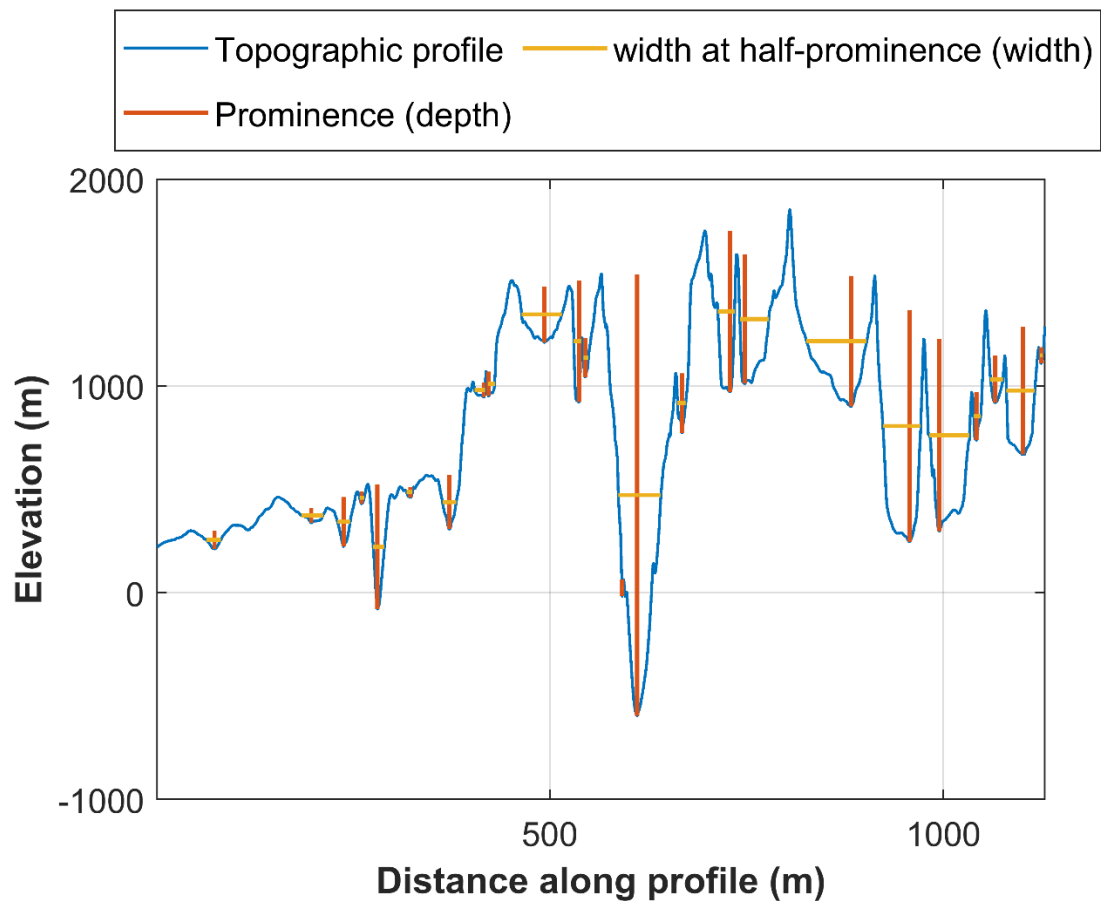
Figure 3.3. Schematic representation of "findpeaks" function to determine valley cross-section geometry.

3.3.6 Simulation measurement uncertainty

Both the DEM elevation value and the simulated nadir measurement at each point are subject to absolute and relative uncertainties in the ArcticDEM, which are currently estimated at < ± 1 m and 0.1 m respectively (Porter and others, 2018). In reality, each simulated measurement would be subject to "ice bottom errors" described by CReSIS, 2018 (pp. 26-27), and errors inherent in RES surveying highlighted by Lapazaran and others (2016). These errors are typically to the order of 10s of metres, we acknowledged the additional scale of these errors throughout our interpretation of the 'off-nadir elevation difference' error we investigated here.

3.4 Results

3.4.1 Synthetic RES survey results summary

In total 2,647,090 bed measurements were simulated across the four study sites. Simulated bed measurements had a mean off-nadir elevation difference of -1.8 ± 11.6 m. Across all study sites, the mean and total off-nadir elevation difference were consistently negative. Importantly, this study site scale underestimation was spatially heterogeneous; greater mismeasurement occurred across highlands compared to lowlands, and extreme mismeasurements (> 3σ from the mean) were likely to be over-estimates in lowlands as opposed to under-estimates in highlands. In addition, valley cross-section measurements showed widespread under-estimation of valley depth and CSA, albeit, high variation was observed in the measurement of these characteristics. In marginal simulations, where the maximum local footprint size is reduced, off-nadir elevation difference size was reduced and higher magnitude off-nadir elevation differences (> 10 m) were less likely. Accordingly, mismeasurement of valley morphometry was also reduced.

Table 3.1. Off-nadir elevation difference from DEM nadir elevation for all study sites and simulation set up. Σ is the sum, μ the mean and σ the standard off-nadir elevation difference.

Study sites	Simulated survey geometry and ice thickness *(off-nadir elevation difference from actual bed elevation statistics, m)*											
	MP						MO					
	Marginal			Interior			Marginal			Interior		
	Σ	μ	σ	Σ	μ	σ	Σ	μ	σ	Σ	μ	σ
ING	-2.38E+04	0	4	-1.20E+04	0	7	-2.84E+04	-0	4	-3.96E+04	0	7
KG	-2.32E+05	-1	5	-3.62E+05	-2	10	-2.84E+05	-2	8	-3.90E+05	-2	14
PGA	-1.68E+05	-1	7	-2.62E+05	-2	11	-2.72E+05	-2	8	-3.88E+05	-2	12
EGA	-4.23E+05	-2	12	-6.17E+05	-4	22	-4.76E+05	-3	11	-6.58E+05	-4	21

3.4.2 Off-nadir elevation difference at the study site scale

Negative bias in off-nadir elevation difference was found to occur across all study sites (Table 3.1). Both the sum of all off-nadir elevation differences across a study site and the mean off-nadir elevation difference were consistently negative. Sums of off-nadir elevation differences were more negative for MO simulations compared to their respective MP runs (Table 3.1). The EGA had the most

negative total and mean off-nadir elevation difference in all simulations. Additionally, standard deviation was greatest for the EGA, hence, elevation mismeasurement is greatest in such landscapes.

3.4.3 Off-nadir elevation difference for individual survey points

Ordinary least-squares linear regression found the simulated measured elevation to be on average 0.3% lower than the DEM elevation plus 0.3 m. RMSE from this regression found each simulated elevation to be within 10.6 m of the DEM elevation, or ~ 0.1% of ice thickness.

There is no distinguishable relationship in the magnitude of the off-nadir elevation difference and ice thickness (Figure 3.4). It can be seen in Figure 3.4 that survey point off-nadir elevation difference was predominantly negative, particularly where ice thickness was less than 500 m. As ice-thickness increased off-nadir elevation differences were more often positive and their error as a percentage of ice thickness greatly reduced.
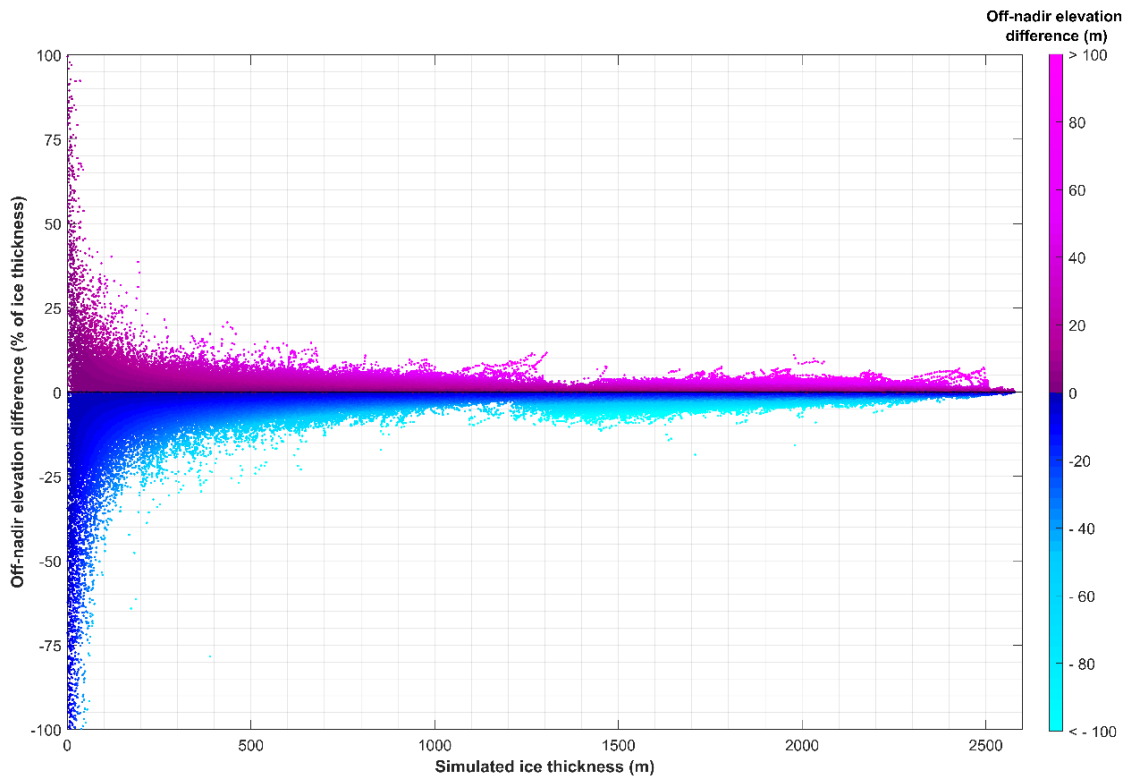
Figure 3.4. Off-nadir elevation difference as a percentage of ice thickness against simulated ice thickness. Colour illustrates the off-nadir elevation difference values in metres.

Across all simulations, the probability of negative off-nadir elevation differences was greater for highlands than lowlands (Figure 3.5 & skewness in Table A3.1). Metre scale error (~0.1% of ice thickness) occurred for the majority of survey points (~80%, Figure 3.5). Off-nadir elevation differences greater than 10 m in scale (~1% of ice thickness) occurred for ~20% of survey points. In lowlands, such off-nadir elevation differences were equally likely to be positive or negative, whereas in highlands, they were twice as likely to be negative than positive. Off-nadir elevation differences greater than a 100 m in scale (~10% of ice thickness) were rare (0.1% of measurements). However, as RES surveys sample many thousands of locations they are not inconsequential. When found, these extremely large off-nadir elevation differences were always negative in highlands but positive in lowlands.

Probability density functions also varied between study sites. Although MP marginal simulations showed lower probability of high magnitude off-nadir elevation differences across all study sites and elevation provinces, probability of negative 10 m scale off-nadir elevation differences remained high for EGA highlands, with 30% of off-nadir elevation differences more than 10 m below zero.
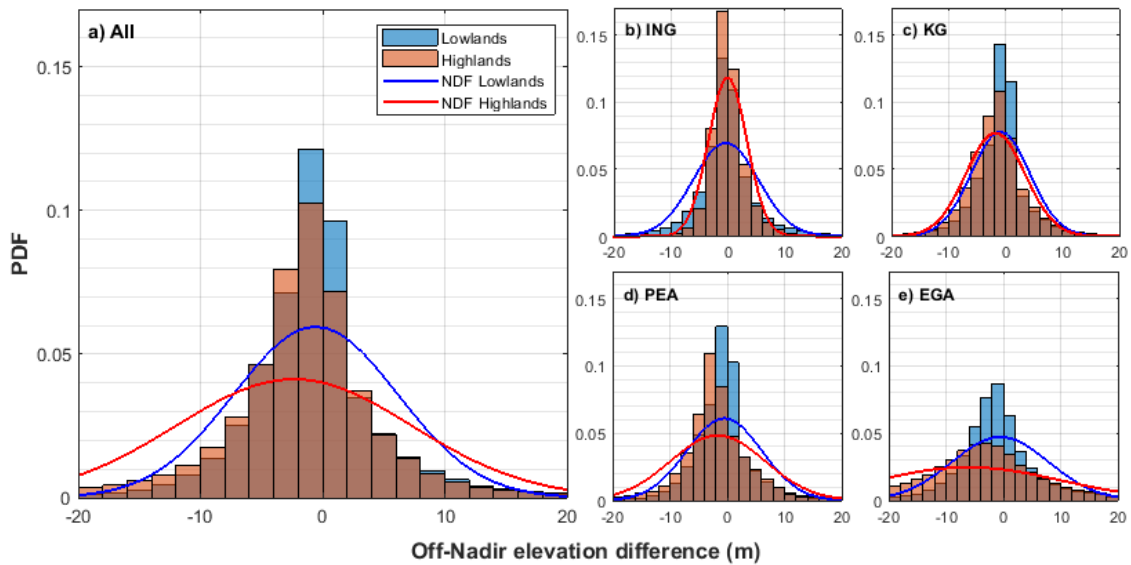
Figure 3.5. Probability density functions for off-nadir elevation difference across all highland provinces and all lowland provinces. Bin size is 2 m. Normalized distribution functions are plotted as lines with colour corresponding to elevation province. a) All points from MP marginal simulations. b) Inglefield land. c) Kangerlussuaq. d) Peary Land. e) East Greenland Analogue.

Absolute values of off-nadir elevation difference mapped in figure 3.6 highlighted the spatial pattern of greater error in highlands as opposed to lowlands. Additionally, boundaries between highlands and lowlands, typically valley slopes, exhibited some of the largest errors, particularly for narrow valleys with varied orientation. EGA like topography exhibited overall larger off-nadir elevation difference values in general compared to Kangerlussuaq style topography (overall darker colouration in Figure 3.6).
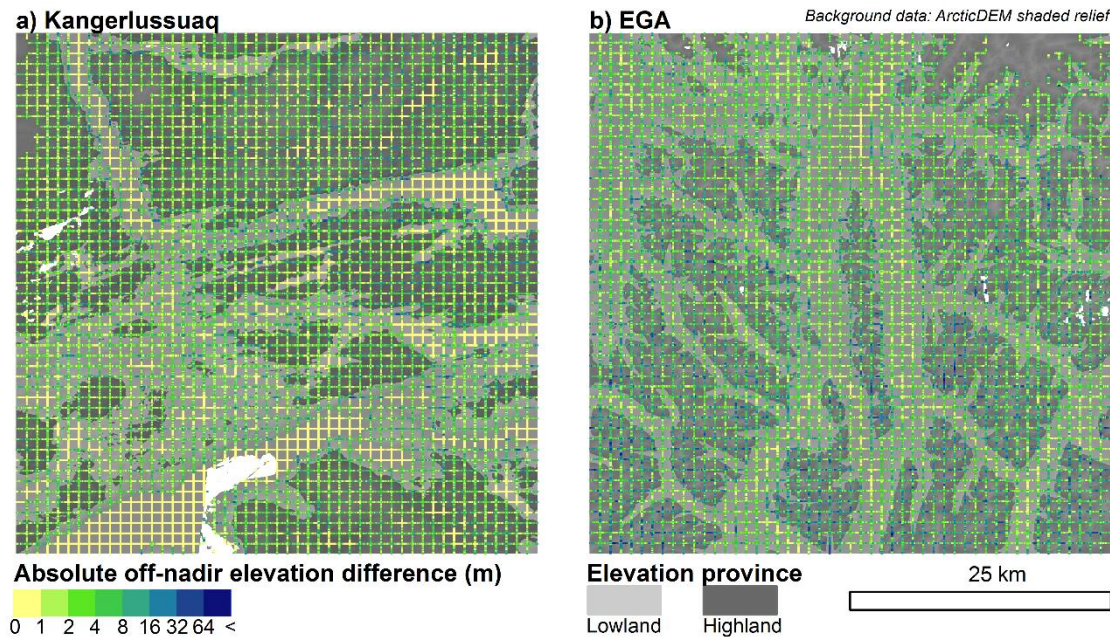
Figure 3.6. Maps of absolute off-nadir elevation difference, coloured lines, across a landscape and elevation provinces, grey shading, from marginal ice thickness simulations. a) Kangerlussuaq. b) EGA.

3.4.4 Valley cross-section geometry errors

In total, 2145 valley cross-sections were identified across marginal MP flight-lines (summary statistics for all simulations in Table A3.2). Width, depth and CSA measurements were all found to be measured with highly variable accuracy across all valley cross-sections (Table A3.2). However, simulated measurements of depth and CSA were predominantly negative, where ~70% of depth, and ~55% of CSA measurements were underestimates for interior simulations. Valley cross-section widths were under and overestimated in equal amounts. Finally, all the maximum magnitude differences in valley characteristics were negative.

Despite the large variation in measurement difference (~10 m), depth was largely underestimated throughout, with the accuracy of valley depth measurements

increasing with total depth (Figure 3.7). Although no clear trend was observed between valley size and depth difference, valley cross-sections with CSA greater than 10^6 m2 exhibited greater underestimates of depth than those between 10^5 m2 and 10^6 m2.
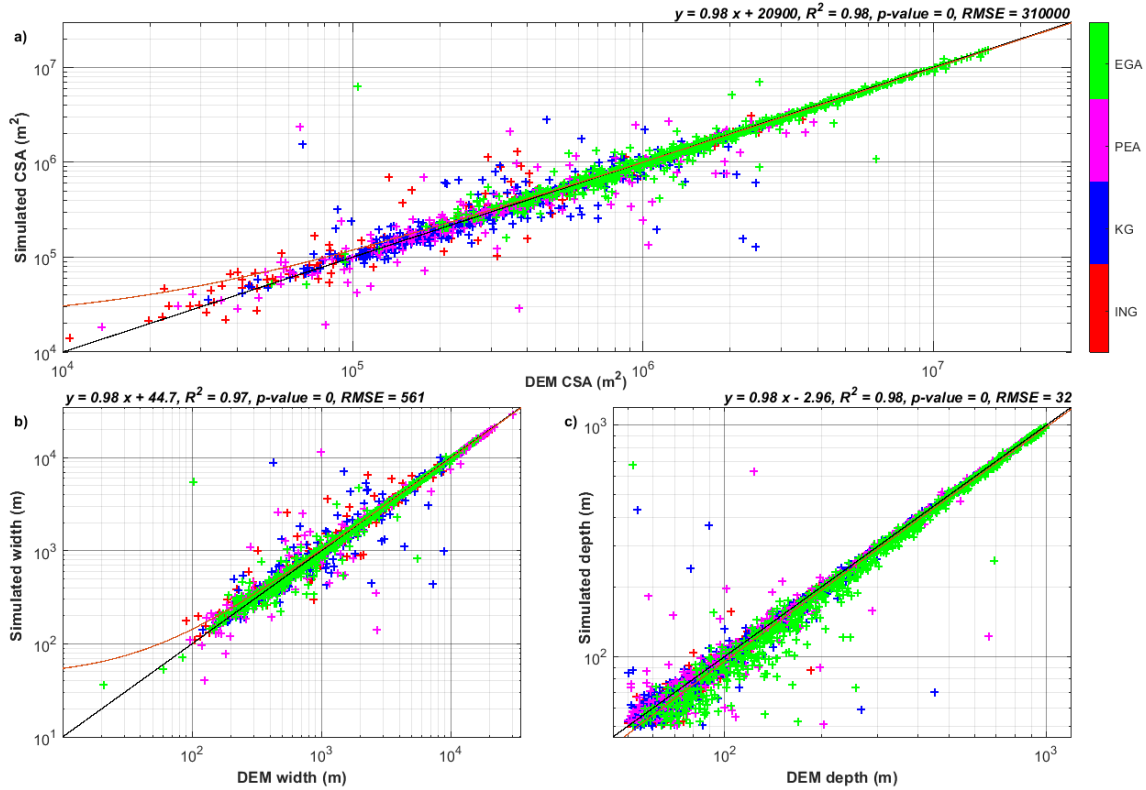
Figure 3.7. Valley geometry measurement accuracy assessment. All measurements from all MP flight-lines are plotted and study areas are colour coded. Each plot a match-line of y = x is plotted. Linear regressions are plotted in dark red with equations at the top right of each plot. a) Marginal ice thickness simulation DEM valley CSA vs simulated valley CSA. b) Marginal, DEM valley width vs simulated valley width. c) Marginal, DEM valley depth vs simulated valley depth. Coefficients for interior setups in Table A3.3.

CSA mean differences were negative for all areas but Inglefield Land and the EGA interior simulation (Table A3.2). Figure 3.7 shows a large variation in simulated CSA and actual CSA. However, most valley cross-sections fall below the equal match line (y = x). Off-nadir elevation differences from the actual CSA became lesser for larger valley cross-sections (CSA > 10^5 m2), yet they were still predominantly negative (70%). Mean percentage difference in CSA for these large valley cross-sections was -3 ± 18%. For those smaller than 10^6 m2 mean

CSA difference was always positive. Conversely, valley cross-sections larger than 10^6 m2 across all study sites and ice thickness setups were smaller in RES simulated bed-profiles compared with the DEM derived profile.

3.5 Discussion

3.5.1 Spatial uncertainty in RES survey measurements

Measurement error due to off-nadir returns typically results in the under-estimation of bed elevation (Table 3.1). Preferential measurement of slopes orientated favourably with respect to the sensor location, as opposed to the immediate nadir location, results in most of the topography being under-estimated. Consequently, ice-thicknesses derived from RES surveys are generally overestimated. Although individual measurement error is modest at a given location (typically -1.8 ± 11.6 m), due to the many measurements made in a survey, these small off-nadir elevation differences accumulate to larger total over-estimation of ice thickness (Table 3.1). Additionally, for surveys over interior portions of an ice sheet, this may be further exacerbated due to the increased likelihood of larger errors in bed elevation measurement (Table 3.1). Furthermore, MO flight-lines should be treated with greater uncertainty than MP flight-lines as they exhibit larger mean off-nadir elevation difference and cumulative off-nadir elevation difference values (Table 3.1). As MO flight-lines typically constitute the predominant measurement of glacier centrelines, this has implications for the accuracy of such measurements and any subsequently derived ice dynamics and mass balance metrics. Moreover, MO components of gridded surveys will likely be slightly less accurate than the MP components. However, all the above is dependent on the configuration of the subglacial topography being surveyed.

Widespread under-estimation of bed elevation is spatially heterogeneous. In highland areas, under-estimation is prevalent as local peaks and their slopes, present as areas of highly variable orientation of the landscape with respect to the sensor (Figure 3.8). This results in off-nadir returns from areas of preferentially facing lower elevation. Furthermore, this is exacerbated in areas where the mean orientation of the topography is parallel to the direction of flight, where topography predominantly slopes away from the sensor (Figure 3.6). Conversely, in areas of low elevation, this bias is reduced and the likelihood of

over-estimation of bed elevation is increased (Figures 3.5, 3.6 & 3.8, Table A3.1). In the bottoms of valleys, surface slopes are lower and less variable in orientation, therefore regions of higher slope in valley bottoms have greater influence on recorded nadir elevation, which is predominantly the valley sides (Figure 3.8). Consequently, this is less of a problem in wider flatter valleys (Figures 3.6 & 3.8). Similarly to highlands, the orientation of lowland features fundamentally influences the magnitude of measurement off-nadir elevation difference. Flight-lines along a valley are more likely to be influenced by off-nadir returns from the valley sides, as opposed to flight-lines across valleys (Figures 3.6 & 3.8; Holt et al., 2006; Farinotti et al., 2013; Gogineni et al., 2014). However, the wider the valley the lesser the impact orientation has on measurement error.
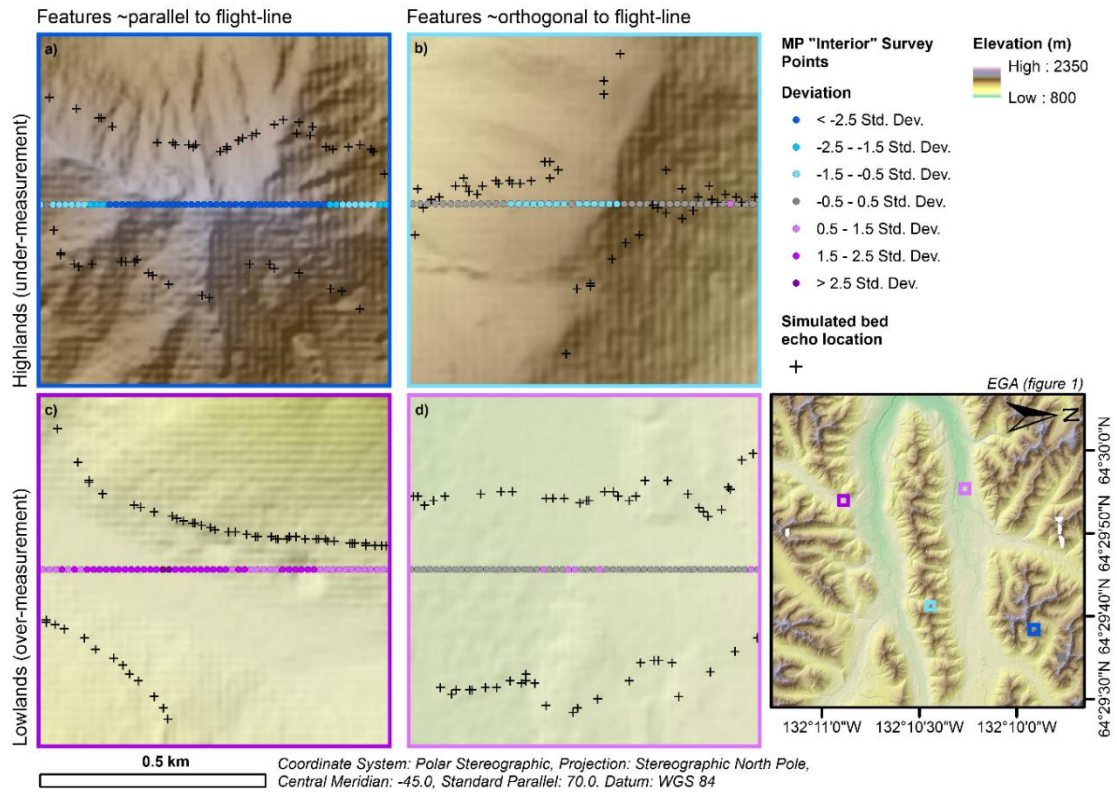
Figure 3.8. Off-nadir elevation difference magnitude and sign as a result of survey orientation, examples from EGA MP "interior" simulation. a) Highland elevations approximately parallel to flight-line orientation. b) Highland elevations approximately orthogonal to flight-line orientation. c) Lowland elevations approximately parallel to flight line orientation. d) Lowland elevations approximately orthogonal to flight line orientation.

Spatial uncertainty in bed measurement alone can be seen to cause measurement off-nadir elevation differences from the order of one metre to 100

m. While this error is modest compared to 10 m scale errors arising from: physical ice bottom conditions (CReSIS, 2018), scattering and attenuation due to crevasses, subglacial or englacial meltwater (Paden and others, 2010), and horizontal positioning (Lapazaran and others, 2016), it presents as a systematic bias which is nonetheless important to consider.

3.5.2 Potential for correction of RES survey measurement bias

As off-nadir elevation differences systematically underestimate bed elevation, potential exists for "correction" factors to be derived and applied to existing and future RES survey data conducted with the MCoRDS system simulated here. Here we explore the potential of developing corrections to counter off-nadir elevation difference errors.

3.5.3 Global elevation correction

To broadly adjust picked bed elevations as a first-order correction of RES survey data the ordinary least squares regression mentioned previously may be used (coefficients in Table 3.2). This correction would alleviate the global negative bias and provide more accurate quantification of ice thickness and accordingly potential sea-level rise contribution from the ice sheet surveyed. Such a correction may be an appropriate step before widespread interpolation of bed topography.

Table 3.2. Coefficients for ordinary least squares regression "global elevation correction".

x		m	c	RMSE	R^2
Picked elevation	bed	0.997	0.266	10.6	0.98

3.5.4 Statistical topographic profile correction

Ice thickness error in topographically constrained outlet glaciers has far higher consequences for mass balance estimation than the difference in ice-thickness over largely static, highland areas (Enderlin and others, 2014). Applying a statistical correction to flux-gate flight-lines, which elevates underestimated highland areas may replicate the landscape better which in-turn generates more

representative ice flux and outlet glacier geometry estimates (Table 3.3, other flight-line configurations and ice thicknesses see Table A3.1).

A statistical approach may be taken to simulate the boundaries of uncertainty in bed elevation and consequently valley depth and geometry, from which a range of discharge estimates may be calculated. Table 3.3 includes mean adjustments to be added to the input topography and confidence intervals for this method. Furthermore, this correction has potential to minimise the propagation of mismeasurements of valley morphometry downstream by mass-conservation and ice-flux modelling.

This would be best used for areas of subglacial topography like the EGA, which have the highest potential for producing higher magnitudes of error (Figures 3.6 & 3.8, Table A3.1). Up to 40% of points may deviate from the actual elevation by 10 m or more. Subglacial topography of this type is ubiquitous in the northwest and southeast of Greenland, which are the two most dominant sectors of the ice sheet in terms of ice discharge (Morlighem and others, 2017; King and others, 2018; Mouginot and others, 2019). Therefore, large errors in bed measurement will have a compounding effect on the certainty of ice discharge estimates made here. Improving bed topography accuracy is particularly important here, where outlet glacier geometry has a significant influence on the stability and retreat potential of such glaciers (Catania and others, 2018; Millan and others, 2018; Bunce et al., 2018).

Table 3.3. Potential correction factors for highlands and lowlands in marginal MP flight-lines based on subglacial landscape. For confidence intervals, x is the input elevation

Landscape type (description)	Mean elevation addition (m)		99% Confidence interval (m)	
	Highlands	*Lowlands*	*Highlands*	*Lowlands*
ING (*mostly flat*)	0 ± 3	0 ± 6	x - 9 – x + 9	x - 18 – x + 18
KG (*low relief valleys*)	2 ± 5	1 ± 5	x – 17– x + 13	x - 16 – x + 14
PEA (*high relief valleys with plateau highlands*)	2 ± 8	1 ± 6	x - 26 – x + 22	x - 19 – x + 17

| EGA *(high relief valleys with peaked highlands)* | 6 ± 16 | 1 ± 8 | x - 54 – x + 42 | x - 25 – x + 23 |

3.5.5 Valley cross-section geometry correction

An alternative to the statistical topographic profile correction could be to only correct CSA and depth measurements which are used for ice-flux calculations (Figure 3.7 and coefficients in Table 3.4). Although valleys with CSAs larger than 100,000 m^2 are typically well-measured, differences in the area are to the order of a few percent which will influence total ice flux by the same ratio, assuming ice-flux is equivalent to the CSA multiplied by the depth-averaged ice velocity through the CSA (Mouginot and others, 2019). Nevertheless, ice velocity through a valley is calculated as a function of depth, which we find to be largely underestimated even for larger valleys. Furthermore, valley CSA in this study is a conservative underestimate of full valley CSAs and so the full difference is expected to be greater. This bears significance for flight-lines used as ice flux gates. Off-nadir elevation differences along these flight-lines, and the consequent misrepresentation of subglacial valley geometry, has a direct effect on quantifying ice-flux as part of the ice sheet's mass budget, modelling ice sheet dynamics and deriving ice thickness via mass conservation (Enderlin and others, 2014; Aschwanden and others, 2016; Morlighem and others, 2017). Although mean off-nadir elevation difference is modest, the influence of large measurement errors across these flight-lines is substantial (PDFs in Figure 3.4). Mass budget studies using RES data to estimate ice discharge estimate bed elevation errors to be ± 30 m (Enderlin and others, 2014; Mouginot and others, 2019), which matches the RMSE for differences of valley depth found in our study for marginal measurements (Figure 3.7). However, we estimate bed elevation errors for valleys further inland to be more than 50% greater (52.2 m on average, Table A3.3). Applying a correction to the depths and CSAs based on the regression functions calculated (Figure 3.7), could be a "quick fix" to improve ice flux estimates by effectively expanding and deepening valleys accordingly.

Table 3.4. Coefficients for correcting CSA and depth for valley cross-sections in marginal RES survey profiles.

x		*m*	*c*	*RMSE*	*R²*
Valley CSA	cross-section	0.98	2.08E+04	3.10E+05	0.98
Valley depth	cross-section	0.98	-2.96	32	0.98

3.5.6 Applying potential RES corrections to GRIS outlet glaciers

Taking the outlet glaciers of Helheim, Fenris and Midgard as a case study, we highlight the influence of potential RES survey mismeasurement on outlet glacier CSA and consequently the derived ice-flux (Figure 3.9). Here, we show the bed topography at an OIB flight-line location taken from BedMachine v3 (Morlighem and others, 2017). When our valley cross-section correction is applied to the outlet glaciers, we find CSAs, and consequently ice fluxes, are typically underestimated by 1 ± 1% (Figure 3.9c). For mass budget studies, this underestimation is an additional uncertainty to those previously determined for estimates of outlet glacier ice flux (Enderlin and others, 2014; King and others, 2018). Furthermore, as CSA in this paper is an automated approximation for predominantly the bottom half of valleys, this is a conservative underestimate. For the entire lateral extent of the valley, extending upwards from the valley sides to the ice surface, the percentage error will be higher as the elevation of highlands surrounding the valley are more often underestimated at 10 m scales compared to similar scale overestimation of valley bottom elevation (Figure 3.9b), effectively smoothing the bed profile and reducing overall bed elevation. Applying the statistical topographic profile correction derived from the probability density function for the EGA MP marginal experiment (Figure 3.9, Table 3.3), it can be seen that the simulated topography could differ by approximately 50 m from the actual topography and the difference in valley CSA and consequently potential ice-flux increases markedly, by as much as ±7% (Figure 3.9).
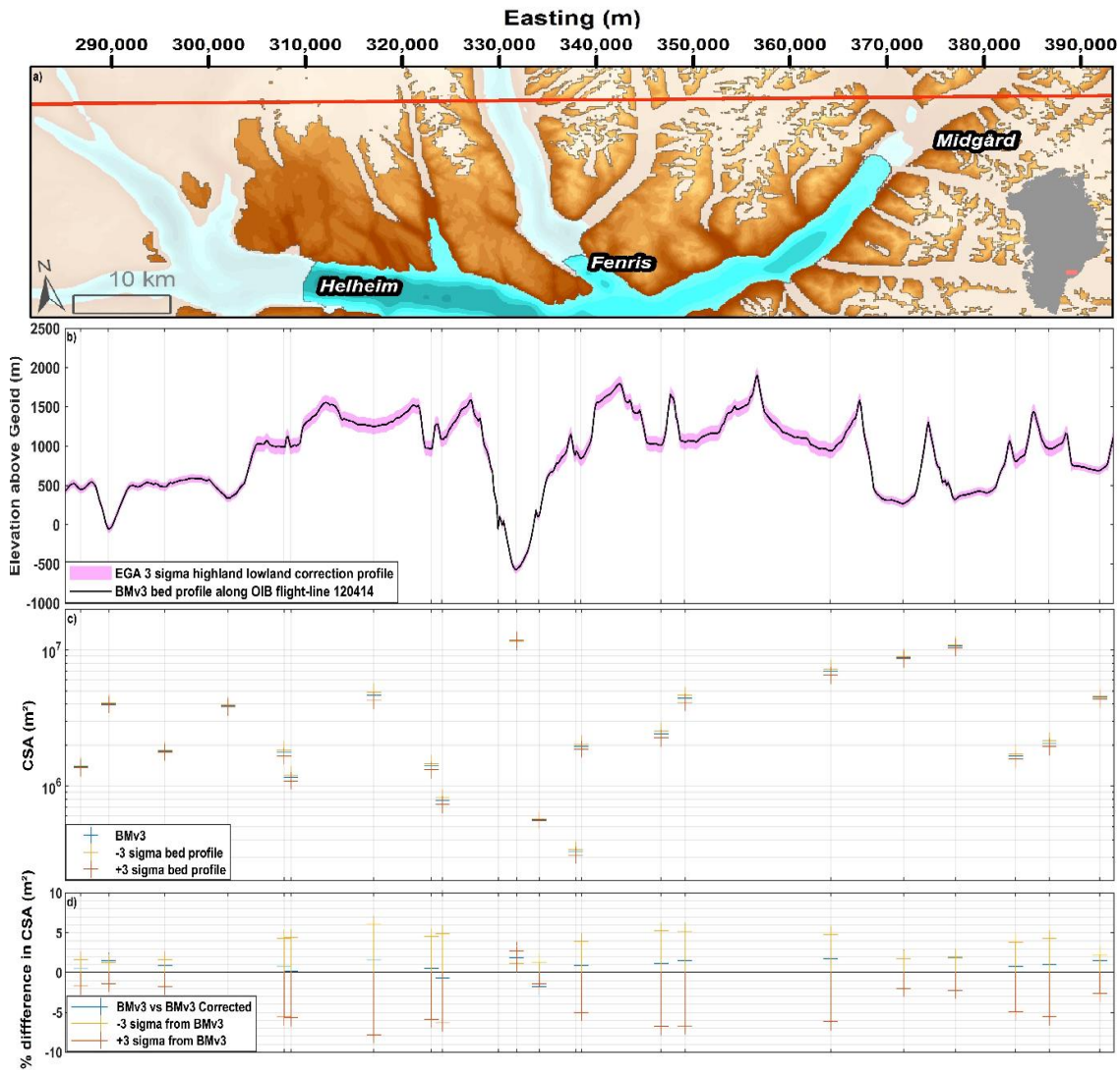
Figure 3.9. a) Red shows OIB spring 2012 flight 120414, subglacial areas are indicated by the translucent white fill, background data is relief-shaded subglacial topography from BedMachine v3 (Morlighem and others, 2017). Differences in bed topography (ab), CSA (c), and CSA percentage difference (d) along a flight-line using 99% confidence interval correction based on highland and lowland off-nadir elevation differences for the EGA study site. BMv3 corrected uses the CSA correction derived from Figure 3.8 b).

3.5.7 Implications for appreciation of outlet glacier stability

Apparent smoothing of outlet glacier valleys by off-nadir elevation difference typically results in smaller valley CSA being measured (Table A3.2, Figure 3.7). This has implications for ice flux and ice discharge estimations as these are derived in part using outlet glacier CSA. Consequently, when valley profiles are corrected, so that the bottoms become deeper and the highlands higher, the CSA

101

may increase, showing that current estimates of ice discharge may, in fact, be slightly too low.

Our study suggests that greatest mismeasurement of valley geometry occurs for interior, high ice thickness settings and for tributary glaciers to main outlets. These errors can scale up to 100s of metres but are predominantly to the order of 10s of metres. As these errors are propagated downstream in any mass budgeting or mass conservation analyses, errors become greatest at the glacier terminus and margin (Morlighem and others, 2017; Millan and others, 2018). Gravimetric measurements of outlet glacier valley depth are reportedly deeper by 10s to 100s of metres than corresponding depths in BedMachine v3 (Millan and others, 2018). This could in part be explained by the results in our study where valley bottom elevation is being overestimated and subsequently carried downstream in interpolation. Albeit gravimetric measurements are subject to significant uncertainty where variation in substrate density and the occurrence of high-density geologic deposits may skew the estimated bed elevation, whereas this does not affect RES measurements. Accurate determination of outlet glacier valley depth is of particular importance when assessing outlet glacier stability, as this is often highly dependent on bed topography geometry (Choi and others, 2017; Catania and others, 2018).

Mismeasurement of outlet glacier valley geometry may complicate predictions of outlet glacier stability. The depth and gradient of the beds of GrIS outlet glaciers determine whether the glacier may be exposed to warm Atlantic Water and if they are able to establish a grounding line position after the initiation of retreat (Catania and others, 2018). Glaciers such as Umiamako Isbrae and Kangilerngata Sermia have grounding line depths, 264 m and 260 m below sea level respectively, within the potential depth error ranges presented in Table A3.2 that could make them susceptible to ingress of Atlantic Water into their fjords (Catania and others, 2018; Choi and others, 2017). Additionally, the portion of the bed that is retrograde for some glaciers may not be adequately captured by underestimated valley depths and bed topography derived from erroneous inputs. This important condition is reported for Skinfaxe Glacier and Qajuuttap Sermia when using gravimetric measurements, however, in BedMachine v3 which is derived from RES data, both glaciers have relatively flat beds and are grounded close to sea level (Millan and others, 2018). Consistent under-estimation of depth also poses additional

uncertainty when considering how much of the ice sheet bed is grounded below sea-level. Ikertivaq and Koge Bugt North glaciers have beds below sea level in gravimetric data but not in RES derived bed topography, with depth measurements differing by a magnitude of 100 m (Millan and others, 2018). Whilst underestimation of depth was typically found to be an order of magnitude less than this, potentially more common mismeasurements to the order of 10 m are enough to differentiate whether these glaciers are grounded below sea-level or not. Finally, the extra 10s of metres that may be gained in depth in cases within one standard deviation of the mean depth difference may alter predictions as to whether a glacier is at the floatation point, further influencing predictions of glacier stability (McMillan and others, 2014). All of the glaciers mentioned above are found in the Southeast and Northwest sectors of the GrIS, which as previously mentioned exhibit similar topography to the EGA site used in our study. Consequently, these areas are subject to heightened probability of larger mismeasurements of bed topography.

3.6 Conclusions

- We observed a systematic underestimation bias of subglacial elevation inherent to RES surveying, termed off-nadir elevation difference (mean = 1.8 ± 11.6 m), which implies current estimates of ice thickness are slightly high.

- We find CSA and consequently ice-flux for outlet glaciers across the GrIS in landscapes similar to the EGA site presented here have typically been underestimated by approximately -3 ± 18%, potentially increasing up to five percent up-glacier.

- Widespread overestimation of valley bottom elevation may have implications for our appreciation of outlet glacier stability.

- We highlight three potential corrections for RES survey data, namely: global elevation correction, statistical topographic profile correction, and valley cross-section geometry correction.

Chapter 4: Reduced uncertainty in subglacial topography for sparsely surveyed regions of the Greenland Ice Sheet

This chapter describes the development and implementation of methods for better quantifying and reducing the uncertainty in Greenland Ice Sheet bed topography. This chapter is in preparation for submission to Journal of Geophysical Research: Earth Surface

Bartlett, O.T., Palmer, S.J., and Morlighem, M. in prep. Reduced uncertainty in subglacial topography for sparsely surveyed regions of the Greenland Ice Sheet, Journal of Geophysical Research: Earth Surface

I developed and implemented the uncertainty quantification and reduction methods, produced and analysed the results and wrote the manuscript. Palmer assisted with the analysis of the results, and the writing of the manuscript. Morlighem reviewed and commented on the manuscript.

4.1 Abstract

Subglacial topography is a fundamental boundary condition for ice sheet models, which aim to predict ice sheet interaction with climate. While contemporary ice-sheet-wide bed topography datasets for the GrIS are derived partly using mass conservation, the majority of previous datasets and ~75% of the latest dataset have used kriging of airborne radio-echo sounding (RES) measurements. Due to a paucity of independent validation data, errors and biases inherent in this approach are not well understood, leading to undefined or poorly constrained uncertainties in subglacial topography. Here we interpolate synthetic RES observations of bed topography over ice-free areas for which the topography is known at a spatial resolution of 5 m, and quantify the differences. We find absolute error in kriged bed topography increases with distance from an input at a reduced rate than previously estimated. We find the difference of an interpolated elevation estimate from the local interpolated mean elevation is a strong predictor of real values of bed error ($R^2 = 0.72$), and improves with increased sparsity of input observations ($R^2 > 0.82$). Hence, we propose a method for quantifying and reducing uncertainty in kriged bed topography in sparsely surveyed regions. We report reduced uncertainty for 56% of the kriged interior area of the GrIS bed. Our results suggest ice thickness has been underestimated by 5 ± 41 m on average. Consequently, the area of the GrIS grounded below sea-level is underestimated by 2%, and 29% for the area below -200 m a.s.l. Hence, our findings have potential implications for the perceived stability of the GrIS, particularly, the extent and gradient of reverse bed slopes which promote enhanced grounding line retreat.

Keywords: Greenland Ice Sheet, subglacial topography, radio-echo sounding, glaciological instruments and methods, geostatistical interpolation

4.2 Introduction

Quantification of ice thickness and subglacial topography over an entire ice sheet is essential for understanding how it is likely to change with the climate (Bamber et al., 2013). Ice sheet wide ice thickness estimates are used to determine the volume and subsequently, mass of an ice sheet. From this, a measure of the total potential contribution to sea-level rise contained by the ice sheet can be derived (Alley et al., 2005). Moreover, quantification of subglacial topography is essential as it is a first-order control on the rate at which the ice sheet responds to perturbations such as climate change (Schoof, 2002). Hence, an accurate description of the bed topography and ice thickness is of paramount importance for predicting future sea-level rise. Ice thickness is predominantly measured using airborne radio-echo sounding (RES) techniques. Subsequently, subglacial topography is derived from subtracting the thickness measurement from the surface elevation (Dowdeswell & Evans, 2004), which is typically measured simultaneously using an airborne laser altimeter. While RES surveys have been conducted for decades and cover hundreds of thousands of kilometres of ice (Schroeder et al., 2020), due to the scale of ice sheets, ice caps and glaciers, overall measurement coverage is sparse (Rodriguez-Morales et al., 2014). For example, mean flight-line spacing across the Greenland Ice Sheet (GrIS) interior is ~18 ± 24 thousand km. In order to quantify ice thickness and bed elevation in areas between measurements, some type of interpolation is required (Bamber et al., 2001). Various methods have been implemented to achieve this, all of which have associated uncertainties. As current projections of sea-level change are increasingly using ice dynamical models, robust quantification and reduction of these uncertainties is essential for producing reliable projections (Nowicki et al., 2016).

Ice thickness has been surveyed for almost 5 decades across the continental ice sheets (Greenland: Rodriguez-Morales et al., 2014; Antarctica: Pritchard, 2014). From these surveys, it has been possible to map ice thickness and subsequently bed topography across the GrIS (Bamber et al., 2001; Bamber et al., 2013; Morlighem et al., 2017) and Antarctic Ice Sheets (Lythe et al., 2001; Le Brocq et al., 2010 Fretwell et al., 2013; Morlighem et al., 2020) through interpolation and modelling. The most recent efforts have used mass conservation techniques typically within 50 km of the ice margin, where RES instruments typically perform

less well, to achieve this (Morlighem et al., 2011; Morlighem et al., 2017; Morlighem et al., 2020). These datasets are becoming widely used for studies of ice sheet bed topography. Mass conservation combines observations of surface velocity with measurements of ice thickness to infer ice sheet bed topography in regions of fast flow (>50 ma^{-1}) (Morlighem et al., 2014). However, ice flow in many marginal areas of the GrIS has been observed to be highly variable (Sundal et al., 2011), as such, velocity selected to generate the bed may not be entirely representative of a "steady-state" which may lead to the introduction of errors. Furthermore, in areas of slower ice flow (<50 ma^{-1}), other interpolation approaches are required (Morlighem et al., 2020). For instance, in Bedmachine Antarctica, streamline diffusion is used as an alternative, which utilises the direction of ice flow to interpolate ice thickness between flight-lines anisotropically, resulting in a "realistic" bed profile consistent with the mass-conservation derived regions (Morlighem et al., 2020). For Greenland, however, ordinary kriging is instead implemented over an area of the dataset equivalent to 75% of the ice sheet bed (Morlighem et al., 2017).

Kriging is a geostatistical interpolator that has traditionally been the chosen method for deriving wide-scale bed topography of ice masses (Deutsch and Journel, 1997; Bamber et al., 2001; Bamber et al., 2013; Fretwell et al., 2013), because it is optimal for irregularly sampled input measurements and provides a best estimate for values in under-sampled regions (Dowdeswell et al., 2004). However, known limitations of the method are that it tends to smooth a landscape towards a mean value and that it cannot accurately reproduce channel-like subglacial landforms (Goff et al., 2014; Williams et al., 2017). This leads to the introduction of artefacts in derived subglacial topography datasets, which occur at scales that ice dynamics are sensitive to (~1 km) (Durand et al., 2011; Morlighem et al., 2020). It also leads to the underestimation of bed elevation in upland areas, and the overestimation of elevations in lowlands, thereby consistently underestimating subglacial relief. Smoothing topography in such a way has implications for the overall roughness of the bed in the output data. Furthermore, this obfuscates potentially important bedforms or areas of local roughness which potentially exert a strong influence on ice dynamics (Durand et al., 2011), resulting in erroneous bed inputs to ice sheet models, which subsequently may not be able to accurately replicate observed flow dynamics.

However, ordinary kriging remains a widely-used and expedient method of interpolating subglacial topography. Despite these well-known limitations, the quantification of uncertainties in the method is rarely constrained other than simple inverse distance relationships with respect to the location of the input data (Bamber et al., 2013). Furthermore, various analytical outputs derived from bed topography often implement broad uncertainties in ice thickness, which carry through into important assessments of ice sheet mass balance and stability (e.g. Shepherd et al., 2019).

Ice sheet models used in ISMIP6, which contributes to CMIP6 projections of sea-level change, use a variety of bed topography datasets as inputs (Nowicki et al., 2016; Morlighem et al., 2020). As ordinary kriging is employed for much of the preceding subglacial topography data (Bamber et al., 2013; Fretwell et al., 2013), and for significant portions of newer data (Morlighem et al., 2017), it is important that uncertainties associated with these datasets are well constrained in order to provide reliable uncertainties in the contribution of the ice sheets to sea level rise. Therefore, assessing the uncertainty in kriged bed topography more precisely and investigating alternative means of improving accuracy, would be beneficial to our comprehension of ice sheets and future projections of sea-level change (Nowicki et al., 2016; Nias et al., 2018).

Validation of ice thickness datasets is logistically challenging as it requires physically accessing the ice sheet bed, so comparable alternatives are necessary. With the recent availability of high resolution (two metres) Arctic DEM digital elevation data across the Arctic, including the GrIS margin (Porter et al., 2018), it is possible to investigate the uncertainties and biases of interpolation techniques by simulating RES surveys over DEMs of known topography, interpolating the resultant synthetic measurements, and differencing the output interpolation from the input DEM. Errors in the derivation of subglacial topography can then be quantified and investigated (Bartlett et al., 2020). This study aims to quantify and improve the uncertainty in interpolated subglacial topography datasets, by developing a method for estimating the error in subglacial topography using proximal and geomorphologically similar ice-free topography. From this, previous datasets of kriged bed topography may be used with higher confidence and new bed topography may be generated with reliable accompanying maps of uncertainty. Here we focus on the GrIS as a case study,

note the implications of our results for GrIS, and discuss the implications for other ice masses and bed topography datasets derived by kriging.

4.3 Data and methods

4.3.1 Study locations and datasets

Digital elevation model (DEM) tiles of the four study sites of glaciated terrain investigated throughout this thesis were acquired from the ArcticDEM. Subsequently, these DEMs were aggregated to five-metre cell sizes for computational efficiency (Porter et al., 2018; Figure 4.1).

.
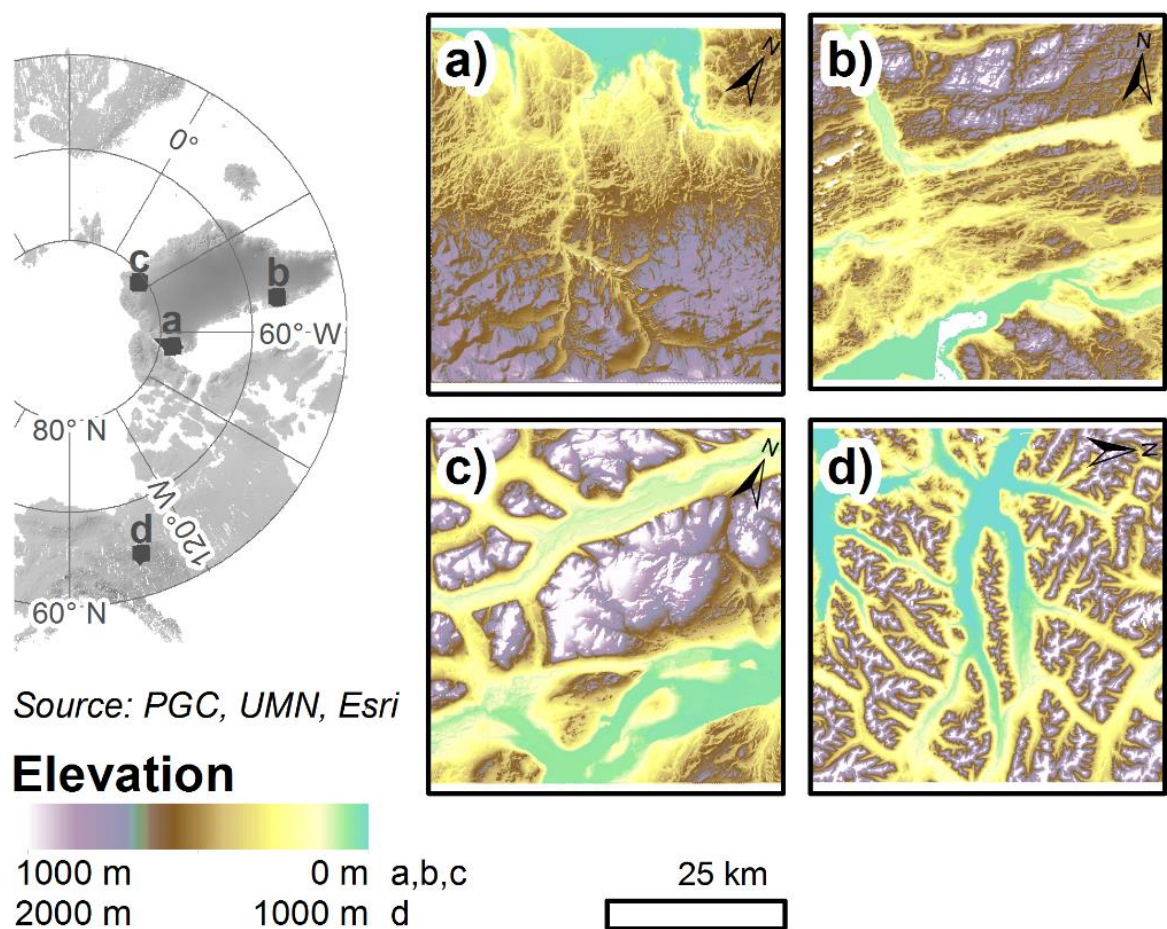
Figure 4.1. Study sites a) Inglefield Land. b) Kangerlussuaq. c) Peary Land. d) EGA

4.3.2 Synthetic RES survey data

To fully simulate the generation of subglacial topography from acquisition through interpolation we conducted synthetic RES surveys over the input DEMs.

Synthetic RES surveys were simulated implementing the geospatial RES simulation method outlined by Bartlett and others (2020). We mimic the various geometries and spacings of RES surveys conducted by Operation IceBridge over Greenland (Studinger et al., 2010). Accordingly, flight-lines were simulated for margin parallel (MP) and margin orthogonal (MO) orientations as well for gridded surveys. Flight-line density is variable across surveys, therefore, we conducted synthetic surveys at 1, 5, 10, and 15 km spacings. This also enabled the investigation of output bed topography quality due to survey design, which has previously been found to significantly influence the detection of bedforms and the measurement and interpretation of bed roughness (Falcini et al., 2018). Simulated picked elevations were sampled at ~15 m spacing along-track. Negative bias resulting from off-nadir elevation differences was alleviated by applying a mean shift to the input data points (Bartlett et al., 2020). As ice bottom errors resulting from the attenuation and scattering of the radar signal by various facets of the ice sheet environment are not parameterised, the uncertainty in simulated measurements is equivalent to the uncertainty of the ArcticDEM (~1 m vertically and ~0.1 m horizontally).

4.3.3 Kriging

Due to its widespread use and our overarching aim to simulate and quantify uncertainty in bed topography akin to previous and ongoing studies, we interpolate surfaces from our synthetic RES survey data using kriging (Deutsch and Journel, 1997). Surfaces were interpolated for each study site for the three survey geometries (MP, MO, grids) and the four line spacings (1, 5, 10, 15 km). Ordinary kriging was conducted in ArcGIS 10.5.1 using the inbuilt geostatistical tools, following the method of Jezek and others (2013), which generated 48 different topography grids. A spherical model was used and algorithm parameters were optimised using ArcMap's inbuilt iterative cross-validation technique (Table A4.1).

4.3.4 Quality assessment of bed topography interpolations

Each realisation of interpolated bed topography was differenced from the source DEM for each study site. Spatially random sample points were generated across each study site with a minimum spacing of 150 m to replicate the gridded resolution of Bedmachine Greenland v3. For each 50 x 50 km approximately

20,000 points could be generated at this spacing, across all output surfaces this totalled 1.5 million observations. At each point, the differences in elevation between the interpolations and the DEM were sampled. Differences in elevation of an interpolated point from the same location on the DEM are herein referred to as interpolation errors. Overall interpolation error was defined as the standard deviation of all the interpolation errors. Root mean square deviation along each input flight-line was calculated as a measure of bed roughness. This measure was also compared with overall elevation error for the interpolated bed. Additionally, the Euclidean distance of each point from and input location was calculated for all survey geometries.

4.3.5 Uncertainty reduction

In order to improve the estimates of the uncertainty in bed topography and consequently ice thickness, firstly, interpolation error magnitude was compared with the distance from an input. This assessed the interpolation error as a function of distance, as opposed to the traditional method of posing a prescribed exponential increase in interpolation uncertainty with distance which is a by-product of Kriging. Secondly, the difference of an interpolated elevation from the regional (50km x 50km neighbourhood) mean elevation of the interpolation, termed difference from mean elevation (DME), was compared with interpolation error. This aimed to exploit the known limitation of kriging that the output surface is smoothed towards the mean elevation of the inputs. Ordinary-least-squares regression was calculated for these variables to develop a function to be applied to kriged bed topography. Where suitable, this function was applied to kriged regions of Bedmachine Greenland v3 (referred to herein as BedMachine) to calculate a new uncertainty estimate.

4.4 Results

4.4.1 Summary of results

Altogether, 48 synthetic bed topography datasets were interpolated by kriging across the study sites, survey geometries and ice thicknesses (Figure A4.1). Overall, the correlation between flight-line density and output interpolation error was moderately negative ($R^2 = 0.947 - 0.965$, Figure 4.2a). Input flight-line roughness and interpolation error were weakly and positively correlated ($R^2 = 0.3$). For a given point, interpolation error magnitude increased the greater the

interpolated elevation at that point differed from the local mean elevation of the interpolation. Similarly, the further an interpolated cell was from an input location, the larger the error, as expected.

4.4.2 Overall error in kriged subglacial topography

Flight-line density was found to be the strongest predictor of overall error in the interpolated outputs, where error decreased exponentially with increased flight-line density (Figure 4.2). While flight-line density is a strong predictor (Figure 4.2, R2 values > 0.9) of overall error within an individual study area when all interpolated surfaces were considered the correlation was found to be moderate (R2 = 0.6). This highlighted additional factors likely contributed to the overall error. Mean flight-line roughness, quantified as the root-mean-square deviation (RMSD) of input measurements, was found to be a weak predictor of overall error (Figure 4.2). Although no statistically significant difference was found in errors due to flight-line orientation and mean proximity to the bed, a subtle improvement was found for margin parallel inputs compared to margin orthogonal (Figure A4.2). Finally, only 4% of errors exceeded the maximum expected error, using the distance-error function estimated for BedMachine, of 395 m for a distance from an input of 8360 m.
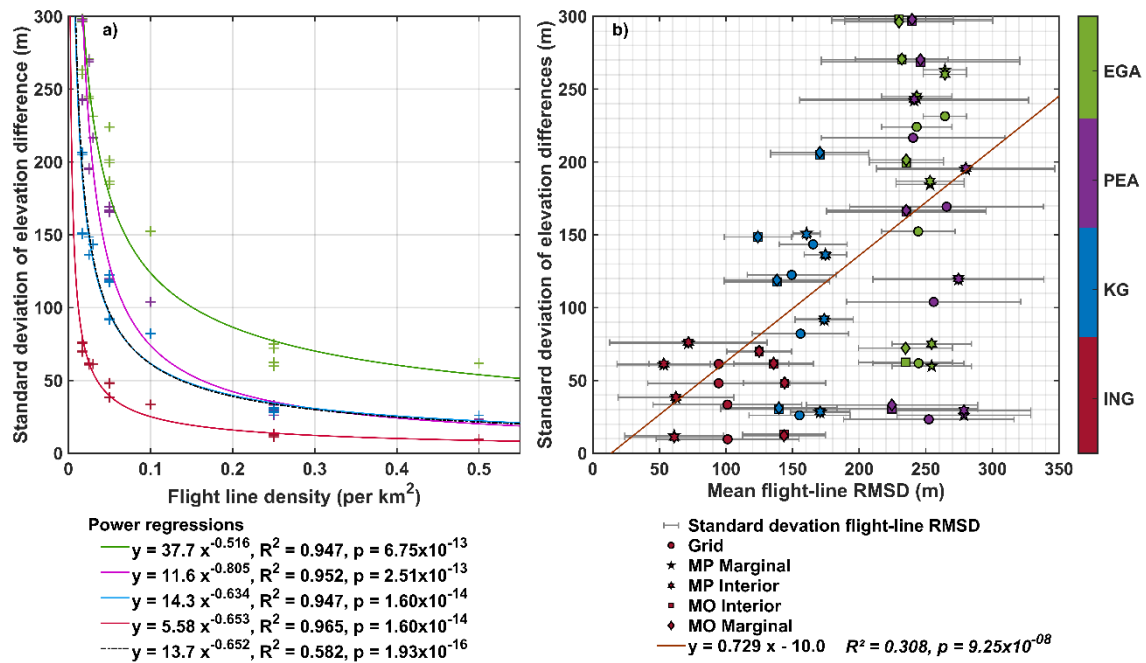
Figure 4.2. a) Flight-line density versus overall interpolation error, power regressions coloured to study sites. Black dotted line is the power-law model for all the interpolations and flight-line densities. b) RMSD versus overall

interpolation error for the various survey geometries, ordinary least squares linear regression plotted in red.

Interpolation error magnitude varied across the study sites (Table A4.2). Overall interpolation error was greatest for the EGA across all survey setups (Figure 4.2). Increased prevalence of elevations with absolute DME values exceeding 500 m across the EGA leads to a corresponding increase in interpolation errors (Figure 4.3). Compared with Kangerlussuaq, EGA interpolation errors from a 15 km spaced grid survey are typically one and a half times greater for the same Euclidean distance from inputs. Furthermore, estimated error from BedMachine is comparable to interpolation errors across the EGA for the first 2000 m from an input point, however, for Kangerlussuaq, BedMachine uncertainty is always greater than for the distance derived error function (Figure 4.3).
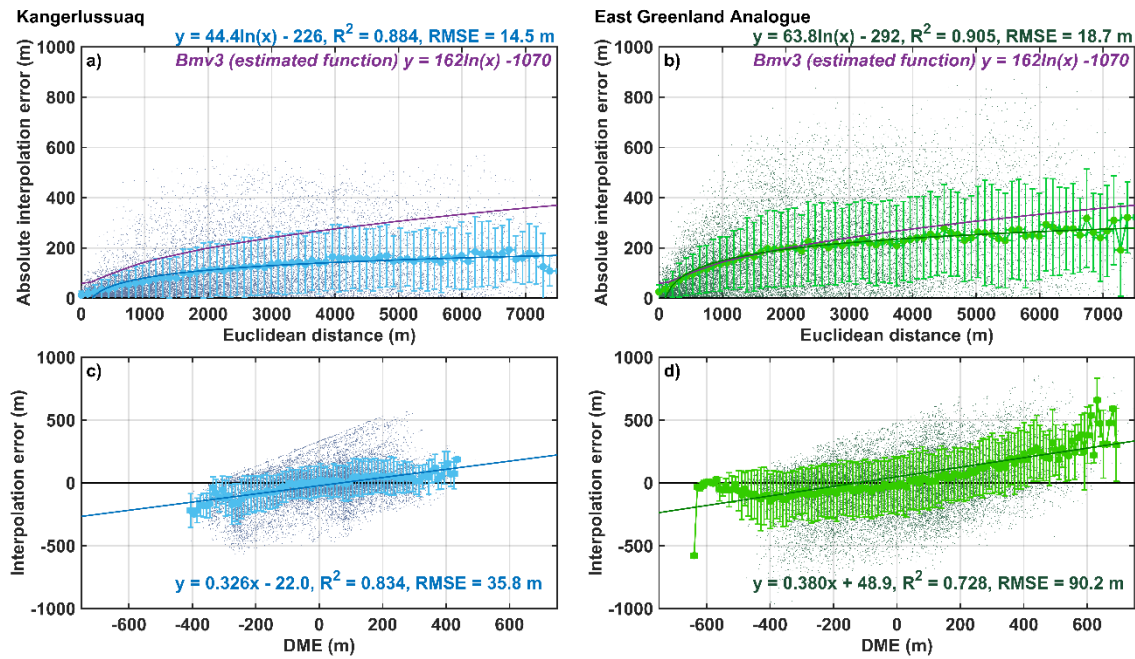
Figure 4.3. Individual interpolation errors, kriged elevation – DEM elevation, (shaded dots) vs distance and DME, for 15 km grid surveys over the Kangerlussuaq and EGA study sites. Moving means are every 150 m for distance and 10 m for DME (filled circles), error bars represent standard deviation in y and the moving mean window in x. Ordinary-least-squares regressions for the moving mean and error (solid lines) are described above the plot. a) Kangerlussuaq, Euclidean distance versus interpolation error. b) EGA, Euclidean distance versus interpolation error. c) Kangerlussuaq, DME versus interpolation error. d) EGA, DME versus interpolation error.

4.4.3 Individual interpolation errors for kriged subglacial topography

For individual interpolation errors, Euclidean distance of an interpolated cell from an input did not correlate with absolute error ($R^2 = 0.197$). Furthermore, Euclidean distance shows no correlation with the real value for the error. We found the correlation to strengthen when mean interpolation error was computed for every 150 m of distance (figure 4.4, $R^2 = 0.952$). As the gridded output for our sites and BedMachine is posted at 150 m, no accuracy is lost by grouping distances into 150 m intervals. Notably, the mean interpolation errors are consistently below the function applied to distance from an input for Bedmachine (Figure 4.4, green dotted line). While some errors exceed this, 91% fall below the function line. Accordingly, the function established from these results predicts reduced uncertainty for all interpolation locations further than 1600 m from an input location compared to BedMachine.
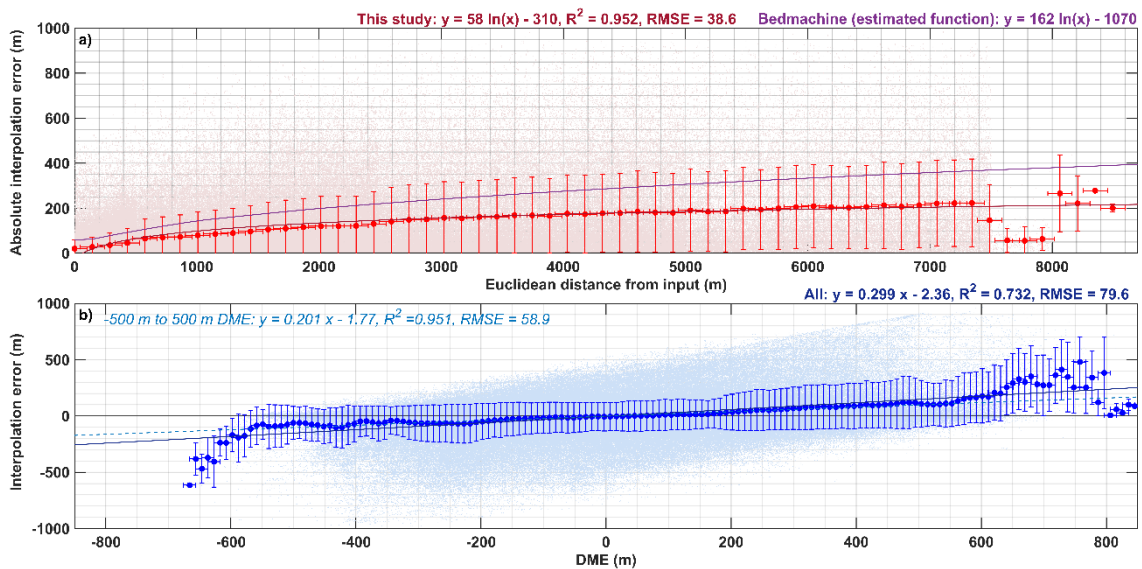
Figure 4.4 All observations (shaded dots) of interpolation error versus Euclidean distance (a) and DME (b). Filled circles represent moving means, 150 m for distance and 10 m for DME, error bars represent standard deviation in y and the moving mean window in x. Ordinary-least-squares regressions calculated for the moving mean and error are described above the plots (solid lines, and dashed light blue line in b).

Individually, DME of an interpolation point did not correlate with interpolation error at that point (Figure 4.4). However, when grouped into 10 m intervals, DME is a strong predictor of interpolation error, albeit this sacrifices precision in the

interpolated bed elevation (Figure 4.4). Moreover, when locations with absolute DME exceeding 500 m are removed due to their limited abundance in comparison to the rest of the data, the correlation strengthens and RMSE is reduced. For consistency, the function incorporating all the observations is used throughout. DME provides a robust alternative estimate of error as it is based on the topography of the interpolated dataset opposed to distance from an input. As such it can still be applied in sparsely surveyed areas. Additionally, the real value of interpolation error can be determined as opposed to just the absolute value. At reduced flight-line density, the correlation between DME and interpolation error strengthens (Table 4.1). For high-density surveys, no correlation exists as the errors become more random, albeit significantly reduced (lower RMSE Table 4.1).

Table 4.1. Coefficients for DME-error functions for various flight survey geometries. Line survey coefficients are means with standard deviations for MP and MO, marginal and interior simulated surveys.

Survey geometry	Flight-line density (lines km^{-2})	R^2	RMSE	m	c
1 km Grid	0.5	0.075	15.4	0.011	-0.598
5 km Grid	0.1	0.331	62.9	0.112	11.1
10 km Grid	0.05	0.789	43	0.223	14.7
15 km Grid	0.03	0.708	90.1	0.360	48.2
1 km Lines	0.25	0.127 ± 0.200	18.7 ± 9.2	-0.004 ± 0.061	-1.33 ± 1.16
5 km Lines	0.05	0.582 ± 0.084	60.0 ± 8.5	0.183 ± 0.009	12.7 ± 1.5
10 km Lines	0.025	0.845 ± 0.008	78.6 ± 29.6	0.412 ± 0.073	14.9 ± 3.2
15 km Lines	0.017	0.867 ± 0.042	86.0 ± 2.9	0.630 ± 0.193	27.4 ± 2.8

4.4.4 Application to BedMachine

When applied to the input flight-line coverage for BedMachine, our observation-based Euclidean distance versus interpolation error function (Figure 4.4a) provides a first-order error estimate for bed topography in the ice sheet interior (Figure 4.5). We find uncertainty in ice thickness and bed elevation was reduced on average by 104 ± 174 m. Uncertainties within one standard deviation of the predicted error are reduced for 67% of the kriged area of BedMachine (Figure 4.5b). For the 99% confidence interval (3σ), 37% of the area has lower estimates

of error where our observation-based distance function is applied (Figure 4.5c). Importantly, substantial improvement i.e. over 200 m of uncertainty reduction occurs in areas where flight-line density is exceedingly sparse (green regions Figure 4.5).
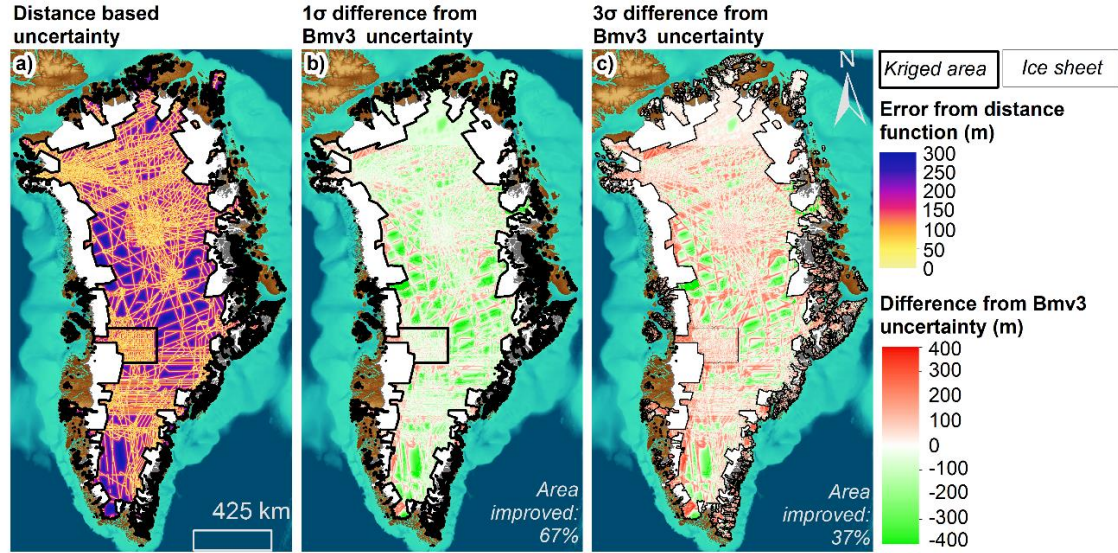
Figure 4.5. Distance-error function from Figure 4. applied to the kriged areas of BedMachine (Morlighem et al., 2017). a) Derived uncertainty estimate. b) Derived uncertainty plus one standard deviation differenced from BedMachine uncertainty. c) Derived uncertainty plus three standard deviations differenced from BedMachine uncertainty.

In regions of lowest flight-line density (<0.1 lines km^{-2}), we find mean reduction of uncertainty is approximately 89 ± 235 m within one standard deviation and 12 ± 236 m for a 99% confidence interval (CI). However, as real values for interpolation error show no relationship with distance, distance alone cannot predict whether the error is likely positive or negative. Additional information is required to predict whether the bed topography is expected to be lower or higher at a location.

As 10 m moving mean DME correlates strongly with real values for interpolation error, it can be used to apply a mean probable difference adaptation to the kriged areas of BedMachine, with associated confidence estimates (Figure 4.6). The mean for this difference is -5 ± 41 m, resulting in a deepening of the bed topography across the interior. Figure 4.5b shows the 99% CI for the absolute mean probable difference from the DME method. In locations with survey density greater than 0.1 lines km^{-2}, the BedMachine uncertainty is lower by 90 ± 114 m,

whereas in areas with sparse flight-line coverage the DME based uncertainty is reduced (-29 ± 252 m).
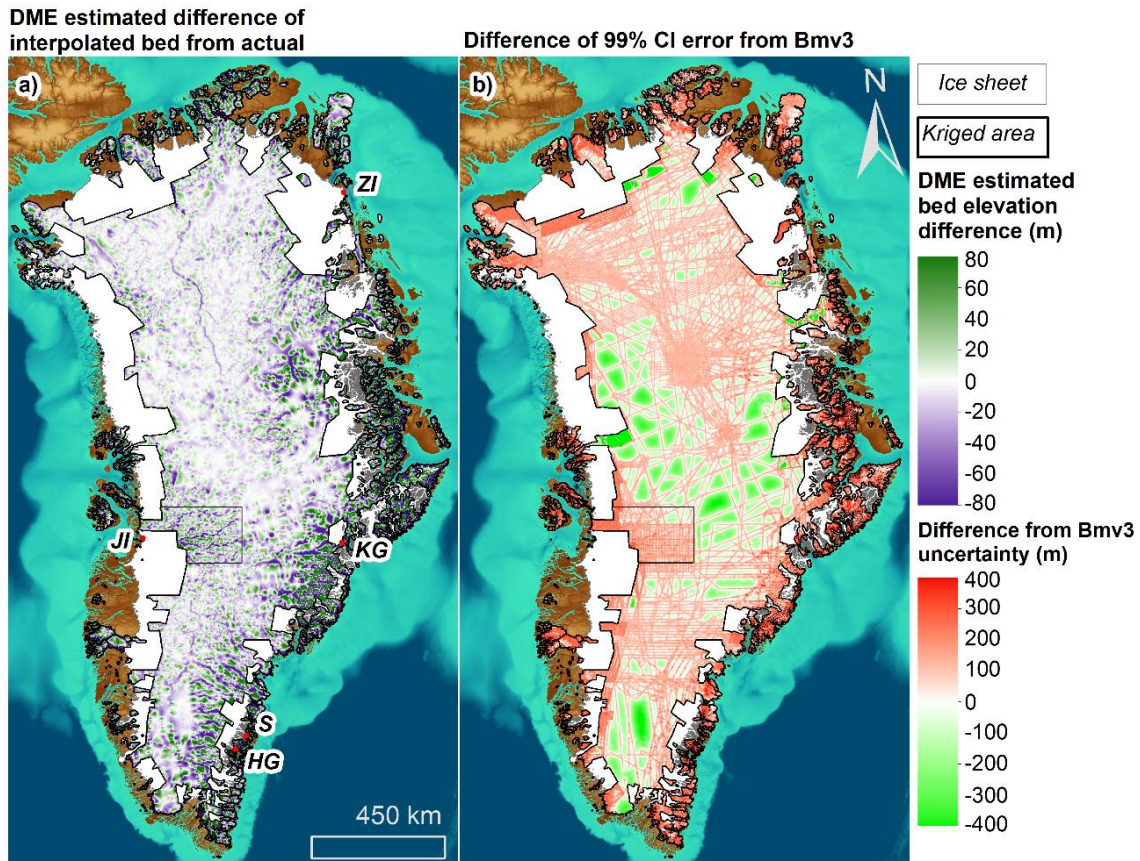
Figure 4.6. The DME-error function applied to the kriged area of BedMachine. a) The predicted mean difference of the bed elevation from the actual bed elevation. Outlet glaciers with extensive deepening in their interior portions are labelled (HG: Heimdal Glacier, JI: Jakobshavn Isbræ, KG: Kangerlussuaq, ZI: Zachariae Isstrøm. b) The predicted mean difference plus three standard deviations difference from Bedmachine uncertainty.

For areas of kriged bed topography where flight-line density is less than 0.14 lines per km^2, the DME method will provide lower estimates of uncertainty in subglacial topography than currently estimated (Figure 4.7). Such a flight-line density is equivalent to conducting a 3.5 km spaced grid or 1.8 km spaced line survey. Furthermore, our method increasingly improves uncertainty estimates, relative to other datasets, with decreasing flight line density. Conversely, for denser surveys, the method is less precise than the current estimates of uncertainty (Figures 4.5, 4.6 & 4.7). From this the mean likely difference may be applied to kriged bed topography to deepen lowlands and raise highlands, addressing one

of the main drawbacks of kriging (Williams et al., 2017), with an accompanying 99% confidence interval (Figure 4.6).

When applied to the kriged areas of BedMachine Greenland v3, our DME method can reliably reduce uncertainty and predict whether the topography is higher or lower than it should be over an area approximate to 56% of the ice sheet interior (Figure 4.7).
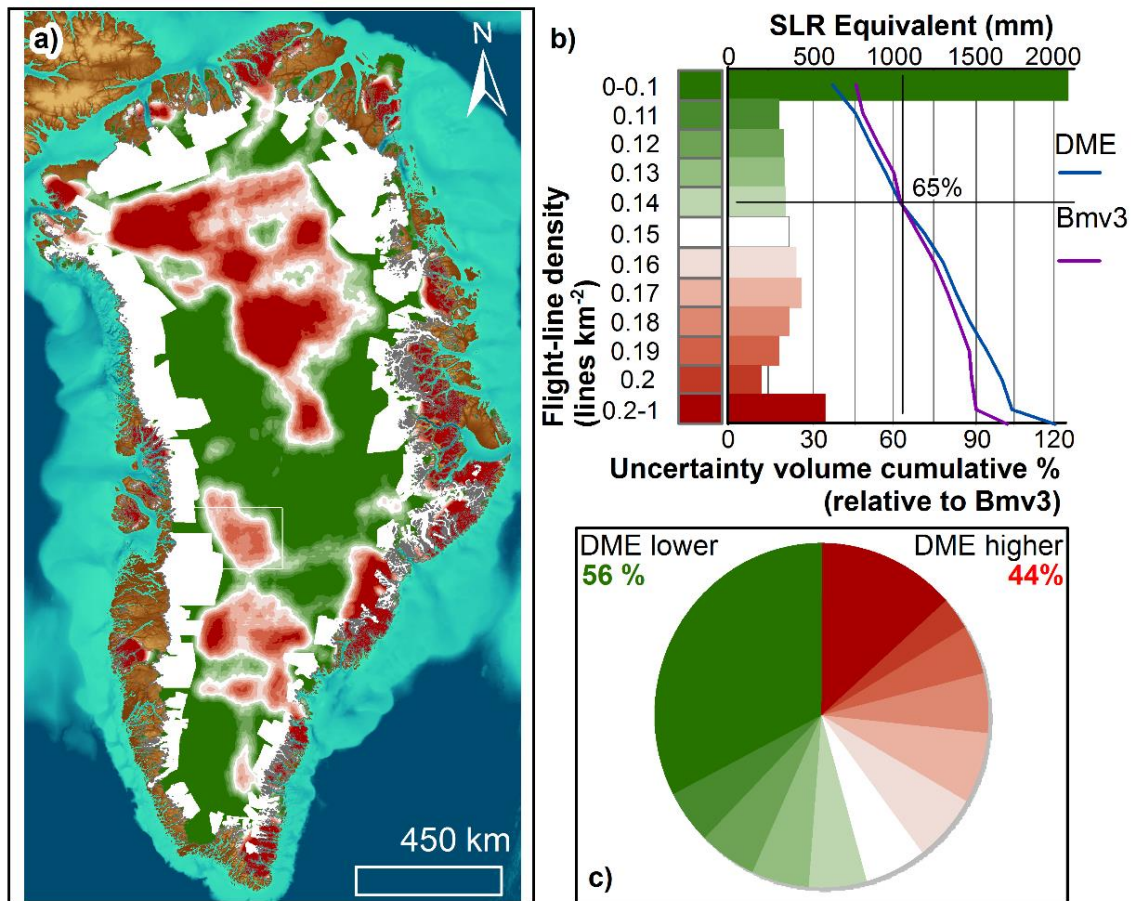
Figure 4.7. Flight-line density within a 50 km search window (lines km^{-2}) across the kriged area of BedMachine. a) Mapped flight-line density, green shows where DME-error function is predicted to reduce uncertainty with respect to Bedmachine and red is *vice-versa*. b) Bar chart shows the amount of sea-level rise (SLR) equivalent is estimated in each region using Bedmachine, lines show the cumulative percentage of the uncertainty volume (uncertainty in elevation multiplied by area) at each flight-line density for DME (blue) and BedMachine (purple). c) Pie chart shows representative areas of each flight-line density class, the sum of green segments is the area where DME uncertainty is likely to be lower than for BedMachine.

4.5 Discussion

4.5.1 Recommendations for future survey planning

The above results provide useful information for planning future RES surveys over ice masses. For an assumed topographic setting akin to the ones investigated here, figure 4.2 may be used to approximate the accuracy of an interpolated bed dataset from a given flight-line density. Our results also provide solutions for minimising uncertainty in outputs where sparse surveys are flown. Figure 4.7 highlights that this can be beneficial for large swathes of subglacial topography.

4.5.2 Uncertainty improvement in sparsely surveyed regions

In regions of low survey density, uncertainties in any bed topography dataset are greatest (Bamber et al., 2001). Firstly, our results show currently implemented distance error functions overestimate the likely interpolation error at a given location, hence, we implement a refined error estimate based on the results of the 1.5 million sample points taken in this study. Secondly, we propose a method for obtaining significantly reduced uncertainty based on the bed topography estimate itself constrained by knowledge of the elevation. This second uncertainty estimate sacrifices 10 m of accuracy in bed topography estimates to provide a probable difference at a location which may be used to adapt the bed topography. Previous studies have reported bed elevation uncertainties of 20 - 70 m (Enderlin et al., 2014; King et al., 2018), hence, a 10 m reduction in accuracy is well within largely reported uncertainties in analysis derived from bed topography. As this method is expedient, it may be applied to kriged bed topography datasets as a quick alternative to other methods.

Sparsely surveyed regions of the GrIS constitute large volumes of ice (Bamber et al., 2013; Morlighem et al., 2017). High uncertainties in these regions, therefore, have a greater effect on the overall estimate of volume for the ice sheet. Subsequently, this results in higher uncertainties in potential future sea-level contribution from Greenland, and our method poses a means of reducing this. Furthermore, our method may increase model performance over large areas of the ice sheet where bed topography uncertainty is significantly reduced (Sun et al., 2014). Where our method deepens or raises the bed to its probable elevation consistently over long-wavelength features (continuous areas of deep purple and

green in Figure6) a significant improvement in model performance may be gained (Sun et al., 2014).

Our DME method can be efficaciously applied to approximately 56% of the kriged area of BedMachine, which equates to an area of 48% of the entire ice sheet. This area contains a potential sea-level rise (SLR) contribution of 3.5 m, which equates to roughly 47% of the ice sheet total (7.4 m, Morlighem et al., 2017). We estimate the reduction in uncertainty volume across this region, the area of the uncertainty in ice thickness multiplied by its scale, is equivalent to 8.5 centimetres of sea-level contribution (Figure 4.7). This estimate is conservative as the above analysis is based on regions where the 99% confidence interval of our uncertainty can be expected to be lower than Bedmachine. While this is a marked reduction in uncertainty, the regions in which our method is most effective are interior portions of the ice sheet that are unlikely to contribute to sea-level rise in the current century (Calov et al., 2018).

4.5.3 Implications for the stability of the GrIS interior

As our approach leads to a deepening of areas lower than the local mean elevation, we predict the current inland expanse of the GrIS below mean sea level may be 2% greater than previously reported (Morlighem et al., 2017). Notably, areas of the ice sheet bed over 200 m below sea level were found to be nearly 30% more expansive (examples in Figures 4.8 and 4.9). An increase of the area below 200 m is important as Atlantic water occurs at depths between 200 and 300 m (Morlighem et al., 2017; Holland et al., 2008; Rignot et al., 2016). Where this relatively warm water is able to reach Greenland outlet glacier margins enhanced oceanic melting is expected (Morlighem et al., 2017; Shaffer et al., 2020), and areas of the ice sheet grounded below this depth and connected to the ocean are susceptible to its influence. Hence, if areas beneath 200 m below sea-level are more expansive as we predict, 30% more of the ice sheet interior becomes susceptible to the incursion of Atlantic water when the ice retreats into these locations. Although it can be reasonably assumed that neighbouring expanded deeper areas are connected, our results do not show this (Figure 4.8). As our results predominantly modify kriged bed topography in the vertical domain they do not improve the horizontal connectivity of deep basins, hence, "bullseye" like interpolation artefacts still exist in the dataset (Figure 4.8; Williams et al., 2017). Though the interior portion of the GrIS is unlikely to contribute to sea-level

rise in the current century (Calov et al., 2018), these findings have implications for our appreciation of the stability of the GrIS into the far future (Aschwanden et al., 2019). Nevertheless, isostatic uplift of the bed with deglaciation will act to alleviate this and it is uncertain how ocean temperature and circulation will evolve into the future (Aschwanden et al., 2019).
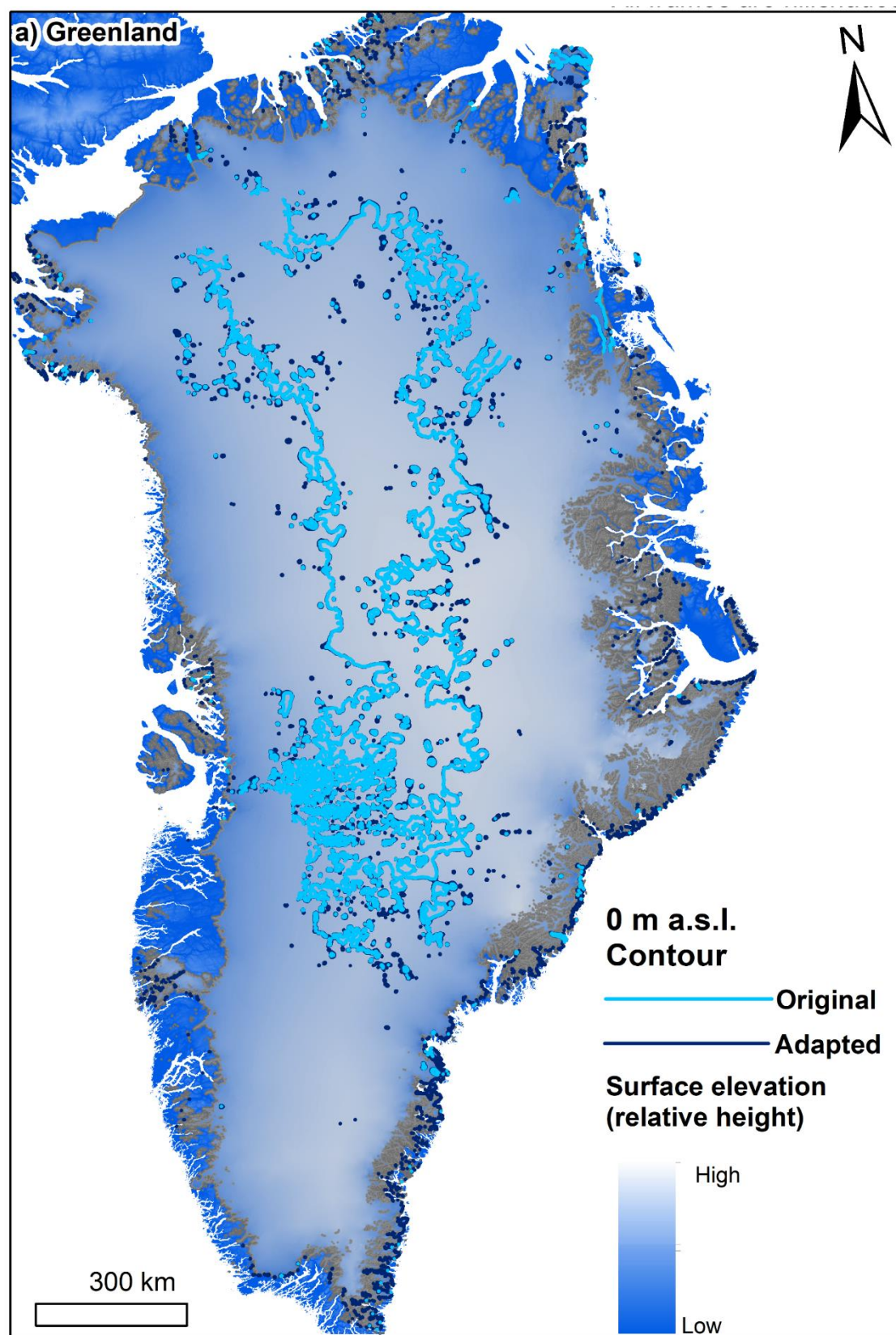
Figure 4.8 BedMachine V3 ('Original'; Morlighem et al., 2017) and adapted kriged region bed topography sea level contours for the GrIS. Isolated "bullseyes" outside of the "original" sea-level contour are exacerbated artefacts of the kriging process and hence should be treated with increased uncertainty.

As surface elevation is well known (Howat et al., 2014; Porter et al., 2018), a deeper bed than currently estimated results in greater ice thickness. Subsequently, this results in a more inherently dynamic system (Cornford et al., 2015), as a result, estimates of the evolution of the Greenland interior based on current bed topography likely underrepresent its future dynamic response to warming. Increased depth below sea-level combined with increased ice thickness brings the ice sheet closer to flotation meaning future retreat into the interior will likely be enhanced, due to reduced effective pressure at the grounding line (Meier and Post, 1984; Stearns and van der Veen, 2018). Because the interior of the ice sheet is strongly grounded it is more sensitive to this effect (Favier et al., 2014). Moreover, sea-level rise contribution is found to increase with deeper beds, regardless of sliding law (Nias et al., 2018). While our method does not remove interpolation artefacts that hinder accurate numerical modelling (Sun et al., 2014), estimates of sea-level rise contribution would still be greater than the unmodified dataset purely from the deepening of the bed (Nias et al., 2018).
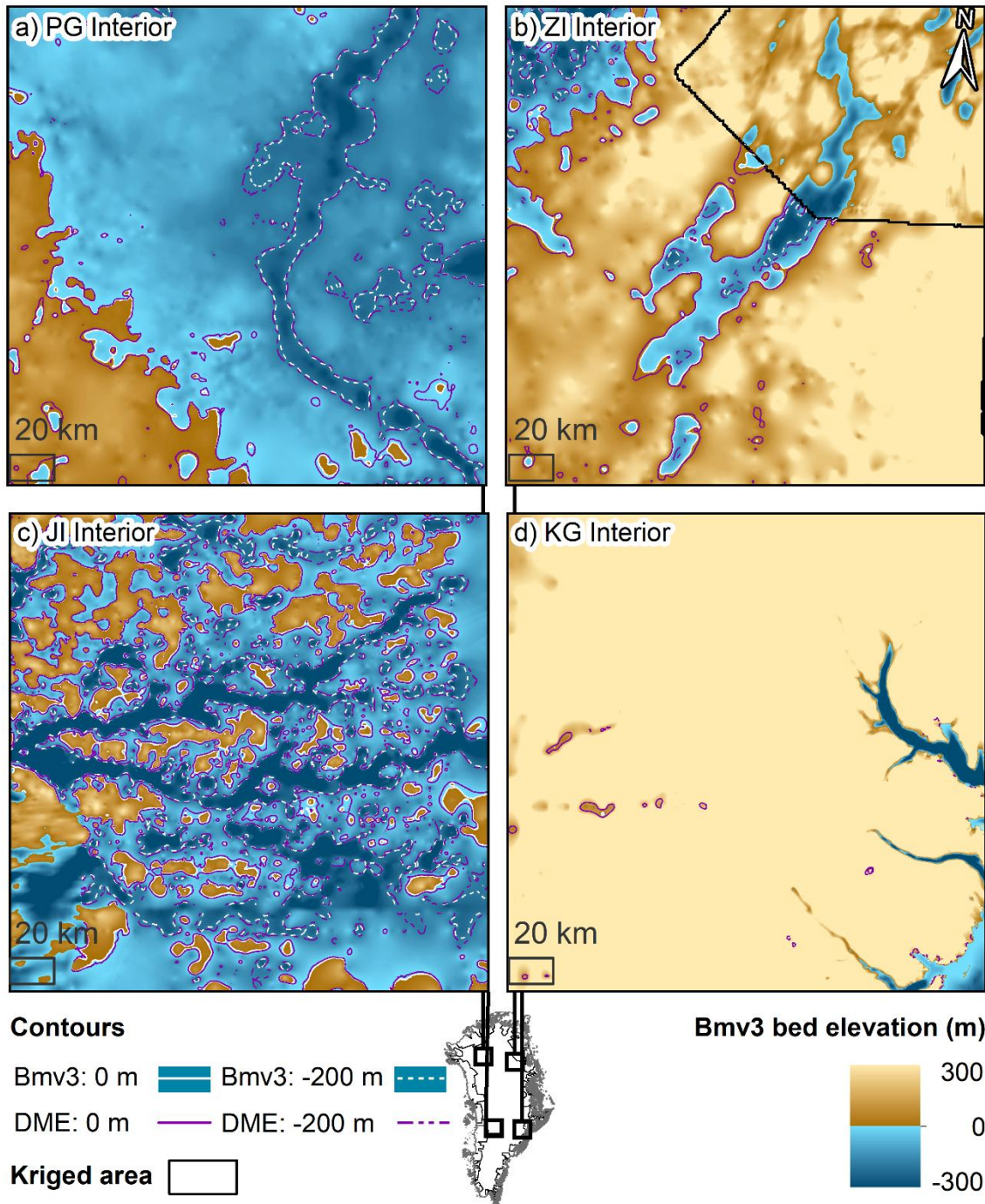
Figure 4.9 Sub-sea-level contours for Bedmachine (white) and DME adapted Bedmachine subglacial elevation (purple). Dashed contours illustrate areas 200 m below sea-level. a) Interior area of the Petermann Glacier canyon and the ice sheet interior. b) Interior area of Zachariae Isstrøm. c) Jakobshavn Isbræ interior. d) Kangerlussuaq glacier interior.

4.5.4 Implications for the stability of Greenland outlet glaciers

Our results suggest the greatest differences in bed elevation are prevalent where the elevation is significantly above or below the local mean elevation. Therefore,

where valley cross-sections are derived from bed topography for ice-discharge calculations, these calculations are likely underestimates. Valley cross-sectional area, widely used to calculate ice flux (Shepherd et al., 2007), is found to increase by 1 ± 1% if our DME estimated elevation difference is applied (Figure 4.11 [locations shown in Figure 4.10]). Therefore, where flux-gates have been drawn from kriged bed topography, cross-sectional area should be increased by one per cent. Additionally, DME estimated bed elevation across flux-gates at the downglacier edge of the kriged area (i.e. the transition zone to mass conservation derived bed topography) was found to be 7 ± 20% lower than in the original kriging (Figure 4.11), which has implications for the depth-averaged velocity parameter in ice discharge calculations (Van Wychen et al., 2014).
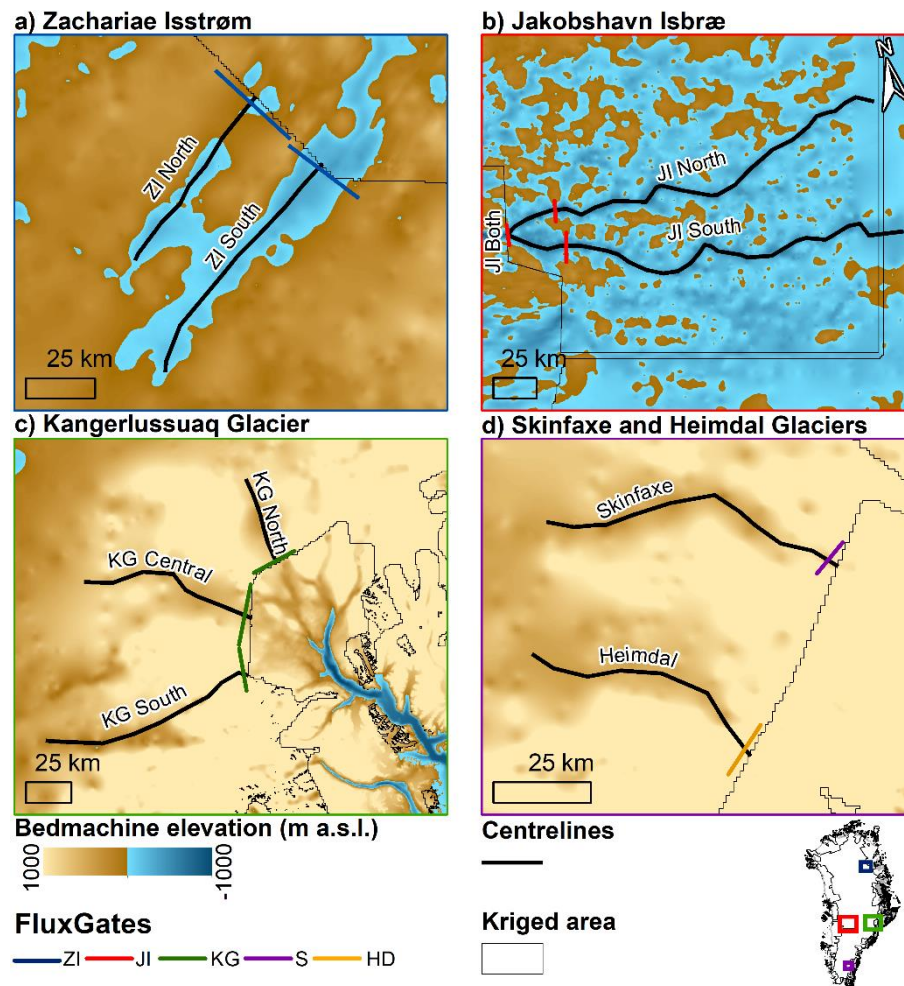
Figure 4.10 Map of centreline and flux-gate bed elevation profile locations highlighted in figures 4.11 and 4.12. a) Zachariæ Isstrøm flux-gate and centreline locations, b) Jakobshavn Isbræ flux-gate and centreline locations, c) Kangerlussuaq flux-gate and centreline locations, d) Skinfaxe and Heimdal flux-gate and centreline locations.
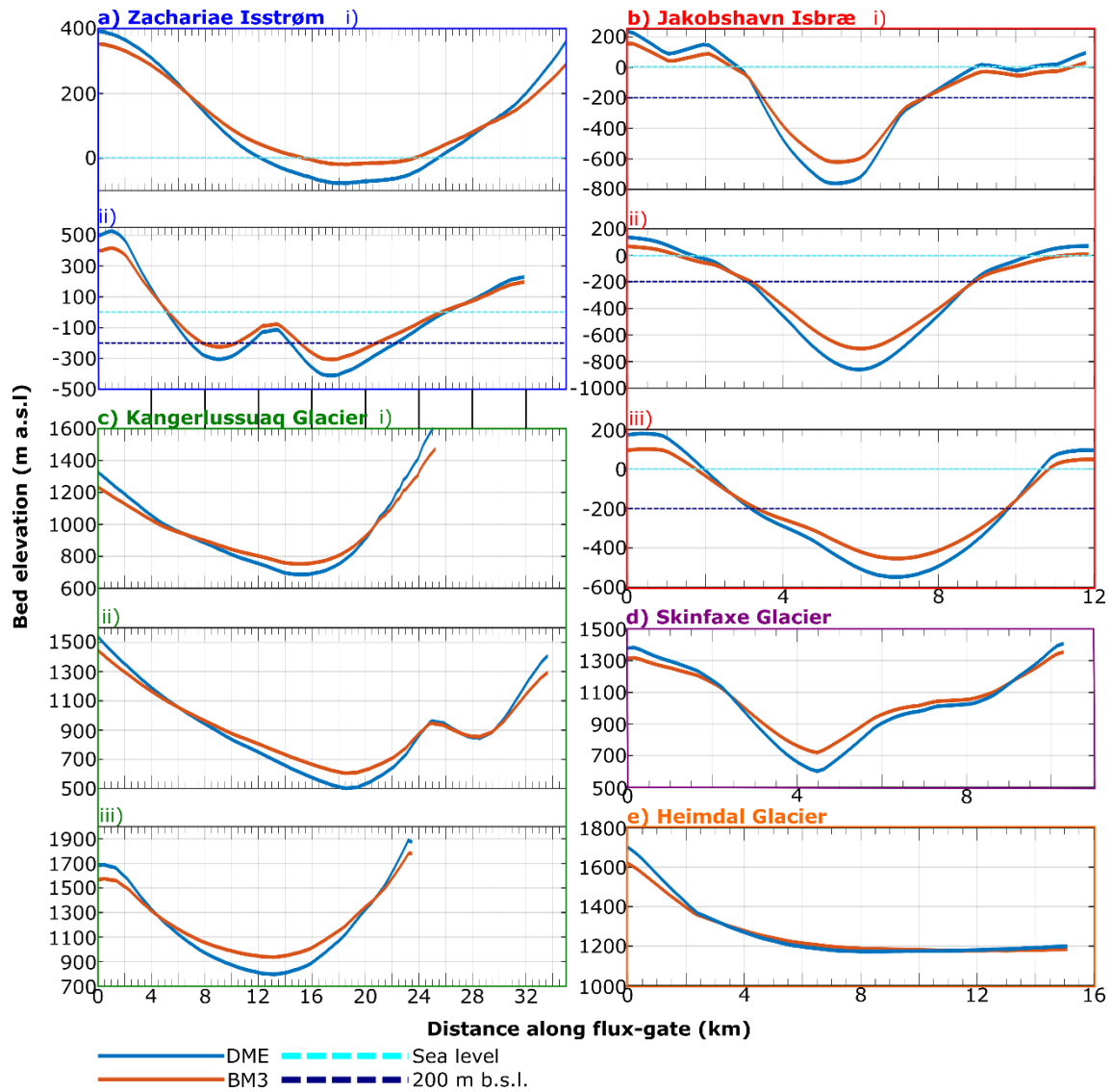
Figure 4.11 Comparison of Bedmachine (orange profiles) and DME (blue profiles) altered flux-gate bed elevation cross-sections for major outlet glaciers (labelled in figure 4.6). a) Zachariae Isstrøm i) North ii) South, b) Jakobshavn Isbræ i) North, ii) Central, iii) South, c) Kangerlussuaq Glacier, North, ii) Central, iii) South, d) Skinfaxe Glacier, e) Heimdal Glacier.

Flux-gate mean depths were found to be deeper on average for eight of the ten outlet cross-sections, six of which were significantly deeper at the 95% confidence interval. Consequently, discharge through these regions will be underestimated in models evaluating future dynamic mass loss through these catchments as the ice sheet retreats into them (Aschwanden et al., 2019). Importantly, our method may be able to contribute improved bed topography for modelling into the future as we are able to reduce uncertainty in bed topography over large areas of the interior (Figures 4.5 & 4.6). It has been found that

126

reduction in bed topography uncertainty over long-wavelength features significantly improves numerical modelling (Sun et al., 2014). Perturbations of 10's of meters have been observed to strongly influence predicted grounding line retreat (Sun et al., 2014). As we provide reduced uncertainty in bed topography and its likely difference (deeper or shallower), our method could be used to improve predictions of the evolution of the interior portions of the GrIS grounded below sea-level.

Mean depth along the approximate centrelines of the interior portions of the outlet glaciers labelled in figure 4.6 was found to be deeper by 86 ± 20 m (Figure 4.12). Importantly, for outlets with extensive sub-sea-level bed topography connected to the ice sheet interior (Zachariae Isstrøm and Jakobshavn Isbræ), retrograde bed slopes were found to be steeper by 0.3 ± 0.1° (or 0.5 ± 0.2 as percentage slope, Figure 4.12). This is of crucial importance to our understanding of the stability of the GrIS as sub-sea-level retrograde beds are potentially susceptible to MISI (Schoof, 2007; Durand et al., 2009). The same gradient increase was observed across all the sampled retrograde beds, suggesting gradients of such beds in other kriged bed topography datasets are likely underestimated. Additionally, expanse of the area 200 m below sea-level is observed across subglacial topography for Petermann Glacier, Zachariae Isstrøm and Jakobshavn Isbræ (Figure 4.9), which, when modelled, would increase the susceptibility of these glaciers to Atlantic water incursions and consequently their perceived stability (Schaffer et al., 2020). Deepening of the bed also occurs at the interior of the southern branch of the Kangerlussuaq glacier, where a portion of the bed is lowered below sea-level approximately 100 km from the margin along a retrograde bed slope, potentially increasing the susceptibility of this rapidly retreating portion of the ice sheet interior to enhanced retreat in the far term (Brough et al., 2019; Durand et al., 2009). However, the connecting subglacial topography between the current sub-sea level portion of the glacier and this upglacier section is well above sea level (Figure 4.9 d). Hence, it is likely retreat inland here will be reduced in the near-term when the outlet retreats onto land. These glaciers comprise four of the eight largest contributors to ice discharge from the GrIS (Mankoff et al., 2019). Consequently, long term forecasts of their sensitivity to grounding line retreat may be underestimated.
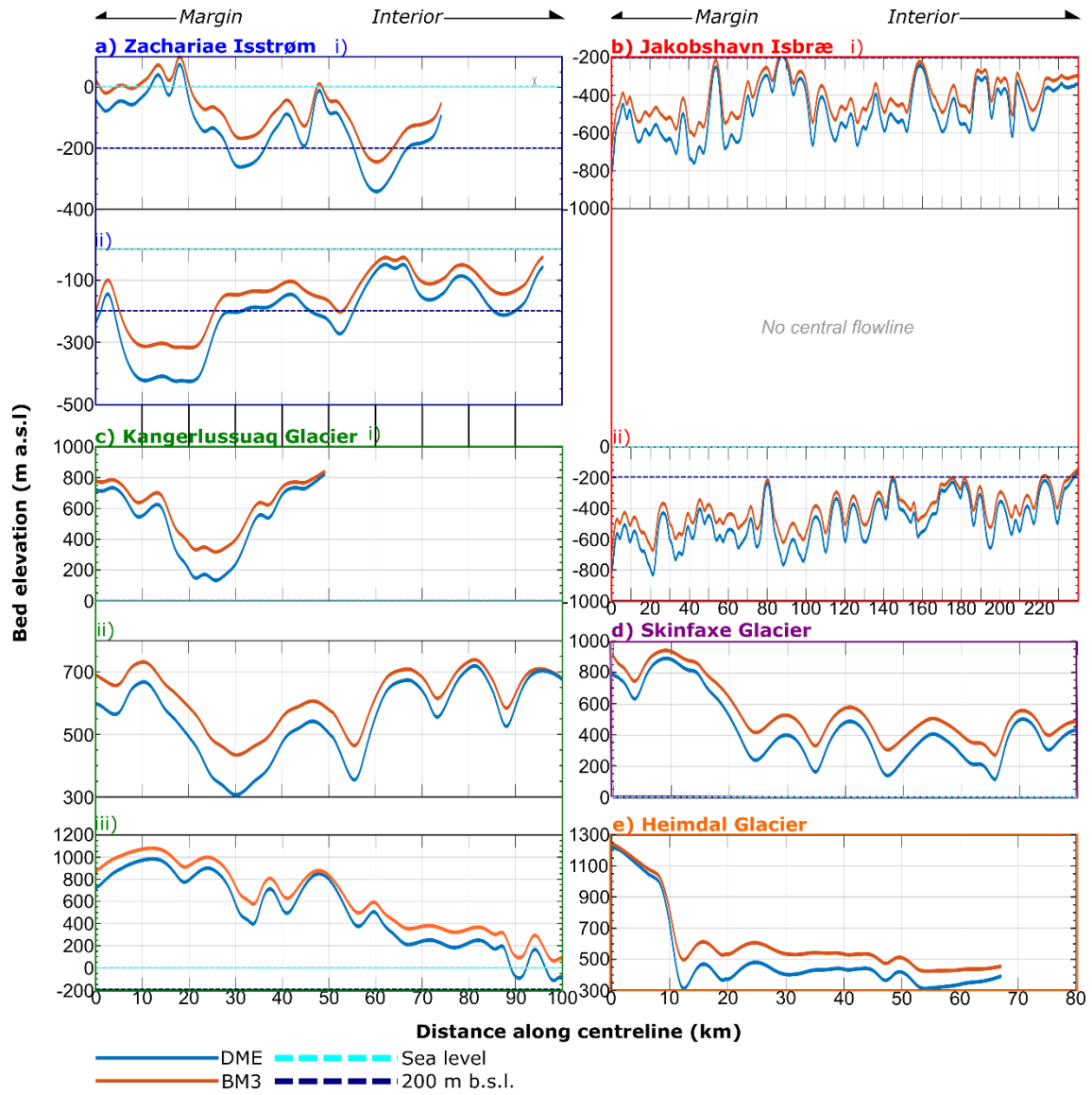
Figure 4.12 Comparison of Bedmachine (orange profiles) and DME (blue profiles) altered centreline bed elevation cross-sections for major outlet glaciers (labelled in figure 4.6). a) Zachariae Isstrøm i) North ii) South, b) Jakobshavn Isbræ i) North, ii) South, c) Kangerlussuaq Glacier, North, ii) Central, iii) South, d) Skinfaxe Glacier, e) Heimdal Glacier.

4.6 Conclusions

We present two methods for quantifying and reducing uncertainty in kriged subglacial bed topography datasets. Firstly, a revised distance-error function is presented which reduces uncertainty in bed topography for interpolated locations over 1.5 km from input flight-lines. Secondly, an alternative method is presented which may be used to predict the probable difference in subglacial elevation at an interpolated point. We find this method works best in areas where flight-line density is sparser than a 3.5 km spaced grid or 1.8 km spaced parallel flight-line,

approximately 56% of the GrIS interior. Consequently, our method reduces uncertainty over an area of the interior which contains 65% of its ice volume. Reduction of uncertainty by up to hundreds of metres provides improved confidence in bed topography input conditions for numerical modelling of the GrIS (Sun et al., 2014).

Adaptation of Bedmachine Greenland v3 subglacial topography using our DME method results in the deepening of valleys and raising of highlands across the ice sheet interior. Elevation lowering is more prevalent than elevation heightening leading to a seven-millimetre increase in the potential sea-level contribution for the GrIS. Moreover, the total area below sea-level expands by 2%. Of particular importance is that the area 200 m below sea-level expands by 29%. This improvement in the confidence of the area significantly below sea-level is important for more reliably modelling the susceptibility of major outlet glaciers to enhanced grounding line retreat in the future, as the ice sheet retreats into these bed elevation lows (Aschwanden et al., 2019). Consequently, assessments of the future stability of the GrIS should account for the potential for a wider area of the bed to be susceptible to incursions of Atlantic Water (Schaffer et al., 2020). Importantly, these regions are overlain by three of the eight largest glaciers in terms of solid ice discharge from the ice sheet (Mankoff et al., 2019). While, the region adjusted in this study consists mostly of the interior of the ice sheet which has implications for sea-level change in the latter centuries of this millennium (Aschwanden et al., 2019), the connectivity of these regions to the ocean through major outlets, which were found to have deeper and steeper retrograde beds, may have potential implications in the near term.

Finally, our method is based on observations over a wide suite of topographic settings expected to occur beneath any ice mass. As such it may be applied to bed topography datasets for other ice masses which are derived by kriging (e.g. Martian polar ice caps, Holt et al., 2010). Consequently, this may contribute to reduced uncertainty in bed elevation for ice sheet model inputs and subsequent projections of sea-level change.

Chapter 5: Full quantification of Canadian Arctic Archipelago ice cap subglacial and supraglacial topography

In this chapter, the methods developed in the previous two substantive results chapters are applied to airborne RES measurements from ice caps in the Canadian Arctic Archipelago (CAA). The goal of this chapter is to achieve the third research objective defined in chapter one: Using the methods developed, derive a new dataset of ice thickness with accompanying uncertainty maps for selected Arctic ice caps and assess the potential implications for near term sea-level rise contribution.

5.1. Introduction

Potential global mean sea level rise from ice caps and glaciers separate from the continental ice sheets is estimated at approximately 0.4 m (Huss and Farinotti, 2012). While this is two orders of magnitude less than that of the continental ice sheets combined, glaciers and ice caps have contributed significantly to global mean sea level rise (Hock et al., 2019; Zemp et al., 2019). From 1961 to 2016 ice cap and glacier mass loss is estimated to have raised global mean sea level 27 ± 22 mm (Zemp et al., 2019). Moreover, for the decade 2006 to 2016 an accelerated rise of 0.92 ± 0.39 mm yr^{-1} was observed compared to the overall rate for the observational period 0.5 ± 0.4 mm yr^{-1} (Zemp et al., 2019). In the Arctic, the regional mean temperature is increasing at double the rate of the global mean due to the Arctic amplification effect (Overland et al., 2016). Consequently, this has to lead to increased melting of ice caps across the region and is expected to continue (Gardner et al., 2011; Fisher et al., 2012). In the Canadian Arctic Archipelago (CAA), ice caps contain 85.3 ± 22.1 mm of sea-level rise equivalent, which approximates to 26% of the latest glacier and ice cap global volume consensus estimate (Farinotti et al., 2019). CAA ice caps and glaciers are highly sensitive to climatic changes on annual to decadal timescales (Lenaerts et al., 2013; Noël et al., 2018), consequently, accelerated melting of these ice caps will lead to enhanced 21st-century sea-level rise (Hock et al., 2019).

Surface run-off dominates mass balance in the CAA, and both surface and dynamic mass loss are highly variable spatially and temporally (Millan et al., 2017; Van Wychen et al., 2016). Surface mass balance currently (2005 – 2014) accounts for ~90% of the regional mass balance, some 29.6 ± 3.0 GT yr^{-1} (Millan et a., 2017; Noël et al., 2018). This marks a shift in the mass budget regime for the region, where previously, between 1991 and 2005, ~52% of ice mass was lost dynamically (Millan et al., 2017). The sensitivity of both components of mass loss is strongly related to both the supraglacial and subglacial topographic configuration of ice caps (Colgan et al., 2015; Van Wychen et al., 2016; Harcourt et al., 2020).

Supraglacial hypsometry influences and is influenced by the surface mass balance of a glacier (McGrath et al., 2017). Ice caps with extensive accumulation zones (top-heavy hypsometry) are buffered against melting somewhat as

equilibrium line altitude has to increase further in response to warming to melt more ice (Jiskoot et al., 2009; Noël et al., 2018). Conversely, bottom-heavy glaciers with extensive ablation zones are highly susceptible to increased ablation. Additionally, the potential exists for the albedo-elevation feedback to occur, where ice at lower elevations melts more initially as it occupies warmer air, the surface darkens as it melts which then further exacerbates melting (Box et al., 2012). Surface mass balance and hypsometry have been widely modelled and measured over the CAA (Lenaerts et al., 2013; Millan et al., 2017; Noël et al. 2018). However, a requirement exists for resolving the hypsometry of these ice caps at increased spatial and temporal resolution due to the complex configuration of ice cap surface topography. At the sub-km scale, topography modulates turbulent heat fluxes which significantly increase surface runoff (Lenaerts et al., 2013; Noël et al., 2015).

Subglacial hypsometry impacts the sensitivity of the ice caps to enhanced dynamic mass loss. Where ice is grounded below sea-level it is more sensitive to enhanced retreat (Van Wychen et al., 2014; Harcourt et al., 2020). Consequently, if a significant area of an ice cap is grounded on sub-sea-level topography it is more susceptible to increased dynamic mass loss. Initially, sub-sea-level bed topography permits the incursion of oceanic water to the grounding line and the glacier is subjected to oceanic melting in addition to atmospheric melting (Holland et al., 2008; Cook et al., 2019). Secondly, the reduction of ice thickness sub-aerially and sub-aqueously thins the outlet glacier which can induce dynamic feedbacks. Effective pressure at the grounding line is reduced as the height above buoyancy of the overlying ice is lowered (Stearns and van der Veen, 2018; Milillo et al., 2019). From this, enhanced sliding is increased which further thins the outlet glacier dynamically (Harcourt et al., 2020). Consequently, ice discharge is increased and more ice is calved from the outlet (James et al., 2014). This effect has been observed for outlet glaciers on the Prince of Wales (POW) icefield in the CAA (Harcourt et al., 2020). Furthermore, where the bed is reverse sloping, outlet glaciers may be susceptible to further dynamic instabilities (Schoof, 2007). It is therefore essential to quantify the full morphology of Arctic glaciers and ice caps to improve projections of their contribution to sea-level rise (Moon et al., 2018).

Measurements of ice thickness are sparsely sampled in relation to ice cap size (Rodriguez-Morales et al., 2014). Interpolations are used to predict ice thickness and subsequently bed topography across unsurveyed areas (Dowdeswell et al., 2004; Rutishauser et al., 2018). While the latest maps of the continental ice sheets are derived by mass conservation, the assumption of a steady-state velocity field complicates its adoption for outlet glaciers across the CAA where significant dynamic variability has been observed (Van Wychen et al., 2016). Finally, mass conservation is less accurate in regions of slow flow, which is characteristic of large interior regions of ice caps (Dowdeswell et al., 2002; Dowdeswell et al., 2004). Hence, geostatistical methods still have utility for generating bed topography in these regions, despite their well-documented caveats (Williams et al., 2017). Kriging is the most widely utilised geostatistical interpolator as it provides a best estimate of elevations in unmeasured areas (Deutsch and Journel, 1997). Recent work has looked to exploit the tendency of kriging to tend a surface to the mean of the input measurements (Bartlett et al., in preparation; [chapter 4]). By using high-resolution elevation data which likely mimicks subglacial topography, pseudo-validation is possible for bed elevation in place of direct measurements of ice thickness (Bartlett et al., 2020; [chapter 3]).

This study aims to provide bed topography datasets with accompanying estimates of uncertainty for the major ice caps of the Canadian Arctic Archipelago (CAA). Subsequently, the volume of the ice caps investigated will be quantified along with uncertainty. Where possible this uncertainty will be reduced. Furthermore, this paper will quantify the full 3D morphology of the ice caps investigated, and the uncertainty in this to enable a full assessment of their sensitivity to oceanic and atmospheric forcing.

5.2 Data and methods

5.2.1 Study locations and datasets

5.2.1.1 Canadian Arctic Archipelago

Glaciers and ice caps on the Queen Elizabeth Islands' (QEI), northern CAA, contain a quarter of terrestrial ice in the Arctic outside of Greenland (Van Wychen et al., 2014; Millan et al., 2017). Eight large ice caps occur across the islands, seven of which are topographically constrained icefields (Van Wychen et al., 2020). Conversely, the Devon ice cap is largely topographically unconstrained.

Additionally, the Devon ice cap has been comprehensively researched and is a World Glacier Monitoring Service (WGMS) reference glacier (Dowdeswell et al., 2004; Boon, 2010; Van Wychen et al., 2017; WGMS, 2017). Extensive aerogeophysical surveys have been conducted over these ice caps to measure ice thickness and bed topography (Koerner, 1977; Dowdeswell et al., 2004, Paden et al., 2010, Blankenship et al., 2012). However, apart from the Devon ice cap, no comprehensive dataset of 3D bed topography has been interpolated from these measurements (Figure 5.1, Dowdeswell et al., 2004). Outlines for the ice caps were acquired from the Randolph Glacier Inventory 6.0 (WGMS, 2017). Proximal smaller glaciers and ice fields were combined with the neighbouring ice cap. Polygons outlined in figure 5.1 highlight what each collection of ice caps and glaciers is referred to as throughout. This study does not include the Sydkap and Manson ice caps as they are not as comprehensively surveyed as the others (Van Wychen et al., 2014).

Mean surface mosaics for 2017 were generated at 50 m resolution, to match the latterly described interpolation outputs, for each ice cap from ArcticDEM 2 m strips using Google Earth Engine (Code in figure A5.1; Porter et al., 2018, Gorelick et al., 2017). A 50 m rectangular moving window determined the mean annual surface elevation from all 2 m ArcticDEM pixels that fell inside it, from the all the dates elevation was generated from stereo-pair satellite imagery in the given year (Porter et al., 2018). Uncertainty in the ArcticDEM is < 1 m (Porter et al., 2018).
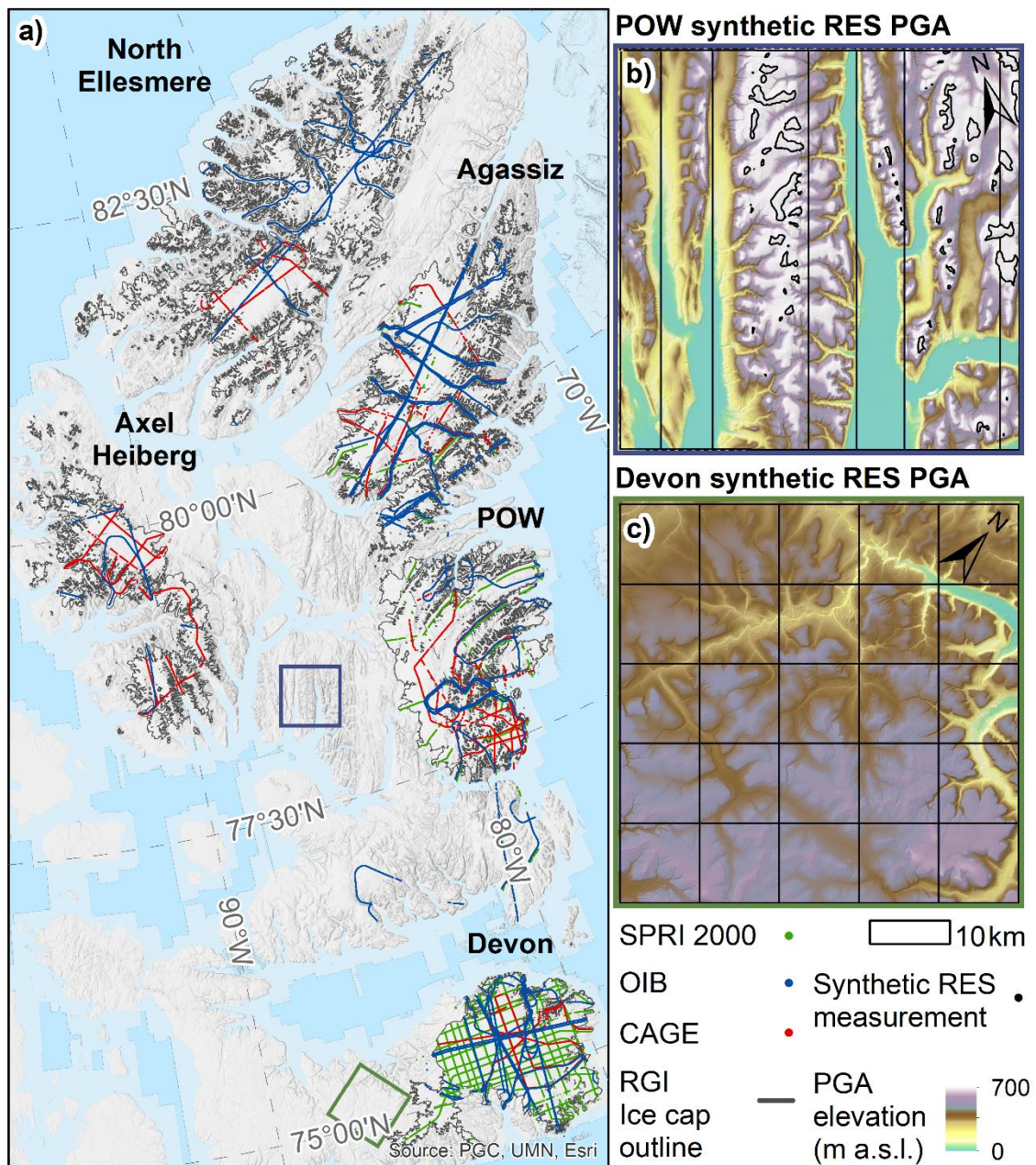
Figure 5.1. Queen Elizabeth Islands ice caps, and synthetic RES proglacial areas (PGAs). a) Regional map of the QEI, Scott Polar Research Institute (SPRI) 2000 flights are shown in green (Dowdeswell et al., 2004), Operation IceBridge (OIB) in blue (Paden et al., 2010), and Canadian Arctic Geophysical Exploration flights in red (Blankenship et al., 2017). b) POW synthetic RES PGA, a predominantly margin orthogonal survey is simulated with nunataks. c) Devon synthetic RES PGA, a 10 km grid is simulated, emulating the SPRI 2000 survey.

5.2.1.2 Ice thickness measurements

Ice thickness measurements were collated from multiple RES campaigns over CAA ice caps (Figure 5.1). The data used in this study comprised the most complete collection of RES data for the CAA to date (Van Wychen et al., 2016).

NASA Operation IceBridge L2 Ice Thickness data were downloaded from the NSIDC Operation IceBridge Data Portal (Paden et al., 2010, Table A5.1 lists subsets). Flights were conducted in spring 2011, 2012, 2014 and 2017 using the Multichannel Coherent Radar Depth Sounder (MCoRDS) (Paden et al., 2010). Uncertainty in MCoRDS measurements due to ice bottom errors is typically reported to be to the order of 10s of metres (CReSIS, 2018). Off-nadir elevation differences result in negative bias in bed elevation measurement (Bartlett et al., 2020). Bartlett and others, (2020) pose various corrections for alleviating this modest systematic bias in RES measurements. This study investigates the potential uncertainty in outlet glacier centreline and flux gates measurements by assessing bed profiles before and after correction.

Canadian Arctic Geophysical Exploration (CAGE) flights were conducted in spring 2014 using the High Capability Radar Sounder (HiCARS-2, Peters et al., 2005). Uncertainty ranged from seven to fifty metres dependent on bed roughness (Peters et al., 2005; Young et al., 2017; Harcourt et al., 2020). CAGE measurements were not adjusted according to Bartlett and others, (2020), as the method could not be parameterised to mimic the HiCARS-2 system. However, as a measurement from this system can be taken from anywhere within a ~700 m footprint (Blankenship et al., 2017), the influence of off-nadir elevation differences can be qualitatively appreciated dependent on the geometry of the subglacial topography (Bartlett et al., 2020). For example, in a valley narrower than 700 m there is a very high probability the bed measurement is taken from a higher elevation on the valley sides as opposed to directly from nadir.

Flights conducted by the Scott Polar Research Institute in spring 2000 used a 100 MHz Radio Echo Sounder detailed in Dowdeswell and others, (2002). Uncertainty in bed measurement from these flights was estimated to be approximately ten metres (Dowdeswell et al., 2004). Outlet glacier centreline flights were conducted over the Agassiz, Devon and POW ice caps. Additionally, a nominal 10 km grid was flown over the Devon Island ice cap (Dowdeswell et

al., 2004). From this survey ice thickness, and subsequently, bed topography were interpolated using an inverse distance weighting method. Previously, kriging was not used as a suitable variogram could not be derived (Dowdeswell et al., 2004). In this study, with the inclusion of the additional RES measurement taken since 2000 a suitable variogram could be derived for kriging detailed below.

5.2.3 Bed topography interpolation

Bed elevation measurements were interpolated across each ice cap using ordinary kriging (Deutsch and Journel, 1997). Following the method of Jezek, and others (2013), a spherical model was implemented, with 100 lags of 100 m. A 30 m nugget was employed to account for uncertainty in the RES measurements additional to the off-nadir elevation differences discussed earlier (Jezek et al., 2013; Bartlett et al., 2020). Semivariogram parameters were optimised using the inbuilt iterative cross-validation technique in the ArcMap Geostatistical wizard.

Preliminary analysis found lower RMSE for output surfaces generated using the elevation of edge inputs opposed to prescribing them as locations of zero ice thickness. When interpolating ice bottom elevation and the ArcticDEM elevation at the margin RMSE between the DEM surface and the interpolation was 251 m. Conversely, the traditional method of interpolating ice thickness and zero thickness values at the margin was more erroneous (RMSE = 259 m). Therefore, the availability of high-resolution elevation at ice margins using the ArcticDEM can provide an initial improvement to kriging bed topography. For each ice cap, point elevations around the GLIMS outline of each ice cap were extracted every 15 m around the perimeter, mimicking the typical sample spacing of the RES surveys.

Output bed topography was gridded to a 50 m resolution, matching the previous interpolation of individual outlet glacier bed topography in the region (Harcourt et al., 2020).

5.2.4 Proglacial landscape validation area

All ice caps exhibit subglacial topography in two-dimensional RES profiles that replicate the proglacial topography (Van Wychen et al., 2020). For the Ellesmere Island and Axel Heiberg ice caps, a proglacial area (PGA) with analogous topography was selected proximal to the POW icefield (Figure 5.1). As Devon Ice

Cap has been shown previously to have very different subglacial terrain to the other ice caps and greater survey density (Dowdeswell et al., 2004), a separate validation PGA was selected on Devon Island (Figure 5.1).

For each PGA a 50 km by 50 km validation area was selected from the ArcticDEM (Porter et al., 2018). Synthetic RES surveys were conducted at a flight-line density and geometry similar to the input IceBridge, CAGE and SPRI measurements, following the method by Bartlett, and others (2020). Subsequently, synthetic measurements are interpolated using kriging with the same parameters used for the ice cap bed topography interpolation. A mean likely difference function, derived from ordinary least squares regression, was developed from the difference of the synthetic interpolation and the input PGA DEM (Figure 5.2), following the method of Bartlett and others, (in preparation). Similarly, a Euclidean distance-error function was derived for each site (Bartlett et al., in preparation). The error functions breakdown where there are limited observations. This occurred mostly at extreme distances and difference from interpolation mean elevation (DME) values for the POW PGA (Figure 5.2). Therefore, functions were revised to ranges where they performed well ($R^2 > 0.7$) and points at distances further than 4000 m from an input and with DME exceeding 300 m were treated with additional uncertainty. Uncertainty from each function was reported as the RMSE of the function. For distance-error functions, this equated to 5 and 235 m for the Devon and POW validation areas respectively. For DME-error functions, maximum RMSE was found to be 30 m for the Devon PGA and 96 m for the POW PGA.
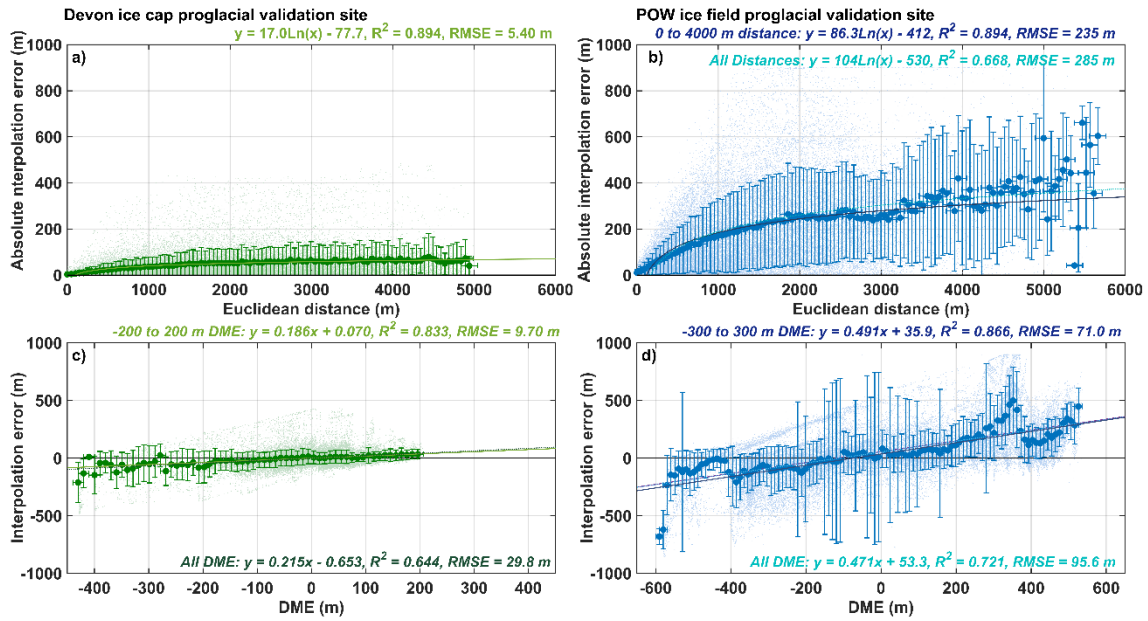
Figure 5.2. Error functions for ordinary kriging of QEI ice cap bed topography, following the method of Bartlett and others, (in preparation). For Euclidean distance-error functions moving means are calculated every 50 m (filled circles), error bars represent standard deviations. For DME-error functions moving means are calculated every 10 m, with accompanying standard deviations.

The DME-error function was used to estimate the difference in elevation between the interpolated bed and actual subglacial topography. Subsequently, each bed topography was adapted with this function to map areas that are potentially higher or lower in elevation than the initial kriging predicts. As the input RES measurements are our closest estimate of bed topography the output adapted surfaces were treated with variable levels of confidence dependent on nearby input measurements. Area certainty was determined by plotting contours above sea level at the uncertainty scale and change in bed topography elevation within these contours could be reasonably assumed given the input observations. Contour elevations were determined as follows: SPRI 2000: 10 m (Dowdeswell et al., 2004), OIB: 30 m (depth RMSE reported in Bartlett et al., 2020), CAGE: 50 m (Young et al., 2017).

5.2.5 Surface and subglacial hypsometry

Subglacial hypsometry was quantified to assess the portion of subglacial topography currently below mean sea-level in the QEI. Establishment of how much ice grounded below sea-level is important for an assessment of the stability of the ice caps into the future (Van Wychen et al., 2016; Harcourt et al., 2020).

Expansive areas of ice grounded sub-sea-level will be susceptible to both oceanic and climate forcing. Nevertheless, enhanced retreated from oceanic forcing is only a factor where these areas are contiguous with the ocean and free from sills which inhibit access of warm deep waters to grounding lines (Schaffer et al., 2020). Additionally, the quantity of ice grounded within a few metres of current sea-level has the potential to be marine-terminating in the future if far-field sources of sea-level rise outpace the local lowering of sea-level (Hsu and Velicogna, 2018).

Additionally, high-resolution surface hypsometry was derived for each ice cap due to its importance for mass balance quantification (Colgan et al., 2015). Furthermore, hypsometry has been used to approximate glacier volume in regional assessments of sea-level rise contribution (Colgan et al., 2015; Zemp et al., 2019). Hence, quantification of this and its evolution can provide an alternative to sparse and interpolated measurements of ice thickness. Mean annual surface hypsometry was extracted for each ice cap using Google Earth Engine (Code in figure A5.1; Gorelick et al., 2017), which enabled the processing of all the ArcticDEM 2m resolution strips (5670 in total) which covered each ice cap from 2012 until 2017. Histograms of mean annual surface elevation were generated from each ice cap mosaic in Google Earth Engine, which determined the frequency distribution of surface elevation for each year from 2012 to 2017 for each ice cap (Code in figure A5.1). Total strip count for individual ice caps ranged from 61 for Devon in 2016 to 555 for North Ellesmere in 2015.

5.3 Results

5.3.1 QEI ice cap morphology

Ice cap wide subglacial topography for the three Ellesmere Island and two Axel Heiberg Island ice caps is mapped for the first time (Figure 5.3a). Additionally, bed topography for the Devon Island ice cap is updated with ice thickness measurements acquired since the survey conducted in 2000 by Dowdeswell and others, (2004). Uncertainty in subglacial topography was quantified using the Euclidean distance from an input error method, as this provided the lowest error estimates (figure 5.3). Furthermore, on average, the estimated error from the functions defined in figure 5.2a and 5.2b, RMSE = 165 ± 65 m, was found to be lower significantly lower than the standard predicted error given by the

interpolation, RMSE = 214 ± 37 m (paired t-test, p = 0). Estimated elevation differences were found to be high in comparison to ice thickness 11 ± 4%. As the DME functions derived in figure 5.2c and 5.2d exhibited high RMSE values and moving standard deviations, it was determined that the Euclidean distance estimated error was more suitable for quantifying uncertainty in the region. Additionally, the DME function could be used to estimate the sign of this error. From herein the uncertainty is treated in this way and where measurements have been taken, it is compared with and constrained by the RES instrument uncertainty.
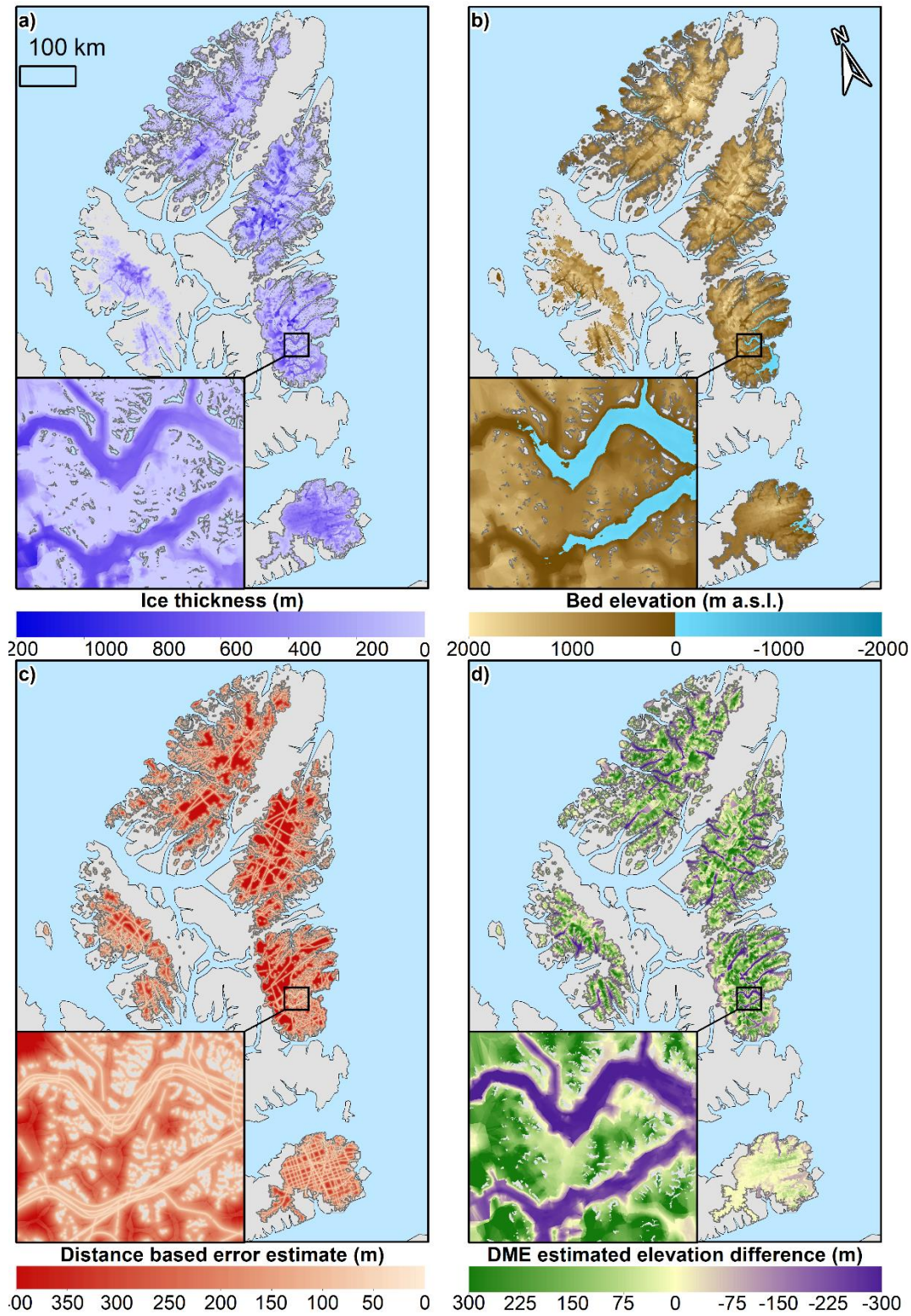
Figure 5.3. Interpolated bed topography and uncertainty maps. a) Kriged ice thickness for the QEI ice caps, the inset map highlights the Trinity-Wykeham outlet glacier basin. b) Kriged bed topography for QEI ice caps, c) Uncertainty in bed topography derived using the Euclidean distance error function in figure 5.2a for Devon and figure 5.2b for the remainder. d) DME function (figure 5.2c and 5.d) estimated elevation differences in bed topography across the QEI ice caps.

5.3.1.1 Ice cap volume

Ice volume across the QEI ice caps investigated approximated 20×10^3 km^3 of ice, which is roughly equivalent to 0.5 m of potential sea-level rise (Table 5.1). Agassiz Ice Cap is the most voluminous ice cap containing 5347 ± 264 km^3 of ice. Total volume reduced through POW, Devon, North Ellesmere, and Axel Heiberg contained the least amount of ice (Table 5.1). Lower volume was found for Devon ice cap than Dowdeswell and others, (2004). However, the previous estimate (4110 km^3) is within the range of uncertainty in table 5.1, hence, this does not represent a quantifiable decrease in volume. When estimated elevation differences were considered in areas where the difference was within CAGE uncertainty bounds ($\pm$ 50 m), ice cap volume in valleys was increased by 1745 ± 214 km^3 (Figure 5.3 and Table 5.1). Uncertainty in ice cap volume, the difference in volume from adjusting ice thickness by the Euclidean distance error (Figure 5.3b), was moderate at approximately 5%.

Table 5.1. Ice cap volumes. Original volume uncertainty is a function of the RMSE of thickness errors predicted by distance from input and the ice cap area. Estimated adapted volume is the total additional volume for an increase in bed depth within the CAGE RES uncertainty level, 50 m. Adapted uncertainty is a function of the RMSE of the probable mean differences in topography and ice cap area.

Ice cap	Volume		Estimated adapted depth within maximum RES uncertainty	
	km^3	SLRE (mm)	Km^3	SLRE (mm)
Agassiz	5347 ± 264	13.5 ± 0.7	$+ 260 \pm 237$	0.7 ± 0.6
Axel Heiberg	1955 ± 133	5.0 ± 0.3	$+ 130 \pm 127$	0.3 ± 0.3
Devon	4042 ± 74.3	10.2 ± 0.2	$+ 266 \pm 79$	0.6 ± 0.2
North Ellesmere	3721 ± 312	9.4 ± 0.8	$+ 576 \pm 320$	1.5 ± 0.8
Prince of Wales	4805 ± 219	12.2 ± 0.6	$+ 421 \pm 217$	1.5 ± 0.5
QEI total	**19869 ± 218**	**50.4 ± 0.6**	$+ 1745 \pm 214$	4.4 ± 0.5

5.3.1.2 Ice cap subglacial hypsometry

Approximately 3% of subglacial topography across the QEI ice caps is below sea-level (Figure 5.4). This area almost entirely consists of the beds of outlet glaciers, with the greatest percentage occurring beneath the POW icefield which

constitutes 52% of the total area below sea level. Less than 0.2% of the subglacial topography is lower than 200 m below sea level. Crucially, approximately 90% of this occurs beneath the POW ice field. Agassiz and North Ellesmere ice cap bed topography are higher than is typical for the region (Figure 5.4). Approximately half the ice in the region is grounded above 900 m across all ice caps. Yet, for Agassiz and North Ellesmere, 65% and 63% of the ice is grounded above this altitude respectively. Axel Heiberg bed topography roughly mimics the regional profile, however, 80% of Devon and 60% of POW subglacial topography is grounded below 900 m (Figure 5.4). This is further demonstrated in the hypsometric indices of the ice cap beds (Figure 5.4). Agassiz, Axel Heiberg, and North Ellesmere beds were typically equidimensional (-1.2 < HI < 1.2), whereas the Devon and POW beds, were bottom-heavy (1.2 < HI < 1.5).

The mean percentage area of ice grounded below sea level was 3.0 ± 2.6% (Figure 5.4). Only one percent of the ice across the Agassiz, Axel Heiberg, and North Ellesmere ice caps was found to be grounded below sea level. Conversely, area grounded below sea level totalled over four percent and seven percent for the Devon and POW ice caps respectively. The total area grounded below sea level for Devon Ice Cap is four percent lower than previously estimated by Dowdeswell and others, (2004). This likely arises from the adoption of a 50 m grid by our study opposed to the 1 km previously, in addition to differences resulting from different means of interpolation.
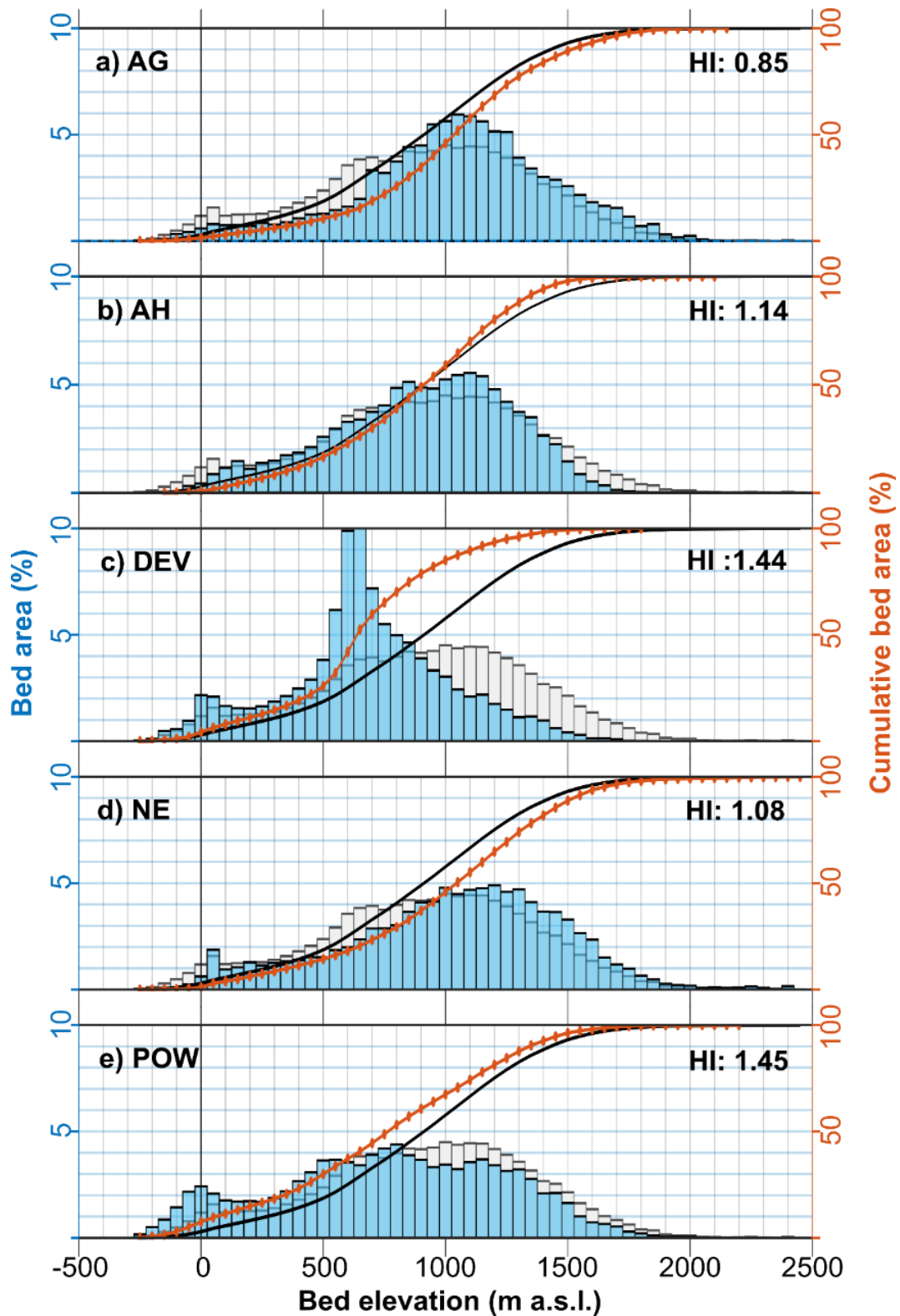
Figure 5.4. Subglacial hypsometry for QEI ice caps. Individual ice cap hypsometry (blue) is overlain on the combined hypsometry for subglacial topography in the region at 50 m intervals (grey). Combined (black) and individual ice cap cumulative bed area percentage (red) are plotted on the right-hand axis. a) Agassiz, b) Axel Heiberg ice caps, c) Devon, d) North Ellesmere, e) POW icefield.

After adapting the bed using the DME estimated elevation difference, area grounded below sea level within RES system uncertainty increased by ~4000 km^2 across all ice caps. Additionally, DME estimated elevation differences suggests a greater percentage of ice is likely grounded at higher elevations than observed for the original kriging (Figure 5.3c), resulting in steeper bed topography. Table 5.2 outlines the percentage increase in the area of ice grounded below sea-level after adaptation of the bed topography and revised totals when constrained with proximal RES measurements.

Table 5.2. Percentage increase in sub-sea level topography after estimate elevation difference in subglacial elevation is applied. Estimated area increase is equivalent to the area of elevation within the specified RES instruments depth uncertainty that coincides with an area deepening by the estimate elevation difference function.

Ice cap		Sub-sea level area increase	Estimated area increase within instrument uncertainty		
			SPRI 2000 (10 m)	OIB (30 m)	CAGE (50 m)
Agassiz	*Area %*	5.00	4.81	11.87	19.27
	100 km^2	8.37	0.40	0.99	1.61
Axel Heiberg	*Area %*	4.67	-	11.34	20.17
	100 km^2	4.83	-	0.55	0.97
Devon	*Area %*	3.12	16.81	42.12	64.67
	100 km^2	4.23	0.71	1.78	2.74
North Ellesmere	*Area %*	5.08	-	30.46	38.35
	100 km^2	12.8	-	3.90	4.91
Prince of Wales	*Area %*	5.60	9.42	23.17	34.84
	100 km^2	10.1	0.95	2.34	3.52
QEI total	**Area %**	**4.47**	**5.12**	**23.71**	**34.10**
	100 km^2	**40.33**	**2.07**	**9.56**	**13.75**

5.3.1.3 Ice cap surface hypsometry

Surface hypsometry for the three northernmost ice caps was relatively similar and exhibited little inter-annual variability in terms of percentage area change across elevations (Figure 5.5). Equally, at least 50% of surface elevations were above the equilibrium line altitude (ELA) estimated from Noël and others, (2018).

Conversely, Inter-annual variability was more pronounced for the Devon ice cap and particularly so for the POW icefield (spread of red lines Figure 5.5). Moreover, the majority of the surface of both ice caps is below the estimated ELA. For the Devon ice cap, 80 – 86% of the surface is below 1300 m for a given year (Figure 5.5). Additionally, 60 – 70% of the POW icefield surface is below 1100 m. No clear trend of increase or decrease of the area at lower or higher elevations was observed across the ice caps. Notably, a 4% increase in the surface area below 1300 m for the Devon ice cap than was reported for 2000 (Dowdeswell et al., 2004).

Hypsometric indices for surface topography of the ice caps somewhat mimics that of the subglacial topography (Figures 5.4 and 5.5). Agassiz and Axel Heiberg ice caps are roughly equidimensional. However, North Ellesmere and POW ice cap surfaces are typically bottom-heavy. Additionally, the Devon ice cap surface is very bottom-heavy (HI > 1.5).
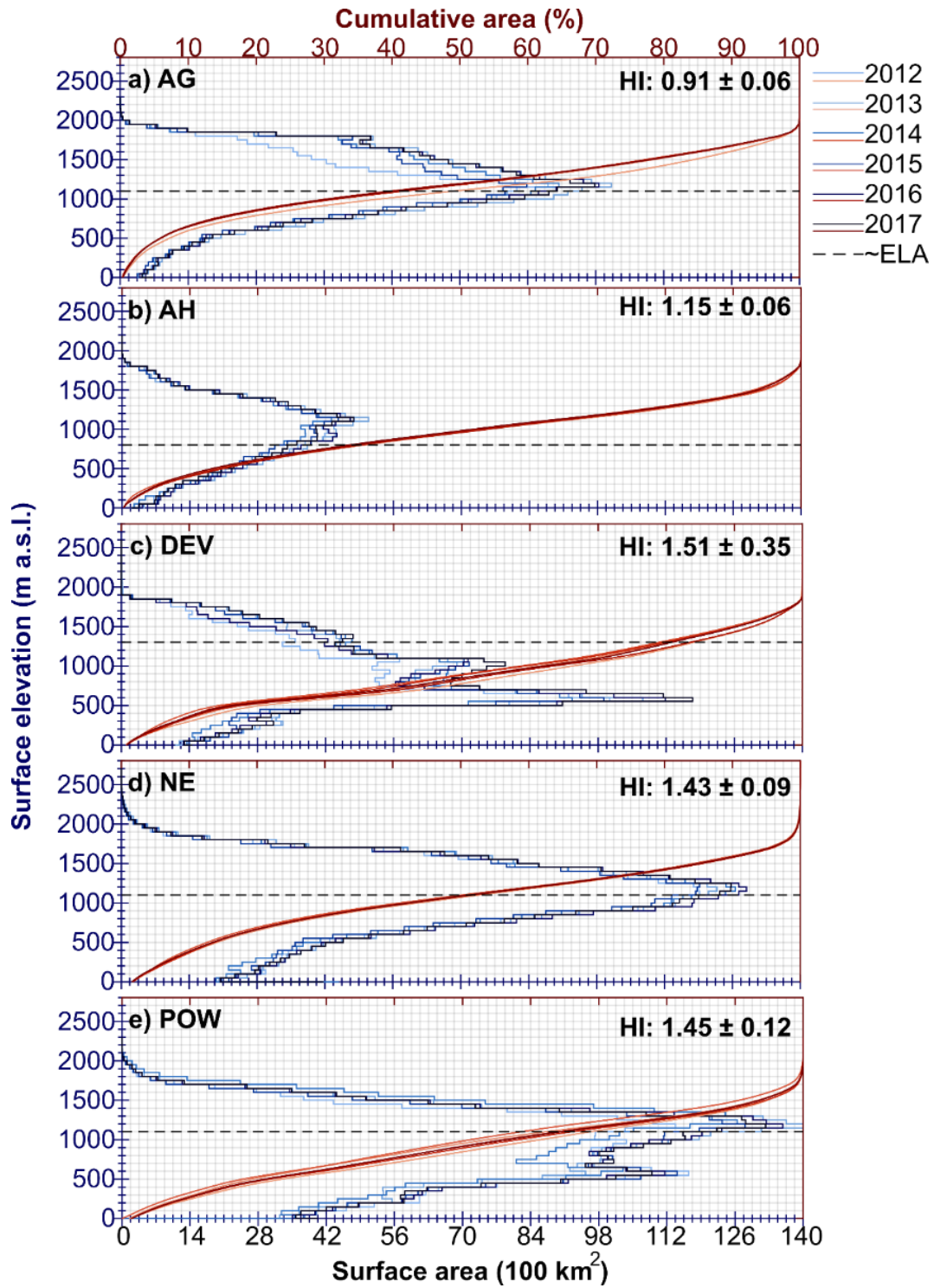
Figure 5.5. Mean annual surface hypsometry for QEI ice caps. Annual surface elevation distribution by area in shades of blue. The cumulative area as a percentage is plotted annually in shades of red. Black dashed lines depict the ELA estimated from Noël and others, (2018). a) Agassiz ice cap, b) Axel Heiberg ice caps, c) Devon ice cap, d) North Ellesmere ice caps, e) POW icefield.

5.3.2 CAA outlet glacier geometry

5.3.2.1 Centrelines

All ice caps exhibit multiple marine-terminating glaciers grounded below sea-level (Figure 5.3). While current levels of discharge through these are limited and exhibit high spatio-temporal variability, the significance of these outlets may increase in future if rising regional temperatures enhance local ice dynamics (Van Wychen et al., 2014). Original centreline length below sea-level ranged from 1 to 61 km. Additionally, when accounting for DME estimated elevation differences (Figure 5.3c) and RES uncertainty, increases in length were observed ranging from 0.1 to 43 km. These results suggest that all outlets are deeper in their upglacier portions than currently estimated, which results in an extension of the sub-sea-level topography into the ice cap interior for all major marine-terminating outlets (Figure 5.6). DME estimated elevation differences predict that sub-sea-level bed topography extends approximately twice as far into ice cap interiors than otherwise estimated (Table 5.3). However, this varied significantly between ice caps ranging from 49 – 178%, with high variability between individual glaciers. This is likely a consequence of different RES flight-line density along outlet centrelines, as bed topography of well-surveyed glaciers is better predicted than for sparsely surveyed ones (Figure 5.3b). This is particularly prevalent across the POW ice cap where the Trinity and Wykeham glaciers are far more densely surveyed than the northern outlets (Figures 5.1 and 5.7). Additionally, the lack of across-flow flight-lines limits the interpolation accuracy, as it cannot reliably recreate the steep elevation changes in bed geometry that occur in the cross-sectional direction (Gogineni et al 2014; Farinotti et al. 2013).
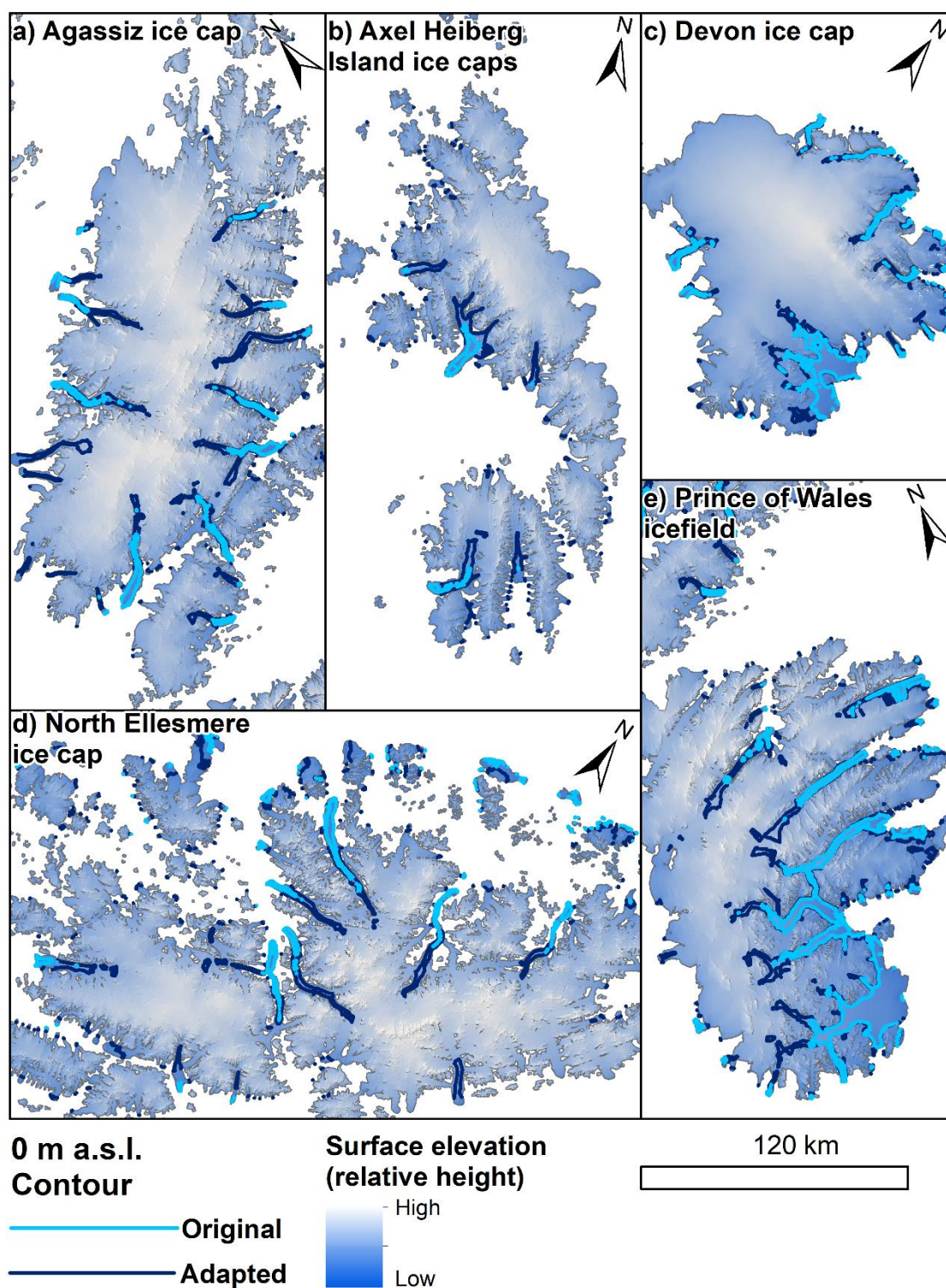
Figure 5.6 Original (cyan) and adapted (dark blue) bed topography sea level contours for CAA ice caps. a) Agassiz b) Axel Heiberg Islands c) Devon d) North Ellesmere e) POW.

Table 5.3. Sub-sea-level centreline length difference within RES instrument uncertainty.

| Ice cap | Mean centreline length percentage increase (*RES survey*) | | | DME estimated sea-level |
	SPRI	*OIB*	*CAGE*	
Agassiz	5.03 ± 8.08%	28.6 ± 47.0%	41.7 ± 58.5%	143 ± 195%
Axel Heiberg	1.42 ± 0.35%	6.42 ± 0.89%	19.7 ± 2.53%	49.5 ± 1.0%
Devon	6.36 ± 7.60%	14.3 ± 16.8%	26.8 ± 34.8%	47.1 ± 42.9%
North Ellesmere	6.44 ± 12.1%	23.6 ± 34.5%	52.3 ± 58.3%	156 ± 104%
POW	20.4 ± 54.8 %	40.8 ± 90.9%	56.6 ± 113%	178 ± 392%
All	7.93 ± 7.26%	23.7 ± 13.2%	39.4 ± 15.9%	114 ± 62.0%

Interpolation quality along centrelines was variable across ice caps and individual glaciers (Figure 5.7, Figure 5.8). Bed roughness, quantified here as the root-mean-square deviation (RMSD) in bed elevation over 1 km transects, was greatest across the Agassiz outlets (16 ± 26 m). However, standard deviations for all measurements overlapped. Unrealistic bed perturbations introduced by interpolations hamper numerical modelling of ice dynamics (Seroussi et al., 2011). Although currently dynamic discharge only constitutes ~10% of mass loss from the region, increased surface melt may lead to enhanced dynamics of major outlets if this additional melt is routed to the bed (Sundal et al., 2011). Furthermore, with the recent collapse of the Milne Ice Shelf, outlet glaciers on the northern margin of the North Ellesmere Ice Cap are subject to less buttressing and may accelerate in the future (WIRL, 2020). Modelling these potential changes to regional dynamics will therefore be important to make robust predictions of future mass loss from CAA ice caps. Mapped and quantified in figure 5.7 are regions where vertical bed perturbations greater than 10 m over a horizontal distance of 1 km exist. Hence, from this, an initial approximation of centreline quality can be assessed, before an analytical investigation is used to determine if the perturbations are real or interpolation artefacts. Uncertainty in bed elevation for modelling can be derived from the associated Euclidean distance error maps (Figure 5.3). Figure 5.8 depicts the centreline bed elevation for the major outlets

across the QEI ice caps. When RES uncertainty is accounted for sub-sea level bed topography extends significantly up glacier for these highlighted outlets (Figure 5.8).
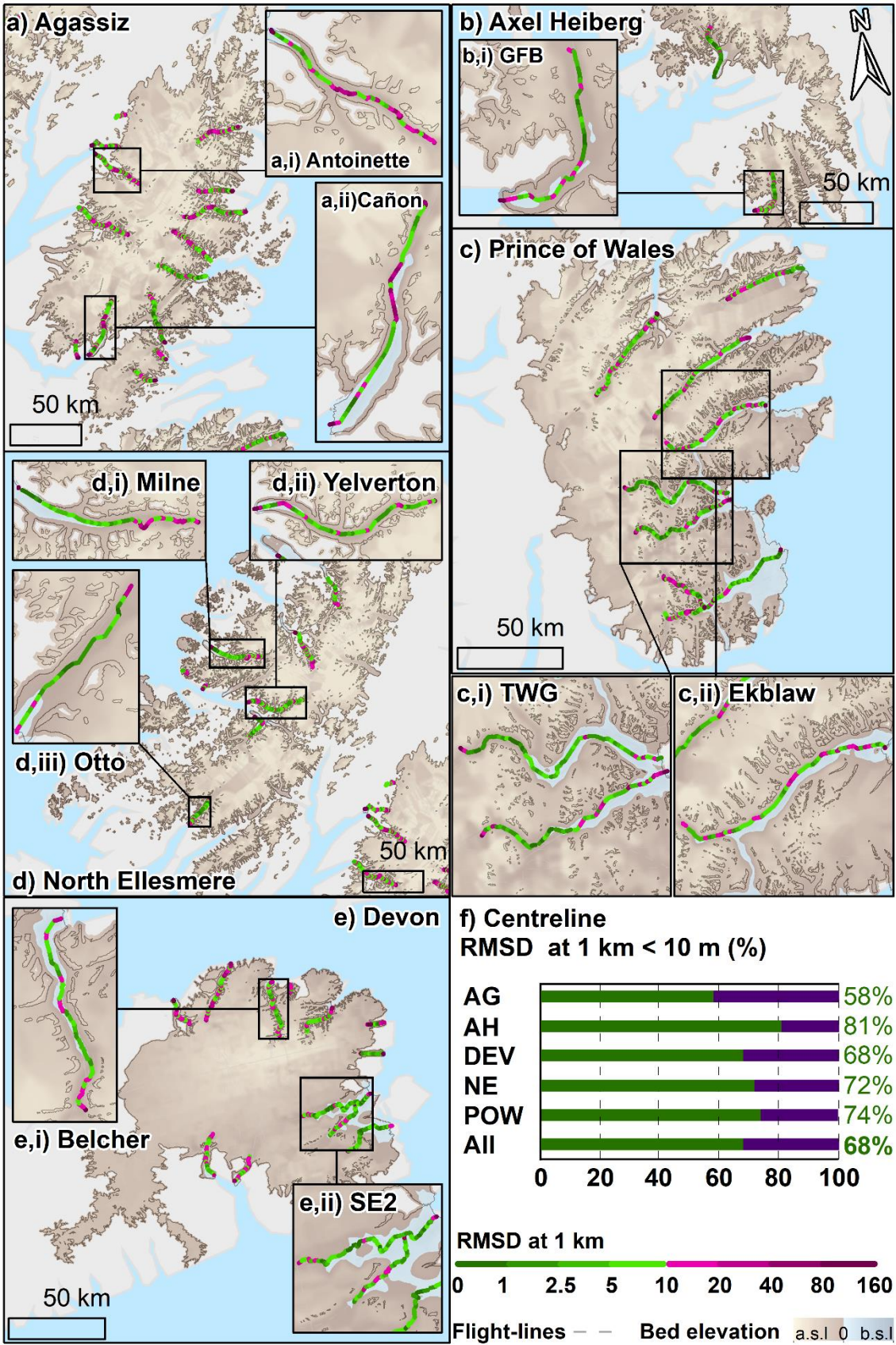
Figure 5.7. Approximated centreline quality for the QEI ice caps. RMSD at one kilometre for approximated centrelines (bed DEM minimum elevation trace), metre scale bed perturbations are highlighted in shades of green, perturbations tens of metres and greater in purple. a) Agassiz i) Antoinette ii) Cañon, b) Axel Heiberg i) Good Friday Bay (GFB), c) POW i) Trinity-Wykeham Glacier (TWG) ii) Ekblaw, d) North Ellesmere i) Milne ii) Yelverton iii) Otto, e) Devon i) Belcher ii) Southeast-2 (SE2). The deviation of some centrelines from the centre of the fjord highlights the influence of bed elevation errors introduced in the interpolation. f) Percentage of approximated centreline metre scale bed perturbations across the CAA.
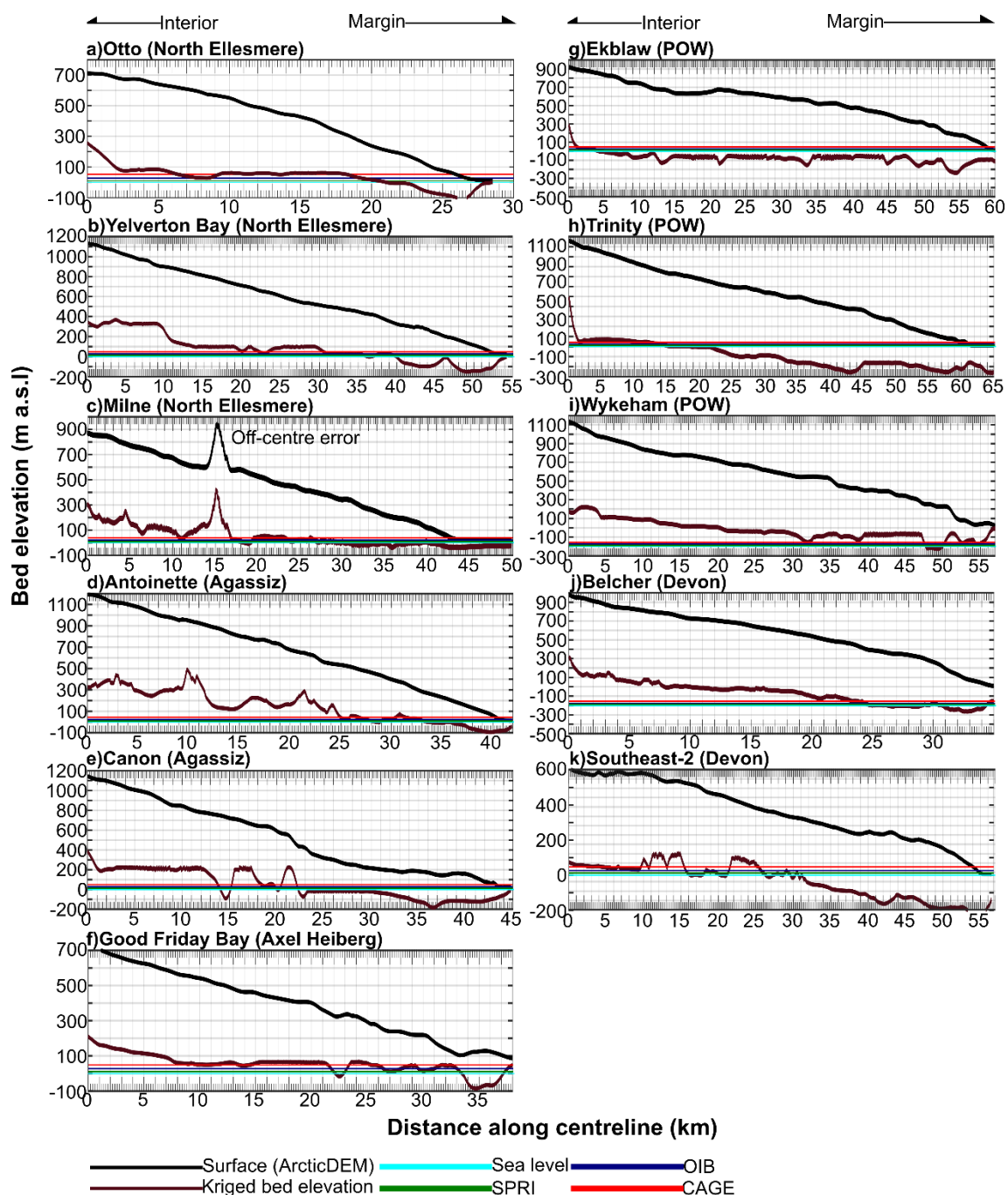
Figure 5.8 Centreline bed and surface elevation profiles for selected glaciers across the QEI ice caps (all remaining transects are compiled in figure A.5.2). RES sensor sea level uncertainty is highlighted as constant horizontal lines in the colours outlined in figure 5.1. a) Otto, b) Yelverton Bay, c) Milne d) Antoinette, e) Cañon, f) Good Friday Bay, g) Ekblaw, h) Trinity, i) Wykeham, j) Belcher, k) Southeast-2.

5.3.2.2 Cross sections for flux-gates

OIB flux gate cross-sectional area (CSA) increased by approximately 2% when corrected (coefficients in Table 3.4, Bartlett et al., 2020). Hence, minimum uncertainty in ice flux can be expected at a similar scale where OIB flight-lines are used as inputs to solid ice discharge calculations.

Table 5.4. OIB flux gate cross-sectional area difference from correction.

Ice Cap	CSA percentage difference
Agassiz	1.99 ± 0.04%
Axel Heiberg	N/A
Devon	1.90 ± 0.27%
North Ellesmere	1.96 ± 0.04%
POW	1.85 ± 0.20%
All	1.90 ± 0.22%

Where flux gates aren't flown, cross-sections across interpolated bed topography are often used where it has been generated (e.g. Enderlin et al., 2014). Minimum uncertainty in kriged flux gates was quantified where they coincide with RES measurements. High variability was found in the difference between RES and kriged flux gate CSA (Table 5.5). At a minimum, kriged flux gates are ~1% different from those measured by a RES survey but can vary as much as 57%. However, the typical difference, and hence the mean minimum kriged CSA uncertainty, was 1.7 ± 20%. As no trend was found towards under or overestimation the mean absolute uncertainty was 14 ± 14%.

For the CAA, an approximation of valley cross-section from centreline measurements has previously been conducted (Van Wychen et al., 2014; Van Wychen et al., 2016). Taking the centreline measurement as the maximum depth, the cross-profile depth of the glacier is estimated using a parabolic function

(equation 3 in Van Wychen et al., 2016). Compared with flux gates drawn from kriged bed topography, no discernible trend was observed towards either over or underestimation (Table 5.5). Furthermore, increased variability was observed. Mean absolute difference between the methods was found to be 23 ± 21%.

Table 5.5. Uncertainty for flux gates derived over kriged bed topography for QEI ice caps. RES method is the kriged flux gate minus the CSA of a RES survey flux gate flight-line. Centreline (CL) method is the kriged flux gate minus the U-shape interpolated flux gate using the centreline depth following Van Wychen and others, (2016).

Ice Cap (*Method*)		Mean percentage difference in CSA (*RES instrument*)		
		SPRI 2000	*OIB*	*CAGE*
AG	*RES*	-	-10.3 ± 3.60%	-
	CL	-4.02 ± 15.3%	-11.5 ± 16.5%	13.1 ± 23.9%
AH	*RES*	-	-	-
	CL	-	-20.2 ± 2.32%	-5.71%
DEV	*RES*	-	-7.73 ± 9.94%	-
	CL	-3.43 ± 23.0%	-33.7 ± 8.40%	13.3 ± 32.5%
NE	*RES*	-	1.69%	-
	CL	-	-21.1 ± 10.1%	-2.67%
POW	*RES*	22.3 ± 1.86%	7.49 ± 25.1%	29.3 ± 27.4%
	CL	-8.12 ± 20.8%	-13.5 ± 46.5%	-8.46 ± 22.2%
All	***RES***	**22.3 ± 1.86%**	**-4.35 ± 15.3%**	**29.3 ± 27.4%**
	CL	**-5.45 ± 20.0%**	**-18.8 ± 31.4%**	**1.67 ± 30.0%**

5.4 Discussion

5.4.1 Total potential sea-level rise contribution

Adjusting for 3% cumulative area below sea-level, a potential contribution to GMSL of 48.8 mm was found for the QEI ice caps investigated here. This approximates to the lower bounds of the latest consensus on glacier volume in

the region, 64.8 ± 16.8 mm (Farinotti et al, 2019). Albeit, not all of the glaciers on the QEI were investigated here, only those with extensive RES measurements. Hence, these results suggest that were the remaining QEI glaciers included the total volume would likely be in line with the consensus estimate. Furthermore, a 9% increase in volume was estimated when ice thickness is adjusted to account for interpolation uncertainty. Consequently, the total SLC of the QEI could be higher by 4.4 ± 0.5 mm. However, this is lessened, as most of the depth increased volume is across areas of ice grounded below sea-level (Figure 5.3a and c).

5.4.2 CAA ice cap stability

From the full quantification of subglacial and supraglacial hypsometry of the QEI ice caps, their sensitivity to atmospheric and oceanic forcing can be assessed.

The Agassiz ice cap is likely the least sensitive to changes in ice dynamic mass loss as it is predominantly grounded at high elevation with respect to the regional distribution of ice (Figure 5.4a). Furthermore, its marine-terminating outlets have been observed to be slowing down (Van Wychen et al., 2018; Millan et al., 2017). Consequently, the discharge has decreased 60% over the past two decades. Minimal subglacial topography (<1%) is within a few metres of sea-level and so the ice cap will remain largely uncoupled from the ocean into the future, as marine-terminating retreat rates remain modest in comparison to the southern Ellesmere Island ice caps (Cook et al., 2019).

Axel Heiberg Island ice caps are similarly grounded well above sea-level (Figure 5.4b). Supraglacial hypsometry is not as top-heavy as the Agassiz ice cap but remains roughly equidimensional, buffering it to regional warming (Noël et al., 2018). While currently, ice discharge is low at 0.05 GT yr^{-1}, the removal of buttressing sea ice in the fjords of its major outlet glaciers could result in a significant increase in output from the ice caps (Cook et al., 2019). Approximately 2% of subglacial elevation is within sea-level plus the RES uncertainty (from 10 – 50 m a.s.l.). As such, potential exists for the ice caps to be subject to enhanced retreat. However, one major outlet, the Good Friday Glacier, has been observed to be advancing for the past 70 years (Medrzycka et al., 2019).

North Ellesmere Island ice cap currently contributes minorly to regional dynamic discharge as floating ice tongues and sea ice buttress marine-terminating glaciers along its northern margins (White and Copland, 2018; Cook et al., 2019).

Although currently, the accumulation and ablation areas are approximately equal (Figure 5.5d), the bottom-heavy configuration of the ice cap surface makes it susceptible to enhanced ablation (McGrath et al., 2017). With the removal of the buttressing ice tongues, which have already decreased some 42% since 1999 (White and Copland, 2018), the northern margin of the ice cap becomes susceptible to enhanced retreat and dynamic mass loss. Importantly, 3% of the ice cap bed is at sea-level and within the RES uncertainty. Additionally, mean sub-sea-level centreline length was consistently found to be increased and larger than the uncertainty for the region (Table 5.3, Figure 5.7, Figure 5.8). This suggests that the North Ellesmere icefield may be highly susceptible to the onset of enhanced retreat that has been observed elsewhere in the region (Cook et al., 2019; Harcourt et al., 2020).

The Devon and POW ice caps which contribute the most in terms of dynamic mass loss, 61% (Van Wychen et al., 2016; Van Wychen et al., 2017), have extensive sub-sea level topography and are largely grounded well below the regional average bed elevation (Figure 5.4). Importantly, the Trinity and Wykeham outlet glaciers which drain the POW icefield were estimated to be significantly deeper in their upglacier portions than previously estimated. Maximum possible centreline extent of sub-sea level topography was found to be 17 km longer for Trinity and 20 km for Wykeham, presenting a 31% and 51% increase respectively. Crucially, these glaciers contribute ~67% of dynamic mass loss from the entire region (Van Wychen et al., 2016). Moreover, they have been observed to retreat faster than the average rate for glaciers in the region, having retreated ~ 5 km over the past fifty years (Cook et al., 2019). Therefore, with extended sub-sea-level topography, enhanced discharge may be facilitated at these glaciers far into the future (Cook et al., 2019). This indicates that the POW icefield is particularly sensitive to dynamic mass loss and will likely continue to be the dominant source of solid ice discharge in the region (Figure 5.8).

5.4.2 Implications for mass-balance quantification across QEI ice caps

A lack of flux-gate RES flight-lines exists for the QEI ice caps, only ~50% of outlets are surveyed orthogonally (Van Wychen et al., 2016). Therefore, solid ice discharge in the region has been derived in part from interpolated outlet glacier cross-sections which underestimate CSA by ~ 12% (Van Wychen et al., 2014). Flux gates drawn from kriged bed topography vary significantly in CSA to those

directly measured, -4 – 30%, and those derived from U-shape interpolation, -4 – 15%. Such high variability limits the use of kriged flux gates for quantifying the dynamic output of glaciers in the region. However, when OIB flux gates are corrected for underestimation bias, CSA and consequently discharge estimates increase 2% (Figure 5.9.) This increases cumulative solid ice discharge in the region from 2000 to 2015 by 0.15 GT. Moreover, a 2% increase in the most recent rate of discharge constitutes an additional 0.05 GT yr^{-1} for 2014 – 2015 (Van Wychen et al., 2016). Although this represents a modest difference, with increased dynamic output this correspondingly represents increased additional mass loss.
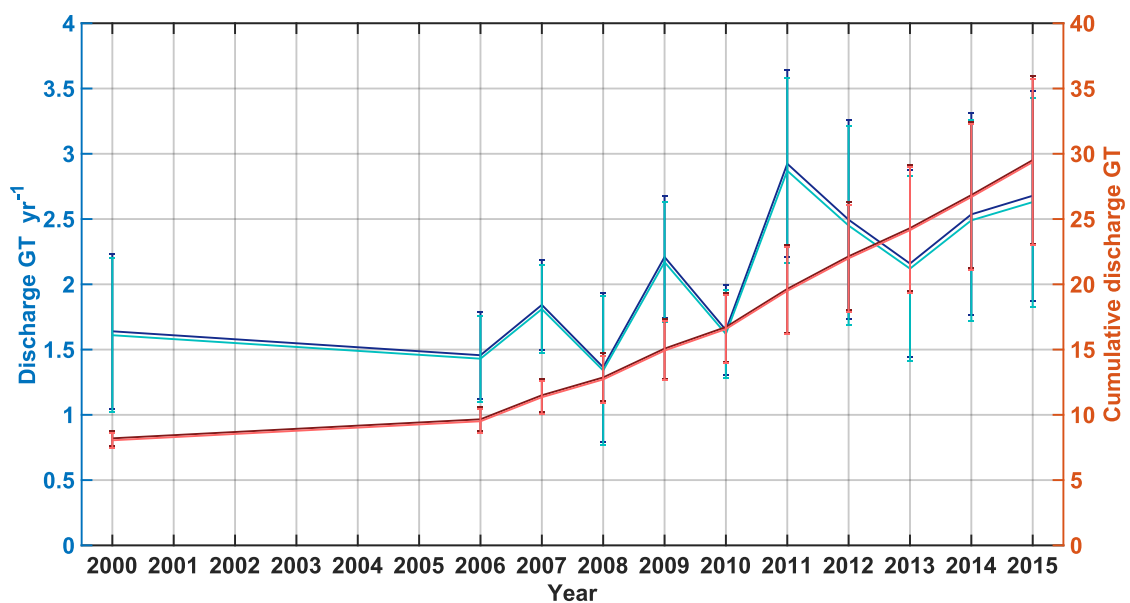
Figure 5.9 Adjusted rates and total solid ice discharge for the QEI ice caps, originally estimated by Van Wychen et al., 2016 and Van Wychen et al., 2017. Darker lines show adjusted flux gate values with lighter lines illustrating the original data. Blues show rates and reds total discharge.

5.5 Conclusions

Presented here is the first ice cap wide, 3D mapping of bed topography across the Agassiz, Axel Heiberg Islands, North Ellesmere, and Prince of Wales ice caps, using all ice thickness measurements collected to date. Additionally, an improved bed topography dataset was generated for the Devon Island ice cap (Dowdeswell et al., 2004). Through the addition of full surface morphometry for each ice cap at 50 m resolution, this study comprises the highest resolution

quantification of the full 3D morphology of the Agassiz, Axel Heiberg, Devon, North Ellesmere, and POW ice caps.

Large areas of the POW icefield and Devon ice cap are grounded below sea level, predominantly beneath highly dynamic outlet glaciers (Van Wychen et al., 2016). Our analysis shows that a further $4.7 \pm 0.84\%$ of the ice caps may also be grounded below sea level, which has implications for their perceived stability. Conversely, Agassiz and Axel Heiberg Island ice caps are predominantly grounded at higher elevations so are likely less sensitive to ice dynamic influenced mass balance. Nevertheless, a ~1% expansion of sub-sea level topography across outlet glaciers for these ice caps was found within the RES sensor uncertainty bounds. Additionally, while the Agassiz and Axel Heiberg ice cap surfaces are largely equidimensional and may buffer against regional mass loss in the current century (Noël et al., 2018), the other three ice caps are bottom-heavy and as such more susceptible to enhanced melting with increased regional warming. Notably, the subglacial and supraglacial configuration of the North Ellesmere ice cap makes it susceptible to enhanced retreat with increased warming and removal of buttressing from floating ice tongues (White and Copland, 2018).

It was found that marine-terminating outlet glacier beds may be grounded below sea-level up to an additional $33 \pm 13\%$ when RES sensor uncertainty and the likely overestimation of bottom elevation is accounted for. Consequently, deepening of the bed further into ice cap interiors increases outlet susceptibility to the onset of dynamic thinning, which has been observed in the region (Van Wychen et al., 2016; Harcourt et al., 2020). Nevertheless, surface melt remains the dominant source (~90%) of mass loss in the region (Millan et al., 2017). Additionally, meltwater runoff is likely to remain the largest component of the regional mass loss in the future as local air temperature continues to rise at twice the global average (Overland et al., 2016). Correction of OIB flux gates results in a systematic increase in cross-sectional area of $2 \pm 0.2\%$ (Bartlett et al., 2020). Hence, the dynamic output from the QEI ice caps investigated is underestimated by at least this amount. Flux gates drawn from kriged bed topography are exceedingly variable ($\sigma \sim 20\%$) in their geometry and therefore unsuitable for use in estimating solid ice discharge. However, large and potentially erroneous centreline bed perturbations are limited over extended portions of kriged outlet

glacier topography. Hence, these datasets have the potential to be used in numerical models.

Inputting combined ice margin ArcticDEM elevations and bed elevation estimates from radio-echo sounding surveys into kriging was found to reduce the RMSE in the output interpolated surface. This contrasts with the traditional method of inputting ice thickness with a zero value at the margin (e.g. Bamber et al., 2013). Furthermore, by combining the cloud-based computational capacity of Google Earth Engine, and the entire collection of ArcticDEM strips this study was able to monitor Arctic ice cap hypsometry change at previously unachievable spatial-temporal resolution. These findings may lead the way to improve quantifications of ice mass subglacial and supraglacial geometry across the Arctic.

Chapter 6: Synthesis

6.1 Introduction

This thesis has explored the potential for using high-resolution elevation data as a pseudo-validation tool in the absence of validated measurements of ice thickness and subglacial topography. Previously, uncertainty in ice thickness and bed topography measurements and interpolations has been broadly approximated (Lapazaran et al., 2016). Measurements are prescribed an uncertainty that parameterises roughly the effects of scattering and attenuation from the various facets of an ice sheet environment (Paden et al., 2010). Whereas, interpolations use simple inverse distance derived estimates of error (Bamber et al., 2001). Subsequently, the accuracy of subglacial topography derived from these measurements and interpolations is somewhat limited. Presented in this thesis are robust alternatives for quantifying, and where possible reducing uncertainty in subglacial topography data, obviating the need for logistically challenging and expensive field measurements. However, aerogeophysical measurements remain the most efficient, cost-effective, and reliable way of measuring ice-mass thickness, bed topography, englacial layers, and bed conditions at scale (Schroder et al., 2020). Additionally, repeat flights are required for quantifying change and improving confidence in measurements (Schroder et al., 2020). In the substantive results chapters, instrumental airborne ice thickness measurement error is fully quantified (chapter three), and subsequently propagated through to the interpolation of ice mass wide bed topography (chapter four). From this, potential methods for reduction of these uncertainties are posed and tested (chapters three, four, and five). In chapter three a synthetic RES dataset has been developed which can be used to correct RES measurements of ice thickness and bed topography. In chapter four, these synthetic measurements were interpolated, subsequently, error in the interpolated surface was quantified, lastly, methods were developed which reduced the uncertainty and estimated where and by how much the interpolated elevation should be adjusted. Finally, in chapter five, the full bed topography for five ice caps in the Canadian Arctic was derived for the first time and improved for the Devon Island ice cap. These interpolations were accompanied by uncertainty maps and adjustments made in line with the methods developed in chapters three and four.

In this chapter, the findings of this thesis are synthesised, and the implications for improved quantification of bed topography and the analysis drawn from such datasets are assessed in section 6.2. Wider implications of this work primarily concern the quantity and rate of sea-level change from the investigated ice masses, these implications are highlighted in section 6.3. The chapter concludes with an assessment of the limitations of this thesis in section 6.4.

6.2 Synthesis

6.2.1 Linking proglacial and subglacial topography

The overarching concept of this thesis is based on is the utilisation of high accuracy elevation data from previously glaciated landscapes for quantifying uncertainty in estimates of subglacial topography. It has been shown in this work that uncertainties in subglacial elevation can be reduced by stimulating the acquisition and interpolation of ice thickness measurements. Admittedly, it will remain logistically challenging to validate measurements so the methods presented here are at best pseudo-validation techniques. Nevertheless, the abundance of observations made by this work provides strong support for the efficacy of these methods. Over 2.5 million RES measurements were simulated in chapter three, and over 1.5 million sample points were used in chapter four to establish the revised distance and DME error functions. In chapter five these methods were both applied to provide fully quantified uncertainty for ice cap bed topography for the first time.

6.2.1.2 Potential for uncertainty reduction in bed topography datasets

OIB flew more than 1000 missions and over 600 publications have been written using the data collected (NASA, 2019). Hence, the findings of this thesis regarding the correction of OIB gathered ice thickness data where the MCoRDS instrument was employed, constitute a significant contribution when this data and these analyses are further investigated. Although, OIB was completed in 2019 future RES surveys will likely be conducted over ice masses and this thesis provides the means for quantifying uncertainty in any survey measurements (corrections in chapter three), information for developing flight plans where flight-line density is important for the scientific output of the survey (chapter four), and methods for determining the uncertainty in interpolated bed products where kriging is used (chapters four and five).

Due to its widespread availability and efficiency kriging continues to be widely used to interpolate ice mass bed topography (Jezek et al., 2013; Bamber et al., 2013). As mentioned in prior chapters many ice dynamic models use kriged bed topography as an input. For these models to provide accurate projections, the input topography has to be accurate and of high resolution (Durand et al., 2011). Presented in this thesis are the means for quantifying and reducing uncertainty in kriged bed topography with respect to previous datasets (Bamber et al., 2013; Fretwell et al., 2013; Morlighem et al., 2017). The revised Euclidean distance error functions provide a first-order estimate of uncertainty that is significantly reduced with regard to previous datasets, particularly at distances exceeding 1500 m from an observation. To estimate the magnitude and sign of elevation error in kriged bed topography, the DME function, can be applied with 99% confidence in improvement, in areas where flight-line density is less than 0.14 lines km^{-2}. Figure 6.1 outlines the area suitable for improvement with the DME function and applicable datasets. Fundamentally, DME estimated uncertainty, and indeed the Euclidean distance uncertainty estimates presented in this work do not have to be used as alternatives to existing bed topography datasets they may be combined to create an ice mass wide best estimate of bed topography.
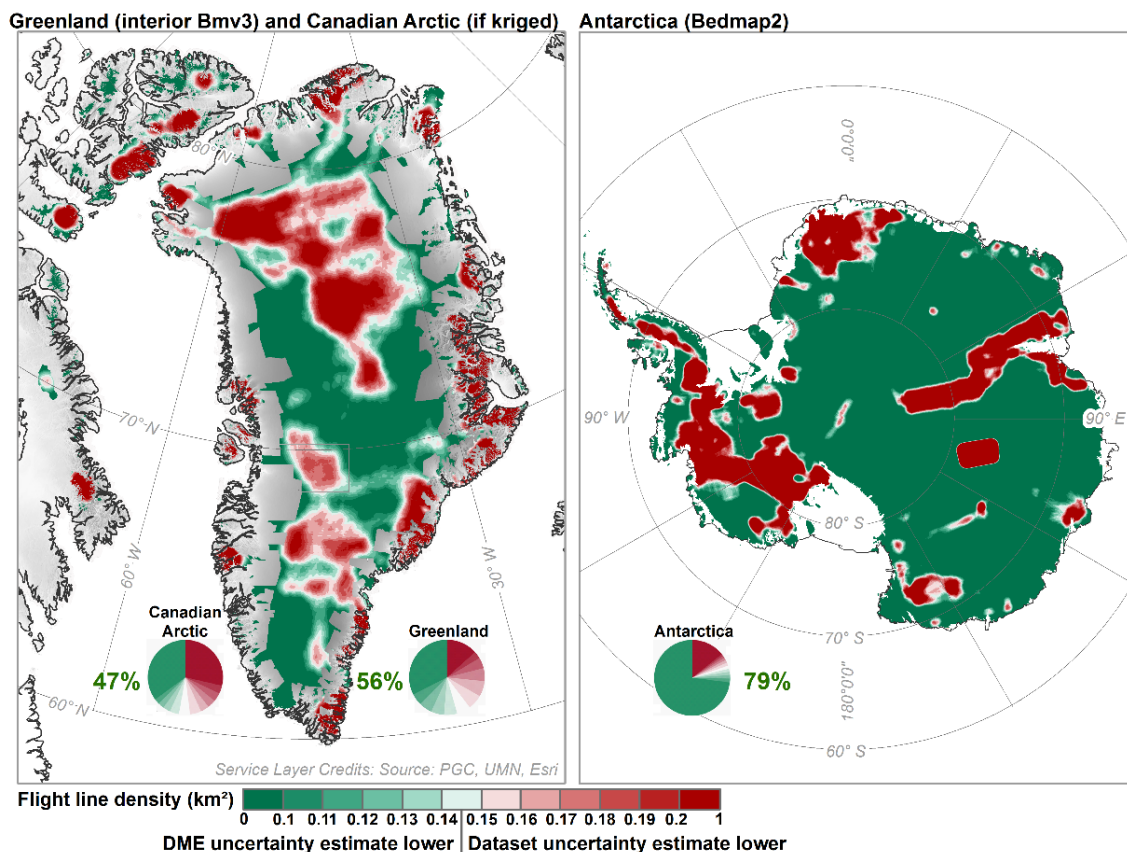
Figure 6.1 Potential for application of the DME-error function to kriged bed topography datasets. Green colouration highlights regions where the DME method can be applied efficaciously. Red shows where the dataset uncertainty will be lower than the DME estimated value. The pie charts quantify the area of improvement as a percentage.

6.2.1.2 Application to Antarctic bed topography

Due to the absence of expansive proglacial areas proximal to the Antarctic Ice Sheet, there are limited suitable training sites to implement the synthetic RES simulation and interpolation approach developed in this thesis. However, assuming similar landscapes occur beneath the Antarctic Ice Sheet as sampled for the development of the methods in this thesis, Bedmap2 topography can be adjusted similarly to Greenland (chapter 4) and the CAA (chapter 5) (Fretwell et al., 2013). Although the Bedmap2 dataset has been superseded by BedMachine Antarctica (Morlighem et al., 2020), it is still widely used in ice sheet models and previous work (Nowicki et al., 2016; Goelzer et al., 2018; Barthel et al., 2020), so a requirement exists for investigating uncertainty in the dataset.

Application of the DME estimated elevation difference results in a mean deepening of the Antarctic bed by 8 ± 58 m. Significant portions of large outlet glaciers and ice streams are deepened with adjoining upland areas elevated (figure 6.2). Areas of estimated improvement are reduced in comparison to the prediction in figure 6.1. However, these are conservative estimates of uncertainty for the two methods compared with the standard uncertainty reported by Bedmap2 (figure 6.2 d-l, 1σ in Bedmap2). Notably, 34% of the DME predicted elevation difference is within the Bedmachine Antarctica elevation ± 1/4 σ (σ = 1 standard deviation, from BedMachine Antarctica uncertainty), and 60% within ± 1 σ (Morlighem et al., 2020). As mass conservation generated bed topography is increasingly used as the *de facto* bed, this highlights the value of applying the DME elevation difference estimate to kriged bed datasets as an efficient alternative for dynamic ice sheet models. Furthermore, as highlighted in figure 6.2 b) and c), even in areas of estimated increased uncertainty the estimated elevation difference is comparable to the Bedmachine estimate. Hence, application of the DME method may reduce uncertainty in bedrock for dynamic ice sheet models and provide better quantifications of sea-level (Sun et al., 2014).

164

Nevertheless, any artefacts in the bed topography remain which limits the accuracy of the adjusted bed (Goff et al., 2014; Sun et al., 2014).
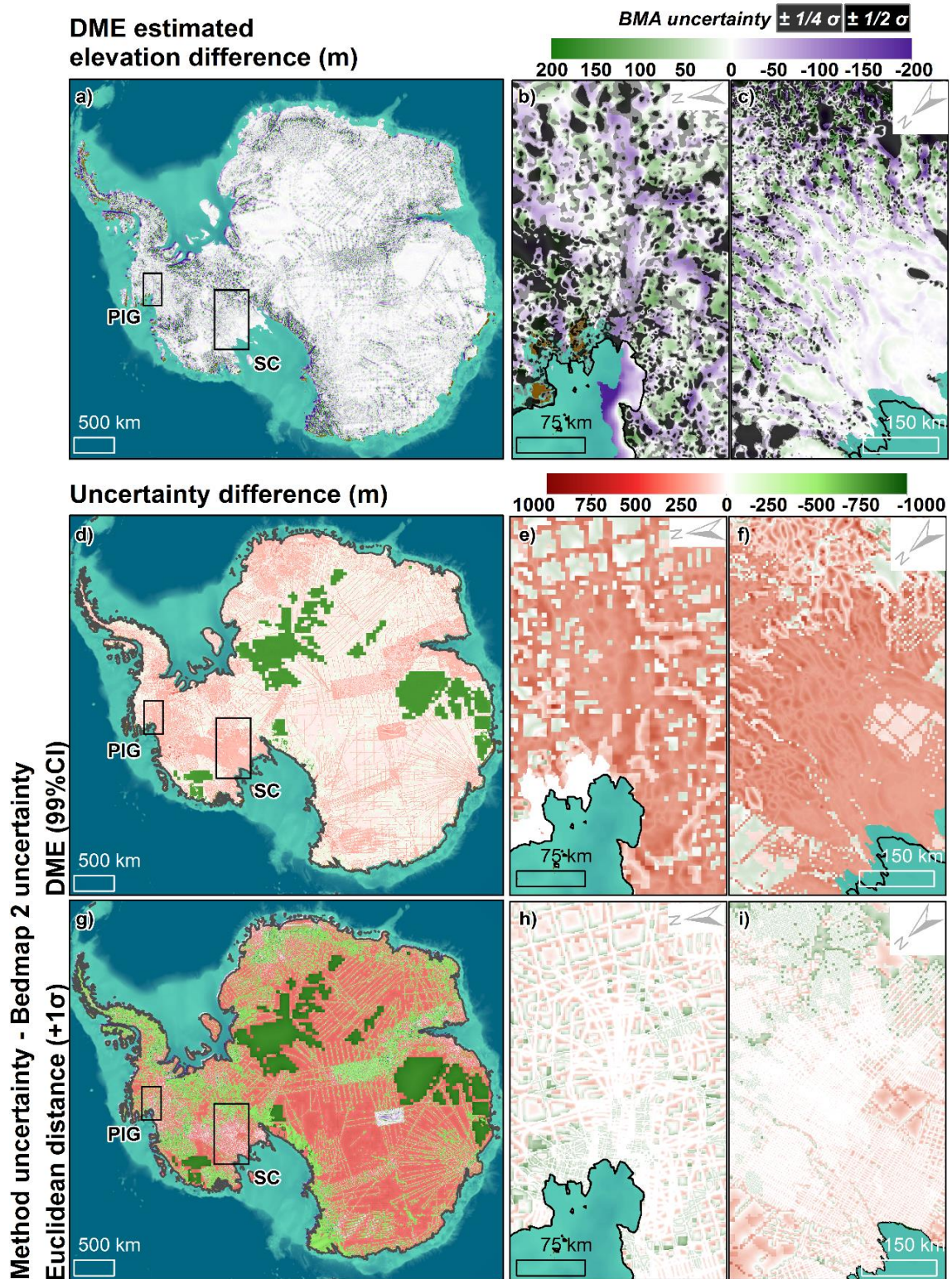
Figure 6.2. Application of the methods developed in this thesis to Bedmap 2 (Fretwell et al., 2013). DME estimated elevation difference is shown for a) Antarctica, b) Pine Island Glacier (PIG) and c) Siple Coast ice streams E, D and C. Where the DME estimated elevation difference is clearly visible it is within a ¼

165

σ of Bedmachine Antarctica's uncertainty (Morlighem et al., 2020), grey shades show increases labelled in the legend. The difference in uncertainty for DME estimated elevation 99% confidence interval and Bedmap2 uncertainty is shown for the above locations in d), e), and f). Similarly, the difference of Euclidean distance uncertainty plus one σ from Bedmap2 uncertainty is shown in g), h), and i).

6.2.2 Underestimation of subglacial relief

As stated previously, this work has implications for assessments of the ice dynamical output component of sea-level change projections. Significantly, ice dynamical output is the largest uncertainty when projecting future sea-level contribution from ice sheets (Shepherd and Nowicki, 2017; Oppenheimer et al., 2019). Where ice discharge is measured using RES survey flux gate flight lines, ice flux, and subsequently, discharge is typically underestimated by 3 ± 18% in addition to uncertainties arising from the RES system, data processing, and selected bed picking procedure (Lapazaran et al., 2016; Bartlett et al., 2020). Moreover, where flux gates are derived from cross-sections of interpolated bed topography, uncertainty rises considerably (-4% – 30%). Finally, bed topography generated by mass conservation is primarily derived from flux-gate flight-lines (Morlighem et al., 2011). Therefore, the uncertainties identified and quantified here constitute the minimum error in mass conservation and are propagated and exacerbated the further down glacier from the input (Millan et al., 2018). Consequently, estimates of ice dynamical contribution to sea-level rise likely underestimate the output of major outlet glaciers, even when mass conservation bed topography is used.

6.2.3 Underestimation of dynamic mass balance

Large outlet glacier cross-sectional area (CSA) was found to be underestimated by 3 ± 18% in chapter 3. In chapter five, after applying the CSA correction developed in chapter 3 (table 3.4), CSA was increased by 2 ± 0.2% for CAA ice cap outlets. Consequently, estimates of solid ice discharge through these outlet glaciers is underestimated when flux-gate flight lines are used to quantify the thickness component of discharge. This is compounded by further underestimation of outlet glacier bed relief when flux-gates are sampled from interpolated bed topography, as shown in chapters four (1 ± 1%, with a 7 ± 20%

depth increase) and five (1.9 ± 0.2%). To quantify the probability of the mean underestimation in solid ice discharge and the overall change in uncertainty added by the large standard deviation around this, solid ice discharge estimates from the latest studies of the continental ice sheets were adjusted through Monte Carlo simulation (Rignot et al., 2018 for Antarctica; Mankoff et al., 2019 for Greenland). Each discharge measurement was adjusted by a random percentage generated from the distribution of cross-sectional area error identified in chapter 3, the descriptive statistics of which are shown in table 6.1. This was conducted 10,000 times for each discharge estimate, the mean and root-mean-square error for these simulations are plotted in figures 6.3 and 6.4.

Table 6.1. Descriptive statistics for random flux-gate uncertainty assessment. n is the number of simulations, *μ is the mean, σ is standard deviations, γ is the skewness and κ kurtosis.*

n	*μ*	*σ*	*γ*	*κ*
10000	3	18	2	29

As all ice thickness measurements from which discharge is estimated are either directly from RES surveys or data products interpolated from them. The initial outlet glacier cross-sectional area error is the minimum uncertainty in discharge measurements. Hence, quantifying the impact this has on estimates of discharge gives a first-order estimate of how erroneous discharge estimates are.

Greenland solid ice discharge was simulated to be higher than the reported estimate for 52% of simulations. Uncertainty in the discharge estimate was on average 2.0 ± 0.4 times greater than originally reported (figure 6.3). Importantly, this was greater for regions with higher discharge (figure 6.3). Mean increase in discharge by 3% was found to be within the original uncertainty bounds (Mankoff et al., 2019). Nevertheless, when applied to the cumulative solid ice discharge from the Greenland Ice Sheet, the total mass lost increases by ~630 GT or 2 mm SLE.

Antarctic solid ice discharge, from regions where it is derived from RES data, was found to be higher than the reported estimate for 52% of simulations. Uncertainty ranges overlapped but the simulated mean solid ice discharge was always greater than the observed. For the Antarctic Peninsula and East Antarctica,

simulated mean solid ice discharge was greater than the Rignot et al., (2018) amount plus one standard deviation. Hence, there is greater confidence that discharge from these glaciers is underestimated. Nevertheless, uncertainty was typically 2.4 ± 1.1 times greater when the standard deviation of flux-gate cross-sectional area was accounted for. This suggests that uncertainty is under quantified in estimates of ice discharge. Applied to the estimated discharge for the regions in figure 6.4 total mass lost increases by ~150 GT or 0.4 mm SLE.
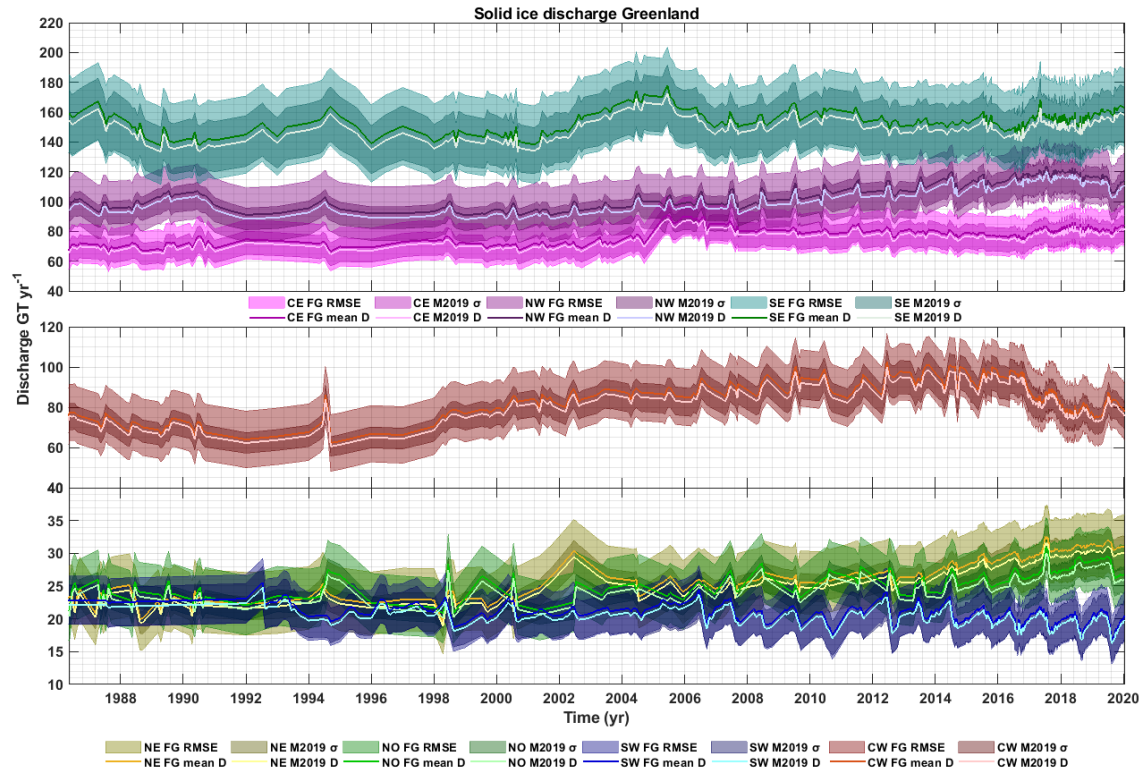
Figure 6.3 Monte Carlo simulated uncertainty of regional Greenland solid ice discharge (region notation follows Mankoff et al., 2019). Brighter lines and darker patches represent the Mankoff et al., (2019) estimates of ice discharge and the uncertainty in the estimates respectively (M2019). Darker lines and lighter patches represent the simulated mean discharge and uncertainty respectively. Data is from Mankoff et al., (2019).
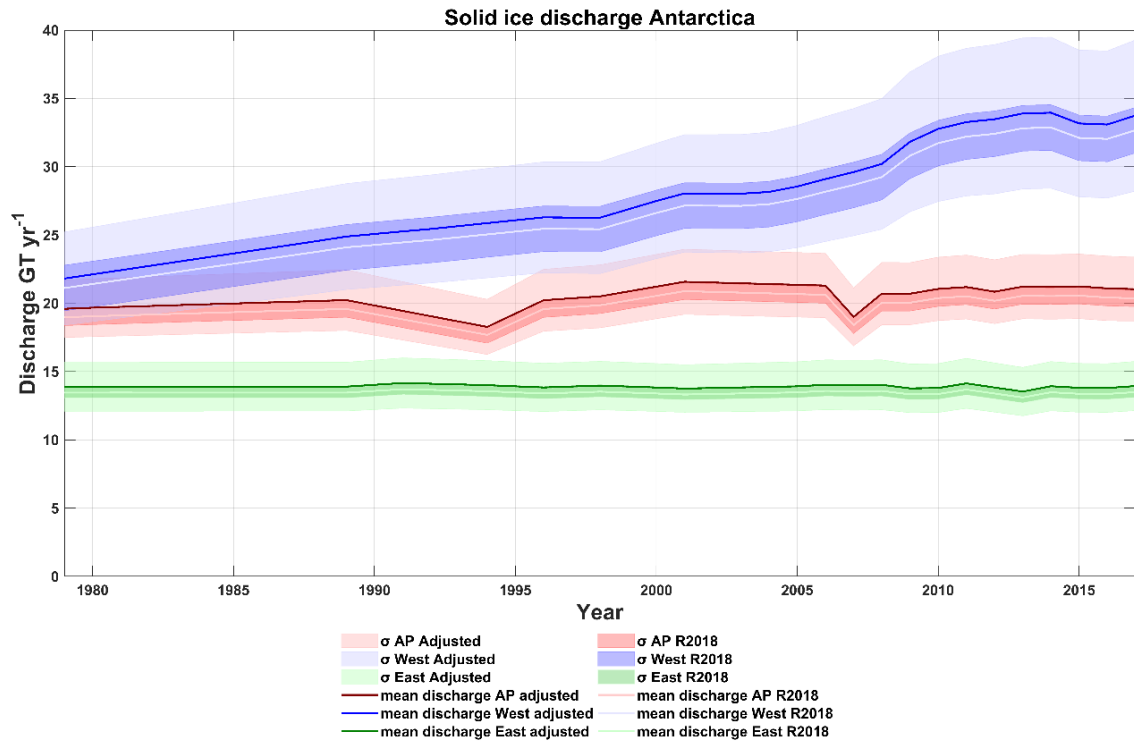
Figure 6.4 Monte Carlo simulated uncertainty of regional Antarctic solid ice discharge. Brighter lines and darker patches represent the Rignot et al., (2018) estimates of ice discharge and the uncertainty in the estimates respectively (R2018). Darker lines and lighter patches represent the simulated mean discharge and uncertainty respectively. Data is from Rignot et al., (2018).

6.3 Wider implications

6.3.1 Increase in dynamic potential of ice mass interior regions

Underestimation of the depth of bed topography has implications for the predicted dynamics of an ice mass when modelled. Initially, RES tends to underestimate depth due to the preferential measurement of valley walls opposed to floors. Additionally, RES errors arising from system positioning and set-up, signal attenuation and scattering, and from bed picking contribute to the mismeasurement of bed topography elevation (Lapazaran et al., 2016). Subsequently, interpolation tends to smooth areas of extreme lows and highs, valley floors and adjacent peaks, towards the mean of the inputs, resulting in a shallower subglacial topography estimate than what the topography likely is. Shallower bed topography results in less dynamic overlying ice as the basal shear stress (T_b) is lower and the height above floatation (H_f) is greater, resulting in increased effective pressure (Stearns and van der Veen, 2018). Adapting

169

Bedmachine Greenland v3 with the methods derived by this thesis results in a widespread deepening of the GrIS interior. Consequently, the mean height above floatation decreases by -0.5 ± 4 m. However, due to the increase in elevation of subglacial highlands, across the entire interior basal shear stress decreases by 18 ± 227 Pa. Conversely, when CAA ice cap bed topography is adapted an increase in height above floatation, 4 ± 17 m, and a mean increase in basal shear stress is observed, 25 ± 1042 Pa. However, comparably with the GrIS, the standard deviation is at least an order of magnitude greater than the mean. For the QEI ice caps, the scale of change was far greater than for Greenland. This is largely attributable to the steeper DME function derived from the synthetic RES survey and interpolation for the CAA PGA (figures 4.3 and 5.2). Consequently, estimated elevation differences are larger for greater interpolation DME values. As the estimated elevation differences were found to be large in comparison to ice thickness (~10%), this should be considered a high estimate. However, for the Devon ice cap where the function is well constrained by a high density of input measurements, shear stress difference values were similar in scale to those of the other ice caps. Therefore, the results of this study suggest the potential for high variability in modelled dynamic discharge from the QEI ice caps dependent on the method of bed topography generation. This is problematic as ice discharge across QEI outlet glaciers has been estimated to have complex spatiotemporal variability (Van Wychen et al., 2016).

Albeit, changes are modest at the ice sheet, and ice cap scale as well as highly uncertain. This arises from the increased difference in T_b and H_f between subglacial uplands and lowlands. Hence, it is more efficacious to investigate the changes for important individual outlet glaciers when assessing the change in apparent dynamic potential of the ice masses. However, it is important to note that to some extent these effects are mitigated in models using contemporary dynamics as basal friction is inverted from contemporaneous observations of velocity (Morlighem et al., 2013). Nevertheless, for the interior regions investigated in detail here, currently flow is slow, and the inferences made relate to long term modelling of the ice masses, where interior regions become marginal with retreat (Calov et al., 2018; Golledge et al., 2019). Moreover, changes in height above floatation are for current ice thickness, this quantity will significantly

change as the ice masses retreat and thin and as the underlying topography undergoes isostatic adjustment (Aschwanden et al., 2019).

In the following sections, the difference in the dynamic configuration of important outlets across the ice masses investigated here is assessed.

6.3.2.1 Greenland

For Greenland, T_b increased across the interior portions of the Jakobshavn isbræ and Zachariæ Isström outlet glaciers, by 209 ± 139 Pa and 143 ± 83 Pa respectively. Correspondingly, hf lowered by -9 ± 4 m for Jakobshavn Isbrae, and -7 ± 3 m for Zachariæ Isström. This constitutes a percentage increase of ~5% and ~3% for Tb and a percentage decrease of 0.4% in Hf for both outlets. The increased dynamic potential across the interior sectors of these glaciers is critical as bed topography here is both retrograde and at Atlantic Water depth (Figure 4.6 and Fig 4.8, Holland et al., 2008; Morlighem et al., 2017, Schaffer et al., 2020). Furthermore, these regions are particularly important as they connect the large sub-sea-level basin in the interior of the ice sheet to the ocean (Morlighem et al., 2017). Consequently, significant potential exists for the persistent enhanced retreat of these glaciers well into the GrIS interior. This is of importance for models aiming to predict the GrIS contribution to sea-level rise over the next millennium (Golledge, 2019; Aschwanden et al., 2019; Barthel et al., 2020).

6.3.2.2 Canadian Arctic Archipelago

For the Trinity, Wykeham, and North Ellesmere Island glaciers, where this study found an increase in the extent of sub-sea-level bed topography, T_b and H_f differed by 1.7 ± 1.5 KPa and -36 ± 8 m respectively. Dynamic thinning and enhanced mass loss are already observed at Trinity and Wykeham (Harcourt et al., 2020). These results highlight the potential for this to continue here. However, North Ellesmere Island glaciers are currently buttressed by floating ice tongues (White and Copland, 2018). Regional warming is expected to remove this buttressing and as shown in figure 5.6 these glaciers have the potential for enhanced dynamics. Furthermore, enhanced retreat above 10 m yr^{-1} has already been observed at the Otto glacier on the North Ellesmere ice cap (Cook et al., 2019). Consequently. The North Ellesmere ice cap could be susceptible to increased dynamic output similar to the POW icefield outlets.

6.3.2.3 Antarctica

For Antarctica, overall a -64 ± 933 Pa change in basal shear stress was found. Additionally, height above floatation decreased on average with a difference of -2 ± 21 m. Highlighting the large variability in dynamic configuration dependent on bed topography dataset choice. Similarly, to the GrIS the increase in elevation of interior uplands leads to an ice sheet wide negative average difference in T_b. Overall, adaptation of Bedmap2 exhibits some of the observed ice dynamic conditions in BedMachine Antarctica (Morlighem et al., 2020). The maximum magnitude of differences is the largest of any of the ice masses. While this will partly be due to the scale of Antarctica, this is also largely a consequence of broadly applying the methods developed here without tailored amendments suited to Antarctic bed topography and as such should be treated with caution.

6.3.2 Implications for projections of sea-level rise

Combined, the wider implications outlined above have a compounding effect on projections of future sea-level rise, predominantly in the far-term (after 2100, Golledge et al., 2019). Hence, ice dynamic models predicting sea-level rise long into the future likely underestimate the scale of the dynamic component of mass loss (beyond 2100, Golledge et al., 2019; Aschwanden et al., 2019). This is of crucial importance as projections of sea-level change into the future are essential for policy and planning for coastal populations (WCRP, 2018). At a minimum dynamic GMSL rise contribution is underestimated by 3%, yet, there is high uncertainty in this ± 18%. Applying this to the latest estimates of dynamic discharge for the continental ice sheets results in an additional 2.4 mm of GMSL (Rignot et al., 2018; Mankoff et al., 2019). For future projections, modelled and extrapolated trends of dynamic mass loss based on underestimates will not capture the full quantity or rate at which ice mass dynamics contribute to sea-level rise.

Sea-level rise is globally heterogeneous (Tamisiea and Mitrovica, 2011). Mass loss from ice sheets and ice caps results in increased sea-level at distal locations but a relative lowering of sea-level locally (Mitrovica et al., 2009). This has a compounding effect for equatorial coastlines and where the ice sheet sea-level fingerprints overlap (Hsu and Velicogna, 2017). Moreover, this has the potential to influence the stability of the ice masses themselves if regional sea-level

lowering is outpaced by a sea-level contribution from a far-field source. Correspondingly, the amount of ice grounded within a few metres of sea-level becomes important for ice mass stability. For the CAA this constitutes ~3% of regional subglacial topography and ~4-8% at the most dynamically active ice caps. In Greenland, it was found 2% more ice was grounded below sea-level, with a like similar increase in the near sea-level area. For this scenario of increased susceptibility to enhanced dynamic mass loss due to increased sub-sea-level grounded ice, mass loss from Antarctica must outpace the regional lowering of sea-level around Greenland and the CAA (Hsu and Velicogna, 2017). However, the collapse of the West Antarctic Ice Sheet is required for this and the occurrence and rate of this collapse are highly uncertain (DeConto and Pollard, 2016).

6.4 Limitations

6.4.1 Assumption of the continuation of proglacial topography beyond the margin

The overarching limitation of the work undertaken by this thesis arises from the use of previously glaciated terrain as a control dataset for current subglacial topography quality assessment. While the selected PGAs were once subglacial (Dalton et al., 2020), it is a major assumption of the study that similar landscape geometry continues underneath the present-day margin proximal regions of the ice sheet. The efficacy of this increasingly breaks down the further inland from the margin that the topographic similarity is assumed. Measurements of the topography beneath the Russell Glacier catchment are extensive and show a continuation of similar terrain (Lindbäck et al., 2014; Lindbäck and Petterson, 2015), and it is not unreasonable to assume similar conditions across ice masses where lithology and geological structure are estimated to be comparable. Yet, radar measurements are rarely independently validated, as discussed throughout.

6.4.2 Limitations of synthetic RES simulation

Parameters for the geospatial RES simulator outlined in chapter three are based on the MCoRDS instrument only. Hence, the numeric results and corrections are largely only applicable to surveys conducted using this system. Nevertheless, the observed bias due to the geometry of the underlying landscape will be observed

on all radar systems, it will only vary in scale. Chapter five highlights this issue as OIB RES data could be amended but SPRI 2000 and CAGE RES data could not. Nevertheless, this work presents the method for developing a RES simulation and can, therefore, be adapted to other sensors if needed.

Additionally, for the synthetic RES surveying, the simulated off-nadir elevation difference error is only the result of the interaction of the radar pulse with the geometry of the underlying topography. Physical interactions of the radar pulse with other facets of the ice mass environment are not parameterised. These include but are not limited to subglacial and englacial water (Chu and others, 2016; Kendrick and others, 2018), heavily crevassed ice (Gogineni et al 2001; Jezek et al., 2013), and online and offline reflections from englacial and basal debris (Irvine-Fynn et al., 2006). Hence, the synthetic RES method could be improved by parameterisation of these conditions which typically occur near ice mass margins.

The RES simulation developed here assumed the bed elevation was picked using the brightest echo. This approach is widely used but is subject to uncertainty as brightness is heavily influenced by roughness, the presence or absence of water, and bed lithology (Gogineni et al., 2001; Holt et al., 2006; Farinotti et al., 2013). This version of the RES simulation only investigates the influence of bed roughness. Additionally, bed elevations may also be picked using the first return which could be easily implemented into the simulation in future work. Consequently, the results here are only applicable to bed elevation measurements picked using the brightest reflector.

As this work makes conservative underestimates of valley CSA, the wider implication of underestimated solid ice discharge from RES derived outlet glacier CSAs is also an underestimate. This arises from the automation of the valley cross-sectional area calculation. Future work that employs the synthetic RES simulation method should look to quantify valley CSA from the ice surface down as opposed to just for the bottom half of the valley. This was chosen for this thesis for computational efficiency. As it was shown that highland areas are subdued both in the initial RES survey and subsequently more so in interpolated bed topography, the addition of the entirety of the simulated ice column to the CSA calculation would refine this uncertainty estimate.

6.4.3 Limitations of the interpolation elevation uncertainty reduction

Interpolation in this work has been conducted using ordinary kriging. While every effort has been made to increase accuracy when using this method it still generates bed topography that is susceptible to all the publicised pitfalls of kriging (Goff et al., 2014; Williams et al., 2017; Morlighem et al., 2020). Deepening of the bed by the DME method increases the dynamic potential of the bed topography for modelling, however, as it subtracts elevation according to the surrounding mean elevation it does not remove artefacts or better resolve potential small scale pinning points (Sun et al., 2014; Durand et al., 2011).

Neighbourhood size for the initial difference from mean calculation was arbitrarily set from the sample area size. In future, it would be beneficial to investigate the influence of varying this neighbourhood size. The optimal neighbourhood size for the DME-function in a given area is likely a product of the scale of relief locally. For example, in the EGA sample site, there are large fjords intersected by narrow peaks. Over a 50 km x 50 km neighbourhood this results in high values of DME for both, whereas at a reduced scale they would be lower and consequently, the estimated elevation difference would be reduced. Adaptation of the technique based on this limitation would prove beneficial for the CAA study where it was often found that the DME estimated elevation difference would exceed the ice cap's surfaces.

Although the DME-error method predicts elevation difference based on a large number of observations with generally strong predictive capability ($R^2 > 0.7$), it is still fundamentally an estimate. As such, while it can be applied to kriged bed topography to change it into a surface that has a higher probability of matching the actual elevation (in areas of sparse input data), it does not unequivocally correct bed topography. Consequently, estimates of the magnitude of bed elevation change and the derived confidence intervals provide a first-order refinement of kriged bed topography but not a fully validated correction.

6.4.4 Limitations of the CAA bed topography investigation

Due to the sparsity of the input RES measurements and the implementation of kriging as an interpolator the output quality of these bed topography datasets is limited. However, as flight-line density was increased along outlet glacier centrelines the bed topography is likely of sufficient quality for numerical

modelling of the largest outlets. While RMSD at 1km was used as a proxy for the quality it would require further analysis to determine if these perturbations were real or artificial. Numerical modelling of ice flow over the dataset and validation with velocity observations would help achieve this.

Flux gate quality from kriged bed topography was found to be highly variable (Table 5.5). Hence, they would largely be unsuitable for deriving discharge estimates. Furthermore, this quality was validated based on RES flux gates which are also an estimated quantity. Therefore, kriged flux gate accuracy is limited.

For the Canadian Arctic Archipelago, flight-line density exceeds 0.14 lines km^{-2} across the Agassiz, POW, and Devon ice caps. Hence, the DME method is less reliable in these locations (at the 99%CI). Using it as a first estimate of uncertainty found an average estimated elevation difference equivalent to 10% of ice thickness. This was deemed too excessive for widespread use in chapter five. Furthermore, limited observations for the POW DME-error function limit its effectiveness and in areas of higher elevation, the method breaks down as adjusted elevation exceeds the observed ice surface height. With greater computational resources a larger sample area of proglacial topography for the Canadian Arctic could be sampled and a stronger DME-error function derived.

7. Conclusions

7.1 Principal conclusions

The principal conclusions of this thesis are:

1. High-resolution elevation data over proximal ice-free terrain can be used as an analogue to reduce uncertainty in ice thickness measurements and bed topography estimates.

2. Airborne RES surveys underestimate subglacial relief. Heights of peaks and uplands are underestimated and valley and fjord bottom elevations are overestimated.

3. Interpolations of bed topography exacerbate the errors in RES survey measurements and subglacial relief is underestimated further.

4. As underestimation of subglacial relief is systematic it should be considered when deriving the dynamic mass budget component of mass balance.

7.2 Summary of conclusions

7.2.1 Quantifying and reducing uncertainty in airborne RES measurements

This thesis identified a systematic overestimation bias in measuring ice thickness. Accordingly, this results in a systematic underestimation of subglacial elevation. This bias is modest (-1.8 ± 11.6 m), but the accumulation of errors when RES measurements are employed for analysis has a more marked influence. Bed topography lows are estimated to be higher in elevation, subglacial peaks are estimated to be lower in elevation, and slopes across bed topography are estimated to have lower gradients. This underestimation of relief has a knock-on effect for flux-gate and centreline surveys which are used to quantify solid ice discharge and model ice dynamics, which in turn, form the basis of glacier and ice sheet mass balance estimates. The cross-sectional area of outlet glaciers is predominantly underestimated (52%), of particular importance is that large outlet glacier valley geometry is underestimated by 3 ± 18%, in 70% of cases. Depth is underestimated in 70% of RES measurements by approximately 2%. This has potential implications for the perceived stability of outlet glaciers. Hence, RES measurements should be adjusted to account for this effect. Correction factors are determined and presented for this purpose.

177

7.2.2 Quantifying and reducing uncertainty in bed topography interpolation

This thesis quantified and reduced uncertainty in the kriged portion of Bedmachine Greenland v3 using analogous proglacial topography as a pseudo-validation dataset (Morlighem et al., 2017). Firstly, it was found that previous studies overestimated interpolation error. Secondly, a new function (referred to as the DME-error function) was implemented to estimate the difference in elevation of a kriged elevation in Bedmachine Greenland v3 from the actual subglacial elevation, exploiting known caveats of kriging. Through this, knowledge of subglacial elevation was improved over an area which approximates to 48% of the ice sheet bed. The DME-error method could reduce uncertainty in kriged bed topography from RES surveys conducted more sparsely than a 3.5 km spaced grid or 1.8 km spaced lines. A refined estimate of error based on distance from an input was also derived which outperformed previous estimates of uncertainty for 67% of the ice sheet (within one standard deviation of error). Uncertainty could be reduced by up to 100's of metres across large swathes of bed topography, however, the mean reduction of error was typically to the magnitude of 10's of metres. Application of the DME estimated elevation difference to the Bedmachine dataset resulted in a deepening of the bed on average (-5 ± 41 m). The area of ice grounded below sea-level expanded by 2%, and the area grounded below the Atlantic Water depth of -200 m a.s.l. expanded by 29%. Retrograde slopes beneath major outlet glaciers were steepened significantly (0.3 ± 0.1°, t-test p-value = 0). These findings highlight that the interior region of the Greenland Ice Sheet has the potential to be more susceptible to dynamic instabilities than previously anticipated.

7.2.3 Application to Canadian Arctic Archipelago (CAA) ice caps

In chapter five, ice cap wide bed topography datasets were derived for five ice caps on the Queen Elizabeth Islands (QEI) for the first time and updated for the Devon ice cap (previously derived by Dowdeswell et al., 2004). Additionally, these datasets were accompanied by maps of uncertainty generated using the methods established in chapter four. Ice cap volume totalled ~19869 ± 218 km^3 which equates to approximately 48.8 ± 0.6 mm when adjusted for area grounded below sea-level. Full hypsometric investigation of subglacial and supraglacial topography highlighted that the ice caps are predominantly susceptible to surface melt. However, the Devon, POW and North Ellesmere Island ice caps are also

susceptible to enhanced dynamic retreat. Bed topography was found to be 1% deeper when accounting for uncertainty in the input RES measurements. DME estimated elevation differences suggested the area grounded below sea-level was 4.5% more expansive than estimated by kriging. This potential additional depth suggests more outlet glaciers are closer to floatation and are susceptible to enhanced dynamics. Along major centrelines, vertical perturbations over one-kilometre wavelengths were largely limited to < 10 m (68% of total centreline length). Finally, Euclidean distance-error uncertainty maps, based on the method in chapter four, were produced for all ice caps and resulted in significantly (paired t-test p = 0) reduced uncertainty (RMSE = 165 ± 65 m) compared to the standard predicted error given by the interpolation (RMSE = 214 ± 37 m). Flux-gate uncertainty due to the use of kriged bed topography is large at approximately 43% of ice thickness (mean error = 74 ± 45 m) nonetheless it was quantified enabling the use of it in future research.

7.3 Future research

7.3.1 Synthetic RES surveying and bed topography generation

This thesis has shown the potential for using high-precision elevation of ice-free, previously glaciated topography for improving uncertainty in ice mass bed topography, and consequently, their contribution to sea-level change. As the underpinning method of this thesis is based in geostatistics, the potential exists to build on the probability-based methods defined in this work with machine learning (Eidsvik et al., 2014). In chapter three, the distribution of RES measurement errors was defined and as such a probabilistic approach can be developed to, at the very least, better refine ice thickness uncertainty for point measurements based on their topographic position, if not fully correct them. Furthermore, the potential exists for the development of the synthetic RES survey simulator into a tool for future survey optimisation. With some assumption of the underlying topography intended for surveying and the parameters of the RES instrument, surveys can be simulated across analogous terrain. As much of the domain of the ArcticDEM covers previously subglacial topography, potential high-resolution training sites are abundant (Porter et al., 2018). However, geomorphological information will also be required, as large areas of the Arctic have potentially never been glaciated or have been exposed for so long that they have been heavily modified by non-glacial depositional and erosional processes.

Accordingly, data from the simulated survey can then be applied to correct the measurements made by the actual RES survey with a corresponding estimate of uncertainty.

Potential also exists to develop the RES survey simulator for other instrument setups and to include physical-based errors. From this, the RES simulator could be used as a flight-planning tool and used to provide an estimate on the amount of error resulting from off-nadir elevation differences to be expected from a survey.

In chapters four and five, linear models were developed which may be used to estimate the difference of an interpolated surface from the actual topography, this has potential for further refinement. Initially, the scale of landscape assessment in this work was limited to 50 km squares. This could be improved by using larger areas and a wider array of ice-free landscapes. It would be beneficial to investigate the range over which the DME function is best applied, as seen in the CAA results using a similar scale to the GrIS developed functions leads to large uncertainties. With the development of cloud computing and machine learning the potential to expand this research and refine the prediction models is vast. Google Earth Engine provides a platform for server-based processing of global scale datasets (Gorelick et al., 2017). This work could be applied on a pan-Arctic scale to refine the DME functions for every type of landscape and kriging set up, and indeed alternate geostatistical interpolations (Goff et al., 2014; MacKie et al., 2020). Vast areas of topography across the Arctic could be sampled, interpolated and differenced to improve the global DME function applied to Greenland. Additionally, this scale of investigation would allow for the development of landscape similarity-based adaptation functions. From this, the geometry of a subglacial landscape at various scales could be matched with ice-free areas and the DME function derived for these areas, from this the kriged output can be adapted more robustly.

All the above however remains an alternative to the validation of ice thickness measurements without the need to access the ice-bed interface (Schroeder et al., 2020). All the predicted changes to bed elevation datasets would require further surveys of the ice caps they are used on to refine its validity.

7.3.2 Application to ongoing and future methods of bed topography generation

While this thesis has highlighted the historical use of kriging and the need to refine it, mass conservation has become the go-to method for predicting subglacial topography. The concept of this thesis could be built on using mass conservation, whereby synthetic ice sheet velocity fields are simulated through synthetic RES measurements and the output beds compared with the underlying ArcticDEM. While this would require significant computational resources and robust development of the synthetic ice sheets, it would provide invaluable uncertainty parameterization for mass conservation estimates of ice mass beds. Furthermore, velocity fields may be manipulated to replicate the variable and complex nature of outlet glaciers across the polar ice masses, to verify the influence of velocity on the potential error of the output bed.

Conditional simulation is being increasingly used to develop multiple realisations of ice mass bed topography (Goff et al., 2014; MacKie et al., 2020). While the method aims to generate topography that better resembles the spatial statistics of the input data at scale as opposed to best estimate the elevation at a location, the latter could be achieved by following the differencing based approach outlined in this thesis. Through differencing the average simulation of simulated RES data against the input ArcticDEM, the typical error for the output elevations can be quantified and applied to similar subglacial topography as illustrated throughout this thesis.

7.3.3 Reduction of uncertainty in sea-level rise contribution

Throughout this thesis, the implications of the findings for sea-level change estimates has been alluded too. Future work could look to extend this to quantify uncertainties in the contribution of ice masses to global mean sea-level rise. Additionally, with refined estimates of sea-level change from the individual ice masses, the potential exists for determining regional sea-level rise fingerprints for the ice masses (Hsu and Velicogna, 2017). In the near term, this would be of interest around the CAA ice caps, where this thesis finds an increased extent of bed topography beneath the POW and Devon ice caps below or within metres of sea-level. Similarly, the estimated increase in the extent of the Greenland Ice Sheet interior grounded below sea-level highlights increased susceptibility of the

ice sheet to enhanced retreat. However, this region is unlikely to be marine-terminating in the near term, but if the regional sea-level decrease is outpaced by Antarctic sourced sea-level rise the Greenland Ice Sheet interior could be more susceptible to enhanced retreat in the far-term (Aschwanden et al., 2019).

Scope exists for a recalculation of mass budgets for glaciers where the bed topography is kriged and the uncertainty unlikely parameterises the likely extra depth of their beds. Such work would aid the reduction of uncertainty in the ice dynamical component of sea-level change.

Numerical modelling of ice sheet evolution over adapted bed topography would quantify more robustly the inferences made here about the increased potential for interior ice sheet dynamic instability.

References

Alley, R.B., Clark, P.U., Huybrechts, P. and Joughin, I., 2005. Ice-sheet and sea-level changes, *Science*, 310(5747), pp. 456-460.

Aschwanden A, Fahnestock MA and Truffer M, 2016. Complex Greenland outlet glacier flow captured, *Nature communications*, 7(10524), pp. 1-8.

Aschwanden, A., Fahnestock, M.A., Truffer, M., Brinkerhoff, D.J., Hock, R., Khroulev, C., Mottram, R. and Khan, S.A., 2019. Contribution of the Greenland Ice Sheet to sea level over the next millennium, *Science advances*, 5(6), p.eaav9396.

Bailey, J.T., Evans, S. and Robin, G.D.Q., 1964. Radio echo sounding of polar ice sheets, *Nature*, 204(4957), pp. 420-421.

Bamber, J.L., Griggs, J.A., Hurkmans, R.T.W.L., Dowdeswell, J.A., Gogineni, S.P., Howat, I., Mouginot, J., Paden, J., Palmer, S., Rignot, E. and Steinhage, D., 2013. A new bed elevation dataset for Greenland, *The Cryosphere*, 7(2), pp. 499-510.

Bamber, J.L., Layberry, R.L. and Gogineni, S.P., 2001. A new ice thickness and bed data set for the Greenland Ice Sheet: 1. Measurement, data reduction, and errors, *Journal of Geophysical Research: Atmospheres*, 106(D24), pp. 33773-33780.

Bamber, J.L., Tedstone, A.J., King, M.D., Howat, I.M., Enderlin, E.M., van den Broeke, M.R. and Noel, B., 2018a. Land ice freshwater budget of the Arctic and North Atlantic Oceans: 1. Data, methods, and results, *Journal of Geophysical Research: Oceans*, 123(3), pp. 1827-1837.

Bamber, J.L., Vaughan, D.G. and Joughin, I., 2000. Widespread complex flow in the interior of the Antarctic Ice Sheet, *Science*, 287(5456), pp. 1248-1250.

Bamber, J.L., Westaway, R.M., Marzeion, B. and Wouters, B., 2018. The land ice contribution to sea level during the satellite era, *Environmental Research Letters*, 13(6), p.063008.

Barthel, A., Agosta, C., Little, C.M., Hattermann, T., Jourdain, N.C., Goelzer, H., Nowicki, S., Seroussi, H., Straneo, F. and Bracegirdle, T., 2020. CMIP5 model

selection for ISMIP6 ice sheet model forcing: Greenland and Antarctica, *The Cryosphere*, 14(3), pp. 855-879.

Bartlett, O.T., Palmer, S.J., and Morlighem, M. in preparation. Reduced uncertainty in subglacial topography for sparsely surveyed regions of the Greenland Ice Sheet, *Journal of Geophysical Research: Earth Surface.*

Bartlett, O.T., Palmer, S.J., Schroeder, D.M., MacKie, E.J., Barrows, T.T., and Graham, A.G.C, 2020. Geospatial simulations of airborne ice-penetrating radar surveying reveal elevation under-measurement bias for ice sheet bed topography, *Annals of Glaciology*, 61(81), pp. 46-57.

Bassford, R.P., Siegert, M.J., Dowdeswell, J.A., Oerlemans, J., Glazovsky, A.F., and Macheret Y.Y., 2006a. Quantifying the Mass Balance of Ice Caps on Severnaya Zemlya, Russian High Arctic. I: Climate and Mass Balance of the Vavilov Ice Cap, *Arctic, Antarctic, and Alpine Research*, 38(1), pp. 1-12.

Bassford, R.P., Siegert, M.J., and Dowdeswell, J.A., 2006b. Quantifying the Mass Balance of Ice Caps on Severnaya Zemlya, Russian High Arctic. II: Modeling the Flow of the Vavilov Ice Cap under the Present Climate, *Arctic, Antarctic, and Alpine Research*, 38(1), pp. 13-20.

Bassford, R.P., Siegert, M.J., and Dowdeswell, J.A., 2006c. Quantifying the Mass Balance of Ice Caps on Severnaya Zemlya, Russian High Arctic. III: Sensitivity of Ice Caps in Severnaya Zemlya to Future Climate Change, *Arctic, Antarctic, and Alpine Research*, 38(1), pp. 21-33.

Bassis, J.N. and Walker, C.C., 2012. Upper and lower limits on the stability of calving glaciers from the yield strength envelope of ice. *Proceedings of the Royal Society A: Mathematical, Physical and Engineering Sciences*, 468(2140), pp. 913-931.

Batchelor, C.L., Dowdeswell, J.A., Rignot, E. and Millan, R., 2019. Submarine Moraines in Southeast Greenland Fjords Reveal Contrasting Outlet-Glacier Behavior since the Last Glacial Maximum, *Geophysical Research Letters*, 46(6), pp. 3279-3286.

Benham, T.J. and Dowdeswell, J.A., 2003. A simple visualization method for distinguishing subglacial-bed and side-wall returns in radio-echo records from outlet and valley glaciers, *Journal of Glaciology*, 49(166), pp. 463-468.

Bentley, C.R., 1987. Antarctic ice streams: a review, *Journal of Geophysical Research: Solid Earth*, 92(B9), pp. 8843-8858.

Bevis, M., Harig, C., Khan, S.A., Brown, A., Simons, F.J., Willis, M., Fettweis, X., Van Den Broeke, M.R., Madsen, F.B., Kendrick, E. and Caccamise, D.J., 2019. Accelerating changes in ice mass within Greenland, and the ice sheet's sensitivity to atmospheric forcing, *Proceedings of the National Academy of Sciences*, 116(6), pp. 1934-1939.

Bingham, R.G. and Siegert, M.J., 2007. Radio-echo sounding over polar ice masses, *Journal of Environmental and Engineering Geophysics*, 12(1), pp. 47-62.

Bingham, R.G. and Siegert, M.J. 2009. Quantifying subglacial bed roughness in Antarctica: implications for ice-sheet dynamics and history, Quaternary Science Reviews, 28(3-4), pp. 223–236.

Blankenship, D.D., Kempf, S., Young, D., Richter, T.G., Schroeder, D.M., Ng, G., Greenbaum, J.S., van Ommen, T.D., Warner, R.C., Roberts, J.L. and Young, N.W., 2012. IceBridge HiCARS 1 L2 geolocated ice thickness. Digital media, NASA DAAC at the National Snow and Ice Data Center, Boulder, Colorado, USA.

Blindow, N., Suckro, S.K., Rückamp, M., Braun, M., Schindler, M., Breuer, B., Saurer, H., Simões, J.C. and Lange, M.A., 2010. Geometry and thermal regime of the King George Island ice cap, Antarctica, from GPR and GPS, *Annals of Glaciology*, 51(55), pp. 103-109.

Bogorodsky, V.V., Bentley, C.R. and Gudmandsen, P.E., 1985. Scientific Results in Radioglaciology. In: *Radioglaciology*. (pp. 84-249). Springer, Dordrecht.

Boon, S., Burgess, D.O., Koerner, R.M. and Sharp, M.J., 2010. Forty-seven years of research on the devon island ice cap, Arctic Canada, *Arctic*, 63(1), pp. 13-29.

Box, J.E., Colgan, W.T., Wouters, B., Burgess, D.O., O'Neel, S., Thomson, L.I. and Mernild, S.H., 2018. Global sea-level contribution from Arctic land ice: 1971–2017, *Environmental Research Letters*, 13(12), p.125012.

Box, J.E., Fettweis, X., Stroeve, J.C., Tedesco, M., Hall, D.K. and Steffen, K., 2012. Greenland Ice Sheet albedo feedback: thermodynamics and atmospheric drivers, *The Cryosphere*, 6, pp. 821-839.

Box, J.E., Sharp, M., Aðalgeirsdóttir, G., Ananicheva, M., Anderson, M.L., Carr, R., Clason, C.C., Colgan, W.T., Copland, L., Glazovsky, A. and Hubbard, A., 2017. Changes to Arctic land ice. In Snow, water, ice and permafrost in the Arctic (SWIPA) 2017. *Arctic Monitoring and Assessment Programme (AMAP); Summary for Policy Makers*.

Brinkerhoff, D.J., Aschwanden, A. and Truffer, M., 2016. Bayesian inference of subglacial topography using mass conservation, *Frontiers in Earth Science*, 4, p.8.

Brough, S., Carr, J. R., Ross, N., and Lea, J. M.: Exceptional Retreat of Kangerlussuaq Glacier, East Greenland, Between 2016 and 2018, *Frontiers in Earth Science*, 7, p. 123.

Brun, F., Berthier, E., Wagnon, P., Kääb, A. and Treichler, D., 2017. A spatially resolved estimate of High Mountain Asia glacier mass balances from 2000 to 2016, *Nature geoscience*, 10(9), pp. 668-673.

Bunce, C., Carr, J.R., Nienow, P.W., Ross, N. and Killick, R., 2018. Ice front change of marine-terminating outlet glaciers in northwest and southeast Greenland during the 21st century, *Journal of Glaciology*, 64(246), pp. 523-535.

Calov, R., Beyer, S., Greve, R., Beckmann, J., Willeit, M., Kleiner, T., Rückamp, M., Humbert, A. and Ganopolski, A., 2018. Simulation of the future sea level contribution of Greenland with a new glacial system model, *The Cryosphere*, 12(10), pp. 3097-3121.

Carrivick, J.L., Yde, J., Russell, A.J., Quincey, D.J., Ingeman-Nielsen, T. and Mallalieu, J., 2017. Ice-margin and meltwater dynamics during the mid-Holocene in the Kangerlussuaq area of west Greenland, *Boreas*, 46(3), pp. 369-387.

Catania GA and 7 others, 2018. Geometric controls on tidewater glacier retreat in central western Greenland, *Journal of Geophysical Research: Earth Surface*, 123(8), pp. 2024-2038.

Catania, G.A., Stearns, L.A., Moon, T.A., Enderlin, E.M. and Jackson, R.H., 2020. Future Evolution of Greenland's Marine-Terminating Outlet Glaciers, *Journal of Geophysical Research: Earth Surface*, 125(2), p.e2018JF004873.

Choi Y, Morlighem M, Rignot E, Mouginot J and Wood M, 2017. Modeling the response of Nioghalvfjerdsfjorden and Zachariae Isstrøm Glaciers, Greenland, to ocean forcing over the next century, *Geophysical Research Letters*, 44(21), pp. 11-071.

Chu W, Schroeder DM, Seroussi H, Creyts TT, Palmer SJ and Bell RE, 2016. Extensive winter subglacial water storage beneath the Greenland Ice Sheet, *Geophysical Research Letters*, 43(24), pp. 12-484.

Chu, V.W., 2014. Greenland Ice Sheet hydrology: A review, *Progress in Physical Geography*, 38(1), pp. 19-54.

Church JA and 13 others, 2013: Sea Level Change. In: *Climate Change 2013: The Physical Science Basis. Contribution of Working Group I to the Fifth Assessment Report of the Intergovernmental Panel on Climate Change* [Stocker TF, Qin D, Plattner GK, Tignor M, Allen SK, Boschung J, Nauels A, Xia Y, Bex V and Midgley PM (eds.)]. Cambridge University Press, Cambridge, United Kingdom and New York, NY, USA.

Clark, C.D., Evans, D.J., Khatwa, A., Bradwell, T., Jordan, C.J., Marsh, S.H., Mitchell, W.A. and Bateman, M.D., 2004. Map and GIS database of glacial landforms and features related to the last British Ice Sheet, *Boreas*, 33(4), pp. 359-375.

Clark, P.U., Dyke, A.S., Shakun, J.D., Carlson, A.E., Clark, J., Wohlfarth, B., Mitrovica, J.X., Hostetler, S.W. and McCabe, A.M., 2009. The last glacial maximum, *Science*, 325(5941), pp. 710-714.

Clark, P.U., Shakun, J.D., Marcott, S.A., Mix, A.C., Eby, M., Kulp, S., Levermann, A., Milne, G.A., Pfister, P.L., Santer, B.D. and Schrag, D.P., 2016. Consequences of twenty-first-century policy for multi-millennial climate and sea-level change, *Nature climate change*, 6(4), pp. 360-369.

Colgan, W., Abdalati, W., Citterio, M., Csatho, B., Fettweis, X., Luthcke, S., Moholdt, G., Simonsen, S.B. and Stober, M., 2015. Hybrid glacier Inventory, Gravimetry and Altimetry (HIGA) mass balance product for Greenland and the Canadian Arctic, *Remote Sensing of Environment*, 100(168), pp. 24-39.

Cook, A.J., Copland, L., Noël, B.P., Stokes, C.R., Bentley, M.J., Sharp, M.J., Bingham, R.G. and van den Broeke, M.R., 2019. Atmospheric forcing of rapid

marine-terminating glacier retreat in the Canadian Arctic Archipelago, *Science advances*, 5(3), p.eaau8507.

Cooper, M.A., Jordan, T.M., Schroeder, D.M., Siegert, M.J., Williams, C.N. and Bamber, J.L., 2019. Subglacial roughness of the Greenland Ice Sheet: relationship with contemporary ice velocity and geology, *The Cryosphere*, 13(11), pp. 3093-3115.

Cooper, A.P.R., 1987. Interface tracking in digitally recorded glaciological data, *Annals of Glaciology*, 9, pp. 50-54.

Cornford, S.L., Martin, D.F., Graves, D.T., Ranken, D.F., Le Brocq, A.M., Gladstone, R.M., Payne, A.J., Ng, E.G. and Lipscomb, W.H., 2013. Adaptive mesh, finite volume modeling of marine ice sheets, *Journal of Computational Physics*, 232(1), pp. 529-549.

Cornford, S.L., Martin, D.F., Payne, A.J., Ng, E.G., Le Brocq, A.M., Gladstone, R.M., Edwards, T.L., Shannon, S.R., Agosta, C., Van Den Broeke, M.R. and Hellmer, H.H., 2015. Century-scale simulations of the response of the West Antarctic Ice Sheet to a warming climate, *The Cryosphere*, 9(4), p.1579.

CReSIS. 2020. CReSIS Radar Depth Sounder Data, Lawrence, Kansas, USA. Digital Media. http://data.cresis.ku.edu/. Subset used: "East Central bed Gap IS-2" 201905512_01_061.

CReSIS. 2018. *CReSIS Radar Depth Sounder Data Report*, Lawrence, Kansas, USA. Digital Media. http://data.cresis.ku.edu/.

Dalton, A.S., Margold, M., Stokes, C.R., Tarasov, L., Dyke, A.S., Adams, R.S., Allard, S., Arends, H.E., Atkinson, N., Attig, J.W. and Barnett, P.J., 2020. An updated radiocarbon-based ice margin chronology for the last deglaciation of the North American Ice Sheet Complex, *Quaternary Science Reviews*, 234, p.106223.

DeConto, R.M. and Pollard, D., 2016. Contribution of Antarctica to past and future sea-level rise, *Nature*, 531(7596), pp. 591-597.

Deutsch, C. L. and Journel, A. G., 1997: *GSLIB, Geostatistical Software Library and User's Guide*, Second ed., Oxford University Press, Oxford.

Dowdeswell JA and Evans S, 2004. Investigations of the form and flow of ice sheets and glaciers using radio-echo sounding, *Reports on Progress in Physics*, 67(10), p.1821.

Dowdeswell, J.A. and Bamber, J.L., 1995. On the glaciology of Edgeøya and Barentsøya, Svalbard, *Polar Research*, 14(2), pp. 105-122.

Dowdeswell, J.A., Bassford, R.P., Gorman, M.R., Williams, M., Glazovsky, A.F., Macheret, Y.Y., Shepherd, A.P., Vasilenko, Y.V., Savatyuguin, L.M., Hubberten, H.W. and Miller, H., 2002. Form and flow of the Academy of Sciences Ice Cap, Severnaya Zemlya, Russian High Arctic, *Journal of Geophysical Research: Solid Earth*, 107(B4), p.EPM-5.

Dowdeswell, J.A., Benham, T.J., Gorman, M.R., Burgess, D. and Sharp, M.J., 2004. Form and flow of the Devon Island ice cap, Canadian Arctic, *Journal of Geophysical Research: Earth Surface*, 109, p.F02002.

Dowdeswell, J.A., Drewry, D.J., Cooper, A.P.R., Gorman, M.R., Liestøl, O. and Orheim, O., 1986. Digital mapping of the Nordaustlandet ice caps from airborne geophysical investigations, *Annals of Glaciology*, 8, pp. 51-58.

Dowdeswell, J.A., Evans, J. and Cofaigh, C.Ó., 2010. Submarine landforms and shallow acoustic stratigraphy of a 400 km-long fjord-shelf-slope transect, Kangerlussuaq margin, East Greenland, *Quaternary Science Reviews*, 29(25-26), pp. 3359-3369.

Drewry, D.J., Liestøl, O., Neal, C.S., Orheim, O. and Wold, B., 1980. Airborne radio echo sounding of glaciers in Svalbard, *Polar Record*, 20(126), pp. 261-266.

Dupont, T.K. and Alley, R.B., 2005. Assessment of the importance of ice-shelf buttressing to ice-sheet flow, *Geophysical Research Letters*, 32(4), p.L04503.

Durand G, Gagliardini O, Favier L, Zwinger T and Le Meur E, 2011. Impact of bedrock description on modeling ice sheet dynamics, *Geophysical Research Letters*, 38(20), *p.L20501.*

Durand, G., Gagliardini, O., De Fleurian, B., Zwinger, T. and Le Meur, E., 2009. Marine ice sheet dynamics: Hysteresis and neutral equilibrium, *Journal of Geophysical Research: Earth Surface*, 114(F3). p.F03009.

Edwards, T.L., Brandon, M.A., Durand, G., Edwards, N.R., Golledge, N.R., Holden, P.B., Nias, I.J., Payne, A.J., Ritz, C. and Wernecke, A., 2019. Revisiting Antarctic ice loss due to marine ice-cliff instability, *Nature*, 566(7742), pp. 58-64.

Edwards, T.L., Fettweis, X., Gagliardini, O., Gillet-Chaulet, F., Goelzer, H., Gregory, J.M., Hoffman, M., Huybrechts, P., Payne, A.J., Perego, M. and Price, S., 2014. Effect of uncertainty in surface mass balance–elevation feedback on projections of the future sea level contribution of the Greenland Ice Sheet, *The Cryosphere*, 8(1), pp. 195-208.

Eidsvik, J., Shaby, B.A., Reich, B.J., Wheeler, M. and Niemi, J., 2014. Estimation and prediction in spatial models with block composite likelihoods, *Journal of Computational and Graphical Statistics,* 23(2), pp. 295-315.

Enderlin EM, Howat IM, Jeong S, Noh MJ, van Angelen JH and van den Broeke MR, 2014. An improved mass budget for the Greenland Ice Sheet, *Geophysical Research Letters*, 41(3), pp. 866-872.

Evans S and Robin GDQ, 1966. Glacier depth-sounding from the air, *Nature*, 210(5039), p. 883.

Evans, S., 1965. Dielectric properties of ice and snow–a review, *Journal of Glaciology*, 5(42), pp. 773-792.

Eyles N, Moreno LA and Sookhan S, 2018. Ice streams of the Late Wisconsin Cordilleran Ice Sheet in western North America, *Quaternary Science Reviews*, 179, pp. 87-122.

Eyring, V., Bony, S., Meehl, G.A., Senior, C.A., Stevens, B., Stouffer, R.J. and Taylor, K.E., 2016. Overview of the Coupled Model Intercomparison Project Phase 6 (CMIP6) experimental design and organization, *Geoscientific Model Development*, 9(5), pp. 1937-1958.

Fahnestock, M., Abdalati, W., Luo, S. and Gogineni, S., 2001. Internal layer tracing and age-depth-accumulation relationships for the northern Greenland ice sheet, Journal of Geophysical Research: Atmospheres, 106(D24), pp. 33789-33797.

Fahnestock, M., Scambos, T., Moon, T., Gardner, A., Haran, T. and Klinger, M., 2016. Rapid large-area mapping of ice flow using Landsat 8, *Remote Sensing of Environment*, 185, pp. 84-94.

Falcini, F.A., Rippin, D.M., Krabbendam, M. and Selby, K.A., 2018. Quantifying bed roughness beneath contemporary and palaeo-ice streams, *Journal of Glaciology*, 64(247), pp. 822-834.

Farinotti, D., Corr, H. and Gudmundsson, G.H., 2013. The ice thickness distribution of Flask Glacier, Antarctic Peninsula, determined by combining radio-echo soundings, surface velocity data and flow modelling, *Annals of glaciology*, 54(63), pp. 18-24.

Farinotti, D., Huss, M., Fürst, J.J., Landmann, J., Machguth, H., Maussion, F. and Pandit, A., 2019. A consensus estimate for the ice thickness distribution of all glaciers on Earth, *Nature Geoscience*, 12(3), pp. 168-173.

Favier, L., Durand, G., Cornford, S.L., Gudmundsson, G.H., Gagliardini, O., Gillet-Chaulet, F., Zwinger, T., Payne, A.J. and Le Brocq, A.M., 2014. Retreat of Pine Island Glacier controlled by marine ice-sheet instability, *Nature Climate Change*, 4(2), pp. 117-121.

Favier, L., Pattyn, F., Berger, S. and Drews, R., 2016. Dynamic influence of pinning points on marine ice-sheet stability: a numerical study in Dronning Maud Land, East Antarctica, *The Cryosphere*, 10(6), pp .2623-2635

Fisher, D., Zheng, J., Burgess, D., Zdanowicz, C., Kinnard, C., Sharp, M. and Bourgeois, J., 2012. Recent melt rates of Canadian Arctic ice caps are the highest in four millennia, *Global and Planetary Change*, 84, pp. 3-7.

Fretwell, P., Pritchard, H.D., Vaughan, D.G., Bamber, J.L., Barrand, N.E., Bell, R., Bianchi, C., Bingham, R.G., Blankenship, D.D., Casassa, G. and Catania, G., 2013. Bedmap2: improved ice bed, surface and thickness datasets for Antarctica, *The Cryosphere*, 7(1), pp. 375-393.

Fujita, S., Matsuoka, T., Ishida, T., Matsuoka, K. and Mae, S., 2000. A summary of the complex dielectric permittivity of ice in the megahertz range and its applications for radar sounding of polar ice sheets. In: *Physics of ice core records.* (pp. 185-212). Hokkaido University Press.

Fürst, J.J., Navarro, F., Gillet-Chaulet, F., Huss, M., Moholdt, G., Fettweis, X., Lang, C., Seehaus, T., Ai, S., Benham, T.J. and Benn, D.I., 2018. The ice-free topography of Svalbard, *Geophysical Research Letters*, 45(21), pp. 11-760.

Gardner, A. S., M. A. Fahnestock, and T. A. Scambos, 2019 [08/09/2020]: ITS_LIVE Regional Glacier and Ice Sheet Surface Velocities. Data archived at National Snow and Ice Data Center; doi:10.5067/6II6VW8LLWJ7.

Gardner, A.S., Moholdt, G., Cogley, J.G., Wouters, B., Arendt, A.A., Wahr, J., Berthier, E., Hock, R., Pfeffer, W.T., Kaser, G. and Ligtenberg, S.R., 2013. A reconciled estimate of glacier contributions to sea level rise: 2003 to 2009, *Science*, 340(6134), pp. 852-857.

Gardner, A.S., Moholdt, G., Wouters, B., Wolken, G.J., Burgess, D.O., Sharp, M.J., Cogley, J.G., Braun, C. and Labine, C., 2011. Sharply increased mass loss from glaciers and ice caps in the Canadian Arctic Archipelago, *Nature*, 473(7347), pp. 357-360.

Gärtner-Roer, I., Naegeli, K., Huss, M., Knecht, T., Machguth, H. and Zemp, M., 2014. A database of worldwide glacier thickness observations, *Global and Planetary Change*, 122, pp. 330-344.

Gladstone, R.M., Lee, V., Rougier, J., Payne, A.J., Hellmer, H., Le Brocq, A., Shepherd, A., Edwards, T.L., Gregory, J. and Cornford, S.L., 2012. Calibrated prediction of Pine Island Glacier retreat during the 21st and 22nd centuries with a coupled flowline model, *Earth and Planetary Science Letters*, 333, pp. 191-199.

Goelzer, H., Nowicki, S., Edwards, T., Beckley, M., Abe-Ouchi, A., Aschwanden, A., Calov, R., Gagliardini, O., Gillet-Chaulet, F., Golledge, N.R. and Gregory, J., 2018. Design and results of the ice sheet model initialisation initMIP-Greenland: An ISMIP6 intercomparison, *The Cryosphere*, 12(4), pp. 1433-1460.

Goff JA, Powell EM, Young DA and Blankenship DD, 2014. Instruments and Methods Conditional simulation of Thwaites Glacier (Antarctica) bed topography for flow models: incorporating inhomogeneous statistics and channelized morphology, *Journal of Glaciology*, 60(222), pp. 635-646.

Gogineni S and 9 others, 2001. Coherent radar ice thickness measurements over the Greenland Ice Sheet, *Journal of Geophysical Research: Atmospheres*, 106(D24), pp. 33761-33772.

Gogineni, S., Yan, J.B., Paden, J., Leuschen, C., Li, J., Rodriguez-Morales, F., Braaten, D., Purdon, K., Wang, Z., Liu, W. and Gauch, J., 2014. Bed topography of Jakobshavn Isbræ, Greenland, and Byrd Glacier, Antarctica, *Journal of Glaciology*, 60(223), pp. 813-833.

Golledge, N.R., Keller, E.D., Gomez, N., Naughten, K.A., Bernales, J., Trusel, L.D. and Edwards, T.L., 2019. Global environmental consequences of twenty-first-century ice-sheet melt, *Nature*, 566(7742), pp. 65-72.

Gorelick, N., Hancher, M., Dixon, M., Ilyushchenko, S., Thau, D. and Moore, R., 2017. Google Earth Engine: Planetary-scale geospatial analysis for everyone, *Remote sensing of Environment*, 202, pp. 18-27.

Gudmundsson GH, 1997. Basal-flow characteristics of a non-linear flow sliding frictionless over strongly undulating bedrock, *Journal of Glaciology*, 43(143), pp. 80-89.

Hanna, E., Cropper, T.E., Hall, R.J. and Cappelen, J., 2016. Greenland Blocking Index 1851–2015: a regional climate change signal, *International Journal of Climatology*, 36(15), pp. 4847-4861.

Hanna, E., Pattyn, F., Navarro, F., Favier, V., Goelzer, H., van den Broeke, M.R., Vizcaino, M., Whitehouse, P.L., Ritz, C., Bulthuis, K. and Smith, B., 2019. Mass balance of the ice sheets and glaciers–progress since AR5 and challenges, *Earth-Science Reviews*, 201, p.102976.

Harcourt, W.D., Palmer, S.J., Mansell, D.T., Le Brocq, A., Bartlett, O., Gourmelen, N., Tepes, P., Dowdeswell, J.A., Blankenship, D.D. and Young, D.A., 2020. Subglacial controls on dynamic thinning at Trinity-Wykeham Glacier, Prince of Wales Ice Field, Canadian Arctic, *International Journal of Remote Sensing*, 41(3), pp. 1191-1213.

Harrison, D., Ross, N., Russell, A.J. and Dunning, S.A., 2019. Post-jökulhlaup geomorphic evolution of the Gígjökull Basin, Iceland, *Annals of Glaciology*, 60(80), pp. 127-137.

Haylock, M.R., Hofstra, N., Klein Tank, A.M.G., Klok, E.J., Jones, P.D. and New, M., 2008. A European daily high-resolution gridded data set of surface temperature and precipitation for 1950–2006, *Journal of Geophysical Research*: Atmospheres, 113(D20). p.D20119.

Hempel, L., Thyssen, F., Gundestrup, N., Clausen, H.B. and Miller, H., 2000. A comparison of radio-echo sounding data and electrical conductivity of the GRIP ice core, *Journal of Glaciology*, 46(154), pp. 369-374.

Herzfeld, U.C. and Holmlund, P., 1988. Geostatistical analyses of radio-echo data from Scharffenbergbotnen, Dronning Maud Land, East Antarctica, *Zeitschrift für Gletscherkunde und Glazialgeologie*, 24(2), pp. 95-110.

Herzfeld, U.C., 1990. Geostatistical software for evaluation of line survey data applied to radio-echo soundings in glaciology. In: *Microcomputer Applications in Geology 2* (pp. 119-136). Pergamon. New York. USA.

Herzfeld, U.C., Eriksson, M.G. and Holmlund, P., 1993. On the influence of kriging parameters on the cartographic output—a study in mapping subglacial topography, *Mathematical Geology*, 25(7), pp. 881-900.

Herzfeld, U.C., Mayer, H., Higginson, C.A. and Matassa, M., 1996, July. Geostatistical approaches to interpolation and classification of remote-sensing data from ice surfaces, *Remote Sensing of the Polar Environments*, 391, p. 59.

Herzfeld, U.C., Wallin, B.F., Leuschen, C.J. and Plummer, J., 2011. An algorithm for generalizing topography to grids while preserving subscale morphologic characteristics—creating a glacier bed DEM for Jakobshavn trough as low-resolution input for dynamic ice-sheet models, *Computers & geosciences*, 37(11), pp. 1793-1801.

Hock, R., Bliss, A., Marzeion, B., Giesen, R.H., Hirabayashi, Y., Huss, M., Radić, V. and Slangen, A.B., 2019. GlacierMIP–A model intercomparison of global-scale glacier mass-balance models and projections, *Journal of Glaciology*, 65(251), pp. 453-467.

Hoffman, M.J., Andrews, L.C., Price, S.F., Catania, G.A., Neumann, T.A., Lüthi, M.P., Gulley, J., Ryser, C., Hawley, R.L. and Morriss, B., 2016. Greenland subglacial drainage evolution regulated by weakly connected regions of the bed, *Nature communications*, 7(1), pp. 1-12.

Holland, D.M., Thomas, R.H., De Young, B., Ribergaard, M.H. and Lyberth, B., 2008. Acceleration of Jakobshavn Isbræ triggered by warm subsurface ocean waters, *Nature geoscience*, 1(10), pp. 659-664.

Holschuh, N., Christianson, K., Paden, J., Alley, R.B. and Anandakrishnan, S., 2020. Linking postglacial landscapes to glacier dynamics using swath radar at Thwaites Glacier, Antarctica, *Geology*, 48(3), pp. 268-272.

Holt, J.W., Peters, M.E., Kempf, S.D., Morse, D.L. and Blankenship, D.D., 2006. Echo source discrimination in single-pass airborne radar sounding data from the Dry Valleys, Antarctica: Implications for orbital sounding of Mars, *Journal of Geophysical Research*: Planets, 111(E6), p.E06S24.

Holt, J.W., Fishbaugh, K.E., Byrne, S., Christian, S., Tanaka, K., Russell, P.S., Herkenhoff, K.E., Safaeinili, A., Putzig, N.E. and Phillips, R.J., 2010. The construction of chasma boreale on Mars, *Nature*, 465(7297), pp. 446-449.

Howat, I.M., Joughin, I. and Scambos, T.A., 2007. Rapid changes in ice discharge from Greenland outlet glaciers, *Science*, 315(5818), pp. 1559-1561.

Howat, I., A. Negrete, and B. Smith. 2014. The Greenland Ice Mapping Project (GIMP) land classification and surface elevation data sets, *The Cryosphere*, 8(4), pp.1509-1518.

Hsu, C.W. and Velicogna, I., 2017. Detection of sea level fingerprints derived from GRACE gravity data, *Geophysical Research Letters*, 44(17), pp. 8953-8961.

Hughes T, D.G. and Grosswald, M.G., 1977. Was there a Late-Wurm Arctic ice sheet, *Nature*, 266(5603), pp. 596-602.

Hughes, A.L., Gyllencreutz, R., Lohne, Ø.S., Mangerud, J. and Svendsen, J.I., 2016. The last Eurasian ice sheets–a chronological database and time-slice reconstruction, DATED-1, *Boreas*, 45(1), pp. 1-45.

Hughes, T., 1975. The West Antarctic Ice Sheet: instability, disintegration, and initiation of ice ages, *Reviews of Geophysics*, 13(4), pp. 502-526.

Huss, M. and Farinotti, D., 2012. Distributed ice thickness and volume of all glaciers around the globe, *Journal of Geophysical Research: Earth Surface*, 117(F4). p.F04010.

Huss, M. and Hock, R., 2015. A new model for global glacier change and sea-level rise, *Frontiers in Earth Science*, 3, p.54.

Hutchinson, M.F., 1988. Calculation of hydrologically sound digital elevation models, *Proc. Third Intern. Syrup. on Spatial Data Handling I*, 17, p.133.

IPCC, I.P.O.C.C., 2019. Special report on global warming of 1.5 C (SR15).

Irvine-Fynn, T.D.L., Moorman, B.J., Williams, J.L.M. and Walter, F.S.A., 2006. Seasonal changes in ground-penetrating radar signature observed at a polythermal glacier, Bylot Island, Canada, *Earth Surface Processes and Landforms: The Journal of the British Geomorphological Research Group*, 31(7), pp. 892-909.

Jacobs, S.S., Jenkins, A., Giulivi, C.F. and Dutrieux, P., 2011. Stronger ocean circulation and increased melting under Pine Island Glacier ice shelf, *Nature Geoscience*, 4(8), pp. 519-523.

Jakobsson, M., Hogan, K.A., Mayer, L.A., Mix, A., Jennings, A., Stoner, J., Eriksson, B., Jerram, K., Mohammad, R., Pearce, C. and Reilly, B., 2018. The Holocene retreat dynamics and stability of Petermann Glacier in northwest Greenland, *Nature communications*, 9(1), p.2104.

James, T.D., Murray, T., Selmes, N., Scharrer, K. and O'Leary, M., 2014. Buoyant flexure and basal crevassing in dynamic mass loss at Helheim Glacier, *Nature Geoscience*, 7(8), pp. 593-596.

Jamieson, S.S., Stokes, C.R., Ross, N., Rippin, D.M., Bingham, R.G., Wilson, D.S., Margold, M. and Bentley, M.J., 2014. The glacial geomorphology of the Antarctic Ice Sheet bed, *Antarctic Science*, 26(6), pp. 724-741.

Jeofry, H., Ross, N., Corr, H.F., Li, J., Morlighem, M., Gogineni, P. and Siegert, M.J., 2018. A new bed elevation model for the Weddell Sea sector of the West Antarctic Ice Sheet, *Earth System Science Data*, 10(2), pp. 711-725.

Jezek K, Wu X, Paden J and Leuschen C, 2013. Radar mapping of Isunnguata Sermia, Greenland, *Journal of Glaciology*, 59(218), pp. 1135-1146.

Jezek, K.C., Clough, J.W., Bentley, C.R. and Shabtaie, S., 1978. Dielectric permittivity of glacier ice measured in situ by radar wide-angle reflection, *Journal of Glaciology*, 21(85), pp. 315-329.

Jiskoot, H., Curran, C.J., Tessler, D.L. and Shenton, L.R., 2009. Changes in Clemenceau Icefield and Chaba Group glaciers, Canada, related to hypsometry,

tributary detachment, length–slope and area–aspect relations, *Annals of Glaciology*, 50(53), pp. 133-143.

Jordan, T.M., Cooper, M.A., Schroeder, D.M., Williams, C.N., Paden, J.D., Siegert, M.J. and Bamber, J.L., 2017. Self-affine subglacial roughness: Consequences for radar scattering and basal water discrimination in northern Greenland, *Cryosphere*, pp. 1247-1264.

Joughin, I. 2018, updated 2019. MEaSUREs Greenland Quarterly Ice Sheet Velocity Mosaics from SAR and Landsat, Version 1. [greenland_vel_mosaic_2018-09-01_2018-11-30]. Boulder, Colorado USA. NASA National Snow and Ice Data Center Distributed Active Archive Center. doi: https://doi.org/10.5067/1Q1AM4U8Y892. [08/09/2020].

Joughin, I., B. Smith, I. Howat, T. Scambos, and T. Moon. 2010. Greenland flow variability from ice-sheet-wide velocity mapping, *Journal of Glaciology*. 56, pp. 415-430.

Joughin, I., B. Smith, and I. Howat. 2018. Greenland Ice Mapping Project: ice flow velocity variation at sub-monthly to decadal timescales, *The Cryosphere*. 12, pp. 2211-2227.

Joughin, I. and Alley, R.B., 2011. Stability of the West Antarctic Ice Sheet in a warming world, *Nature Geoscience*, 4(8), pp. 506-513.

Joughin, I., Howat, I., Alley, R.B., Ekstrom, G., Fahnestock, M., Moon, T., Nettles, M., Truffer, M. and Tsai, V.C., 2008. Ice-front variation and tidewater behavior on Helheim and Kangerdlugssuaq Glaciers, Greenland, *Journal of Geophysical Research: Earth Surface*, 113(F1). p.F01004.

Joughin, I., Smith, B.E. and Holland, D.M., 2010. Sensitivity of 21st century sea level to ocean-induced thinning of Pine Island Glacier, Antarctica, *Geophysical Research Letters*, 37(20), p.L20502.

Joughin, I., Smith, B.E. and Medley, B., 2014. Marine ice sheet collapse potentially under way for the Thwaites Glacier Basin, West Antarctica, *Science*, 344(6185), pp. 735-738.

Journel, A.G. and Huijbregts, C.J., 1978. Mining geostatistics (Vol. 600). London: Academic press.

Kendrick, A.K., Schroeder, D.M., Chu, W., Young, T.J., Christoffersen, P., Todd, J., Doyle, S.H., Box, J.E., Hubbard, A., Hubbard, B. and Brennan, P.V., 2018. Surface meltwater impounded by seasonal englacial storage in West Greenland, *Geophysical Research Letters*, 45(19), pp. 10-474.

Khan, S.A., Aschwanden, A., Bjørk, A.A., Wahr, J., Kjeldsen, K.K. and Kjaer, K.H., 2015. Greenland Ice Sheet mass balance: a review, *Reports on Progress in Physics*, 78(4), p.046801.

King, M.D., Howat, I.M., Jeong, S., Noh, M.J., Wouters, B., Noël, B. and van den Broeke, M.R., 2018. Seasonal to decadal variability in ice discharge from the Greenland Ice Sheet. The cryosphere, 12(12), p.3813.

Kjær, K.H., Larsen, N.K., Binder, T., Bjørk, A.A., Eisen, O., Fahnestock, M.A., Funder, S., Garde, A.A., Haack, H., Helm, V. and Houmark-Nielsen, M., 2018. A large impact crater beneath Hiawatha Glacier in northwest Greenland, *Science advances*, 4(11), p.eaar8173.

Koerner, R.M., 1977. Ice thickness measurements and their implications with respect to past and present ice volumes in the Canadian High Arctic ice caps, *Canadian Journal of Earth Sciences*, 14(12), pp. 2697-2705.

Kolmogorov, A.N., 1930. On the strong law of large numbers. *Theory of Probability and Mathematical Statistics*, pp. 59-60.

Krige, D.G., 1951. A statistical approach to some basic mine valuation problems on the Witwatersrand, *Journal of the Southern African Institute of Mining and Metallurgy*, 52(6), pp.119-139.

Lapazaran JJ, Otero J, Martín-Español A. and Navarro FJ, 2016. On the errors involved in ice-thickness estimates I: ground-penetrating radar measurement errors, *Journal of Glaciology*, 62(236), pp. 1008-1020.

Larour, E., Seroussi, H., Morlighem, M. and Rignot, E., 2012. Continental scale, high order, high spatial resolution, ice sheet modeling using the Ice Sheet System Model (ISSM), *Journal of Geophysical Research: Earth Surface*, 117(F1), p.F01022.

Larsen, C.F., Motyka, R.J., Arendt, A.A., Echelmeyer, K.A. and Geissler, P.E., 2007. Glacier changes in southeast Alaska and northwest British Columbia and

contribution to sea level rise, *Journal of Geophysical Research: Earth Surface*, 112(F1), p.F01007.

Layberry, R.L. and Bamber, J.L., 2001. A new ice thickness and bed data set for the Greenland Ice Sheet: 2. Relationship between dynamics and basal topography, *Journal of Geophysical Research: Atmospheres*, 106(D24), pp. 33781-33788.

Le Brocq, A.M., Payne, A.J. and Vieli, A., 2010. An improved Antarctic dataset for high resolution numerical ice sheet models (ALBMAP v1), *Earth system science data*, 2(2), pp. 247-260.

Lenaerts, J.T., van Angelen, J.H., van den Broeke, M.R., Gardner, A.S., Wouters, B. and van Meijgaard, E., 2013. Irreversible mass loss of Canadian Arctic Archipelago glaciers, *Geophysical Research Letters*, 40(5), pp. 870-874.

Lindbäck, K., Pettersson, R., Doyle, S.H., Helanow, C., Jansson, P., Kristensen, S.S., Stenseng, L., Forsberg, R. and Hubbard, A.L., 2014. High-resolution ice thickness and bed topography of a land-terminating section of the Greenland Ice Sheet, *Earth System Science Data*, 6(2), pp. 331-338.

Linsbauer, A., Paul, F. and Haeberli, W., 2012. Modeling glacier thickness distribution and bed topography over entire mountain ranges with GlabTop: Application of a fast and robust approach, *Journal of Geophysical Research: Earth Surface*, 117(F3), p.F03007.

Lythe, M.B. and Vaughan, D.G., 2001. BEDMAP: A new ice thickness and subglacial topographic model of Antarctica, *Journal of Geophysical Research: Solid Earth*, 106(B6), pp. 11335-11351.

MacGregor, J.A., Catania, G.A., Conway, H., Schroeder, D.M., Joughin, I., Young, D.A., Kempf, S.D. and Blankenship, D.D., 2013. Weak bed control of the eastern shear margin of Thwaites Glacier, West Antarctica, *Journal of Glaciology*, 59(217), pp. 900-912.

MacGregor, J.A., Fahnestock, M.A., Catania, G.A., Paden, J.D., Gogineni, S.P., Young, S.K., Rybarski, S.C., Mabrey, A.N., Wagman, B.M. and Morlighem, M., 2015. Radiostratigraphy and age structure of the Greenland Ice Sheet, *Journal of Geophysical Research: Earth Surface*, 120(2), pp. 212-241.

Macheret, Y.Y. and Moskalevsky, M.Y., 1999. Study of Lange Glacier on King George Island, Antarctica, *Annals of Glaciology*, 29, pp. 202-206.

Macheret, Y.Y., Otero, J., Navarro, F.J., Vasilenko, E.V., Corcuera, M.I., Cuadrado, M.L. and Glazovsky, A.F., 2009. Ice thickness, internal structure and subglacial topography of Bowles Plateau ice cap and the main ice divides of Livingston Island, Antarctica, by ground-based radio-echo sounding, *Annals of glaciology*, 50(51), pp. 49-56.

MacKie, E.J., Schroeder, D.M., Caers, J., Siegfried, M.R. and Scheidt, C., Antarctic Topographic Realizations and Geostatistical Modeling Used to Map Subglacial Lakes, *Journal of Geophysical Research: Earth Surface*, 25(3), p.e2019JF005420.

Mankoff, K.D., Colgan, W., Solgaard, A., Karlsson, N.B., Ahlstrøm, A.P., Van As, D., Box, J.E., Khan, S.A., Kjeldsen, K.K., Mouginot, J. and Fausto, R.S., 2019. Greenland Ice Sheet solid ice discharge from 1986 through 2017, *Earth System Science Data*, 11(2), pp. 769-786.

Margold, M., Jansson, K.N., Kleman, J. and Stroeven, A.P., 2013. Lateglacial ice dynamics of the Cordilleran Ice Sheet in northern British Columbia and southern Yukon Territory: retreat pattern of the Liard Lobe reconstructed from the glacial landform record, *Journal of Quaternary Science*, 28(2), pp. 180-188.

Marzeion, B., Champollion, N., Haeberli, W., Langley, K., Leclercq, P. and Paul, F., 2017. Observation-based estimates of global glacier mass change and its contribution to sea-level change. In: Integrative Study of the Mean Sea Level and Its Components (pp. 107-132). Springer, Cham.

Matheron, G., 1963. Principles of geostatistics, *Economic geology*, 58(8), pp. 1246-1266.

McBratney, A. B., and Webster, R., 1986. Choosing Functions for Semi-variograms of Soil Properties and Fitting Them to Sampling Estimates, *Journal of Soil Science*, 37, pp. 617–639

Mcgrath, D., Sass, L., O'Neel, S., Arendt, A. and Kienholz, C., 2017. Hypsometric control on glacier mass balance sensitivity in Alaska and northwest Canada, *Earth's Future*, 5(3), pp. 324-336.

McMillan, M., Leeson, A., Shepherd, A., Briggs, K., Armitage, T.W., Hogg, A., Kuipers Munneke, P., Van Den Broeke, M., Noel, B., van de Berg, W.J. and Ligtenberg, S., 2016. A high-resolution record of Greenland mass balance, *Geophysical Research Letters*, 43(13), pp. 7002-7010.

McNabb, R.W., Hock, R., O'Neel, S., Rasmussen, L.A., Ahn, Y., Braun, M., Conway, H., Herreid, S., Joughin, I., Pfeffer, W.T. and Smith, B.E., 2012. Using surface velocities to calculate ice thickness and bed topography: a case study at Columbia Glacier, Alaska, USA, *Journal of Glaciology*, 58(212), pp. 1151-1164.

Medrzycka, D., Copland, L., Van Wychen, W. and Burgess, D., 2019. Seven decades of uninterrupted advance of Good Friday Glacier, Axel Heiberg Island, Arctic Canada, *Journal of Glaciology*, 65(251), pp. 440-452.

Meier, M.F. and Post, A., 1987. Fast tidewater glaciers, *Journal of Geophysical Research: Solid Earth*, 92(B9), pp. 9051-9058.

Mercer, J.H., 1978. West Antarctic Ice Sheet and CO2 greenhouse effect: a threat of disaster, *Nature*, 271(5643), pp. 321-325.

Milillo, P., Rignot, E., Rizzoli, P., Scheuchl, B., Mouginot, J., Bueso-Bello, J. and Prats-Iraola, P., 2019. Heterogeneous retreat and ice melt of Thwaites Glacier, West Antarctica, *Science advances*, 5(1), p.eaau3433.

Millan R, Rignot E, Mouginot J, Wood M, Bjørk AA and Morlighem M, 2018. Vulnerability of Southeast Greenland Glaciers to Warm Atlantic Water From Operation IceBridge and Ocean Melting Greenland Data, *Geophysical Research Letters*, 45, pp. 2688-2696.

Millan, R., Mouginot, J. and Rignot, E., 2017. Mass budget of the glaciers and ice caps of the Queen Elizabeth Islands, Canada, from 1991 to 2015, *Environmental Research Letters*, 12(2), p.024016.

Millan, R., Rignot, E., Mouginot, J., Wood, M., Bjørk, A.A. and Morlighem, M., 2018. Vulnerability of southeast greenland glaciers to warm atlantic water from Operation Icebridge and Ocean Melting Greenland data, *Geophysical research letters*, 45(6), pp. 2688-2696.

Mitrovica, J.X., Gomez, N. and Clark, P.U., 2009. The sea-level fingerprint of West Antarctic collapse, *Science*, 323(5915), pp. 753-753.

Moon, T., Ahlstrøm, A., Goelzer, H., Lipscomb, W. and Nowicki, S., 2018. Rising oceans guaranteed: Arctic land ice loss and sea level rise, *Current climate change reports*, 4(3), pp. 211-222.

Morlighem M, Rignot E, Mouginot J, Seroussi H and Larour E, 2014. Deeply incised submarine glacial valleys beneath the Greenland Ice Sheet, *Nature Geoscience*, 7(6), p.418.

Morlighem, M., Rignot, E., Binder, T., Blankenship, D., Drews, R., Eagles, G., Eisen, O., Ferraccioli, F., Forsberg, R., Fretwell, P. and Goel, V., 2020. Deep glacial troughs and stabilizing ridges unveiled beneath the margins of the Antarctic Ice Sheet, *Nature Geoscience,* 13(2), pp. 132-137.

Morlighem, M., Rignot, E., Seroussi, H., Larour, E., Ben Dhia, H. and Aubry, D., 2011. A mass conservation approach for mapping glacier ice thickness. *Geophysical Research Letters*, 38(19), p.L19503.

Morlighem, M., Williams, C.N., Rignot, E., An, L., Arndt, J.E., Bamber, J.L., Catania, G., Chauché, N., Dowdeswell, J.A., Dorschel, B. and Fenty, I., 2017. BedMachine v3: Complete bed topography and ocean bathymetry mapping of Greenland from multibeam echo sounding combined with mass conservation, *Geophysical research letters*, 44(21), pp. 11-51.

Mouginot, J., Rignot, E., Bjørk, A.A., Van Den Broeke, M., Millan, R., Morlighem, M., Noël, B., Scheuchl, B. and Wood, M., 2019. Forty-six years of Greenland Ice Sheet mass balance from 1972 to 2018, *Proceedings of the National Academy of Sciences*, 116(19), pp. 9239-9244.

NASA. (2019). NASA's Operation IceBridge Completes Eleven Years of Polar Surveys. Available: https://www.nasa.gov/feature/goddard/2019/nasa-s-operation-icebridge-completes-eleven-years-of-polar-surveys. Last accessed 31st Mar 2020.

Navarro, F.J., Lapazaran, J., Martín-Español, A. and Otero, J., 2016. Ground-penetrating radar studies in Svalbard aimed to the calculation of the ice volume of its glaciers, *Cuadernos de Investigación Geográfica*, 42(2), pp. 399-414.

Nias, I.J., Cornford, S.L. and Payne, A.J., 2018. New mass-conserving bedrock topography for Pine Island Glacier impacts simulated decadal rates of mass loss, *Geophysical Research Letters*, 45(7), pp. 3173-3181.

Nick, F.M., Vieli, A., Andersen, M.L., Joughin, I., Payne, A., Edwards, T.L., Pattyn, F. and van de Wal, R.S., 2013. Future sea-level rise from Greenland's main outlet glaciers in a warming climate, *Nature*, 497(7448), pp. 235-238.

Noël, B., van de Berg, W.J., Lhermitte, S., Wouters, B., Schaffer, N. and van den Broeke, M.R., 2018. Six decades of glacial mass loss in the Canadian Arctic Archipelago, *Journal of Geophysical Research: Earth Surface*, 123(6), pp. 1430-1449.

Noël, B., Van De Berg, W.J., Van Meijgaard, E., Kuipers Munneke, P., Van De Wal, R. and Van Den Broeke, M.R., 2015. Evaluation of the updated regional climate model RACMO2. 3: summer snowfall impact on the Greenland Ice Sheet, *The Cryosphere*, 9(5), pp. 1831-1844.

Noh, M.J. and Howat, I.M., 2015. Automated stereo-photogrammetric DEM generation at high latitudes: Surface Extraction with TIN-based Search-space Minimization (SETSM) validation and demonstration over glaciated regions, *GIScience & Remote Sensing*, 52(2), pp. 198-217.

Noh, M.J. and Howat, I.M., 2017. The surface extraction from TIN based search-space minimization (SETSM) algorithm, *ISPRS Journal of Photogrammetry and Remote Sensing*, 100(129), pp. 55-76.

Noh, M.J. and Howat, I.M., 2018. Automatic relative RPC image model bias compensation through hierarchical image matching for improving DEM quality, *ISPRS journal of photogrammetry and remote sensing*, 136, pp. 120-133.

Nowicki, S.M., Payne, T., Larour, E., Seroussi, H., Goelzer, H., Lipscomb, W., Gregory, J., Abe-Ouchi, A. and Shepherd, A., 2016. Ice sheet model intercomparison project (ISMIP6) contribution to CMIP6, *Geoscientific model development*, 9(12), p.4521.

Oerlemans, J., 1997. A flowline model for Nigardsbreen, Norway: projection of future glacier length based on dynamic calibration with the historic record, *Annals of Glaciology*, 24, pp. 382-389.

Oliver, M.A., 1990. Kriging: A Method of Interpolation for Geographical Information Systems, *International Journal of Geographic Information Systems,* 4(3), pp. 313–332.

Oppenheimer, M., Glavovic, B., Hinkel, J., van de Wal, R., Magnan, A.K., Abd-Elgawad, A., Cai, R., Cifuentes-Jara, M., Deconto, R.M., Ghosh, T. and Hay, J., 2019, Sea level rise and implications for low lying Islands, coasts and communities. In: *IPCC Special Report on the Ocean and Cryosphere in a Changing Climate*, edited by: H.-O. Pörtner, D. C. R., V. Masson-Delmotte, P. Zhai, M. Tignor, E. Poloczanska, K. Mintenbeck, A. Alegría, M. Nicolai, A. Okem, J. Petzold, B. Rama, N.M. Weyer, 2019.

Overland, J.E., Dethloff, K., Francis, J.A., Hall, R.J., Hanna, E., Kim, S.J., Screen, J.A., Shepherd, T.G. and Vihma, T., 2016. Nonlinear response of mid-latitude weather to the changing Arctic, *Nature Climate Change*, 6(11), pp. 992-999.

Paden J, Akins T, Dunson D, Allen C and Gogineni P, 2010. Ice-sheet bed 3-D tomography, *Journal of Glaciology*, 56(195), pp. 3-11.

Palmer, S., McMillan, M. and Morlighem, M., 2015. Subglacial lake drainage detected beneath the Greenland Ice Sheet, *Nature communications*, 6(1), pp. 1-7.

Paterson, W.S.B., 1994. Physics of glaciers. Butterworth-Heinemann. Oxford.

Patton, H., Swift, D.A., Clark, C.D., Livingstone, S.J. and Cook, S.J., 2016. Distribution and characteristics of overdeepenings beneath the Greenland and Antarctic Ice Sheets: Implications for overdeepening origin and evolution, *Quaternary Science Reviews*, 148, pp. 128-145.

Pattyn, F., Ritz, C., Hanna, E., Asay-Davis, X., DeConto, R., Durand, G., Favier, L., Fettweis, X., Goelzer, H., Golledge, N.R. and Munneke, P.K., 2018. The Greenland and Antarctic Ice Sheets under 1.5 C global warming, *Nature climate change*, 8(12), pp. 1053-1061.

Peters, M. E., D. D. Blankenship, and D. L. Morse. 2005. Analysis techniques for coherent airborne radar sounding: Application to West Antarctic ice streams, *Journal Of Geophysical Research*, 110(B6), p.B06303

Plewes, L.A. and Hubbard, B., 2001. A review of the use of radio-echo sounding in glaciology, *Progress in Physical Geography*, 25(2), pp. 203-236.

Popov, S., 2020. Fifty-five years of Russian radio-echo sounding investigations in Antarctica, *Annals of Glaciology*, 61(81), pp. 14–24.

Porter, Claire; Morin, Paul; Howat, Ian; Noh, Myoung-Jon; Bates, Brian; Peterman, Kenneth; Keesey, Scott; Schlenk, Matthew; Gardiner, Judith; Tomko, Karen; Willis, Michael; Kelleher, Cole; Cloutier, Michael; Husby, Eric; Foga, Steven; Nakamura, Hitomi; Platson, Melisa; Wethington, Michael, Jr.; Williamson, Cathleen; Bauer, Gregory; Enos, Jeremy; Arnold, Galen; Kramer, William; Becker, Peter; Doshi, Abhijit; D'Souza, Cristelle; Cummens, Pat; Laurier, Fabien; Bojesen, Mikkel, 2018, "ArcticDEM", https://doi.org/10.7910/DVN/OHHUKH, Harvard Dataverse, V1, [31/03/2020].

Post, A., O'Neel, S., Motyka, R.J. and Streveler, G., 2011. A complex relationship between calving glaciers and climate, *Eos, Transactions American Geophysical Union*, 92(37), pp. 305-306.

Pritchard, H.D., 2014. Bedgap: where next for Antarctic subglacial mapping?, *Antarctic Science*, 26(6), pp. 742-757.

Pritchard, H.D., Arthern, R.J., Vaughan, D.G. and Edwards, L.A., 2009. *Extensive dynamic thinning on the margins of the Greenland and Antarctic Ice Sheets*, *Nature*, 461(7266), pp. 971-975.

Radić, V. and Hock, R., 2010. Regional and global volumes of glaciers derived from statistical upscaling of glacier inventory data, *Journal of Geophysical Research: Earth Surface*, 115(F1), p. F01010.

Radić, V., Bliss, A., Beedlow, A.C., Hock, R., Miles, E. and Cogley, J.G., 2014. Regional and global projections of twenty-first century glacier mass changes in response to climate scenarios from global climate models, *Climate Dynamics*, 42(1-2), pp. 37-58.

Rignot E and Kanagaratnam P, 2006. Changes in the velocity structure of the Greenland Ice Sheet, *Science*, 311(5763), pp. 986-990.

Rignot, E. and Mouginot, J., 2012. Ice flow in Greenland for the international polar year 2008–2009, *Geophysical Research Letters*, 39(11), p.L11501.

Rignot, E., Box, J.E., Burgess, E. and Hanna, E., 2008. Mass balance of the Greenland Ice Sheet from 1958 to 2007, *Geophysical Research Letters*, 35(20), p.L20502.

Rignot, E., Fenty, I., Xu, Y., Cai, C., Velicogna, I., Cofaigh, C.Ó., Dowdeswell, J.A., Weinrebe, W., Catania, G. and Duncan, D., 2016. Bathymetry data reveal glaciers vulnerable to ice-ocean interaction in Uummannaq and Vaigat glacial fjords, west Greenland, *Geophysical Research Letters*, 43(6), pp. 2667-2674.

Rignot, E., Mouginot, J., Scheuchl, B., van den Broeke, M., van Wessem, M.J. and Morlighem, M., 2019. Four decades of Antarctic Ice Sheet mass balance from 1979–2017, *Proceedings of the National Academy of Sciences*, 116(4), pp. 1095-1103.

Ritz, C., Edwards, T.L., Durand, G., Payne, A.J., Peyaud, V. and Hindmarsh, R.C., 2015. Potential sea-level rise from Antarctic ice-sheet instability constrained by observations, *Nature*, 528(7580), pp. 115-118.

Robin, G.D.Q., 1975. Velocity of radio waves in ice by means of a bore-hole interferometric technique, *Journal of Glaciology*, 15(73), pp. 151-159.

Rodriguez-Morales, F., Gogineni, S., Leuschen, C.J., Paden, J.D., Li, J., Lewis, C.C., Panzer, B., Alvestegui, D.G.G., Patel, A., Byers, K. and Crowe, R., 2013. Advanced multifrequency radar instrumentation for polar research, *IEEE Transactions on Geoscience and Remote Sensing*, 52(5), pp. 2824-2842.

Ross, N., Bingham, R.G., Corr, H.F., Ferraccioli, F., Jordan, T.A., Le Brocq, A., Rippin, D.M., Young, D., Blankenship, D.D. and Siegert, M.J., 2012. Steep reverse bed slope at the grounding line of the Weddell Sea sector in West Antarctica, *Nature Geoscience*, 5(6), pp. 393-396.

Rutishauser, A., Blankenship, D.D., Sharp, M., Skidmore, M.L., Greenbaum, J.S., Grima, C., Schroeder, D.M., Dowdeswell, J.A. and Young, D.A., 2018. Discovery of a hypersaline subglacial lake complex beneath Devon Ice Cap, Canadian Arctic, *Science advances*, 4(4), p.eaar4353.

Schaffer, J., Kanzow, T., von Appen, W.J., von Albedyll, L., Arndt, J.E. and Roberts, D.H., 2020. Bathymetry constrains ocean heat supply to Greenland's largest glacier tongue, *Nature Geoscience*, 13, pp. 1-5.

Schoof, C. 2002. Basal perturbations under ice streams: form drag and surface expression, *Journal of Glaciology*, 48(162), pp. 407-416.

Schoof, C., 2007. Ice sheet grounding line dynamics: Steady states, stability, and hysteresis, *Journal of Geophysical Research: Earth Surface*, 112(F3), p.F03S28.

Schoof, C., Davis, A.D. and Popa, T.V., 2017. Boundary layer models for calving marine outlet glaciers, *The Cryosphere*, 11(5), p.2283.

Schroeder, D.M., Bingham, R.G., Blankenship, D.D., Christianson, K., Eisen, O., Flowers, G.E., Karlsson, N.B., Koutnik, M.R., Paden, J.D. and Siegert, M.J., 2020. Five decades of radioglaciology, *Annals of Glaciology*, 61(81), pp. 1-13.

Schroeder, D.M., Romero-Wolf, A., Carrer, L., Grima, C., Campbell, B.A., Kofman, W., Bruzzone, L. and Blankenship, D.D., 2016. Assessing the potential for passive radio sounding of Europa and Ganymede with RIME and REASON, *Planetary and Space Science*, 134, pp. 52-60.

Sergienko, O.V., 2013. Glaciological twins: basally controlled subglacial and supraglacial lakes, *Journal of Glaciology*, 59(213), pp. 3-8.

Seroussi, H., Morlighem, M., Rignot, E., Larour, E., Aubry, D., Ben Dhia, H. and Kristensen, S.S., 2011. Ice flux divergence anomalies on 79north Glacier, Greenland, *Geophysical Research Letters*, 38(9), p.L09501.

Seroussi, H., Nowicki, S., Simon, E., Abe-Ouchi, A., Albrecht, T., Brondex, J., Cornford, S., Dumas, C., Gillet-Chaulet, F., Goelzer, H. and Golledge, N.R., 2019. initMIP-Antarctica: an ice sheet model initialization experiment of ISMIP6, *The Cryosphere*, 13, pp. 1441-1471.

Shepherd, A. and Nowicki, S., 2017. Improvements in ice-sheet sea-level projections, *Nature Climate Change*, 7(10), p.672.

Shepherd, A., Du, Z., Benham, T.J., Dowdeswell, J.A. and Morris, E.M., 2007. Mass balance of Devon Ice Cap, Canadian Arctic, *Annals of Glaciology*, 46, pp. 249-254.

Shepherd, A., Ivins, E., Rignot, E., Smith, B., Van Den Broeke, M., Velicogna, I., Whitehouse, P., Briggs, K., Joughin, I., Krinner, G., Nowicki, S., Payne, T., Scambos, T., Schlegel, N., A, G., Agosta, C., Ahlstrøm, A., Babonis, G., Barletta, V.R., Bjørk, A.A.,

The IMBIE Team (Shepherd, A., et al.), 2019. Mass balance of the Greenland Ice Sheet from 1992 to 2018, *Nature*, 579(7798), pp. 233-239.

Shepherd, A., Ivins, E., Rignot, E., Smith, B., Van Den Broeke, M., Velicogna, I., Whitehouse, P., Briggs, K., Joughin, I., Krinner, G. and Nowicki, S., 2018. Mass balance of the Antarctic Ice Sheet from 1992 to 2017, *Nature*, 558, pp. 219-222.

Shepherd, A., Ivins, E.R., Geruo, A., Barletta, V.R., Bentley, M.J., Bettadpur, S., Briggs, K.H., Bromwich, D.H., Forsberg, R., Galin, N. and Horwath, M., 2012. A reconciled estimate of ice-sheet mass balance, *Science*, 338(6111), pp. 1183-1189.

Solgaard, A.M., Simonsen, S.B., Grinsted, A., Mottram, R., Karlsson, N.B., Hansen, K., Kusk, A. and Sørensen, L.S., 2020. Hagen Bræ: A surging glacier in North Greenland–35 years of observations, *Geophysical Research Letters*, 47(6), p.e2019GL085802

Sorge, E., 1933. The scientific results of the Wegener expeditions to Greenland, *The Geographical Journal*, 81(4), pp. 333-344.

Stearns, L.A. and Van der Veen, C.J., 2018. Friction at the bed does not control fast glacier flow, *Science*, 361(6399), pp. 273-277.

Stibal, M., Box, J.E., Cameron, K.A., Langen, P.L., Yallop, M.L., Mottram, R.H., Khan, A.L., Molotch, N.P., Chrismas, N.A., Quaglia, F.C. and Remias, D., 2017. Algae drive enhanced darkening of bare ice on the Greenland Ice Sheet, *Geophysical Research Letters*, 44(22), pp. 11-463.

Studinger M., Koenig L., Martin S. and Sonntag J., 2010. Operation icebridge: Using instrumented aircraft to bridge the observational gap between icesat and icesat-2, *2010 IEEE International Geoscience and Remote Sensing Symposium, Honolulu, HI*, 2010, pp. 1918-1919

Sugden, D.E., 1974. Landscapes of glacial erosion in Greenland and their relationship to ice, topographic and bedrock conditions. In: Waters, R. S., and Brown, E. H., ed. *Progress in geomorphology*. London, Institute of British Geographers, pp. 177–95.

Sugden, D.E., and John, B.S., 1976. Glaciers and Landscape: A Geomorphological Approach, Arnold, London.

Sugden, D.E., 1978. Glacial erosion by the Laurentide ice sheet, *Journal of Glaciology*, 20(83), pp. 367-391.

Sun, S., Cornford, S.L., Liu, Y. and Moore, J.C., 2014. Dynamic response of Antarctic ice shelves to bedrock uncertainty, *The Cryosphere*, 8(4), pp. 1561-1576.

Sundal, A.V., Shepherd, A., Nienow, P., Hanna, E., Palmer, S., and Huybrechts, P., 2009. Evolution of supra-glacial lakes across the Greenland Ice Sheet, *Remote Sensing of Environment*, 113(10), pp. 2164-2171.

Sundal, A.V., Shepherd, A., Nienow, P., Hanna, E., Palmer, S., and Huybrechts, P., 2011. Melt-induced speed-up of Greenland Ice Sheet offset by efficient subglacial drainage, *Nature*, 469(7331), p.521.

Sutterley, T.C., Velicogna, I., Rignot, E., Mouginot, J., Flament, T., Van Den Broeke, M.R., Van Wessem, J.M. and Reijmer, C.H., 2014. Mass loss of the Amundsen Sea Embayment of West Antarctica from four independent techniques, *Geophysical Research Letters*, 41(23), pp. 8421-8428.

Tamisiea, M.E. and Mitrovica, J.X., 2011. The moving boundaries of sea level change: Understanding the origins of geographic variability, *Oceanography*, 24(2), pp. 24-39.

Tedesco, M., Mote, T., Fettweis, X., Hanna, E., Jeyaratnam, J., Booth, J.F., Datta, R. and Briggs, K., 2016. Arctic cut-off high drives the poleward shift of a new Greenland melting record, *Nature communications*, 7(1), pp. 1-6.

Tedstone, A.J., Nienow, P.W., Gourmelen, N., Dehecq, A., Goldberg, D. and Hanna, E., 2015. Decadal slowdown of a land-terminating sector of the Greenland Ice Sheet despite warming, *Nature*, 526(7575), pp. 692-695.

Trusel, L.D., Das, S.B., Osman, M.B., Evans, M.J., Smith, B.E., Fettweis, X., McConnell, J.R., Noël, B.P. and van den Broeke, M.R., 2018. Nonlinear rise in Greenland runoff in response to post-industrial Arctic warming, *Nature*, 564(7734), pp. 104-108.

Turchetti, S., Dean, K., Naylor, S., and Siegert, M., 2008. Accidents and opportunities: a history of the radio echo-sounding of Antarctica, 1958–79, *The British Journal for the History of Science*, 41(3), pp. 417-444.

van de Wal, R.S.W., Zhang, X., Minobe, S., Jevrejeva, S., Riva, R.E.M., Little, C., Richter, K. and Palmer, M.D., 2019. Uncertainties in long-term twenty-first century

process-based coastal sea-level projections, *Surveys in Geophysics*, 40(6), pp. 1655-1671.

Van den Broeke, M.R., Enderlin, E.M., Howat, I.M., Kuipers Munneke, P., Noël, B.P., Jan Van De Berg, W., Van Meijgaard, E. and Wouters, B., 2016. On the recent contribution of the Greenland ice sheet to sea level change, *The Cryosphere*, 10(5), pp. 1933-1946.

Van den Broeke, M., Bamber, J., Ettema, J., Rignot, E., Schrama, E., van de Berg, W.J., van Meijgaard, E., Velicogna, I. and Wouters, B., 2009. Partitioning recent Greenland mass loss, *Science*, 326(5955), pp. 984-986.

Van Der Veen, C.J. and Whillans, I.M., 1989. Force budget: I. Theory and numerical methods, *Journal of Glaciology*, 35(119), pp. 53-60.

Van der Veen, C.J., 1985. Response of a marine ice sheet to changes at the grounding line, *Quaternary Research*, 24(3), pp. 257-267.

Van Der Veen, C.J., 1996. Tidewater calving, *Journal of Glaciology*, 42(141), pp. 375-385.

Van Wychen, W., Burgess, D.O., Gray, L., Copland, L., Sharp, M., Dowdeswell, J.A. and Benham, T.J., 2014. Glacier velocities and dynamic ice discharge from the Queen Elizabeth Islands, Nunavut, Canada, *Geophysical Research Letters*, 41(2), pp. 484-490.

Van Wychen, W., Copland, L. and Burgess, D., 2020. Ice Masses of the Eastern Canadian Arctic Archipelago. In: *Landscapes and Landforms of Eastern Canada* (pp. 297-314). Springer, Cham.

Van Wychen, W., Davis, J., Burgess, D.O., Copland, L., Gray, L., Sharp, M. and Mortimer, C., 2016. Characterizing interannual variability of glacier dynamics and dynamic discharge (1999–2015) for the ice masses of Ellesmere and Axel Heiberg Islands, Nunavut, Canada, *Journal of Geophysical Research: Earth Surface*, 121(1), pp. 39-63.

Van Wychen, W., Davis, J., Copland, L., Burgess, D.O., Gray, L., Sharp, M., Dowdeswell, J.A. and Benham, T.J., 2017. Variability in ice motion and dynamic discharge from Devon Ice Cap, Nunavut, Canada, *Journal of Glaciology*, 63(239), pp. 436-449.

Vaughan, D.G., 2008. West Antarctic Ice Sheet collapse–the fall and rise of a paradigm, *Climatic Change*, 91(1-2), pp. 65-79.

Vaughan, D.G., J.C. Comiso, I. Allison, J. Carrasco, G. Kaser, R. Kwok, P. Mote, T. Murray, F. Paul, J. Ren, E. Rignot, O. Solomina, K. Steffen and T. Zhang, 2013: Observations: Cryosphere. In: *Climate Change 2013: The Physical Science Basis. Contribution of Working Group I to the Fifth Assessment Report of the Intergovernmental Panel on Climate Change* [Stocker, T.F., D. Qin, G.-K. Plattner, M. Tignor, S.K. Allen, J. Boschung, A. Nauels, Y. Xia, V. Bex and P.M. Midgley (eds.)]. Cambridge University Press, Cambridge, United Kingdom and New York, NY, USA.

Velicogna, I. and Wahr, J., 2006. Measurements of time-variable gravity show mass loss in Antarctica, *Science*, 311(5768), pp. 1754-1756.

Vieli, A., Funk, M. and Blatter, H., 2001. Flow dynamics of tidewater glaciers: a numerical modelling approach, *Journal of Glaciology*, 47(159), pp. 595-606.

WCRP Global Sea Level Budget Group: Global sea-level budget 1993–present, Earth Syst. Sci. Data, 10(3), pp. 1551–1590

WGMS, W., 2017. Fluctuations of glaciers database.

White, A. and Copland, L., 2018. Area change of glaciers across Northern Ellesmere Island, Nunavut, between~ 1999 and~ 2015, *Journal of Glaciology*, 64(246), pp. 609-623.

Williams, C.N., Cornford, S.L., Jordan, T.M., Dowdeswell, J.A., Siegert, M.J., Clark, C.D., Swift, D.A., Sole, A., Fenty, I. and Bamber, J.L., 2017. Generating synthetic fjord bathymetry for coastal Greenland, *Cryosphere Discussions*, 11(1), pp. 363-380.

Wingham, D.J., Shepherd, A., Muir, A. and Marshall, G.J., 2006. Mass balance of the Antarctic Ice Sheet, *Philosophical Transactions of the Royal Society A: Mathematical, Physical and Engineering Sciences*, 364(1844), pp. 1627-1635.

WIRL. (2020). *Summer 2020 loss of Arctic ice shelves*. Available: https://wirl.carleton.ca/research/ice/ice-shelves/calving-2020/. Last accessed 14/09/2020.

Wouters, B., Bamber, J.L., Van den Broeke, M.R., Lenaerts, J.T.M. and Sasgen, I., 2013. Limits in detecting acceleration of ice sheet mass loss due to climate variability, *Nature Geoscience*, 6(8), pp. 613-616.

Young, D.A., Roberts, J.L., Ritz, C., Frezzotti, M., Quartini, E., Cavitte, M.G., Tozer, C.R., Steinhage, D., Urbini, S., Corr, H.F. and Van Ommen, T., 2017. High-resolution boundary conditions of an old ice target near Dome C, Antarctica, *The Cryosphere*, 11(4), pp.1897-1911.

Young, N.E. and Briner, J.P., 2015. Holocene evolution of the western Greenland Ice Sheet: Assessing geophysical ice-sheet models with geological reconstructions of ice-margin change, *Quaternary Science Reviews*, 114, pp. 1-17.

Zemp, M., Huss, M., Thibert, E., Eckert, N., McNabb, R., Huber, J., Barandun, M., Machguth, H., Nussbaumer, S.U., Gärtner-Roer, I. and Thomson, L., 2019. Global glacier mass changes and their contributions to sea-level rise from 1961 to 2016, *Nature*, 568(7752), pp. 382-386.

Appendix

Table A2.1 ArcticDEM tiles used in this study

Greenland	
Inglefield Land	29_36_2m_v3.0
Kangerlussuaq	16_38_2m_v3.0
Peary Land	31_44_2m_v3.0
Canada	
Mackenzie Mountains (EGA)	39_12_2m_v3.0
CAA POW PGA	31_32_2m_v3.0
CAA Devon island PGA	28_30_2m_v3.0

Table A3.1 Probability and descriptive statistics of deviation magnitude and sign for all simulations. To use means as correction factors add to input elevation if negative and subtract if positive

		Probability (scale m)								Descriptive statistics				
		-100	-10	-1	-0.1	0.1	1	10	100	mean (m)	std (m)	sum (m)	skew	kurt
Interior														
MP														
MP all	Elevation province low	0	0.101	0.349	0.117	0.105	0.216	0.11	0.001	-0.031	11.424	-10110	1.432	15.399
	high	0	0.201	0.37	0.063	0.054	0.209	0.103	0	-3.384	15.38	-1120948	-0.884	11.947
	all	0	0.151	0.36	0.09	0.079	0.213	0.106	0	-1.708	13.652	-1131095	-0.318	14.008
ING	low	0	0.083	0.385	0.101	0.088	0.258	0.086	0	-0.328	9.524	-18598	0.337	13.169
	high	0	0.013	0.436	0.108	0.093	0.314	0.037	0	0.078	4.891	6807	0.978	11.042
	all	0	0.094	0.416	0.105	0.091	0.292	0.056	0	-0.082	7.086	-11828	0.46	18.397
KG	low	0	0.103	0.304	0.173	0.148	0.186	0.087	0	-0.8	9.494	-62265	0.21	12.738
	high	0	0.204	0.381	0.071	0.061	0.197	0.085	0	-3.168	10.578	-299329	-0.719	14.941
	all	0	0.158	0.346	0.117	0.1	0.192	0.086	0	-2.099	10.171	-361594	-0.403	14.256
PEA	low	0	0.073	0.38	0.136	0.13	0.205	0.076	0.001	-0.408	9.337	-42669	3.273	39.201
	high	0	0.188	0.48	0.04	0.032	0.17	0.089	0.001	-3.144	13.019	-219947	0.787	16.301
	all	0	0.119	0.42	0.098	0.091	0.191	0.081	0.001	-1.505	11.045	-262616	1.58	24.875
EGA	low	0	0.144	0.332	0.058	0.052	0.23	0.185	0	1.234	15.367	113382	1.039	7.792
	high	0.002	0.416	0.19	0.022	0.02	0.141	0.209	0	-7.699	25.474	-609310	-0.375	4.687
	all	0.001	0.27	0.266	0.041	0.037	0.189	0.196	0.001	-2.899	21.141	-495928	-0.382	6.458
Average all PGAS		0	0.155	0.361	0.089	0.079	0.214	0.106	0	-1.735	12.26	-188658	0.565	15.321
MO														
MO all	low	0	0.131	0.325	0.101	0.101	0.215	0.127	0	-0.397	12.074	-131149	0.713	13.312
	high	0	0.226	0.33	0.064	0.056	0.209	0.114	0	-3.63	15.912	-1201329	-0.771	8.943
	all	0	0.179	0.328	0.083	0.078	0.212	0.121	0	-2.015	14.218	-1332505	-0.413	10.902
ING	low	0	0.109	0.374	0.099	0.086	0.242	0.09	0	-0.674	10.065	-37646	0.722	10.473
	high	0	0.014	0.407	0.129	0.115	0.311	0.026	0	-0.022	4.424	-1976	0.478	8.755
	all	0	0.051	0.394	0.117	0.103	0.284	0.051	0	-0.275	7.161	-39622	0.741	16.439
KG	low	0	0.147	0.225	0.14	0.143	0.202	0.144	0	-0.163	12.549	-12688	-0.083	7.739
	high	0	0.285	0.283	0.055	0.046	0.192	0.185	0	-3.988	14.913	-377319	-0.472	5.209
	all	0	0.223	0.257	0.093	0.09	0.196	0.141	0	-2.263	14.026	-390006	-0.405	6.133
PEA	low	0	0.104	0.359	0.115	0.124	0.203	0.094	0.001	-0.763	10.361	-79903	1.559	29.107
	high	0	0.219	0.455	0.043	0.034	0.167	0.083	0	-4.459	14.234	-309984	-0.638	14.834
	all	0	0.15	0.397	0.086	0.088	0.189	0.089	0	-2.238	12.192	-389913	0.029	20.842
EGA	low	0	0.162	0.342	0.054	0.047	0.221	0.174	0	-0.01	14.357	-927	0.702	9.562
	high	0.001	0.4	0.191	0.022	0.021	0.152	0.213	0	-6.512	23.99	-509770	-0.305	4.468
	all	0.001	0.271	0.273	0.039	0.035	0.189	0.192	0	-2.996	19.654	-510697	-0.343	6.472
Average PGAS		0	0.178	0.33	0.083	0.078	0.212	0.123	0	-2.03	13.16	-221704	0.165	11.669
Marginal														
MP														
MP all	low	0	0.044	0.403	0.154	0.138	0.217	0.046	0	-0.57	6.698	-187333	1.734	24.938
	high	0	0.103	0.398	0.151	0.087	0.219	0.042	0	-2.343	9.661	-781650	-1.971	20.923
	all	0	0.073	0.423	0.13	0.112	0.218	0.044	0	-1.463	8.371	-968983	-1.196	24.671
ING	low	0	0.036	0.368	0.157	0.142	0.26	0.036	0	-0.36	5.713	-20387	-0.002	16.155
	high	0	0.005	0.374	0.179	0.15	0.283	0.01	0	-0.04	3.344	-3540	1.031	22.332
	all	0	0.017	0.372	0.17	0.147	0.274	0.02	0	-0.166	4.431	-23927	0.211	21.974
KG	low	0	0.033	0.371	0.203	0.186	0.183	0.025	0	-0.859	5.102	-66863	-0.129	14.803
	high	0	0.048	0.514	0.118	0.095	0.206	0.019	0	-1.75	5.162	-165402	-0.18	6.527
	all	0	0.041	0.449	0.156	0.136	0.195	0.022	0	-1.348	5.154	-232265	-0.159	10.074
PEA	low	0	0.03	0.4	0.173	0.153	0.208	0.036	0	-0.503	6.528	-52510	3.404	51.823
	high	0	0.073	0.551	0.074	0.055	0.202	0.045	0	-1.648	8.235	-115485	1.237	22.391
	all	0	0.048	0.461	0.133	0.114	0.206	0.04	0	-0.963	7.283	-167995	2.131	34.84
EGA	low	0	0.072	0.455	0.087	0.075	0.229	0.081	0	-0.531	8.455	-47533	1.342	10.644
	high	0.001	0.297	0.341	0.041	0.038	0.182	0.101	0	-6.095	16.117	-496391	-1.225	8.059
	all	0	0.179	0.401	0.065	0.057	0.207	0.091	0	-3.18	12.994	-543924	-1.278	11.516
Average PGAS		0	0.073	0.421	0.13	0.112	0.22	0.044	0	-1.454	7.376	-161352	0.532	19.262
MO														
MO all	low	0	0.061	0.399	0.144	0.127	0.223	0.047	0	-0.877	6.966	-287580	0.181	46.132
	high	0	0.131	0.401	0.109	0.09	0.225	0.044	0	-2.746	10.216	-915616	-2.791	37.137
	all	0	0.096	0.4	0.127	0.108	0.224	0.045	0	-1.819	8.806	-1203223	-2.267	43.876
ING	low	0	0.041	0.393	0.158	0.126	0.248	0.034	0	-0.514	5.856	-28689	0.522	13.255
	high	0	0.004	0.33	0.214	0.17	0.276	0.006	0	0.004	3.005	332	0.229	16.461
	all	0	0.018	0.354	0.192	0.153	0.265	0.017	0	-0.196	4.343	-28357	0.428	19.144
KG	low	0	0.07	0.313	0.187	0.174	0.209	0.048	0	-0.812	7.074	-63141	-2.515	119.517
	high	0	0.127	0.42	0.097	0.084	0.228	0.045	0	-2.336	8.008	-221057	-3.556	151.389
	all	0	0.101	0.372	0.137	0.125	0.219	0.046	0	-1.649	7.638	-284198	-3.186	140.495
PEA	low	0	0.05	0.402	0.156	0.142	0.211	0.038	0	-0.891	6.771	-93145	1.611	40.036
	high	0	0.102	0.543	0.074	0.056	0.19	0.036	0	-2.534	8.365	-176514	-0.375	19.759
	all	0	0.07	0.459	0.123	0.171	0.14	0.037	0	-1.548	7.493	-269686	0.436	28.732
EGA	low	0	0.079	0.473	0.085	0.067	0.233	0.063	0	-1.142	7.682	-102581	0.803	8.706
	high	0.002	0.304	0.332	0.039	0.036	0.196	0.091	0	-6.458	16.248	-520658	-1.683	10.477
	all	0.001	0.185	0.406	0.063	0.052	0.215	0.076	0	-3.657	12.768	-623238	-1.941	15.378
Average PGAS		0	0.096	0.4	0.127	0.113	0.219	0.045	0	-1.811	7.937	-200911	-0.769	48.612

**Table A3.2** Deviation in valley characteristics from DEM values.

DEM Valley CSA		Interior							Marginal						
		n	prominence differen		width difference (m		CSA difference (m2)		n	prominence differen		width difference (m		CSA difference (m2)	
			μ	σ	μ	σ	μ	σ		μ	σ	μ	σ	μ	σ
CSA < 1	ING	39	7.21	44.48	397.63	1,302.06	53,777.31	128,522.78	48	-1.96	9	-14.38	248.43	9,733.43	20,593.68
	KG	31	15.82	71.57	557.05	1,786.87	88,456.78	300,186.20	31	10.1	70	316.15	1,507.28	69,333.41	271,658.22
	PEA	23	17.38	120.63	496.65	2,280.80	116,382.23	486,604.61	27	14.16	103.81	407.92	2,063.85	92,343.72	446,374.12
	EGA	3	-44.12	70.35	12.66	12.11	4,568.44	9,107.58	5	-40.68	48.28	-2.83	10.77	-2,060.62	11,754.36
105 < CS	ING	100	0.58	53.65	385.06	1,545.02	85,304.70	321,061.12	103	-1.29	12.67	167.28	664.32	43,803.12	183,364.06
	KG	561	-3.8	28.91	14.79	533.45	3,323.36	189,941.31	609	-1.89	16.87	38.67	419.94	12,616.93	165,032.25
	PEA	216	3.36	65.39	114.88	863.5	34,495.43	232,043.88	222	-1.95	22.06	23.59	314.77	18,130.43	204,283.73
	EGA	226	-20.35	52.22	65.58	504.13	71,121.63	528,855.16	269	-10.3	41.53	29.02	340.83	33,803.27	401,347.61
106 < CS	ING	38	-7.03	42.77	-644.2	2,297.25	-158,969.00	489,504.45	39	1.85	2.59	-53.26	423.93	-20,726.86	196,666.71
	KG	104	-14.93	61.78	-439.94	1,379.84	-162,893.35	438,707.10	109	-10.39	45.65	-315.51	1,310.33	-129,155.19	466,563.92
	PEA	140	-22.9	104.5	-458.05	2,137.40	-138,713.85	448,948.67	141	-6.65	47.02	-91.91	457.92	-58,721.02	308,265.43
	EGA	508	-32.68	26.95	-13.18	554.24	-29,149.47	679,635.16	542	-17.32	26.32	-26.97	294.78	-39,679.15	400,610.60
Total	ING	177	0.41	49.53	166.86	1,731.79	25,914.83	348,538.31	190	-0.82	10.49	76.12	547.47	21,950.41	163,405.47
	KG	696	-4.59	38.67	-29	831.52	-17,721.76	255,923.73	749	-2.63	27.29	-1.39	708.68	-5,667.38	243,424.23
	PEA	379	-5.49	86.51	-73.59	1,581.66	-24,517.50	355,740.79	390	-2.53	42.64	8.44	656.74	-4,516.48	270,620.26
	EGA	737	-28.94	37.16	11.07	539.09	1,735.77	637,044.68	816	-15.15	32.46	-8.37	310.76	-15,224.66	400,867.22
	All	1989	-13.34	53.1	-5.22	1,046.09	-7,923.72	456,270.66	2145	2.85	1.03	4.61	563.15	-6,647.57	312,251.43

Table A3.3 Coefficients for interior valley geometry correction where valley cross-section profiles surveyed in areas with ice thickness exceeding 2000 m.

x	m	c	RMSE	R^2
Valley cross-section CSA	0.98	2.08E+04	3.10E+05	0.98
Valley cross-section depth	0.96	-1.62	52.2	0.95
Valley cross-section width	0.93	168	1024	0.89

Table A4.1 Kriging parameters for topographic grids generated for interpolation error assessment.

| PGA	Flight-line setup	sill (h)	range (m)	PGA	Flight-line setup	sill (h)	range (m)
Optimised by ArcMap 10.6.1 iterative cross validation function, mimimising RMSE prediction error. All use 100 lags of 100 m in line with previous workflows.						
ING	1 km GRID	383	639	KG	1 km GRID	2595	647
	5 km GRID	29291	47304		5 km GRID	2752	755
	10 km GRID	30885	46980		10 km GRID	22906	8234
	15 km GRID	13	63		15 km GRID	29611	11613
	1 km MO	1565	1963		1 km MO	24302	8315
	5 km MO	7	28		5 km MO	24593	11237
	10 km MO	7	28		10 km MO	11	10490
	15 km MO	6	28		15 km MO	11	28
	1 km MP	25920	42047		1 km MP	9031	1705
	5 km MP	10	28		5 km MP	25307	8184
	10 km MP	5	28		10 km MP	25549	7440
	15 km MP	8	28		15 km MP	25736	8732
PEA	1 km GRID	94184	15088	EGA	1 km GRID	53125	5235
	5 km GRID	96044	15783		5 km GRID	10995	779
	10 km GRID	90697	11122		10 km GRID	49364	5497
	15 km GRID	88334	15645		15 km GRID	3043	341
	1 km MO	409	242		1 km MO	20615	1332
	5 km MO	103880	17439		5 km MO	58729	7553
	10 km MO	109027	17437		10 km MO	271	80
	15 km MO	90326	19997		15 km MO	41983	6217
	1 km MP	465	197		1 km MP	34411	20348
	5 km MP	94087	16345		5 km MP	51762	5198
	10 km MP	91719	12635		10 km MP	59791	5918
	15 km MP	72746	12077		15 km MP	36359	2370
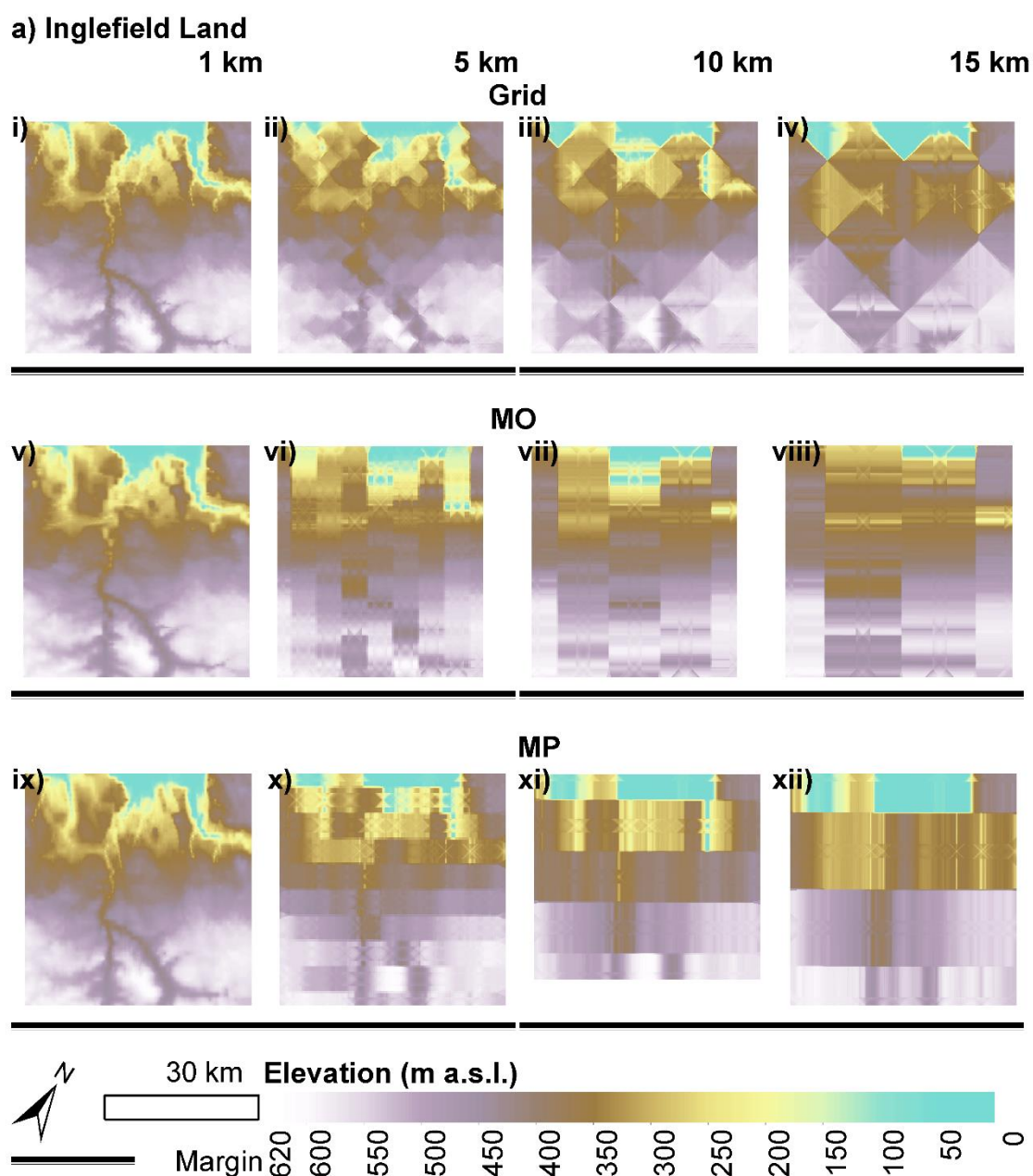
Figure A4.1 a) Kriged bed topography grids of the Inglefield Land PGA. Input flight-line survey density decreases from left to right with increasing line spacing. Margin position and direction is illustrated by the graded black line. Gridded survey results are shown in panels i – iv, margin orthogonal survey results in v – viii, and margin parallel in ix – xii.
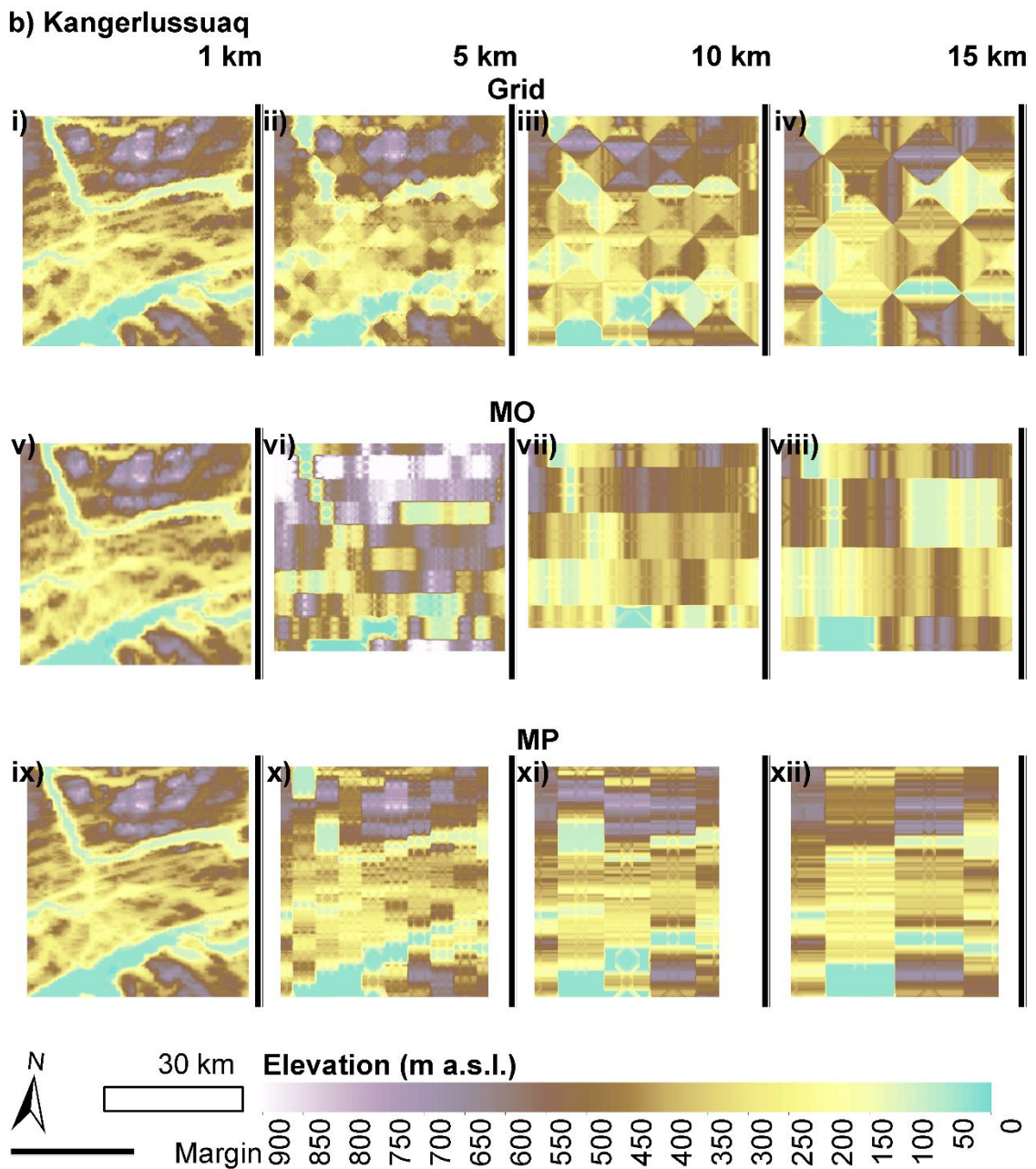
Figure A4.1 cont. b) Kriged bed topography grids of the Kangerlussuaq PGA. Input flight-line survey density decreases from left to right with increasing line spacing. Margin position and direction is illustrated by the graded black line. Gridded survey results are shown in panels i – iv, margin orthogonal survey results in v – viii, and margin parallel in ix – xii.
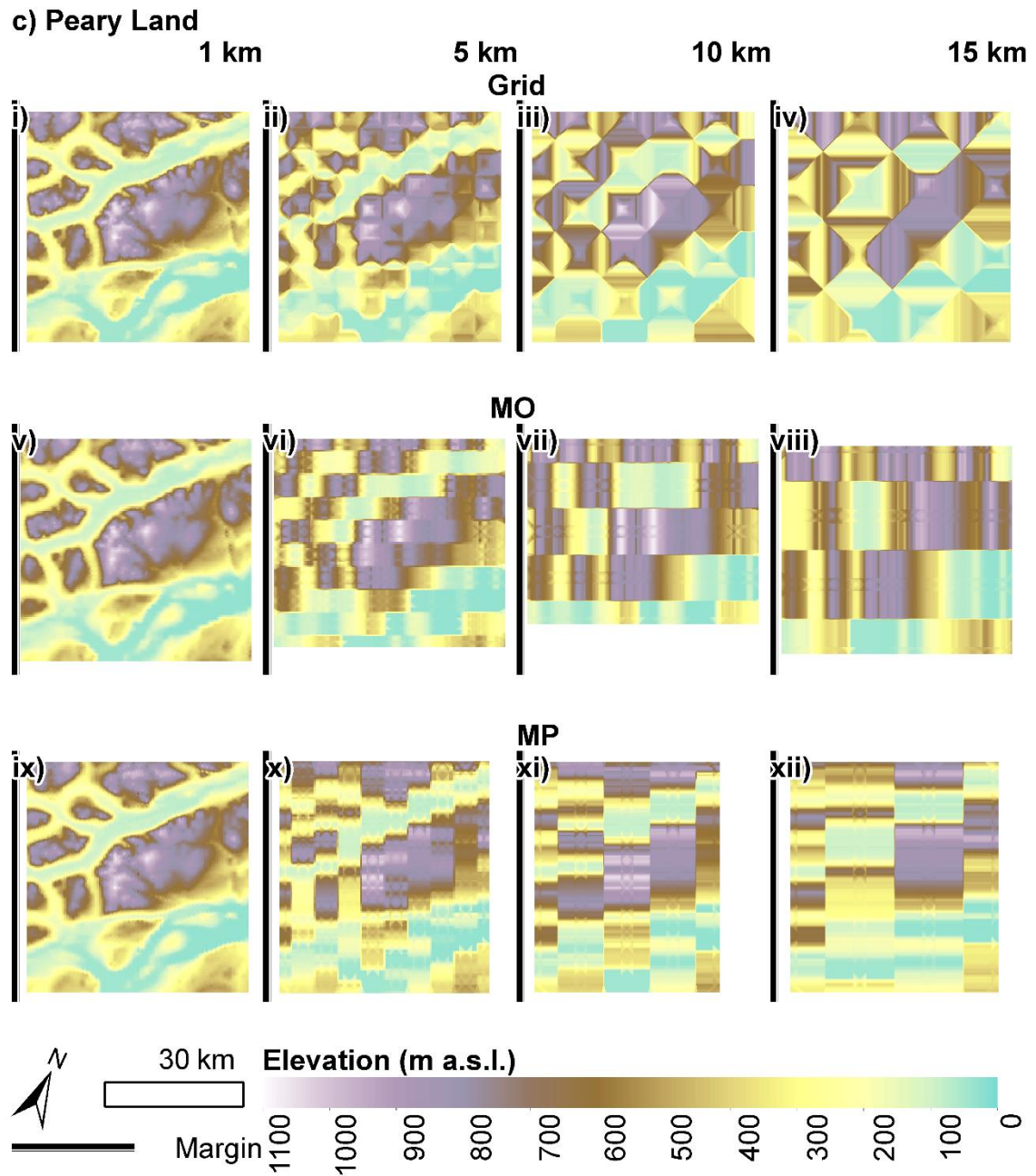
Figure A4.1 cont. c) Kriged bed topography grids of the Peary Land PGA. Input flight-line survey density decreases from left to right with increasing line spacing. Margin position and direction is illustrated by the graded black line. Gridded survey results are shown in panels i – iv, margin orthogonal survey results in v – viii, and margin parallel in ix – xii.
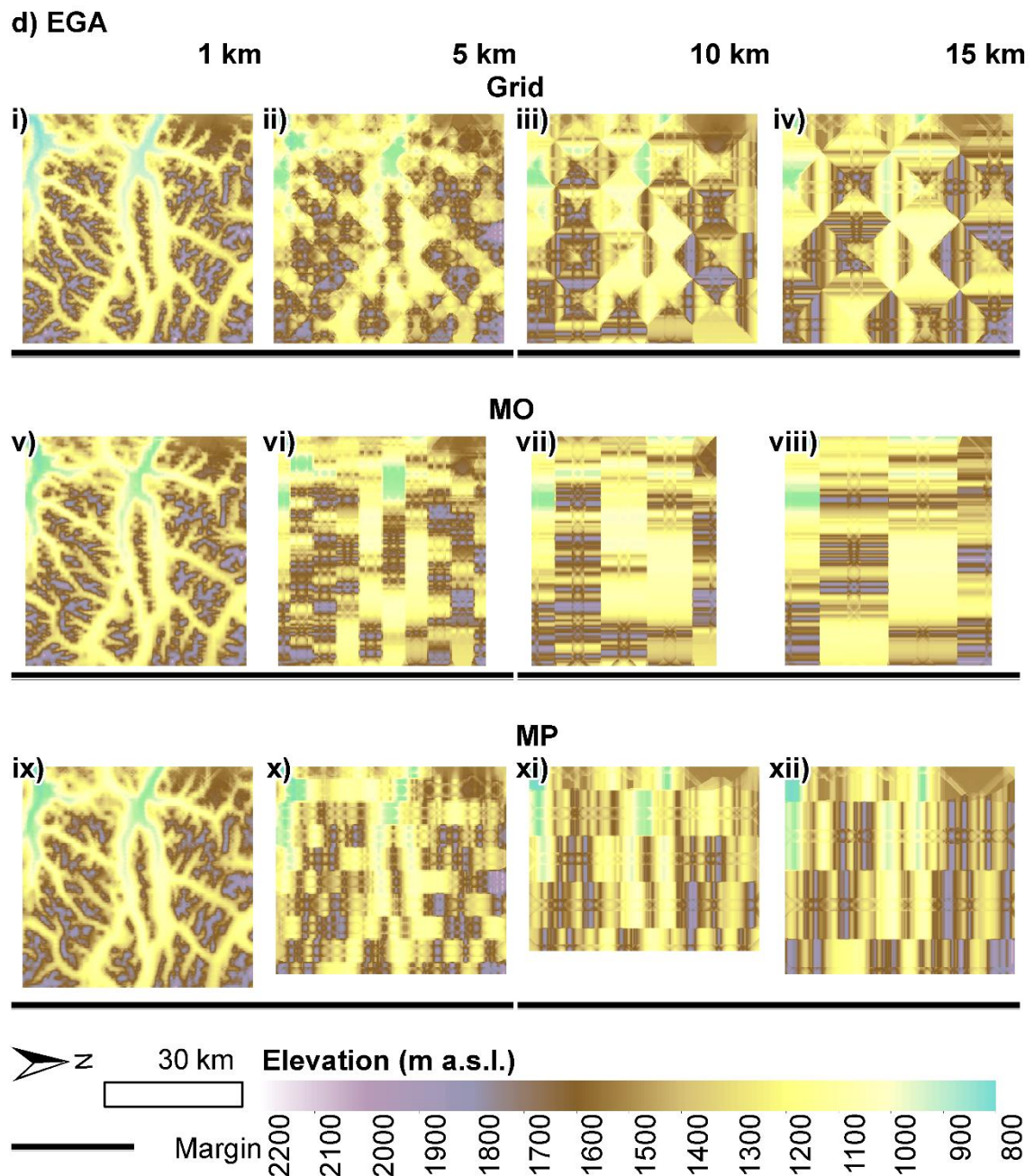
d) EGA

1 km   5 km   10 km   15 km

Grid

i) ii) iii) iv)

MO

v) vi) vii) viii)

MP

ix) x) xi) xii)

z   30 km   **Elevation (m a.s.l.)**

Margin   2200 2100 2000 1900 1800 1700 1600 1500 1400 1300 1200 1100 1000 900 800

Figure A4.1 cont. d) Kriged bed topography grids of the EGA PGA. Input flight-line survey density decreases from left to right with increasing line spacing. Margin position and direction is illustrated by the graded black line. Gridded survey results are shown in panels i – iv, margin orthogonal survey results in v – viii, and margin parallel in ix – xii.
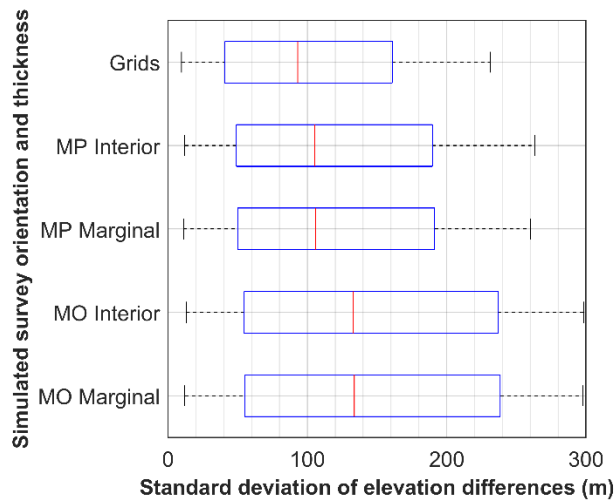
Figure A4.1 Boxplot showing variation in interpolation quality as a result of survey geometry and proximity to the bed.

Table A4.2 Descriptive statistics for interpolation error based on input proglacial area and survey geometry

| | PGA (statistic (m)) | | | | | | | | | | | | | | | | | | | |
| | ING | | | | KG | | | | PEA | | | | EGA | | | | All | | | |
Simulated survey setup	mean	std	skew	kurt	mean	std	skew	kurt	mean	std	skew	kurt	mean	std	skew	kurt	mean	std	skew	kurt
Grid	2.21	42.7	0.284	15.5	-8.47	104	-0.145	8.23	1.92	148	0.081	10.7	-13	181	-0.23	5.24	-4.73	133	-0.198	9.97
MP Marginal	-5.09	53	-1.04	11.18459	-0.45	111	0.479	8.61	-13.4	168	-0.504	8.22	-1.84437	203	0.011	4.69	-5.2	148	-0.151	8.7
MP Interior	-4.92	52.6	-0.989	11.13498	-0.753	111	0.52	8.82	-13.9244	167	-0.511	8.26	7.12	202	0.062	4.88	-3.06	147	-0.071	8.91
MO Marginal	8.37	53.3	0.839	11.4	-17	141	-0.213	5.61	26	216	0.392	6.28	-22.9	225	-0.234	4.43	-2.05	177	0.022	7.45
MO Interior	8.25	53.1	0.867	11.5	-17	140	-0.204	5.619056	25.1	215	0.39	6.31	-18.4	224	-0.234	4.53	-1.1	176	0.033	7.55

Table A5.1 Input OIB flight lines from Paden, J., J. Li, C. Leuschen, F. Rodriguez-Morales, and R. Hale. 2010, updated 2019. IceBridge MCoRDS L2 Ice Thickness, Version 1. Boulder, Colorado USA. NASA National Snow and Ice Data Center Distributed Active Archive Center. doi: https://doi.org/10.5067/GDQ0CUCVTE2Q. [2019].

MCR2_20170329_02
MCR2_20110510_04
MCR2_20120517_02
MCR2_20140506_01
MCR2_20170426_02
MCR2_20140401_03
MCR2_20110510_02
MCR2_20170330_02

```
//Import Ice Cap

var icecap = ee.FeatureCollection(UPLOADED ICE CAP SHAPEFILE(can use GLIMS through EE))

//Import ArcticDEM Strips in region of ice cap

var dataset = ee.ImageCollection('UMN/PGC/ArcticDEM/V3/2m')

var colFilter = ee.Filter.and(

        ee.Filter.bounds(icecap));

        dataset = dataset.filter(colFilter)

         print(dataset)

//Set Visualisation Parameters

var elevation = dataset.select('elevation');

var elevationVis = {

        min: -50.0,

        max: 1000.0,

  palette: ['0d13d8', '60e1ff', 'ffffff'],

};

// Display the region of interest.

Map.centerObject(icecap);

Map.addLayer(icecap, [], 'Ice Cap');

//Mosiac mean elevation over a date range and add mosaic

var meanADEM = dataset.filterDate('2017-01-01', '2017-12-31').mean();

var mosaicADEM = ee.ImageCollection([meanADEM,]).mosaic();

mosaicADEM = mosaicADEM.clip(icecap)

Map.addLayer(mosaicADEM.select('elevation'), elevationVis, 'Mosaic')

// Generate the hypsometry.

var histogram = ui.Chart.image.histogram({

        image: mosaicADEM.select('elevation'),

         region: icecap,

        scale: 50,

        minBucketWidth: 50

});

print(histogram,'Hypsometry');

//Export

Export.image.toDrive({

        image: mosaicADEM.select('elevation'),

        description: 'Ice_Cap_Surf',

        scale: 50,

        fileFormat: 'GeoTIFF',

         maxPixels: 10e11

});
```

Figure A5.1 Google Earth Engine code for determining CAA mean annual surface hypsometry.